**Jorge André Almeida Barreto**

Master of Science in Physics Engineering

# Development of a 40 K to 80 K vibration-free cooler for future Earth observation missions

Thesis submitted in partial fulfillment
of the requirements for the degree of

Doctor of Philosophy in
**Physics Engineering**

Adviser: Grégoire Bonfait,
Professor, Universidade NOVA de Lisboa

Co-adviser: Daniel Martins,
Thermal Engineer, ASML

Examination Committee

Chair: Prof. Doutor José Paulo Moreira dos Santos
Rapporteurs: Prof. Doutor António Joaquim Rosa Amorim Barbosa
Doutor Thomas Prouvé
Members: Prof. Doutor Grégoire Marie Jean Bonfait
Prof. Doutor Daniel Cardoso Vaz
Doutor Diogo Manuel Carvalho Lopes

FACULDADE DE CIÊNCIAS E TECNOLOGIA
UNIVERSIDADE NOVA DE LISBOA

**October, 2020**

**Development of a 40 K to 80 K vibration-free cooler for future Earth observation missions**



This document was created using the (pdf)LaTeX processor, based on the "novathesis" template[1], developed at the Dep. Informática of FCT-NOVA [2].
[1] https://github.com/joaomlourenco/novathesis [2] http://www.di.fct.unl.pt

# Acknowledgements

I would like to deeply thank my advisors, Prof. Grégoire Bonfait and Dr. Daniel Martins, for their guidance, availability and commitment during the course of this challenging journey, and also for the opportunity to learn cryogenics since 2014 in the cryogenics laboratory of the Department of Physics (FCT NOVA). The professional and academic experience I acquired is thanks to them, it is something that will accompany me for the rest of my life. Also to my lab colleagues, Mário Xavier, Miguel Baeta, I express my gratitude for the help in carrying out this work.

I would also like to thank the readiness and companionship of João Faustino and Eduardo Jobling from the workshop of the Department of Physics, without them, everything have been much more difficult and time consuming.

To João Noite and Moritz Branco, our partners from Active Space Technologies, who were always available to receive us for discussions, to share their equipment and knowledge, it was a pleasure to work and learn from them.

To our colleagues and partners in this project, Prof. Paulo Mota, Dr. Rui Ribeiro and Dr. Isabel Esteves from the Department of Chemistry (FCT NOVA), I thank for their technical advices and invaluable help in matters related to adsorption.

To Dr. António Gonçalves and Dr. Joaquim Branco, from the Center for Nuclear Sciences and Technologies (IST), I thank for their help and availability for the development of the metal hydride.

To Prof. Teresa Avilés, Prof. Carlos Salgueiro, Dr. Vitor Rosa and Mani Hosseinzadeh, from the Department of Chemistry (FCT NOVA), who were always available to receive us countless times to use their glove-box, essential for the progress of this project.

To Prof. Rui Silva, from the Department of Materials Science (FCT NOVA), thanks for the images you provided us with the scanning electron microscope.

To Thierry Tirolien, the technical officer at European Space Agency (ESA), my sincere thanks for his support and technical advice during the many discussions throughout this project.

To my friends and colleagues Gonçalo Tomás and João Pedro Lourenço, I would like to express my gratitude for their friendship, help and encouragement over the past few years.

To my family and my girlfriend, Andreia Serrano, I would like to express my gratitude for their patience, help, friendship and support, which undoubtedly made it possible to achieve my goals, without them I would not have the necessary courage and strength.

Lastly, the financial support from ESA is gratefully acknowledged[1].

[1] ref. 4000114171/15/NL/KML

# Abstract

A solution for a sorption-based 40 K to 80 K Joule-Thomson cooler is presented to answer the needs of potential future Earth observation infrared missions with very low micro-vibration levels requirements from the European Space Agency. The studied solution in this thesis is limited to the development of one Joule-Thomson stage using nitrogen gas to provide 1.5 W at 80 K. The fluid circulation and compression are achieved through thermal cycling of an adsorbent material specifically chosen for its purpose: three metal organic framework materials were studied to fulfil this operation. A detailed design and manufacturing of an elegant breadboard model based on the various stringent requirements is shown. The characterization and validation of some of the vibration-free cooler components was carried out: results and its engineering challenges are presented.

**Keywords:** Cryogenics, sorption compressor, Joule-Thomson cooler, vibration-free

# Resumo

Para atender às necessidades de futuras missões infravermelho de observação da Terra com requisitos de níveis de micro-vibração muitos reduzidos da Agência Espacial Europeia, um criorrefrigerador de adsorção entre 40 K a 80 K baseado no efeito Joule-Thomson é apresentado. A solução encontrada e estudada em pormenor nesta dissertação está limitada ao desenvolvimento de um estágio Joule-Thomson usando o gás de azoto para fornecer uma potência frigorífica de 1.5 W a 80 K. A circulação e compressão do fluído é obtida e controlada através de ciclos térmicos de um material de adsorção adequadamente escolhido para esse fim: três materiais com estruturas metalorgânicas (metal organic framework, em inglês) foram estudados para realizar esta operação. Um desenho detalhado e construção do criorrefrigerador tendo em conta os vários requisitos rigorosos de uma missão de observação da Terra são apresentados. A caracterização e validação de alguns componentes deste criorrefrigerador sem vibrações foram realizadas: os resultados e desafios de engenharia são apresentados.

**Palavras-chave:** Criogenia, compressor térmico, criorrefrigerador Joule-Thomson, sem vibrações.

# Contents

# List of Figures

# List of Tables

# Acronyms

| | |
|---|---|
| ADC | Analog-to-Digital Converter |
| AST | Active Space Technologies |
| BET | Brunauer–Emmett–Teller |
| CAD | Computer-Aided Design |
| CFHX | Counter Flow Heat Exchanger |
| CMB | Cosmic Microwave Background |
| COBE | Cosmic Background Explorer |
| COP | Coefficient of Performance |
| CuHX | Copper Heat Exchanger |
| EBW | Electron-Beam Welding |
| E-ELT | European-Extremely Large Telescope |
| ESA | European Space Agency |
| ESO | European Southern Observatory |
| ESU | Energy Storage Unit |
| FCT NOVA | NOVA School of Science and Technology |
| FPGA | Field-Programmable Gate Array |
| GCMC | Grand Canonical Monte Carlo |
| GGHS | Gas Gap Heat Switch |
| GM | Gifford-MacMahon |
| HFI | High Frequency Instrument |
| HP | High-Pressure |
| I/O | Input/Output |
| IR | Infrared Radiation |
| IST | Instituto Superior Técnico |
| JT | Joule-Thomson |
| LFI | Low Frequency Instrument |

| | |
|---|---|
| LH | Linde-Hampson |
| LMTD | Logarithmic Mean Temperature Difference |
| LN2 | Liquid Nitrogen |
| LP | Low-Pressure |
| METIS | Mid-Infrared E-ELT Imager and Spectrograph |
| MOF | Metal-Organic Framework |
| MOSFET | Metal Oxide Semiconductor Field Effect Transistor |
| NASA | National Aeronautics and Space Administration |
| NI | National Instruments |
| NIST | National Institute of Standards and Technology |
| OS | Operating System |
| PID | Proportional–Integral–Derivative |
| PTC | Pulse Tube Cooler |
| PWM | Pulse-Width Modulation * |
| REFPROP | Reference Fluid Thermodynamic and Transport Properties Database |
| RMS | Root Mean Square |
| RT | Room Temperature |
| RTD | Resistance Temperature Detector |
| SC | Sorption Compressor |
| SEM | Scanning Electron Microscopy |
| SS | Stainless Steel |
| TC | Thermocouple |
| TGA | Thermal Gravimetric Analysis |
| TRP | Technical Research Program |
| vdW | van der Walls |
| VFC | Vibration-Free Cooler |
| WMAP | Wilkinson Microwave Anisotropy Probe |

CHAPTER 1

# Introduction

Astronomy began in early historic times with simple observations and predictions of the motion of celestial objects visible to naked eye. Nowadays, it is possible to watch different regions of the electromagnetic spectrum using rather complex systems either in orbit or on Earth. Over the past years, space observation has evolved in such way that many of the developed detectors requires complex systems using cryogenic technologies to allow detection in infrared, gamma-ray and X-ray range with extremely low background noise and improved sensitivity.

Right after the launch of Sputnik in 1957, engineers and scientists seek for means of providing cryogenic cooling for very sensitive detectors either for military defense or Earth science communities. However, it is well known that getting a payload into orbit is a very expensive procedure. So, there is a demand of reliable, long life and light cooling systems and, therefore, the developed cooling systems for space applications are very distinct from typical commercially available equipments. For each mission, each cooling system is developed with a particular design and due to its high level of sophistication and usually hand-built, it corresponds to a high price [1].

Low temperatures may be obtained in a spacecraft by using stored cryogenic fluids or cryocoolers[1]. Stored cryogens are a simpler and cheaper solution but with limited lifespan, which is typically not compatible with long term missions and also not compatible with stringent volume/mass requirements. Therefore, cryocoolers are nowadays the prime choice, mainly for being compact and capable of providing cooling for many years [2]. However, placing a cryocooler inside a spacecraft can be quite challenging: on one hand, it requires a compact system, space-worthy subsystem; on the other hand, such subsystem must minimize its thermal and mechanical impact on its environment. For that reason, the miniaturization of cryocoolers has been a work in

[1] A refrigerator designed to reach cryogenic temperatures.

constant progress for the past twenty years and many advances have been made in that field, such as the development of pulse tube coolers (PTC) or Stirling type cryocoolers for Earth observation missions. These cryocoolers are capable of providing significant cooling power in the region of 50 K for infrared observation.

Nowadays, in most cases, Earth observation detection relies on low temperatures provided by classical mechanical cryocoolers (PTC, Stirling). Such mechanisms contain moving parts to create a wave of pressure and matter (gas), which induce undesirable vibrations and consequently lead to degradation in the performance of the detectors. Even with active vibration cancellation systems and careful screening and manufacturing, unwanted vibrations still remain. For instance, with the development of magnetic bearing reaction wheels and micro-thrusters, classical mechanical cryocoolers become the main source of micro-vibrations in a satellite [3]. Alternatively, by using the Joule-Thomson effect where the flow is provided continuously, contrarily to the PTC or the Stirling cycles, is one solution to avoid pressure oscillations and moving parts. However, they usually rely on mechanical compressors, which also brings undesirable vibrations to a system level.

Hence, it is necessary to develop new cooling solutions or adapt the current cooling technologies. The development studies for the Darwin satellite covered 15 K and 4 K class coolers [4], but a need also exists in the 40 K to 80 K range for infrared detection [5]. To satisfy this need, European Space Agency (ESA) has launched a technical research program in 2014 and this call was answered by a Portuguese consortium: LIBPhys[2] (research center unit) and Active Space Technologies (private company), that has been working together on the development of such vibration-free cooling solution in the temperature range of interest.

This dissertation shows the current development of a 40 K to 80 K Joule-Thomson cooler based on thermal compression (sorption compression), which is a very attractive technology that can provide cooling to instruments, detectors and telescopes when a completely vibration-free system is needed. Moreover, such configuration is, theoretically, a perfect candidate to provide a cold interface for highly-sensitive payloads and has proven to be a reliable solution in previous successful space missions, such as ESA's Plank science mission [6, 7].

The Joule-Thomson cooler mainly consists in two subsystems: the sorption compressor and the Joule-Thomson stage. The sorption compressor provides the circulation of the fluid only by heating and cooling sequentially its sorbent beds. In this subsystem there are no moving parts (no pistons or turbines), then, no mechanical vibration is generated, making it extremely reliable and enduring. The Joule-Thomson

[2]Laboratory for Instrumentation, Biomedical Engineering and Radiation Physics

stage relies on the well known Joule-Thomson effect that simply consists in an forced expansion through a flow restriction, where, upon certain conditions, this fluid cools down and liquefies.

## 1.1 Outline

This dissertation describes the study and development of a 40 K to 80 K vibration-free cooler for future Earth observation missions, it is divided into eight chapters:

- Chapter 1 gives an introduction to this dissertation.
- Chapter 2 describes the theoretical aspects of a sorption-based Joule-Thomson cooler: JT effect, classical thermodynamic analysis of a Linde-Hampson cycle. It also covers some theoretical and practical aspects of adsorption and sorption compressors.
- Chapter 3 shows the baseline design solution of a 40 K to 80 K vibration-free cooler considering the system requirements from ESA. It is also described some other sorption based coolers working in temperature and cooling power close to our requirements.
- Chapter 4 presents the preliminary selection of the adsorbent materials needed to build the sorption compressor and the experimental characterization of three potential adsorbent materials over a wide pressure range of 1 bar to 100 bar and temperature range of 77 K to 500 K.
- Chapter 5 displays the design, dimensioning and characterization of several components of the Joule-Thomson cold stage, such as: orifice restriction, counter-flow heat exchanger and evaporator.
- Chapter 6 shows the detailed design, integration and validation of the components from a nitrogen sorption compressor cell. It also includes the assembly of a new 200 L cryostat to test the cooler.
- Chapter 7 shows the characterization of a JT cooler fed by a single sorption cell of nitrogen.
- Chapter 8 ends with some final remarks and learned lessons.

CHAPTER 2

# Fundamentals of Sorption Based Joule-Thomson Coolers

## 2.1 Joule-Thomson Effect

The Joule-Thomson effect is named after its discovery by James Joule and William Thomson (Lord Kelvin) in 1852. At room temperature, Joule and Thomson found out that almost all gases cool during an expansion (pressure reduction) through small restrictions, behavior not consistent with the ideal gas model. Moreover, the observed "irregularity"of the warming hydrogen as it expands led to the comprehension of the inversion temperature and they concluded that this cooling effect is only obtained upon certain conditions. The effect is actually a manifestation of real gases properties, namely, the existence of intermolecular forces and numerous studies were conducted in a attempt to find an universal equation of state which properly describes the pressure-volume-temperature relationship of gases more accurately than does the ideal gas equation of state.

For instance, in 1873, the Dutch physicist van der Walls (vdW) proposed two simple empirical modifications to the well known ideal gas law $Pv = RT$. The first modification was to replace the specific volume $v$ with $(v - b)$, where $b$ is a small positive constant that takes into account that real gases are not infinitely compressible, since molecules have finite volume. The second modification accounts for the attractive forces between molecules, molecules about to strike the walls experience a restraining force due to their attraction with other molecules placed behind them, so, this lowers the speed that they would strike the walls, hence, reducing the pressure. This pressure reduction proposed by vdW is proportional to $a/v^2$, where $a$ is a small positive constant. Considering

these modifications, the vdW equation of state is obtained as follows,

$$\left(P + \frac{a}{v^2}\right)(v - b) = RT \tag{2.1}$$

In the case that the molar volume, $v$, is large enough, the term $a/v^2$ becomes negligible when compared with $P$ and $b$ becomes negligible in comparison with $v$, thus, the vdW equation reduces to the equation of state of an ideal gas. Later in 2.1.1, it is shown that the vdW equation of state successfully predicts the Joule-Thomson effect.

Nowadays, the Joule-Thomson throttling (another name for the effect) is well understood and it is the driving force that empowers the operation of Linde-Hampson machines, JT cryocoolers, liquefiers and refrigerators.

### 2.1.1 Joule-Thomson Coefficient

The rate of temperature, $T$, change with respect to pressure, $P$, under a Joule-Thomson (JT) expansion at constant enthalpy, $h$, is quantified by the adiabatic Joule-Thomson coefficient, $\mu_{JT}$,

$$\mu_{JT} = \left(\frac{\partial T}{\partial P}\right)_h \tag{2.2}$$

For an ideal gas, the enthalpy is solely function of temperature and pressure independent. Therefore, at constant enthalpy, a change in pressure cannot produce a change in temperature, consequently $\mu = 0$, showing that, for an ideal gas, the temperature does not change during a JT expansion.

By definition, in an expansion, the sign of $\mathrm{d}P$ is always negative, therefore, to obtain a cooling effect ($\mathrm{d}T < 0$) the value $\mu_{JT}$ must be positive. However, since a gas may cool or warm after an expansion, this implies that the quantity $\mu_{JT}$ can either be positive or negative. It was further concluded that all gases have an inversion temperature in which the value $\mu_{JT}$ changes sign. Through thermodynamics, the following equation of $\mu_{JT}$ is obtained,

$$\mu_{JT} = \frac{1}{c_p}\left[T\left(\frac{\partial v}{\partial T}\right)_P - v\right] \tag{2.3}$$

where $c_p$ is the specific heat and $v$ is the specific volume. The volumetric thermal expansion coefficient $\beta$, defined as,

$$\beta = \frac{1}{v}\left(\frac{\partial v}{\partial T}\right)_P \tag{2.4}$$

can be inserted into Equation (2.3), to obtain an expression of $\mu_{JT}$ written as a function of commonly available properties,

$$\mu_{JT} = \frac{v}{c_p}(\beta T - 1) \tag{2.5}$$

This useful expression shows that the value $\mu_{JT}$ changes sign when the coefficient of thermal expansion $\beta$ is equal to the inverse of temperature. Combining Equations (2.1) and (2.3), $\mu_{JT}$ is obtained in terms of vdW coefficients,

$$\mu_{JT} = \frac{b}{c_p}\left(\frac{T_{\text{inv}}}{T} - 1\right), \quad T_{\text{inv}} = \frac{2a}{Rb} \tag{2.6}$$

where $T_{\text{inv}}$ is the inversion temperature. The quite simple vdW equation of state predicts an inversion temperature. But in reality, the state equations of real gases are far more complex and as it will be seen later, $T_{\text{inv}}$ also depends on pressure.

In Figure 2.1 it is shown $\mu_{JT}$ for different gases at atmospheric pressure. Helium, hydrogen and neon are three gases whose inversion temperatures are below 300 K. Consequently, these gases will actually warm up when isenthalpically expanded at room temperature. On the other hand, nitrogen and oxygen, the two most abundant gases in the air, have higher inversion temperatures and can be cooled via JT effect at room temperature.

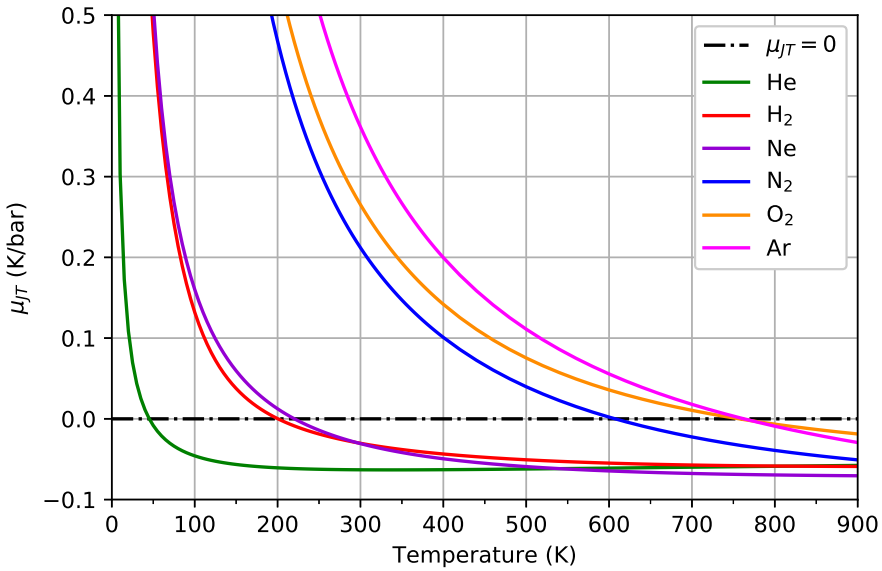


Figure 2.1: Joule-Thomson coefficients, $\mu_{JT}$, for different gases at atmospheric pressure.

By definition, an inversion state defines the transition from cooling to heating under an isenthalpic expansion and, therefore, satisfying the relation: $(\partial T/\partial P)_H = 0$. Figure 2.2 displays the inversion curve (states for which $\mu_{JT} = 0$) of nitrogen in a pressure-temperature, $(P, T)$, plane. Several features are noteworthy:

- Is visible that each isenthalp (dashed lines) is flat when it intersects the inversion curve (solid line). Therefore, satisfying the relation $(\partial T/\partial P)_H = 0$.

- The shaded region corresponds to a positive slope of $(\partial T/\partial P)$, then to a positive $\mu_{JT}$ (i.e. cooling).
- The highest inversion temperature, $T_{\text{MAX}}$, can be identified (point A) and as well as the highest inversion pressure, $P_{\text{MAX}}$ (point B). These values are characteristic of each gas, as visible in Table 2.1. For temperatures or pressures above these limits, no cooling effect is possible under an isenthalpic expansion.
- It is noticeable that in the shaded region some isenthalps are steeper, for instance, the ones closer to the critical point. In this region, the cooling effect is more efficient and it is not by chance that it corresponds to the most common region to obtain liquefaction through JT throttling.

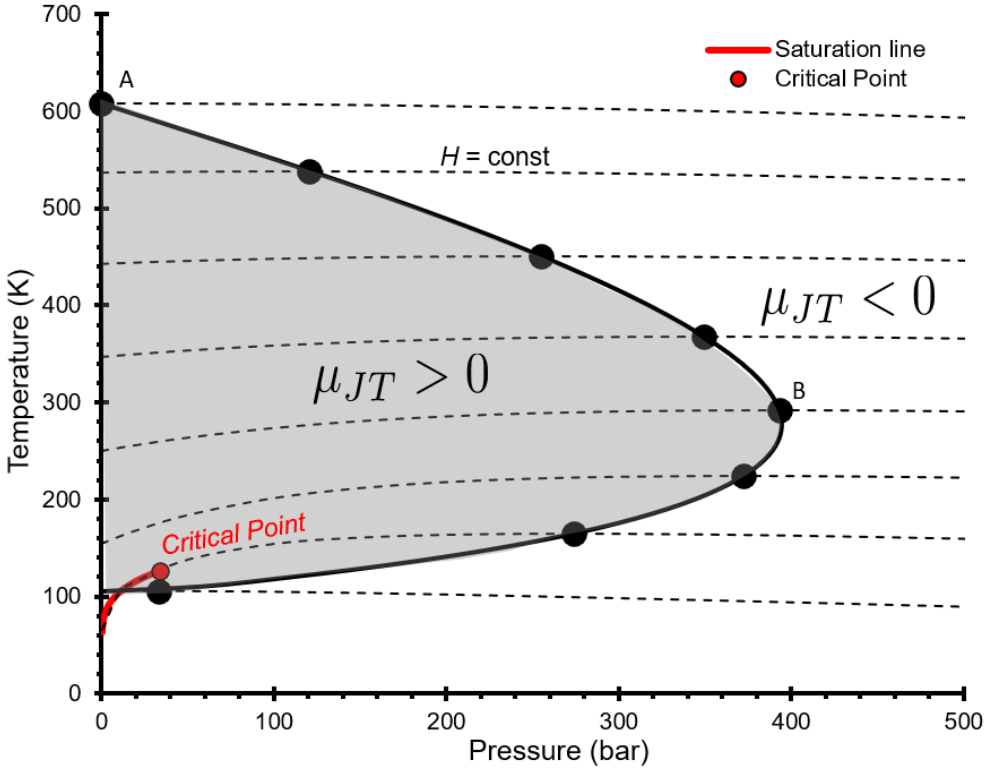


Figure 2.2: Inversion curve of nitrogen in a pressure-temperature plane. Dashed lines are isenthalps and the black solid line is the inversion curve ($\mu_{JT} = 0$).

Table 2.1: Inversion temperatures and pressures (points A and B from Figure 2.2) of various gases.

| Gas | $T_{MAX}$ (K) | $P_{MAX}$ (bar) |
|---|---|---|
| Helium-4 | 43 | 39.2 |
| Hydrogen | 201 | 162.2 |
| Neon | 220 | 297 |
| Nitrogen | 608 | 394 |
| Argon | 763 | 565 |
| Carbon Monoxide | 730 | 400 |
| Oxygen | 757 | 592 |
| Methane | 1009 | 542 |

## 2.2 Joule-Thomson Cold Stage

A basic Joule-Thomson cold stage employs the so-called Linde-Hampson (LH) cycle. This cycle usually starts with pure gases at elevated pressures, typically twice the critical pressure. And, at the cold end, a fraction of this gas is liquefied through a JT throttling process.

### 2.2.1 Linde-Hampson cycle

In 1895, William Hamspon and Carl von Linde independently developed and patented a cooling process to liquefy air. This process was immediately exploited to large-scale air separation plants. Right after Linde's developments, commercially available industrial gases produced by Linde (company) had an huge impact on steel industry: for instance, the invention of the oxyacetylene welding machine in 1903 by Edmond Fouché and Charles Picard makes possible to achieve high temperatures to melt steel, which was really useful to cut or to join steel plates [8]. In Physics, it also had a major impact: in 1908, Kammerlingh Onnes was the first to liquefy helium by using this cycle as a part of a cryogenic chain and allowing the discovery of superconductivity in 1911.

As shown in Figure 2.3, a basic Linde-Hampson cycle consists of a JT restriction, a counter-flow heat exchanger and an evaporator. It is usually driven by a mechanical compressor operating at room temperature. In this cycle, a warm high pressure fluid leaves the compressor (state point 1) and is cooled down in the CFHX ($1 \rightarrow 2$) by exchanging heat with the cooled returning gas, flowing in the opposite direction. After this initial pre-cooling process, the fluid is forced through the JT restriction where it isenthalpically expands to low pressure ($2 \rightarrow 3$). If the fluid is pre-cooled sufficiently below its inversion temperature, it will experience a temperature drop down to its minimum temperature, $T_c$. To optimize the available cooling power at a constant temperature

$T_c$ at the output of the JT valve, it is convenient to produce liquid after this expansion in saturated conditions. In this condition, some part of the fluid is now liquefied at the evaporator (state point 3) and will be vaporized by receiving some heat load $\dot{Q}_c$ (3 → 4). The saturated low pressure vapour leaves the evaporator and flows towards the low-pressure inlet of the CFHX. Then, this low pressure stream is heated up by thermal contact with the incoming flow (4 → 5), before being compressed again to high pressure (5 → 1) and restart the cycle.

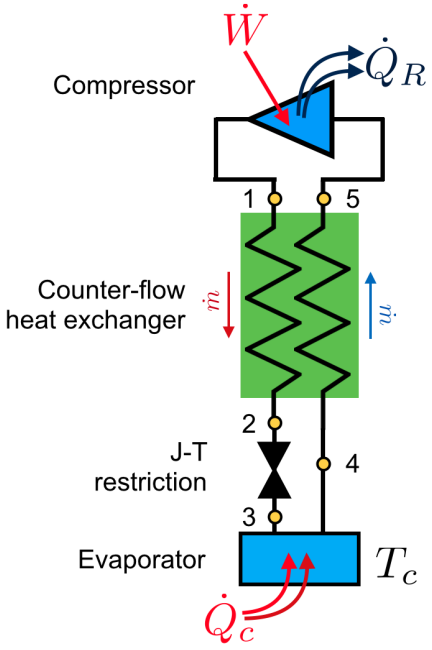


Figure 2.3: Schematic of a Linde-Hampson cryo-cooling process.

### 2.2.2 Thermodynamic Analysis

In order to calculate the cooling power and the efficiency of Linde-Hampson cycle, a detailed thermodynamic analysis is required. By applying the First Law of Thermodynamics on the different parts of the cycle it is possible to obtain the full thermodynamical description of the steady state operation. The following assumptions and constraints were considered in this analysis:

1. Working fluid is pure (no mixtures);
2. High pressure (compressor's output) is defined and above critical pressure (where cooling is more efficient);
3. Fluid expands isenthalpically into the two-phase region;
4. Warm and cold end temperatures are given ($T_1$ and $T_c$);
5. Only saturated vapour returns to the CFHX low-pressure inlet;

6. Steady state operation;
7. Pressure drop loss and radiative heat transfer neglected.

Considering the above assumptions/constraints, the Linde-Hampson cycle is shown in a pressure-enthalpy ($P-h$) diagram, or Mollier diagram (Figure 2.4), where the state numbers correspond to those defined in Figure 2.3. For reasons explained after, this diagram is obtained using the following parameters: $P_1$ =100 bar, $T_1$ =180 K and $T_c$ =80 K. It comprises five distinct phases: three at constant pressure (one of them in the two-phase region, therefore at constant temperature), one at constant enthalpy (expansion) and another one at constant temperature (isothermal compression).

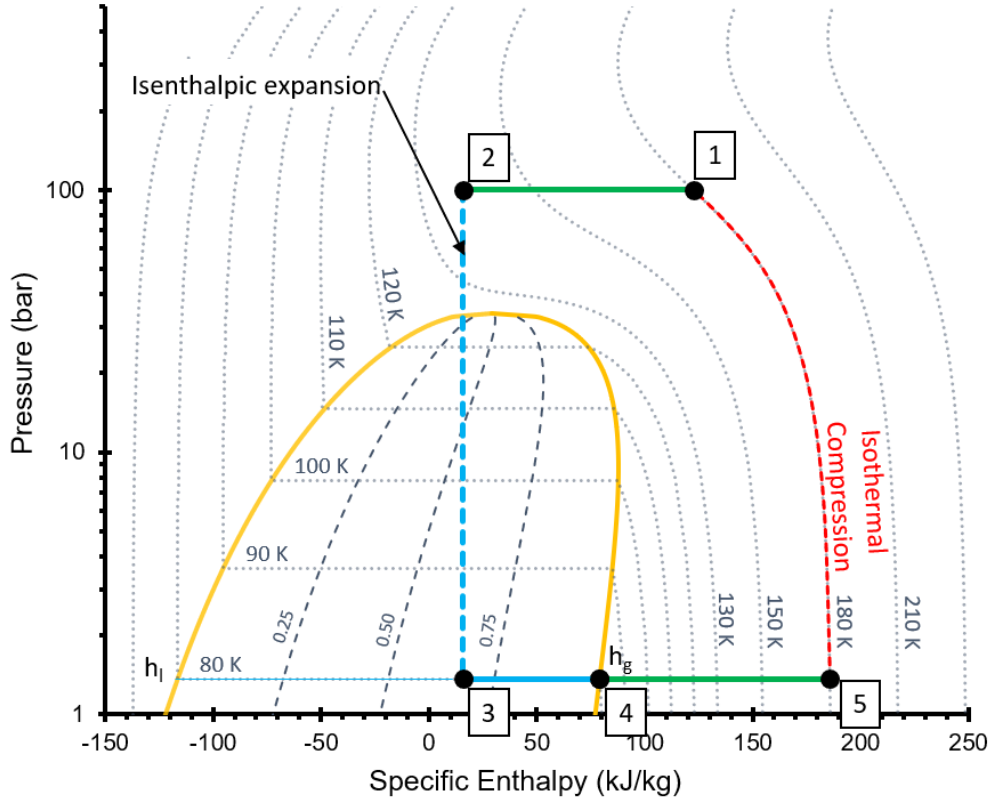


Figure 2.4: Ideal Linde-Hampson cycle on a pressure-enthalpy diagram (Mollier diagram) using nitrogen as the working fluid. The yellow thick line delimits the two-phase region. Within this region, the thicker dashed lines correspond to vapour quality $\chi$.

Between states 1 and 2, the process occurs at constant high pressure, $P_H$, the gas flow is delivered by the compressor and the fluid cools down from $T_1$ to $T_2$. The most distinguishing feature of the Linde-Hampson cycle occurs between states 2 and 3, where the fluid goes through the JT valve. The pressure decreases from $P_H$ to $P_L$ at constant enthalpy and below critical pressure, a temperature drop of the fluid is obtained as a consequence of the JT effect. Since the expansion ends up in the two-phase region, a two-phase mixture at a boiling temperature $T_3 = T_c$ is obtained and, thus, reaching the

coldest temperature of this cycle. The gaseous fraction of this mixture is quantified by the vapour quality $\chi$, which depends on the state 2 locus and it is hereby expressed as,

$$\chi = \frac{h_3 - h_l}{h_g - h_l} \tag{2.7}$$

where $h_3$ is the specific enthalpy at state 3 ($h_3 = h_2$), $h_l$ is the specific enthalpy of the saturated liquid and $h_g$ is the specific enthalpy of the saturated vapour (state 4). Between states 3 and 4, as far as pressure $P_L$ is constant, this process occurs at constant temperature and by boiling of the cryogen it is obtained the cooling power, $\dot{Q}_c$, of this cycle, which is proportional to the enthalpy difference $(h_4 - h_3)$ and to the mass flow rate $\dot{m}$, as it will be shown below.

Applying the First Law of Thermodynamics for open systems in the CFHX, where no work is done and no heat is transferred to or from surroundings, the following relation is obtained,

$$\begin{gathered} -h_1 + h_2 - h_4 + h_5 = 0 \\ \underbrace{h_2 - h_1}_{\text{HP side}} = \underbrace{h_4 - h_5}_{\text{LP side}} \end{gathered} \tag{2.8}$$

Equation (2.8) shows that the enthalpy difference at each side of the CFHX are equal, as evidenced on the $P-h$ diagram (green line). Note that the state points 1, 4 and 5 are given by other considerations, so, this equality determines the locus of state 2 in the $P-h$ diagram. Typically in a Linde-Hampson cooler, the cold stream heat capacity $\dot{C}_L$ is lower than that of the hot stream $\dot{C}_H$ [9], so, consequently in a perfectly effective CFHX (as shown in Equation (2.8)), the condition $T_1 = T_5$ is fulfilled, as also depicted in the $P-h$ diagram. By considering the relation $h_2 = h_3$ (isenthalpic expansion), Equation (2.8) becomes,

$$h_4 - h_3 = h_5 - h_1 \tag{2.9}$$

Applying now the First Law on the system consisting of a JT restriction and an evaporator, the cooling power, $\dot{Q}_c$, of the cycle may be obtained,

$$\dot{Q}_c = \dot{m}(h_5 - h_1) = \dot{m}\Delta h_{51} \tag{2.10}$$

Considering Equations (2.9) and (2.10) and also Figure 2.4, some important remarks are noteworthy:

1. In order to obtain cooling, $(h_5 - h_1)$ must be positive, therefore, the isotherms in a $P-h$ plane cannot be straight and vertical. Otherwise, as with helium or neon at room temperature, the JT expansion warms up the gas.
2. For an ideal gas, the enthalpy does not depend on pressure, then $(h_5 - h_1) = 0$: the shape of the isotherms in the $P-h$ plane describes the deviation from an ideal gas.

3. There is an optimum pressure of operation, as it may be deduced by inspecting the shape of the isotherms in the $P-h$ diagram. It corresponds to the pressure maximizing the length of $\overline{34}$, which consequently increases the liquid fraction $(1-\chi)$. Optimum pressure is found when the following condition is verified,

$$\left(\frac{\partial h}{\partial P}\right)_T = 0 \tag{2.11}$$

corresponding to a local infinite slope of the isotherm in a $P-h$ diagram.

Finally, the Second Law of Thermodynamics is needed to evaluate the input power required to sustain such cooling operation. So, applying the First and Second Law of Thermodynamics on the compression process (isothermal and reversible), the minimum work, $W$, required to run this cycle is,

$$\begin{aligned} -\dot{Q}_R + \dot{W} &= -\dot{m}h_5 + \dot{m}h_1 \\ \dot{W} &= \dot{m}[T_1(s_5 - s_1) - (h_5 - h_1)] \\ \frac{\dot{W}}{\dot{m}} &= T_1\Delta s_{51} - \Delta h_{51} \end{aligned} \tag{2.12}$$

where $s$ is the specific entropy and $\dot{Q}_R$ is the rejected heat by the compressor. The benefit in terms of extracted heat at low temperature per unit of supplied work is the coefficient of performance, $COP_{\text{JT}}$,

$$COP_{\text{JT}} = \frac{\dot{Q}_c}{\dot{W}} \tag{2.13}$$

Considering Equations (2.10) and (2.12), the previous equation becomes [9],

$$COP_{\text{JT}} = \frac{\dot{m}\Delta h_{51}}{\dot{m}(T_1\Delta s_{51} - \Delta h_{51})} \tag{2.14}$$

$$= \left(T_1\frac{\Delta s_{51}}{\Delta h_{51}} - 1\right)^{-1} \tag{2.15}$$

Equations (2.10) and (2.15) are useful to find the optimum operating conditions of the JT cold stage, helping, for instance, to define the range of some critical parameters as the high pressure and the inlet temperature of the CFHX.

### 2.2.3 Pre-cooled Linde-Hampson Cycle

The fluids whose inversion temperatures are below room temperature (neon, hydrogen and helium) will warm up if they are fed into a basic Linde-Hampson cycle. However, it is possible to "reallocate" its initial state somewhere below its inversion curve to achieve sustained cool down and liquefaction.

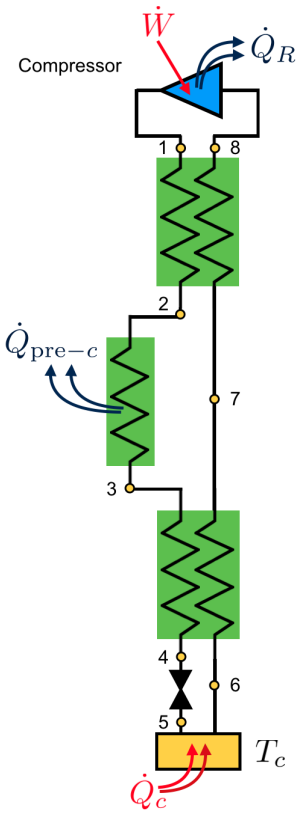


Figure 2.5: Schematic of a pre-cooled Linde-Hampson cycle.

This can be accomplished by employing the so called pre-cooled Linde-Hampson cycle, schematically represented in Figure 2.5. It usually starts with a high pressure stream above its inversion temperature, being cooled down in a first CFHX by exchanging heat with the cooled low-pressure returning stream. Next, it goes trough a pre-cooling stage to further reduce its temperature below its inversion temperature, this precooling process is obtained thanks to an auxiliary cold source. Finally, this precooled high pressure stream goes through a basic Linde-Hampson cycle where it cools again in a second CFHX before entering the JT valve. If needed, many multiple pre-cooling stages may be used sequentially to further reduce the temperature. The $P-h$ diagram of this cycle using neon as the working gas is illustrated in Figure 2.6 and this cooling process is analysed considering the same assumptions (1 to 7) as described earlier in Section 2.2.2. Still, the following assumptions are needed,

8. The pre-cooling source is considered as an heat-sink with a known constant temperature $T_{\text{pre},c}$.
9. The pre-cooling heat exchanger is perfect. Consequently, the gas cools down to $T_{\text{pre},c}$.

Considering those assumptions, the states at point 1, 3 and 6 of Figure 2.5 are fully defined. Moreover, this cycle may be analysed only from the last CFHX and using the same analogy as a basic Linde-Hampson cycle, by considering the inlet temperature of this CFHX (state point 3) as the pre-cooling temperature $T_{\text{pre},c}$. Replacing the subscripts from Equation (2.10), the cooling power, $\dot{Q}_c$, of this cycle becomes,

$$\dot{Q}_c = \dot{m}\Delta h_{73} \tag{2.16}$$

And, the required pre-cooling power, $\dot{Q}_{\text{pre},c}$, at $T_{\text{pre},c}$ is,

$$\dot{Q}_{\text{pre},c} = \dot{m}\Delta h_{32} \tag{2.17}$$

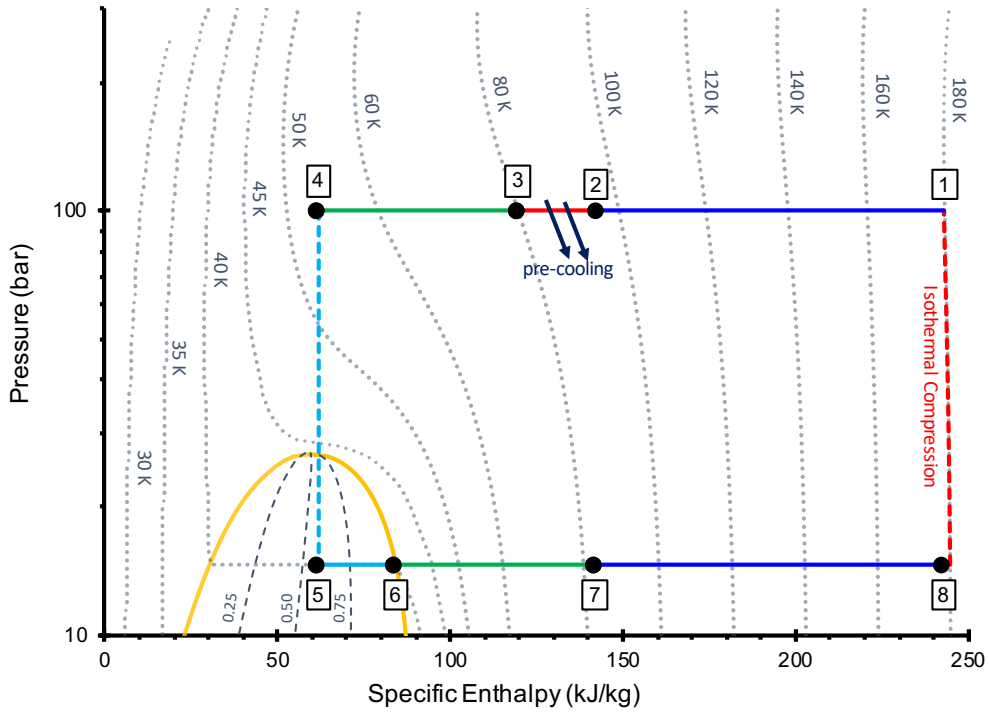


Figure 2.6: Neon pressure-enthalpy diagram of a pre-cooled Linde-Hampson cycle.

### 2.2.4 Cryogenic Liquids

The thermo-physical properties of cryogenic liquids (gases with boiling point below ±120 K) are the primary ingredient to obtain an optimized design of a Joule-Thomson cryocooler. Furthermore, each particular fluid has its unique characteristics which directly influences the design of the cooler.

As explained earlier in Section 2.2.2, the Linde-Hampson cycle is usually associated with a liquid-vapour transition. Therefore, the boiling point temperature and their pressure dependence is of high importance when selecting the cryogen, since this temperature will define the operating low pressure, $P_L$, of the Joule-Thomson cooler. Actually, the list of available cryogenic fluids is rather short, as visible in Figure 2.7. Therefore, once the required temperature is given, little choice remains. Examining the vapour pressure curves of Figure 2.7, one may observe the following characteristics:

1. There is a large temperature gap which is not covered by any pure coolant. Precisely between the triple-point of oxygen, 54.4 K and the critical point of neon, 44.5 K.
2. Above this gap, the shown coolants have inversion temperatures above room temperature, as it may be consulted in Table 2.1. Therefore, liquefaction can be obtained by Joule-Thomson throttling through a basic Linde-Hampson cycle.
3. The region below this gap is characterized by a set of quantum gases (helium and

hydrogen) and neon, whose inversion temperatures are below room temperature. Consequently, liquefaction is not possible using the simple LH cycle: liquefaction is only achievable through the pre-cooled LH cycle.

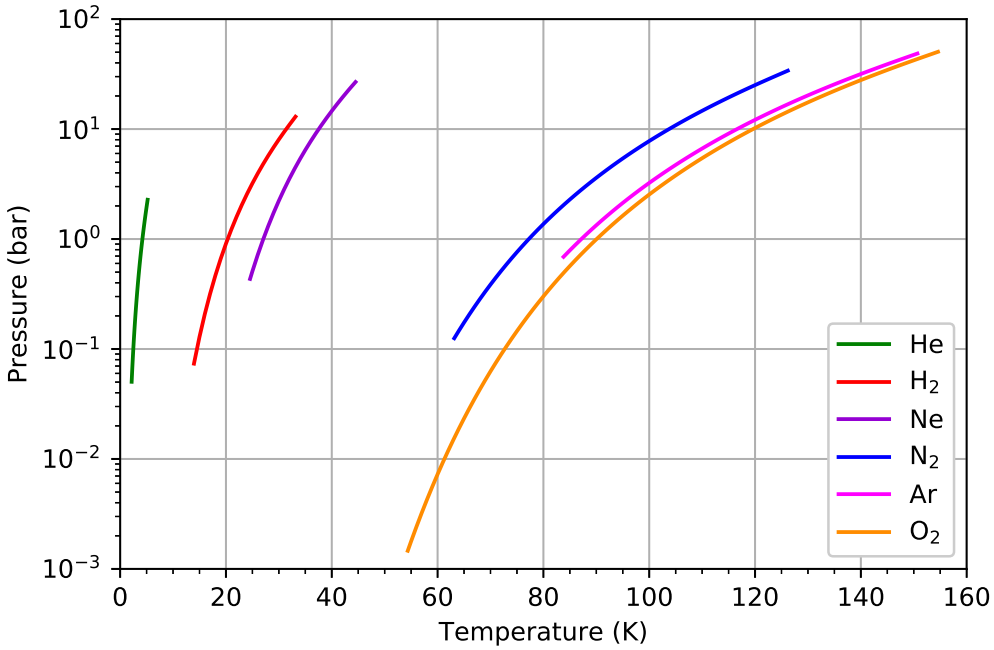


Figure 2.7: Vapour pressure curves between the triple and critical point of some pure cryogenic fluids in the temperature range of 40 K to 80 K.

Considering the targeted temperature range for the development of a vibration-free cooler (40 K to 80 K), two fluids are available at a temperature around 80 K: oxygen and nitrogen; and, only one is available at 40 K, which is neon. The most important characteristics of these three coolants are discussed next.

Oxygen in its liquid state shows a light blue colour, its boiling temperature is 90.2 K (1 bar) and its triple point at 54.4 K. Liquid oxygen is slightly magnetic, in contrast to other fluids, which are non-magnetic. This unique characteristic could be useful under zero gravity conditions since a magnetic field may be used to easily separate the liquid and gaseous phases. Both gaseous and liquid oxygen are highly chemically reactive, particularly when exposed to hydrocarbon materials. It represents a serious safety problem, since several explosions have resulted from the combination of oxygen and hydrocarbon lubricants, that can be found in ordinary compressors or vacuum pumps. Also, valves and pipelines that were exposed to oil-pumped gases must not be used with oxygen. So, by working with oxygen, the systems must be maintained clean of any foreign matter and need careful screening of the materials. Reactive metals, such as titanium or aluminum, must be used with care, because they are potentially hazardous. Unfortunately, these metals are the most common ones in the aerospace industry.

Nitrogen is the most abundant constituent of our atmosphere (78% in volume). It is obtained in large quantities by fractional distillation of liquid air. In its liquid state, is a colorless fluid that resembles water in appearance. It boils at 77.3 K (1 bar) and its triple point is 63.2 K. Liquid Nitrogen (LN2) has a considerable importance to cryogenics, mostly for being considered a cheap and safe coolant, it is also chemically inactive and is neither toxic or explosive.

Neon is a rare gas element present in the atmosphere (18.2 ppm of air by volume). It is obtained via liquefaction of air and separated from other gases by fractional distillation. With a nitrogen-like appearance, it is a clear and colorless fluid and has a boiling and triple point temperatures of 27.1 K and 24.6 K, respectively. Liquid neon is an inert element and it is still trying to find important applications as an economical refrigerant. Even so, some applications of liquid neon can be found in experiments related to dark matter [10].

Other characteristic that should be evaluated is the latent heat of vaporization. Figure 2.8 shows the latent heat, $L$, of nitrogen, oxygen and neon as a function of temperature. For each fluid, as its temperature reaches the critical point ($T/T_c = 1$), the latent heat rapidly decreases; on the other hand, it increases as it approaches the triple point.

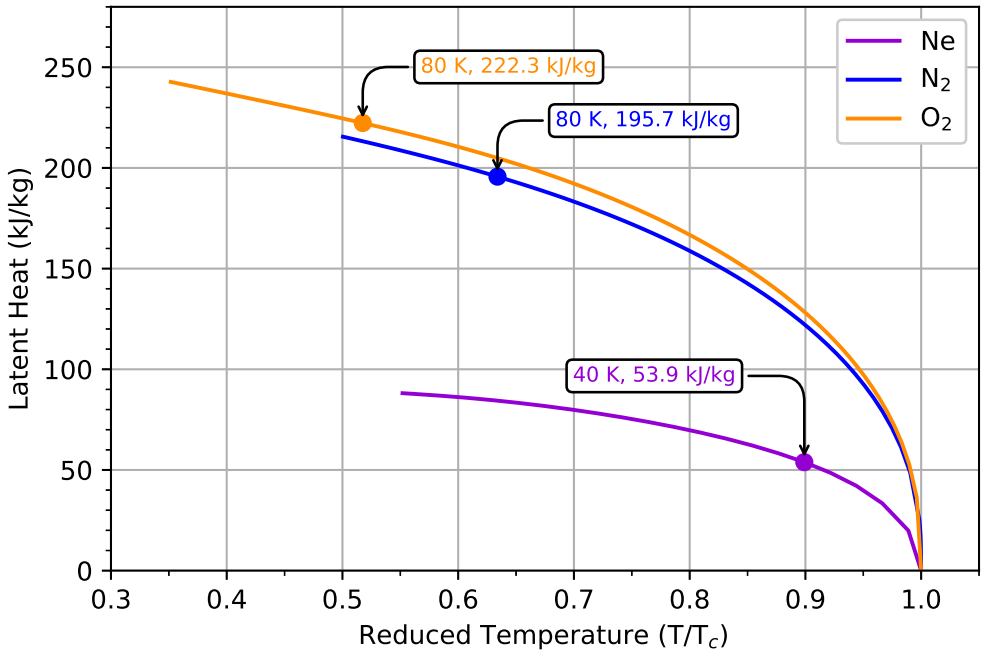


Figure 2.8: Latent heat, $L$, of vaporization as function of the reduced temperature $T/T_C$. The selected points are at the temperatures of interest for neon, nitrogen and oxygen.

However, let us mention that the operation of a Joule-Thomson cooler close to these two points can bring some difficulties:

- Since the latent heat rapidly decreases as it approaches the critical point, higher mass flow rate would be needed to sustain cooling, according to Equation (2.10).
- Close to the triple point, latent heat reaches its maximum, while the vapour pressure reduces significantly. Particularly, for oxygen, this pressure is low as 20 mbar, as shown in Figure 2.7. Achieving such low pressures is certainly quite challenging with adsorption-based compression.

## 2.3 Sorption Compressor

The sorption compressor, being responsible for the circulation of the working fluid, is a vital component of the cooler. This type of compressor does not mechanically compresses the gas, as done by usual compressors, instead it is based on the principle that a large amount of gas can be reversely desorbed and adsorbed just by varying the temperature of a pressure vessel filled with certain solids. In principle, such solids can adsorb the working fluid with much higher density compared to a pressure vessel only occupied with gas.

### 2.3.1 Adsorption Phenomenon

Adsorption is the adhesion of atoms, molecules or ions from a gas to a solid surface. In order to enhance this phenomenon, this surface has small, low-volume pores to increase its surface area. It is a surface phenomenon, where a film of molecules (adsorbate) forms at the surface of the pores (adsorbent). It differs from absorption, where the adsorbate is dissolved or permeates the absorbent. It is also a consequence of the existence of surface energy. In a bulk material, constituent atoms are bonded to their neighbor atoms via ionic, covalent or metallic bonds. However, the atoms of the adsorbent surface are not completely surrounded by another atoms and, therefore, they are susceptible to attract adsorbate. Usually, the adsorption processes are classified as chemical adsorption or physical adsorption, depending on the kind of interaction force involved.

In chemical adsorption or chemisorption, the adsorbate chemically reacts with the adsorbent, thus, forming strong covalent or ionic bonds between the solid surface and the adsorbate. This process implies that the chemical structure of the adsorbent is altered and that the binding enthalpies are quite high (typically between 250 kJ mol$^{-1}$ to 500 kJ mol$^{-1}$) and, in general, it is a very selective process as it depends on the chemical nature of both adsorbate and adsorbent. The typical adsorbents involving chemisorption are metal-hydrides [11] and praseodymium-cerium oxide (to adsorb oxygen).

In physical adsorption or physisorption, the adsorbate weakly interacts with the adsorbent through long-range vdW or London forces, and the interaction mainly occurs at the surface. Since the binding energies are really weak, they are heavily influenced by temperature and pressure: low temperatures and high pressures promote adsorption, while high temperatures and low pressures lead to very low adsorbed quantities. These processes are less chemically sensitive when compared with chemisorption and the heat of adsorption is much smaller (less than 20 kJ mol$^{-1}$) and always exothermic, actually, comparable with the heat of liquefaction of the fluid. The typical adsorbents are activated charcoal [12, 13], zeolites, metal-organic frameworks and silica gel.

The pair adsorbate-adsorbent is crucial to design the sorption compressor. Such adsorption behavior of the pair can be measured either by gravimetric or through volumetric methods and is frequently represented by a series of equilibrium isotherms in a chart of adsorbed quantity versus pressure, for instance, as shown in dashed lines of Figure 2.9.

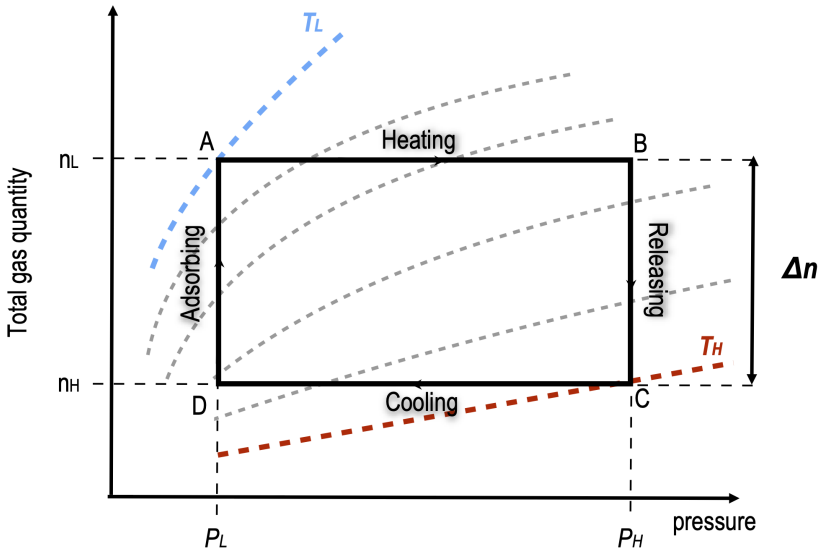


Figure 2.9: Schematic of a compressor cell cycle (black solid lines) in an adsorbed quantity diagram with isotherms (in dashed) as function of pressure. $n_L$ corresponds to the adsorbed quantity at the equilibrium low temperature $T_L$ and low pressure $P_L$ (state A) and $n_H$ to the adsorbed quantity at high temperature $T_H$ and high pressure $P_H$ (state C). $\Delta n$ is net adsorption quantity of a compression cycle, it corresponds to the quantity that can be adsorbed or released during a cycle.

### 2.3.2 Working Principle

Consider a pressure vessel filled with an adsorbent material and some gas adsorbed at low temperature, $T_L$, and pressure, $P_L$. If we close this vessel and increase its temperature, the adsorbed gas will be released from the adsorbent material and, consequently, the pressure will increase. Afterwards, if this high-pressure vessel is opened, the gas flows out of the vessel and can be maintained by further increasing its temperature until most of the gas is released or achieved the maximum allowed temperature, $T_H$. After this phase, the vessel must cool down its temperature to be refilled again at low temperature and pressure.

Figure 2.9 schematically displays a typical sorption compressor cycle overlapped on a series of adsorbent isotherms, thus, it depicts the amount of gas in the cell as a function of temperature and pressure. It is visible that there are four distinct phases: heating (compression, A→B), releasing (out-flow, B→C), cooling (decompression, C→D) and adsorbing (in-flow, D→A). Each of these phases will be explained in detail below:

- **Heating**: Starting at state point A, at the lowest temperature, $T_L$, and low pressure, $P_L$, the sorption cell is being heated up in closed volume, so, operating at constant quantity. As the temperature increases, the gas is being desorbed from the adsorbent material and, so, occupying the void volume of the cell, while the pressure increases. During such phase, the total amount of gas, $n_L$, in the cell remains constant.

- **Releasing**: When the pressure reaches the required high pressure, $P_H$, to feed the Joule-Thomson stage, the sorption cell opens and the gas is released in a controlled way to provide a constant gas flow towards the cold stage (ideally at constant pressure), this is accomplished by continuously increasing the temperature of cell. During this phase, a gas quantity $\Delta n = n_L - n_H$ is released from the cell.

- **Cooling**: When maintaining the high pressure and a constant mass flow rate $\dot{m}$ becomes impossible, state point C is achieved. The cell was heated up to its highest temperature, $T_H$, and, then, starts its cooling phase, where it is again operating in closed volume, so, its pressure decreases at constant quantity, $n_H$.

- **Adsorbing**: When the pressure decreases down to the outlet pressure of the Joule-Thomson stage, $P_L$, the sorption cell opens and is able to adsorb the gas continuously exiting the JT cold stage. Adjusting the temperature decreasing rate of the cell, it should be able to adsorb with the same rate as it is flowing out from the JT stage, while maintaining $P_L$ and the mass flow rate constant. When the

adsorbent material is no longer able to adsorb with this rate, the compression cycle is completed and the cell has reached its minimum temperature, $T_L$.

The duration, $\Delta t$, in which a gas quantity, $\Delta n$, flows into or out of the cell has the following relationship with the mass flow rate, $\dot{m}$, (assuming constant mass flow),

$$\dot{m} = \frac{M\Delta n}{\Delta t} \tag{2.18}$$

where $M$ is the molar mass of the fluid. To achieve best performance, the JT stage requires a more or less stable and continuous supply of gas. Such uninterruptedly gas flow is traditionally provided by a sorption compressor containing at least three or more sorption cells [4], as shown in Figure 2.10. Although a sorption compressor using a single sorbent bed is also found in the literature as viable a configuration and it corresponds to a less complex solution, since less parts are needed. However, it requires two large volume buffers to maintain a stable supply of gas and this layout has a slight fluctuation in the low pressure buffer, which results in some variation in the cold end temperature, $T_c$ [14].

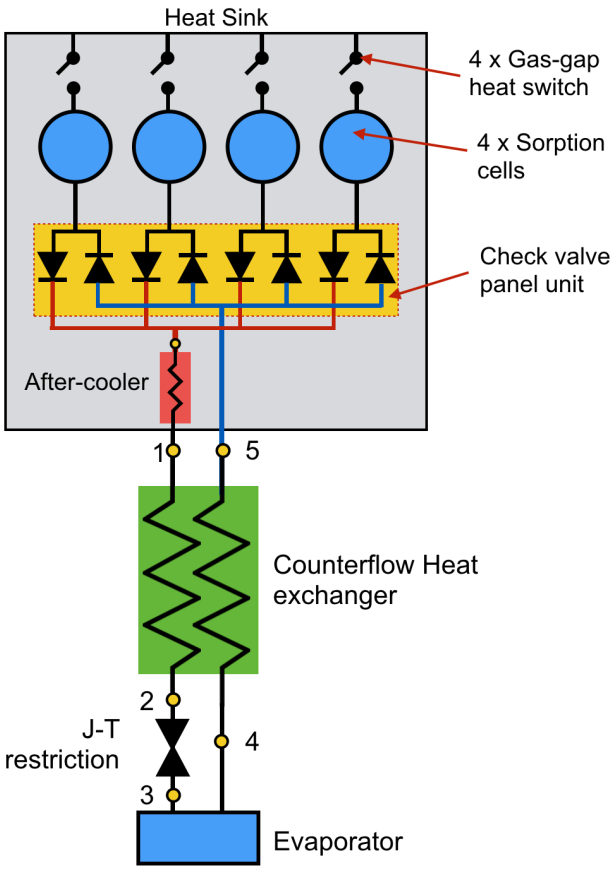


Figure 2.10: Schema of a sorption compressor using four adsorption cells coupled to a Linde-Hampson cold stage.

Using the four cells configuration (Figure 2.10) and by working them sequentially out of phase it is possible to maintain a constant flow into the cold stage, with less fluctuation, and achieve continuous cooling. In practice, each phase must have the same duration $\Delta t$ and the four sorption cells must be evenly distributed in the four distinct phases (quadrature operation), as schematically shown in Figure 2.11. Then, for four cells working in quadrature, one full compression cycle period, $T_{\text{cycle}}$, is $4\Delta t$.

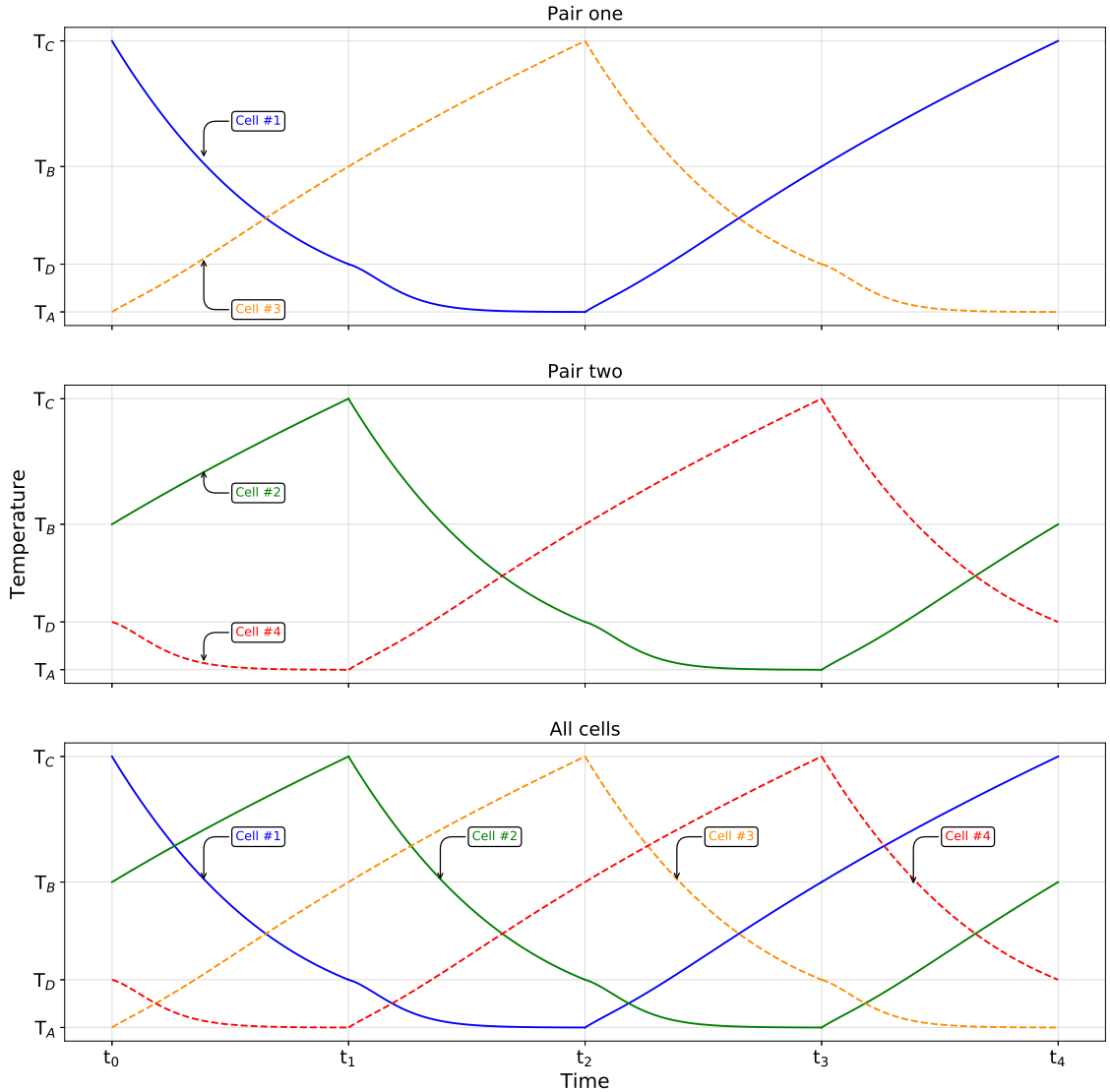


Figure 2.11: Four sorption cells working in quadrature during a compression cycle.

Examining the sorption compressor cycle from Figure 2.11, for instance between $t_0$ and $t_1$, one may observe the following characteristics:

1. Considering the "pair one" (first chart of fig. 2.11), cells #1 and #3 are regenerating (cooling and heating): cell #1 is being cooled down to adsorb gas after, while cell #3 is increasing its temperature to increase its pressure and release gas later.

2. Considering the "pair two" chart, cells #2 and #4 are either receiving or supplying gas: the cell #4 is adsorbing gas at low temperature (adsorbing phase), while cell #2 is releasing gas at high pressure by further increasing its temperature (releasing phase).

3. By working the cells in quadrature, as displayed in the bottom chart "all cells", is visible that anytime during operation there is always one cell adsorbing gas at low temperature/pressure and another one releasing gas at high temperature/-pressure. So, it always exists a flow circulation of gas into and out of the JT stage.

4. Note that is important that each phase has precisely the same duration, $\Delta t$, to obtain a constant mass flow and avoid large fluctuations, which is required to achieve the best performance of a Joule-Thomson stage.

During a compression cycle, the sorption cells need to cool down and, consequently, to reject the heat somewhere. Then, each cell has to be connected to a heat-sink, for instance, a cryogenic flow circulator or a radiator rejecting heat to a lower temperature in deep space. Moreover, during both releasing and heating phases of the cycle, the sorption cells need to reach high temperatures, which can be higher than room temperature. Therefore, to avoid an unacceptable heat load to the heat sink during these phases, which in space must be avoided due to limited resources, the sorption cell has to be thermally connected to the heat sink via a controllable thermal link, for instance, a Gas Gap Heat Switch (GGHS) (Figure 2.10).

A GGHS is a device able to vary its thermal conductance by several orders of magnitude [15]. Usually, it is characterized by two distinct operating states: an ON state, for a highly conducting mode and an OFF state, for a low thermal conductance mode. Such a device is usually integrated in each sorption cell to manage the thermal connection between the cell and the heat-sink. So, as soon as any cell begins to increase its temperature, the heat switch should remain in its OFF state, and as soon as any cell needs cooling, the heat switch must be switched to its ON state to reject the heat somewhere.

A pair of check-valves (one-way valves) are also required for each sorption cell in order to obtain the correct flow direction during the active phases (releasing and adsorbing), further details will be provided later in Section 6.3.

### 2.3.3 Thermodynamic Analysis

In the literature, several studies related to the thermodynamics and optimization of sorption-based coolers can be found [16–18]. For instance, the coefficient of performance of a sorption compressor, $COP_{SC}$, written as function of exergy[1] [19],

$$COP_{SC} = \frac{b\Delta n}{Q_{input}} \tag{2.19}$$

where $\Delta n$ is the gas quantity that flows in or out of a sorption cell during a cycle, $b$ is the specific exergy of the gas and $Q_{input}$ is the required heat input of the sorption cell. Note that in a thermal compressor the heat input to compress a gas is usually supplied by Joule effect. Considering Equation (2.18), $COP_{SC}$ may be written as function of the mass flow rate, $\dot{m}$,

$$COP_{SC} = \frac{\dot{m}b}{\dot{Q}_{input}} \tag{2.20}$$

In sorption compressor analysis, it is assumed that the high pressure gas stream is being pre-cooled in a heat sink at low temperature, $T_L$, before entering the JT cold stage, for instance, as depicted in Figure 2.10). Therefore, in this case, the exergy reduces to the variation of Gibbs free energy $\Delta G$ [19],

$$\begin{aligned} b &= \Delta g(T_L, P_L, P_H) \\ &= [h(T_L, P_H) - h(T_L, P_L)] - T_L[s(T_L, P_H) - s(T_L, P_L)] \end{aligned} \tag{2.21}$$

Considering the state points from Figure 2.10, the previous equation is written as,

$$b = (h_1 - h_5) - T_1(s_1 - s_5) = T_1\Delta s_{51} - \Delta h_{51} \tag{2.22}$$

Substituting this result into Equation (2.19), one obtains,

$$COP_{SC} = \frac{\dot{m}(T_1\Delta s_{51} - \Delta h_{51})}{\dot{Q}_{input}} \tag{2.23}$$

The total heat input, $Q_{input}$, consists of the energy required to heat up the sorption compressor cells from $T_L$ to $T_H$ (or from $T_A$ to $T_D$, Figure 2.11). In Figure 2.12 it is depicted a control volume applied to a single sorption cell where, in a first approximation, such control volume is assumed as adiabatic. Let us note that a sorption cell filled with an adsorbent material does not fully occupies the whole cell volume, as there is a fraction of its volume which is only occupied with gas (void volume), further details later in Chapter 4.

[1] Exergy $B$ is the maximum (ideal) work that can be produced by a system between two distinct states of pressure and temperature.

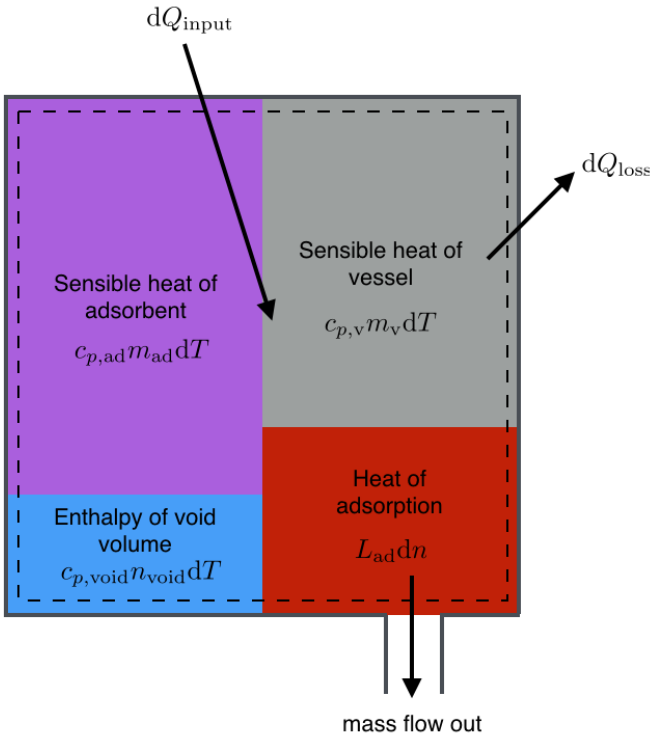


Figure 2.12: Energy balance applied to the control volume in a sorption compressor cell. The area of each contribution in this diagram is merely indicative.

Essentially, $Q_{\text{input}}$ is the required energy to warm up the gas in the void volume ($Q_{\text{void}}$), to desorb the gas ($Q_{\text{sorb}}$), to warm up the sensible heat of the cell's material and of the sorbent material ($Q_{\text{s.heat}}$). Considering an infinitesimal step in the process,

$$dQ_{\text{input}} = dQ_{\text{sorb}} + dQ_{\text{void}} + dQ_{\text{s.heat}} \tag{2.24}$$

where $dQ_{\text{sorb}}$ is,

$$dQ_{\text{sorb}} = L dn \tag{2.25}$$

where $L$ is the isosteric heat of adsorption. $dQ_{\text{void}}$ is,

$$dQ_{\text{void}} = c_{p,\text{void}}(T)\, n_{\text{void}}(T,P)\, dT \tag{2.26}$$

where $n_{\text{void}}$ is the gas quantity occupying the void volume of cell which does not remain constant upon changes in temperature and pressure. And, $dQ_{\text{s.heat}}$ is,

$$dQ_{\text{s.heat}} = (c_{p,\text{s}}(T)\, m_{\text{s}} + c_{p,\text{v}}(T)\, m_{\text{v}})\, dT \tag{2.27}$$

where $m_{\text{s}}$ is the mass of adsorbent and $m_{\text{v}}$ is the mass of vessel. Thus, the total heat input is obtained via integration over the heating and releasing phases of a sorption cell,

$$Q_{\text{input}} = \int_{A\to B} dQ_{\text{input}}\big|_n + \int_{B\to C} dQ_{\text{input}}\big|_{P_H} \tag{2.28}$$

Note that $A \rightarrow B$ corresponds to the heating phase, process occurring at constant quantity $n$, whereas $B \rightarrow C$ corresponds to the releasing phase occurring at constant pressure, $P_H$.

Finally, it is possible to obtain the global Coefficient of Performance of the cooler as it may be obtained by the product of each sub-system COPs, namely, the JT circuit, Equation (2.15), and the sorption compressor, Equation (2.23).

$$\mathrm{COP} = \mathrm{COP}_{\mathrm{JT}} \times \mathrm{COP}_{\mathrm{SC}} = \frac{\dot{m}\Delta h_{51}}{\dot{Q}_{\mathrm{input}}} \tag{2.29}$$

Let us note, however, for space applications, it may not be possible to operate close to the ideal parameters obtained from Equation (2.29) as it can lead to an incompatible configuration considering the various stringent requirements of volume, temperature or mass.

CHAPTER 3

# Baseline Design Solution of a 40 K to 80 K Vibration-Free Cooler

The European Space Agency has launched in 2014 a Technical Research Program (TRP) to develop new or adapt current cooling technologies in the temperature range of 40 K to 80 K without mechanical disturbances to answer the needs of potential future Earth observations infrared missions. The main objectives of this TRP were to design, manufacture and test an elegant breadboard model (close to an engineering model) of a vibration-free cooler.

In this chapter, the main system requirements of this TRP study are presented and followed by a description of the current state of the art of sorption-based coolers working in the temperature range and cooling power close to our requirements. In the second part of this chapter, a baseline design solution of a 40 K to 80 K vibration-free cooler is presented.

## 3.1 System Requirements

The VFC to be developed is constituted at least of the following elements: a compressor/circulator and a cold end. Depending on the technology, other sub-elements can be used to achieve the thermodynamic cycle (e.g. heat exchanger, turbines) or vibration cancellation systems (active or passive). ESA proposed the following possible solutions [3]:

- Active closed-cycle cooling systems based on sorption/desorption technique. This technology was already used for the hydrogen Joule-Thomson stage on Planck (chemisorption) and was the topic of the development of hydrogen and helium physisorption systems (Darwin studies).

- Very high frequency active closed-cycle cooling systems.
- Active closed-cycle cooling with vibration free mechanism and no oscillating fluid flow.

The following solutions should not be considered in the scope of this study:

- Full passive cooling (e.g.radiators), since this solution is very dependent on system parameters like orbit and altitude and cannot cover the whole range of temperature of interest (very difficult to reach temperatures below 70 K in low Earth orbit).
- "Classical" Earth observation coolers (e.g. PTC, 50 K to 80 K Stirling cooler) with complex damping mechanisms.
- As one of the main requirements is continuous cooling, intermittent solutions, for instance, based on coolers with thermal energy storage solutions [20], were also out of the scope of this study.

The Physical and Resource requirements of the VFC are shown in Table 3.1 and the Functional and Performance requirements in Table 3.2. Considering the requirements, a preliminarily design of a cooler based on two Linde-Hampson cycles and two sorption compressors was proposed. Its detailed design, manufacture and components characterization are presented on the following chapters.

Table 3.1: Physical & Resource requirements of the VFC [3].

| | |
|---|---|
| **PR1** | The mass of the cooler shall not exceed 7 kg, excluding electronics. |
| **PR2** | The total radiator surface needed for the cooler (assuming an emissivity $\epsilon$ of 0.8) shall not exceed 1.5 $m^2$. |
| **PR3** | The maximum power consumption in operation of the VFC shall not exceed 180 W during continuous operation (limited by the radiator sizing). |
| **PR4** | The total volume of the cooler without electronics shall not exceed 10 L. |

Table 3.2: Functional and Performance Requirements of the VFC [3].

| | |
|---|---|
| **FPR1** | The cryocooler efficiency shall ensure the following performances considering end of life condition:<br><br>**Functional point @** 40 K<br>• Cold end temperature: ≤40 K<br>• Heat lift: 500 mW to 800 mW<br>• Continuous cooling<br><br>**Functional point @** 80 K<br>• Cold end temperature: 80 K<br>• Heat lift: 1 W to 1.5 W<br>• Continuous cooling |
| Notes: | - The 40 K to 80 K temperature range does not need to be continuously covered, a gap of around 10 K is acceptable.<br>- The two functional temperatures have to be achieved by the same type of cooler (e.g. by changing the working fluid, optimizing the cold part). |
| **FPR2** | The exported vibration at room temperature and atmospheric pressure, at the cooler mechanical interfaces of a nominally operating cooler in all orientations with respect to gravity, shall not exceed 10 mN RMS in all axes in a frequency bandwidth between 0 kHz to 1 kHz |
| **FPR3** | The VFC shall achieve a temperature stability better than 100 mK/15 min in a stable environment, at the nominal operational point in open loop. |

## 3.2 State of the Art

In this section, the state of the art will be focused on sorption-based cryocoolers using the Joule-Thomson effect.

### 3.2.1 ESA's Planck Sorption Cooler

The Planck scientific mission successfully measured very small temperature variation in the Cosmic Microwave Background (CMB) with an unprecedented sensitivity, obtaining CMB images with 2.5 times greater resolution than its ancestor (WMAP), as shown in Figure 3.1. The spacecraft was launched in May 2009 and successfully worked until October 2013.

The amazing images of Planck's were obtained thanks to its complex cryogenic chain, which was designed to reach a low temperature of 100 mK. A 20 K hydrogen

sorption cooler was one of the active cooling systems of the cryogenic chain of Planck's spacecraft. Its successful development and operation during three years was an important milestone to the development of this family of coolers for long term space missions. It was designed and built at the Jet Propulsion Laboratory to provide more than 1 W of heat lift at a temperature 20 K for the Low Frequency Instrument (LFI) and to pre-cool the High Frequency Instrument (HFI).

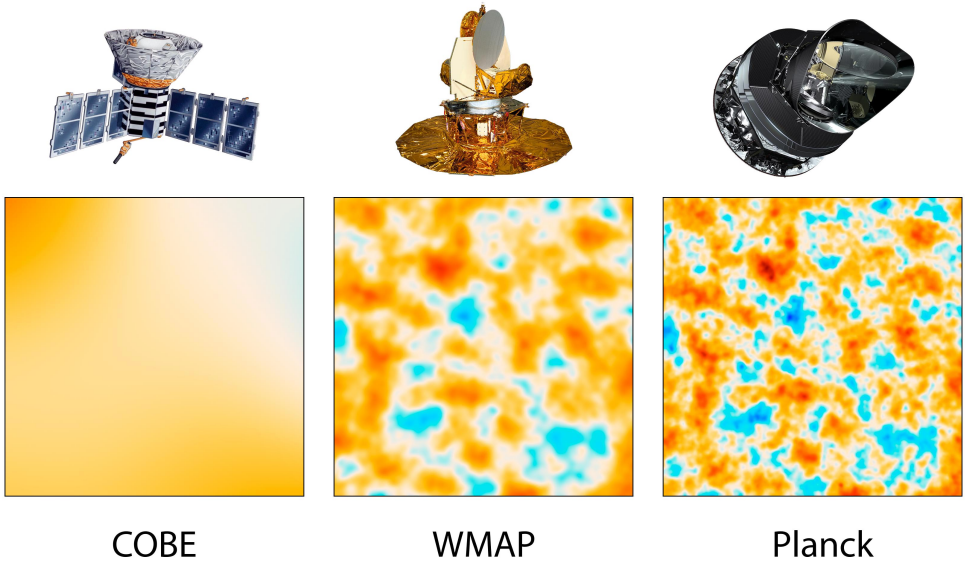


Figure 3.1: CMB measurements detected by NASA's COBE (left) in 1989, NASA's next generation satellite WMAP in 2001 (middle) and ESA's Planck (right) [21].

The HFI uses bolometers, which are cooled down to 100 mK by combining a passive cooling down to 60 K, a 20 K sorption cooler, a 4.5 K JT cooler and a 100 mK $^3$He/$^4$He open cycle helium dilution cooler. Two identical sorption coolers using hydrogen as the working gas were built to provide redundancy for this mission. The hydrogen gas goes through a Joule-Thomson expansion to provide cooling at 20 K. The sorption compressor shown in Figure 3.2 is a fundamental part of this system, it uses six sorbent beds and compresses the gas from 0.5 bar to 48 bar, their temperatures varying between 270 K to 470 K. The selected sorbent material was the metal hydride $LaNi_{4.78}Sn_{0.22}$ and each compressor cell contains approximately 600 g of this hydride powder [22].

At any moment during operation: one bed is releasing gas at high pressure and a controlled stream of hydrogen goes through the cold end; three other sorbent beds are absorbing to maintain the low pressure line constant; the remaining two beds are regenerating, respectively. The heating is accomplished by electrical resistance heaters, while the cooling is achieved by thermally connecting the sorption compressor unit to a radiator, where it rejects the input power at 270 K. Furthermore, each sorbent bed is thermally connected to the radiator via a gas gap heat switch, which enables

to decouple the sorbent bed from the radiator during the heating phases, to avoid unacceptable heat loads on this radiator. These heat switches also use hydrogen as the exchange gas and the switching action (transition between a good and poor thermal conduction) is obtained by heating or cooling a hydrogen sorption pump using a ZiNi intermetallic compound.

The cycle time of the compressor ranges from 9 min to 20 min, the total mass of each cooler is around 53.3 kg (excluding electronics) and the power consumption is less than 470 W (excluding electronics).

The hydrogen cold stage (JT stage) of Planck's sorption cooler includes two liquid reservoirs, one for each instrument, a set of counter-flow heat exchangers and a Joule-Thomson restriction. A porous material was used to create the impedance needed to obtain the JT expansion, it consisted of a sintered powder 316L Stainless Steel (SS) in a housing using the same alloy. A particle filter and a charcoal trap were placed upstream the restriction to reduce risk of contamination and clogging. The expanded hydrogen mixture of liquid and gas flows into two different reservoirs and the liquid confinement under zero-g conditions is assured by capillary forces through a metallic copper foam, which also avoids any temperature gradient inside the reservoir [23].

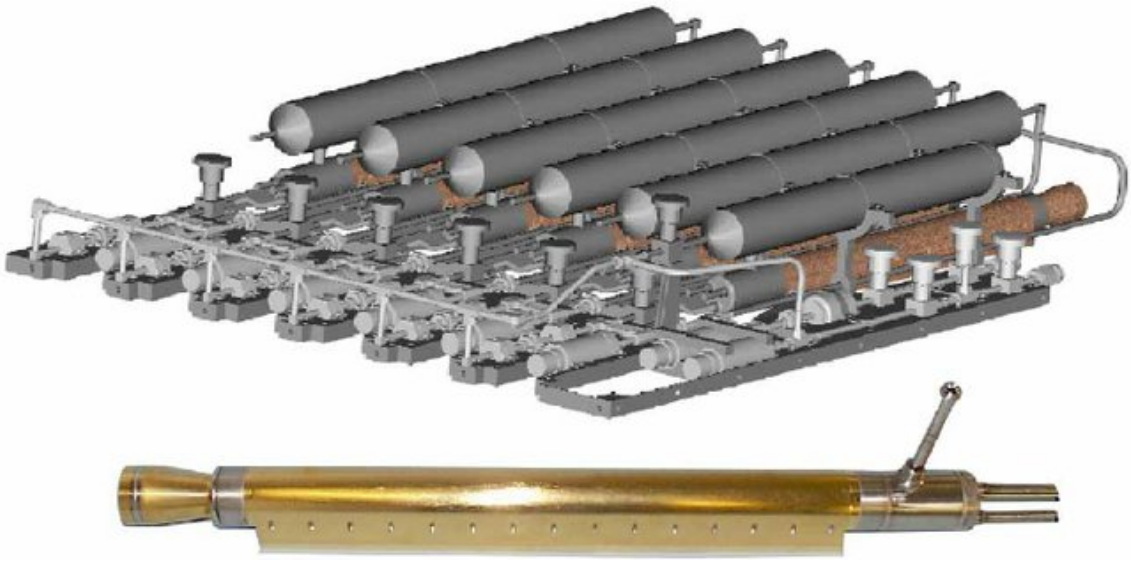

Figure 3.2: 20 K Planck sorption compressor system (top) and fabricated compressor element (bottom), from [24]. Reprinted from AIP Conference Proceedings, Vol. 613:1, pp. 1037-1044, with the permission of AIP Publishing.

### 3.2.2 ESO's METIS

The Mid-Infrared E-ELT Imager and Spectrograph (METIS) is one of the first scientific instruments of the European-Extremely Large Telescope (E-ELT) from the European Southern Observatory (ESO). It will offer imaging and spectroscopy over the wavelength range of 3 µm to 19 µm (L, M and N bands) [25].

METIS will require cryogenic cooling at different functional temperatures in the range of 8 K to 85 K to cool the optics instrumentation. Active cooling systems are needed for temperatures below liquid nitrogen, however, conventional cooling solutions such as pulse-tube coolers or Stirling are excluded, mainly because of their working principle which still induce undesirable vibrations, thus, reducing the imaging quality.

The University of Twente in collaboration with Airbus Defence and Space Netherlands submitted a proposal of a vibration-free cooler solution based on a sorption-based Joule-Thomson cycle. Several studies and improvements were made over the past years to achieve the optimum cryogenic cooler chain for METIS [26]. Helium, hydrogen and neon were found to be the adequate fluids to provide cooling at the various functional temperatures for the optics instrumentation of METIS. The cooling chain is disposed in a multi-stage cascade configuration, as shown in Figure 3.3.

In Figure 3.3, the neon, hydrogen and helium stages are arranged in parallel. During the preliminarily design phase, a different configuration was also considered and it consisted of the hydrogen cooler working in parallel with a cascade of neon and helium coolers. However this configuration was found to be less efficient than the parallel one, particularly, because of the limited performance of the neon stage, its COP being around 1 % to 2 %, whereas it reaches 3.7 % in the parallel configuration [12].

The helium stage is driven by a single-stage sorption compressor, four CFHX and three pre-cooling heat exchangers, which are coupled to the others stages in parallel: 40 K (neon stage), 25 K and 15 K (hydrogen stage), as visible in Figure 3.3. The efficiency of the helium stage is maximized by reducing the pre-cooling temperature as low as possible. However, in this case, it was limited by the vapour pressure of hydrogen and consequent pressure-drop in the low-pressure hydrogen line. At 15 K, the boiling pressure of hydrogen is 0.13 bar, which was found reasonable to be considered as minimum. The hydrogen stage provides two temperature levels and due to its low vapour pressure, a high compression ratio is needed, therefore, a double-stage compressor was found as mandatory. Lastly, the neon stage provides the required cooling power of 1.4 W at 40 K and uses a single-stage sorption compressor to circulate the neon gas with a mass flow rate of 170 $mg\,s^{-1}$. Its cooling capacity is split into cooling of METIS's L/M band detectors and helium and hydrogen pre-cooling interfaces.

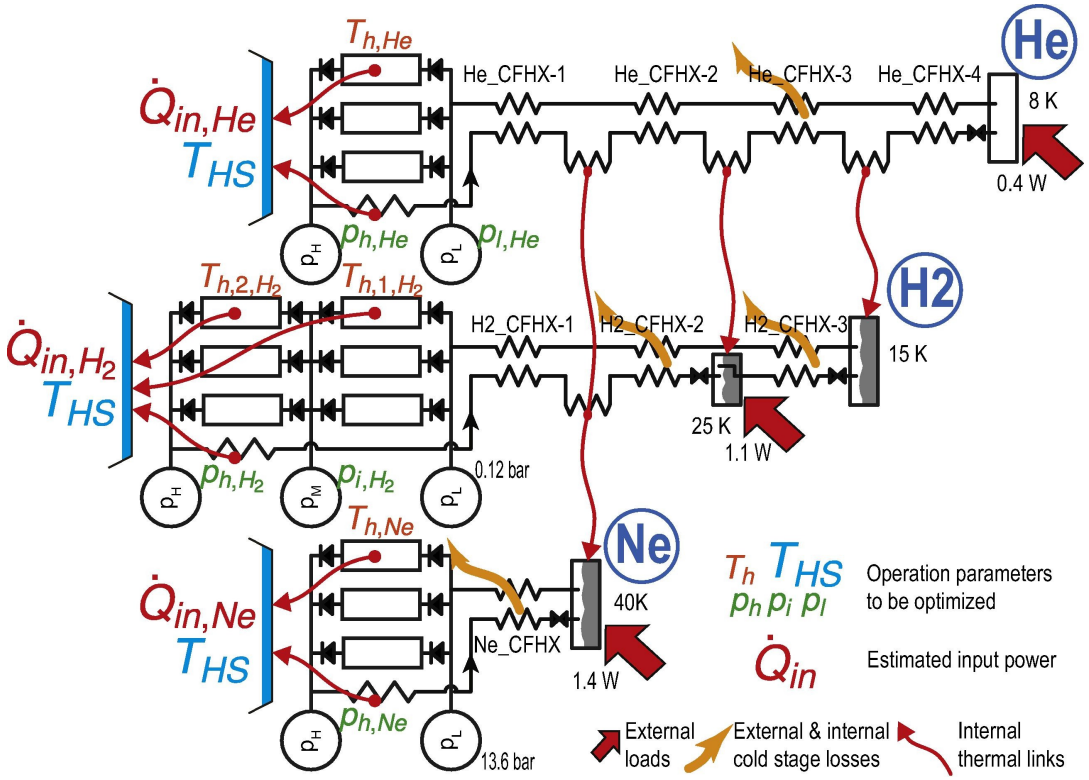


Figure 3.3: Conceptual design of METIS cooler chain from [12]. Reprinted from Cryogenics, Vol. 84, June 2017, Wu et al., pp. 37-52, Copyright 2017, with permission from Elsevier.

The heat-sink temperature $T_{\mathrm{HS}}$ is a critical parameter to size the system and tune its parameters. The lower the heat-sink temperature, the higher is the quantity of adsorbed gas, which deeply affects the size of the sorption compressor cells. In METIS, the heat-sink temperature of the sorption compressors is a dedicated liquid nitrogen bath. In Earth, such cooling solution corresponds to a simpler and vibration-free solution. Moreover, this LN2 bath can be pumped to even further reduce the heat-sink temperature, in the range of 64 K to 74 K. In this system in particular, it was estimated that the sorption cooler consumption decreases about 6% per degree of $T_{\mathrm{HS}}$ [12]. By using a LN2 bath at atmospheric pressure (77.3 K), the cooler needs around 67 compressor cells, considering a carbon-based compressor cell with a dimension of $1.5 \times 50$ cm$^2$. On the other hand, if such LN2 bath is pumped down to 70 K, only 43 cells are required, which corresponds approximately to a mass reduction of 36% and, therefore, one can see that this temperature greatly interferes the design of the compressor. After some trade-off analysis, 70 K was the selected temperature for the LN2 pumped bath.

Each compressor cell consists of a cylindrical, thin-wall container filled with an adsorbent material, it comes also equipped with actively operated gas-gap heat switches, as displayed in Figure 3.4a. Two support spacers are used to hold the container, thus

keeping a gap between the container and the heat-sink. This narrow gap could be used as a gas gap heat switch by varying its internal pressure with a hydrogen getter. The proposed METIS refrigerator requires more than 50 cells, each one 50 cm long. Then, it becomes really expensive and mechanically complex to build such large quantity of cells respecting the tolerances needed to obtain this narrow gap over the full length of the cell. However, since it is a ground-based application, where the efficiency is less of a concern, a different and simpler solution was envisaged.

In the developed alternative solution, the gas-gap was replaced by a solid insulation layer, displayed as green in Figure 3.4b. This layer should have low thermal conductivity, low heat capacity, low porosity, low thermal expansion coefficient and it has to be an inert material: Kapton®, Mylar or Teflon® are feasible candidates and commercially available. It is clear that this solid layer has much higher conductance than an OFF state of a GGHS. However, this thermal conductance can be further reduced by increasing the thickness, although, this also slows down the cooling process, which results in a longer cycle period [26].

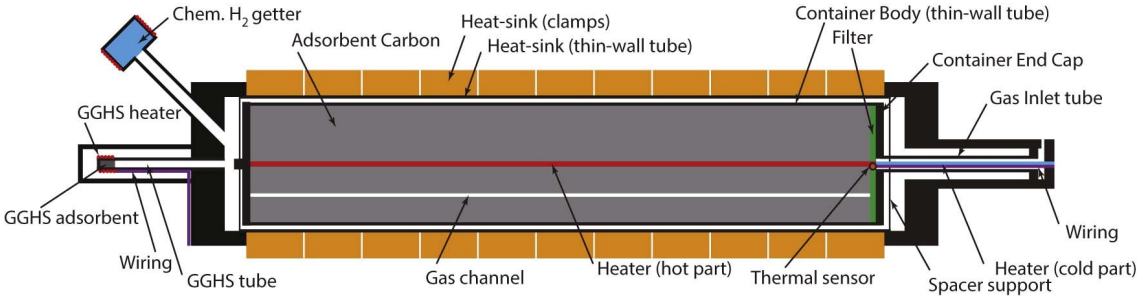


(a) Schematic of a sorption compressor cell operating with a gas-gap heat switch.

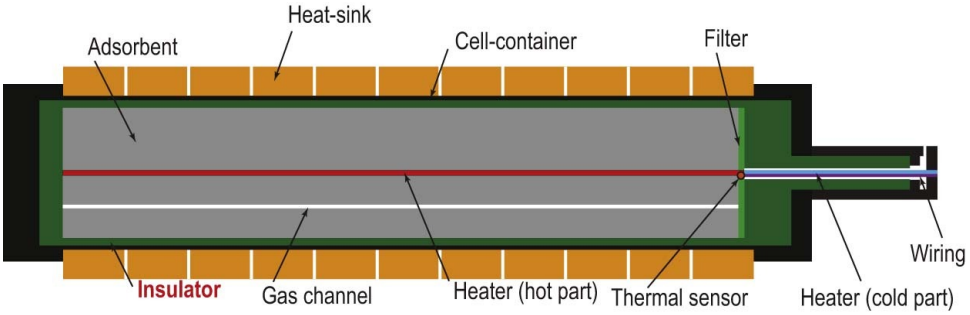


(b) Schematic of a switchless sorption compressor cell, the narrow gap was replaced with an insulation layer.

Figure 3.4: Comparison between two compressor cell designs of METIS's cooler, from [26]. Reprinted from International Journal of Refrigeration, Vol. 82, October 2017, Wu et al., pp. 520-528, Copyright 2017, with permission from Elsevier.

Since many parameters can be adjusted, Wu et al. developed a one-dimensional dynamic model to evaluate and size the METIS cooler using switchless sorbent cells. Of course, such configuration has a lower production cost and is a much more reliable,

mechanically speaking, however, it has a higher heat load to the heat-sink, but still compatible with ground-based applications. On the other hand, it can be quite difficult to use this solution in space-based applications, due to limited resources (low heat-sink rejection capacity).

## 3.3 Baseline System Solution

### 3.3.1 Fluid Selection Tradeoff

The working fluid deeply interferes the design of the VFC. As previously seen in Section 2.2.4, the available pure fluids at saturation conditions within the temperature range of interest is limited. Therefore, for the 40 K functional temperature, neon is the only possible choice and for the 80 K temperature, both nitrogen or oxygen are possible solutions. According to the system requirements shown in Section 3.1, the targeted temperature range does not have to be fully covered. The cooling solution can be adapted for two different functional points by merely changing the working fluid. Thus, a cooling solution using two fluids, each one dedicated for each functional temperature, was studied.

#### 80 K Functional Point

To compare the performance between a JT stage of nitrogen and oxygen, the Joule-Thomson $COP_{\mathrm{JT}}$ for each of the selected fluids can be calculated using Equation (2.15). Figure 3.5 shows the nitrogen and oxygen $COP_{\mathrm{JT}}$ as a function of the working high pressure $P_H$ and of the inlet temperature $T_1$ (considering the state points from Figure 2.3).

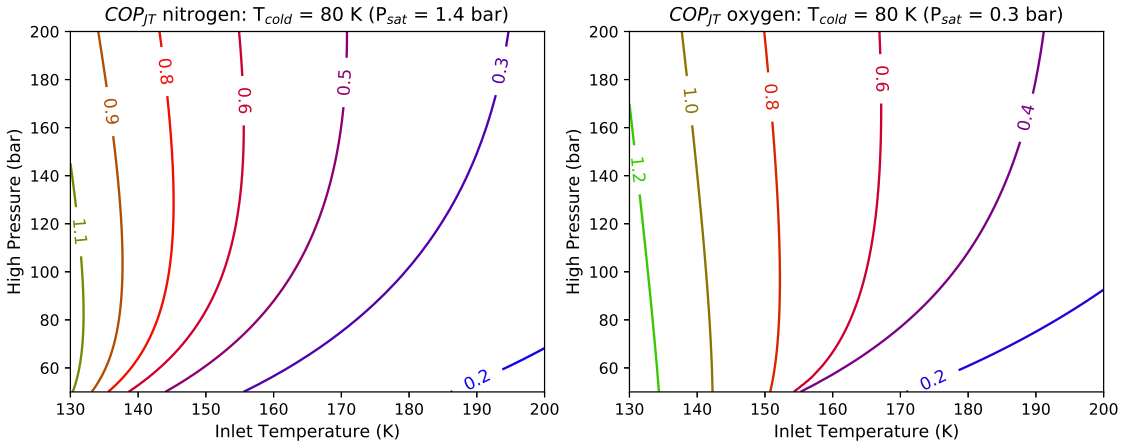


Figure 3.5: Nitrogen (left side) and oxygen (right side) JT stage $COP_{\mathrm{JT}}$.

Evaluating both contour plots, the JT stage either with nitrogen or oxygen have similar performances and, for pressures approximately above 150 bar, the COP is not

strongly pressure dependent. However, it is noticeable that the oxygen performance is slightly better. Regarding the performance of a sorption compressor either with oxygen or nitrogen, a direct comparison is only possible if the adsorptive properties of the adsorbent are known and even if the same adsorbent is considered their sorption properties will be different according to the gas.

In a pre-dimensioning phase carried out by AST, a cooling solution using activated charcoal as the adsorbent material was studied and it consisted in a configuration of four sorption cells, each one having 1 L volume. Taking into account the adsorption isotherms found in the literature for nitrogen [27] and also the simulated adsorption quantities of oxygen on activated charcoal [28], both fluids showed similar performances, hence, both being potential candidates for the 80 K temperature functional point. Anyway, more nitrogen and oxygen adsorption data is required on different materials and over a wider range of both pressure and temperature, since these are found out to be very scarce in the literature. A priori, oxygen is more attractive as it can reach lower temperatures, however, selecting it as working fluid of the 80 K functional point brings some disadvantages and concerns, which are presented below:

- Since adsorption increases with pressure, the oxygen's low saturation pressure of 0.3 bar at 80 K may lead to a very poor gas adsorption and, then, to a very inefficient cycle.
- The commercially available passive check-valves operated by differential pressure have a cracking pressure[1] of 140 mbar which is the same order of magnitude as the oxygen vapour pressure, thus, turning their operation problematic. To overcome this issue, the development of a specific check-valve for this operational range would be required.
- If volume buffers are needed to damp the mass-flow rate and/or the pressure fluctuations between the different phases of the compression cycle, they have to be quite large (compared to the nitrogen ones), to store a significant quantity of gas at a low pressure of 0.3 bar.
- The very reactive oxygen requires careful screening of materials and special cleaning procedures.

In the light of these arguments, it was considered safer and adequate to proceed the development of the cooler with nitrogen for the 80 K functional point.

[1] Refers to the minimum pressure differential needed between the inlet and outlet of the valve at which a steady stream is obtained.

### 40 K Functional Point

Neon is the only fluid under saturation conditions for this functional point and it belongs to the group of gases whose inversion temperatures are below room temperature. Then, to achieve liquefaction, a pre-cooling configuration is needed. The pre-cooling source in space could either be obtained by diverging some cooling power from another cooler arranged in parallel, for instance, the 80 K nitrogen stage, or by passively rejecting the heat through a radiator.

Figure 3.6 shows the $COP_{\mathrm{JT}}$ of a neon JT cycle as a function of the inlet (pre-cooling) temperature $T_3$ (considering the state points from Figure 2.5) and high pressure, $P_H$.

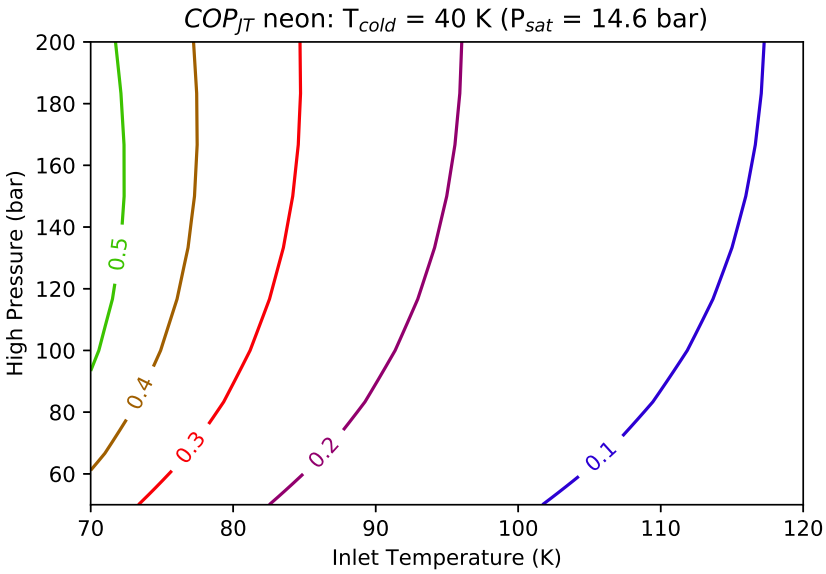


Figure 3.6: Neon JT stage $COP_{\mathrm{JT}}$. The inlet-temperature corresponds to the state point 3 of Figure 2.5.

It is visible that the $COP_{\mathrm{JT}}$ values of neon are significantly lower compared to those of nitrogen and oxygen, note that these values were estimated for lower temperatures (T<120 K). Therefore, the neon stage could not share the same inlet temperature (i.e share a common heat-sink) as the nitrogen stage, so, justifying the need of precooling as schematically displayed in Figure 2.5. If a radiator is considered as the heat-sink, the heat $\dot{Q}_R$ exchanged by a radiator of surface area $A_R$, rejecting at $T_\infty$, is obtained by the following equation,

$$\dot{Q}_R = \sigma \epsilon A_R ({T_R}^4 - T_\infty^4) \tag{3.1}$$

where $\sigma$ is the Stefan-Boltzmann constant and $\epsilon$ is the emissivity of the radiator. According to our system requirements, the radiator background temperature $T_\infty$ is limited to 90 K and the maximum exchange surface area $A_{MAX}$ is 1.5 $\mathrm{m}^2$, then, this radiator could only be used as the precooling source of the neon stage for temperatures higher than $T_\infty$.

However, the $COP_{JT}$ values (less than 0.2) are clearly reduced for an inlet-temperature above 90 K and, therefore, this makes the use of the radiator as a pre-cooling source for the neon stage very inefficient.

Considering the state points from Figure 2.5 and setting $T_1 = 180$ K and $P_H = 100$ bar (as an example), it is possible to estimate, through Equations (2.17) and (3.1), the required radiator surface $A_R$ for the pre-cooling source to obtain 0.5 W of cooling power at 40 K, Figure 3.7 shows such a result. As expected, for temperatures close to $T_\infty$, $A_R$ easily exceeds $A_{MAX}$. For instance, if the pre-cooling temperature is set at 92 K, where $A_R = A_{MAX}$, the whole radiator surface would be needed just to pre-cool the high pressure stream of neon. Let us remind that this radiator also has to cool down the neon and nitrogen sorption cells and the high-pressure stream of nitrogen. By setting $A_R/A_{MAX}$ between 1 % to 5 %, thus using a small fraction of the total area as the pre-cooling source, the pre-cooling temperatures fall in the range of 115 K to 150 K. However, in this condition, the neon's mass flow rate is quite high (from 61 mg s$^{-1}$ to 128 mg s$^{-1}$) in comparison to an alternative configuration that diverges some cooling power from the 80 K nitrogen cold stage to pre-cool the neon gas flow. In such configuration, the required mass flow rate $\dot{m}$ of neon is only 27 mg s$^{-1}$.

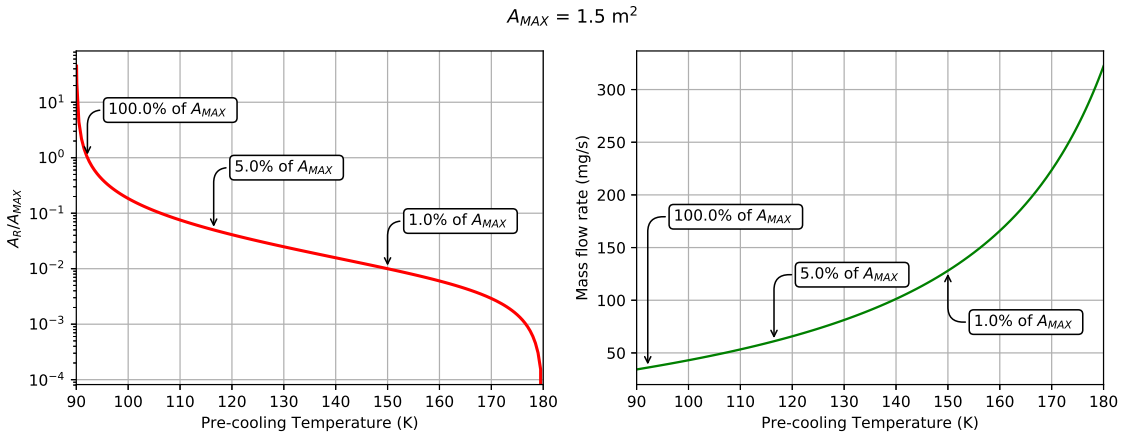


Figure 3.7: Left side: neon's pre-cooling exchange surface ratio to the maximum exchange surface $A_R/A_{MAX}$ as a function of the pre-cooling temperature. Right side: mass flow rate $\dot{m}$ needed to obtain a heat lift of 0.5 W at 40 K, shown as a function of the pre-cooling temperature $T_3$. For both plots, $T_1 = 180$ K and $P_H = 100$ bar, for calculation purposes only.

Actually, according to the system requirements, it is possible to diverge some heat lift from another functional stage (e.g. nitrogen stage). About 0.5 W at 80 K may be used to cool down the high pressure neon stream and, therefore, increase the performance of the neon stage. Also, this solution seems more attractive as it is possible to operate the neon stage with a lower pre-cooling temperature (at 80 K) and, consequently in a

more efficient region (Figure 3.6), since less mass flow rate is needed to obtain the same cooling power at 40 K. Although the sorption compressor behavior was excluded in this trade-off analysis, it is known that adsorbing neon can be a complicated task, therefore, it is preferable to opt for a configuration leading to a reduced mass flow rate.

### 3.3.2 Proposed Design

Based on the trade-off shown in Section 3.3.1, nitrogen is the chosen fluid for the 80 K functional point and neon is the one selected for the 40 K interface. Considering this, a cooling solution using both fluids is presented and displayed in Figure 3.8. The configuration consists in two parallel stages: the nitrogen stage, employing a basic Linde-Hampson cycle, as shown previously in Figure 2.3 and a neon stage, using a pre-cooled LH cycle with the precooling source from the 80 K JT stage (Figure 2.5).

Taking into account the working principle of a sorption compressor, the gas amount released/adsorbed by a sorption cell during a compression cycle should be as high as possible, thus, usually, forcing each sorption cell to operate over a wide range of pressure and temperature. Moreover, to obtain a continuous flow of gas, the four cells working in quadrature, as explained in Section 2.3, are needed. From the JT expansion point of view, higher pressures favours the stage performance. So, in a first preliminary design, it was envisaged that the sorption compressor cells would have to vary their temperatures between 150 K to 500 K and pressure between 1 bar to 100 bar.

The proposed solution also considers that both nitrogen and neon sorption compressors share the same radiator, so, the same heat-sink temperature. Each sorption cell is thermally coupled to this radiator through a gas gap heat switch, to allow a thermal decoupling during the heating phases and also to obtain a good thermal conduction when cooling is needed. Furthermore, the heat input/release of each compressor cell is highly dependent on the adsorbent properties, namely, the sensible heat and isosteric heat of adsorption of the sorbent bed. However, as it is found in the literature, adsorption isotherms data of both nitrogen and neon over a wide range of pressure and temperature is very limited. For this reason, an extensive search and screening of many materials was carried out to find suitable materials that can be used to charge the sorption compressor cells. The conclusions and results of this study can be found in Chapter 4 and it allowed to a more detailed design and, therefore, a more accurate definition of the parameters of the VFC, within the requirements.

Let us note that the activated charcoal has been excluded from our studies, since the found data in the literature of neon was far from our targeted pressure range and it seemed to indicate that the adsorption capacity of neon was quite reduced, lower than hydrogen adsorption, in the temperature range of interest [27, 29]. So, using activated

charcoal may turn the operation of the neon sorption compressor problematic. In fact, as previously mentioned, a first preliminary screening of adsorbent materials showing good neon adsorption pointed to a new class of porous materials: Metal-Organic Framework (MOF), as they seem to be more promising when compared to activated carbon [28].

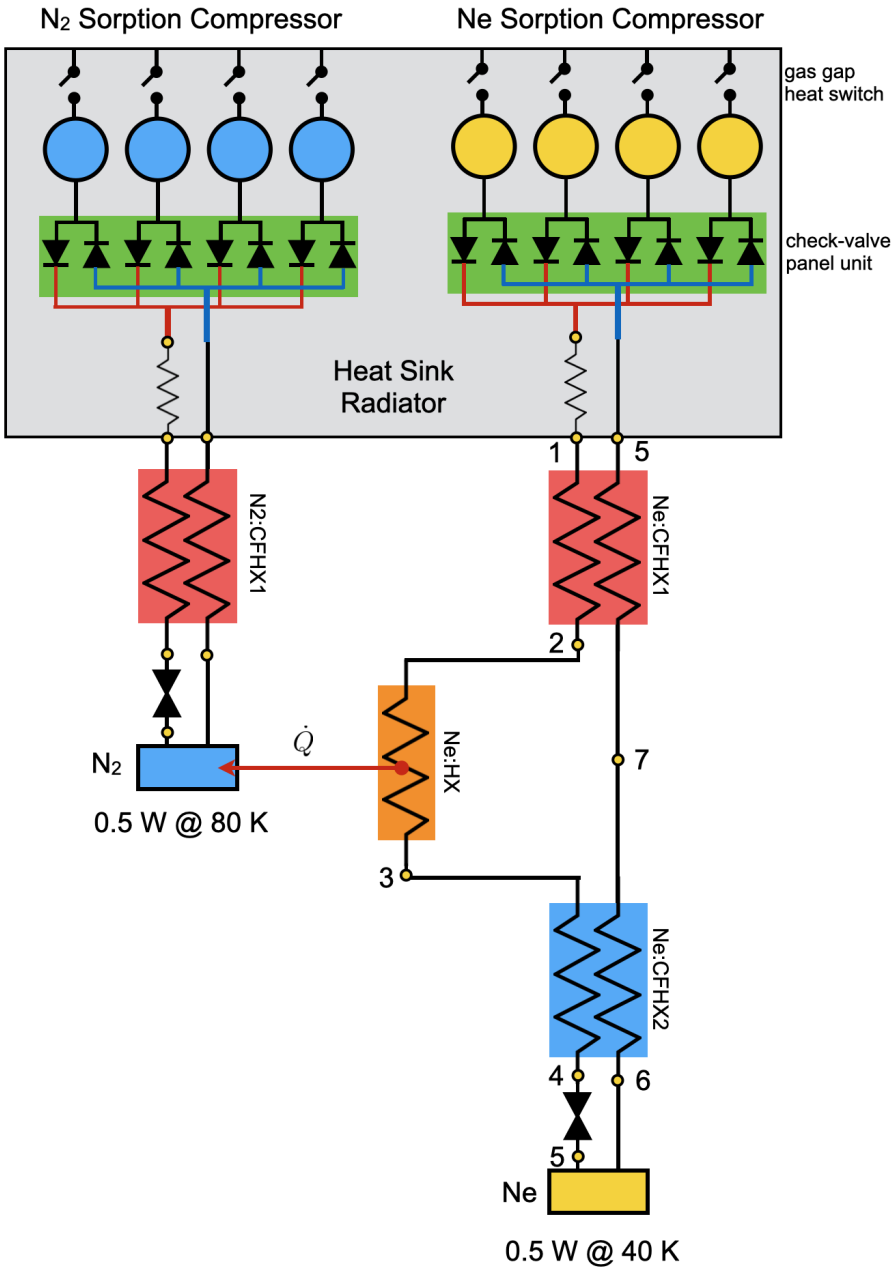


Figure 3.8: Schematic of the proposed design of a two stage vibration-free cooler.

CHAPTER 4

# Adsorbent Materials Characterization

The core element of a sorption compressor is certainly its adsorbent material since the working fluid needs to have a good affinity with the selected adsorbent on the required equilibrium pressure/temperature range. For that reason, an extensive search of materials with large adsorption capacities for both neon and nitrogen was carried out by simulation and three potential materials were pointed out and characterized over a wide range of pressure and temperature.

This chapter includes a brief overview of basic adsorption models, a description of the selected adsorbent materials, the measurement methods and the measured characteristic adsorption isotherms of the three potential materials. This chapter ends with a review of the proposed cooling configuration considering the obtained adsorption behavior. Some results shown in this chapter are published in [30, 31].

## 4.1 Adsorption Isotherms Models

Adsorption isotherm data of a pair adsorbate-adsorbent is an important input for designing sorption compressors. Therefore, for designing purposes, it is convenient to apply a model that correlates the measured adsorption isotherms and expresses the adsorbed quantity as a function of pressure and temperature. By using such model, it allows to analytically obtain the working parameters of the sorption compressor as, for instance, the working high pressure and the required temperature interval to circulate the required gas quantity towards the JT stage.

A wide variety of equilibrium isotherm models have been formulated over the past years. Foo and Hameed have presented in 2010 the current state of the art of the many existent adsorption isotherm models [32]. The empirical model derived by Langmuir in 1918 is still one of the simplest and most versatile models. This model assumes

the adsorbent surface as perfect and homogeneous, where all of the adsorption sites possess the same adsorption energy, without any interaction between the adsorbed molecules. Moreover, adsorption can only take place for a fixed number of localized sites. The adsorption Langmuir equation as a function of pressure, $P$, is given by,

$$C(T,P) = C_0 \frac{K(T)P}{1+K(T)P} \tag{4.1}$$

where $C(T,P)$ is the absorbed concentration at an equilibrium pressure, $P$, and temperature, $T$; $C_0$ is the mono-layer capacity and $K$ is a constant dependent on the adsorption energy of the pair adsorbate-adsorbent and of the temperature. Graphically, it is characterized by a linear increase of $C$ at low pressure (Henry's law) and a saturation at high pressure, where once the adsorption sites are fully occupied, no further adsorption takes place.

The Freundlich isotherm empirical model describes non-ideal adsorption and it may be applied to multilayer adsorption on surfaces with heterogeneous adsorption energy. Basically, it considers that the adsorption sites are not constant for different adsorbed concentrations: stronger binding sites are occupied first, until they exponentially decrease upon completion of the adsorption process. The adsorption Freundlich equation is given by [33],

$$C(T,P) = K_F(T)P^{\frac{1}{n}} \tag{4.2}$$

where $K_F(T)$ is a constant for a given pair of adsorbate-adsorbent at a particular temperature, $n$ is a correction factor. We emphasize that such model does not predict an adsorption saturation, therefore, it is commonly used to describe systems at low adsorbate concentrations.

The Sips model is a combined form of both Langmuir and Freundlich models, where at low adsorbed concentrations it reduces to a Freundlich isotherm, while at high concentrations it predicts a monolayer adsorption as the Langmuir model. The Sips adsorption equation is expressed as [34],

$$C(T,P) = C_0 \frac{(a_s P)^{\frac{1}{n}}}{1+(a_s P)^{\frac{1}{n}}} \tag{4.3}$$

where $a_s$ is a parameter depending on the adsorption energy and $n$ a dimensionless parameter that describes the heterogeneity of the adsorbate-adsorbent system. Note that, for $n = 1$, the previous equation reduces to the Langmuir equation.

In a previous work, the Sips adsorption model has successfully described adsorption isotherms in the temperature range of 300 K to 400 K and for pressures up to 80 bar of nitrogen, methane, ethane and propane on three carbons: Norit RB2, Chemviron

AP 4-60 and the highly activated Saran [34]. Furthermore, in this work, the authors pointed out that the parameter $C_0$ should not be considered as the ultimate saturation adsorption.

As previously explained in Section 2.3, another important parameter to consider in a sorption compressor design is the isosteric heat of adsorption $L$ that can be obtained, in a first approximation, from the equilibrium isotherms. Considering the adsorption phenomenon as a phase change and assuming thermodynamic equilibrium between the gas and the adsorbed phase, the Clausius-Clayperon relation may be used for a series of adsorption isotherms at different temperatures and, hence, obtaining the isosteric heat of adsorption, $L$, defined as [35],

$$L = -\frac{R}{M}\left.\frac{\partial \ln(P)}{\partial(1/T)}\right|_n \tag{4.4}$$

where $R$ is the ideal gas constant and $M$ is the molar mass. It is important to mention that the differential quantity on the expression is evaluated at constant adsorbed concentration, represented by the subscript $n$. Each adsorbed state is defined by one value of $n$ and one value of equilibrium pressure at constant temperature.

## 4.2 MOFs Materials

The Metal-Organic Frameworks (MOFs) are a recent class of promising porous materials consisting of a highly ordered crystalline network of metal ions (or clusters) linked together by organic molecules [36]. Their distinctive features are its high pore volumes, large surface areas, tunable pore size, turning this class of materials very attractive for various applications, namely, adsorptive gas storage [37], separation, catalysis and others [38, 39]. Moreover, they can be tailored for specific applications, by exploring the many possible combinations of metal/organic-ligands [30].

However, as already mentioned, adsorption isotherm data over a wide range of both pressure and temperature is very limited and, as a result, an extensive search for materials with large neon and nitrogen adsorption capacities was carried out by J.P. Mota of LABQV-REQUIMTE (R&D unit at FCT NOVA) to find potential adsorbent materials that could be used in the sorption compressor under development. This search only included MOF materials due to their large portfolio and also the ones that are commercially available in large quantities. From an initial survey of the open literature and online resources, thirty one potential candidates were selected based on its large methane or hydrogen adsorption capacity, since these molecules are the closest to the target molecules and its adsorption capacity, $q(T,P)$, was predicted through Grand

Canonical Monte Carlo (GCMC) molecular simulation [40] over the 130 K to 500 K temperature range and 0.8 bar to 150 bar pressure range. Figure 4.1 shows the simulated net adsorption capacity[1] per unit volume of material of the thirty one potential candidates [41].

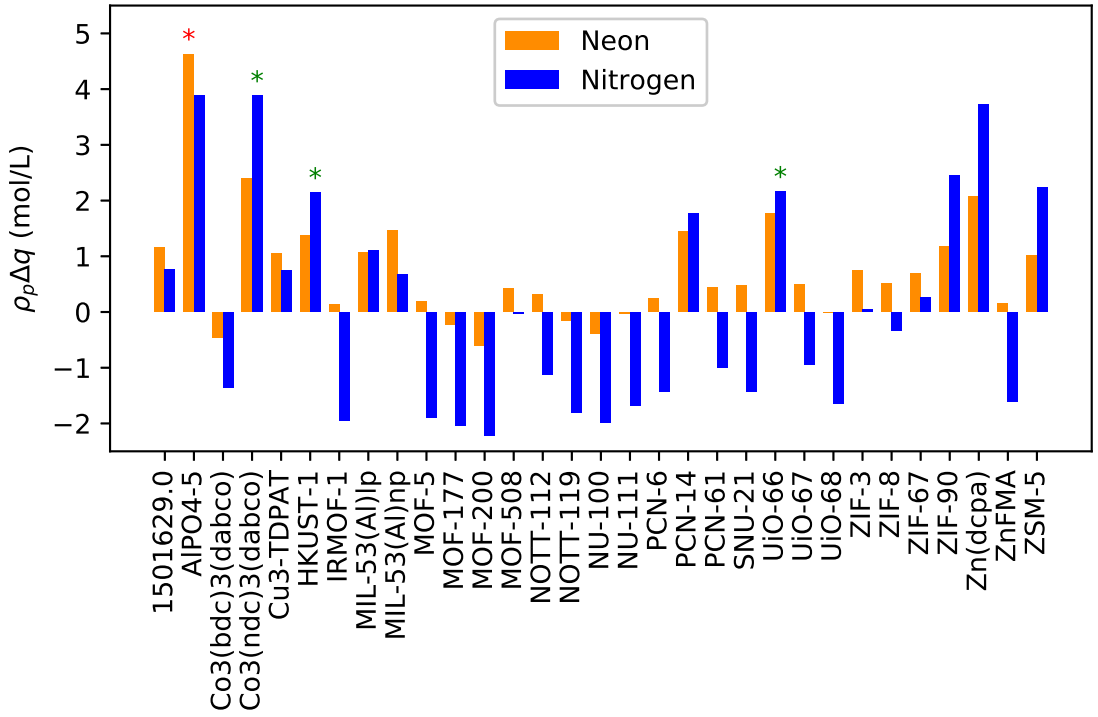


Figure 4.1: Net adsorption capacity of the 31 analyzed porous materials through GCMC molecular simulation for neon (orange) and nitrogen (blue) storage. The net capacities are calculated per unit particle volume for an adsorption cycle of neon operating between (500 K, 100 bar) and (180 K, 16 bar) and nitrogen, between (500 K, 100 bar) and (180 K, 0.8 bar). The material identified by the red asterisk (AIPO4-5) has the best adsorption capacity and the ones identified by the green asterisks are the best candidates for an experimental proof-of-concept of the VFC since they are readily available in large quantities [41].

The results coming from this simulation pointed out three potential materials, which are identified with green asterisks in Figure 4.1: HKUST-1, UiO-66 and $Co_3(ndc)_3(dabco)$ [2]; and displayed in Figure 4.2. The HKUST-1 material has already been experimentally studied and simulated using GCMC in the 40 K to 60 K temperature range for pressures up to 0.8 bar [42].

The HKUST-1 samples were purchased from Sigma-Aldrich (Germany), under the trademark Basolite C300 and also from MOF Technologies (UK), under the trademark

[1] This quantity represents the available quantity per unit volume for circulation during a compression cycle.

[2] ndc stands for 2,6-naphthalenedicarboxylate and dabco for 1,4-diazabicyclo[2.2.2]octane

Porolite C1 CuBTC. Both UiO-66 and $Co_3(ndc)_3(dabco)$ samples were synthesized under request and purchased from the Materials Center of the Technical University of Dresden (Germany).

The BET surface area and pore volumes of HKUST-1, UiO-66 and $Co_3(ndc)_3(dabco)$ powder samples were obtained in a commercial volumetric apparatus (ASAP 2010 from Micromeritics, Norcross, GA). Thermal Gravimetric Analysis (TGA) of the MOF samples were also performed to examine their thermal stability/degradation as a function of temperature, by using a commercial equipment (SETARAM Instrumentation LABSYS Evo TGA–DTA/DSC). Table 4.1 summarizes and highlights some of the interesting measured properties. Let us note that, in this table, $\rho_p$ represents the particle density of the material, which is the mass density of a single particle (weight divided by volume), whereas, $v_p$ is the pore volume per unit mass. These two quantities will be important to estimate the mass flow rate output/input of the sorption compressor under development.

Figure 4.2: Left side: Purplish powder of HKUST-1; Middle: very fine white powder sample of UiO-66; Right side: Purplish powder of $Co_3(ndc)_3(dabco)$ on argon atmosphere glove-box.

Table 4.1: Physical Properties of the tested MOFs.

| Property | HKUST-1[30] | UiO-66[30] | $Co_3(ndc)_3(dabco)$ [31] |
|---|---|---|---|
| Chemical Formula | $C_{18}H_6Cu_3O_{12}$ | $C_{48}H_{28}O_{32}Zr_6$ | - |
| BET surface area [$m^2/g$] | 1407 | 1395 | 1502 |
| Pore volume $v_p$ [$cm^3/g$] | 0.72 | 0.60 | 0.82 |
| Particle density $\rho_p$ [$g/cm^3$] | 0.95 | 1.24 | 0.74 |
| Decomposition Temperature [K] | 580 | 700 | 590 |

## 4.3 Experimental Methods

The characteristic adsorption isotherm of the selected MOFs materials were obtained using a classic volumetric (or manometric) method specifically developed and built in-house [43]. A schematic summarizing the set-up is displayed in Figure 4.3.

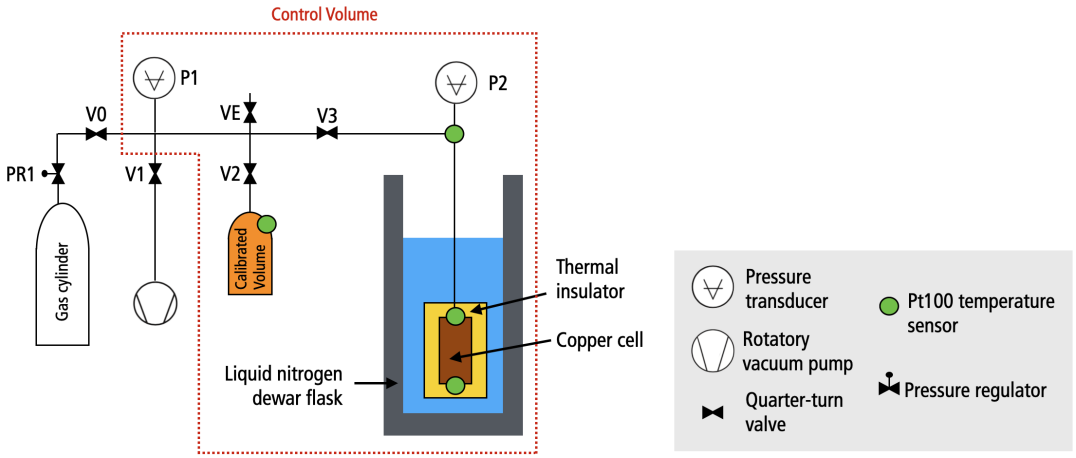


Figure 4.3: Volumetric set-up used for the adsorption measurements. The system has two thermometers attached to the low temperature copper cell and two others to measure the temperature of the calibrated volume and of the gas manifold at room temperature.

The volumetric system consists of a temperature-controlled copper cell, displayed in Figure 4.4a, thermally insulated with polystyrene foam and glass wool and able to be submerged in a liquid nitrogen bath. The cell contains a known quantity of adsorbent material and it is connected to a gas manifold through a stainless-steel capillary tube (outer diameter: ≈1.6 mm). The gas manifold at room temperature contains two piezoelectric pressure transducers (pressure range 0 bar to 300 bar) and a calibrated volume to charge the system with an initial known gas quantity. The set-up contains four platinum thermometers (Pt100), whose readings were measured by a cryogenic temperature controller (Lakeshore Cryotronics): two of them are fitted into the bottom and upper part of the copper cell, while the two others are glued on the calibrated volume and on the gas manifold. The thermal control of the adsorption cell is obtained by a PID algorithm which actuates over a 50 Ω cylindrical heating resistor also inserted into the bottom part of the cell. Such a set-up allows to stabilize the temperature of the cell from 77 K to 500 K and perform automatic acquisitions over this range.

A first adsorption copper cell was developed and it allowed to obtain neon adsorption equilibrium isotherms on HKUST-1 over a wide temperature range of 77 K to 400 K and pressure range of 0 bar to 70 bar [43]. Although this cell was designed to withstand pressures high as 300 bar, it presented some limitations, for instance, leakage when

high pressure and high temperature (100 bar and >400 K) combined simultaneously. These leaks were due to the soft solder used to seal the cell.

Then, taking into account these issues, a new modular adsorption cell, as displayed in Figure 4.4, was manufactured and brazed at our workshop (Department of Physics, FCT NOVA). In this new design, the cell's body and its cap are silver brazed (600 °C) and are not dismountable. This new configuration allows to heat up the cell up to 500 K with high pressure combined, without structural damage. Moreover, by removing the soft soldering procedure, which previously sealed the cell, the risk of sample contamination and exposure to high temperatures is mitigated. It is also possible to force a flow of a cleaning solution (soap water or isopropyl alcohol) since the cell has two inlet/outlet connections. After its manufacture and brazing, the cell underwent a qualification test campaign: leak detection under vacuum and proof pressure, up to 100 bar. The technical drawings of this cell can be consulted in Appendix C.

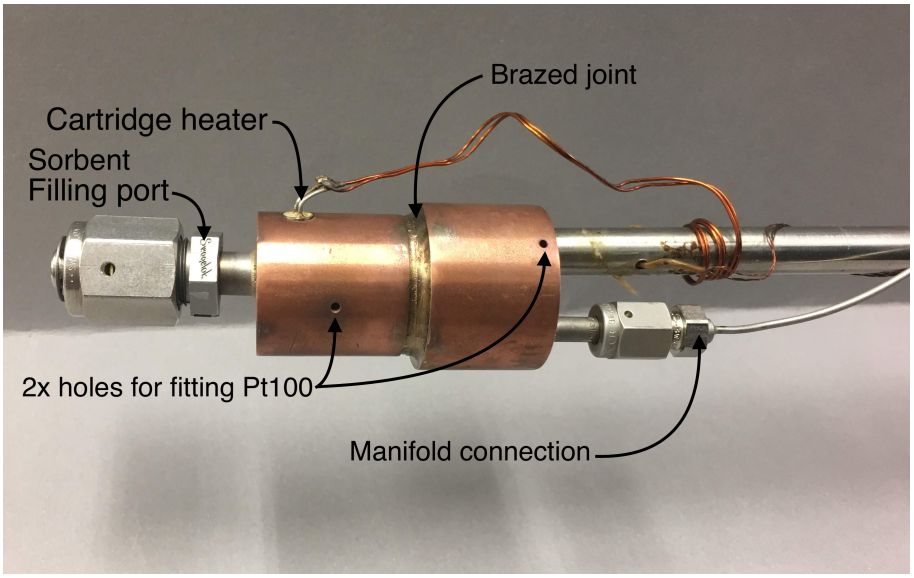


(a) Adsorption cell description.

(b) Modular adsorption cell using Swagelok VCR® fittings.

Figure 4.4: Redesigned copper adsorption cell built in-house.

To fill this cell, the MOF is introduced through a VCR® filling port (4 mm inner diameter), hermetically closed after filling. The cell is connected to a room temperature gas panel through a 1/8 inch VCR® fitting (manifold connection), as visible in Figure 4.4a.

Before an adsorption characterization, the following filling and mounting procedure is performed:

1. Cell is weighted empty;
2. Cell is filled, while trying to obtain the maximum filling capacity;
3. Cell is weighed again;
4. Cell goes in vacuum at 80 °C or higher over 24 h to remove unwanted moisture;
5. After this procedure, the sample is weighed again and connected to the volumetric system for measurements.

According to the supplier, the $Co_3(ndc)_3(dabco)$ sample degrades if exposed to atmospheric conditions, so, the filling procedure of this sample was performed in a argon glove-box controlled environment (less than 1 ppm of oxygen and water).

Referring to Figure 4.3, the volumetric system (including the filled adsorption cell) is purged with the gas under study and pumped by opening valve *V1* to the rotatory vacuum pump, while keeping the quarter-turn valve *V0* closed. With both valves *V3* and *V1* closed, an initial gas quantity $n_0$ is charged into the calibrated volume by using the pressure regulator *PR1* connected to a high purity gas cylinder. The charged quantity, $n_0$, is calculated from the pressure and temperature readings of the calibrated volume and using the molar density values coming from REFPROP [44], $n_0$ corresponds to the total quantity in the control volume shown in Figure 4.3.

Afterwards, valve *V3* can be opened to the adsorption cell for measurements. To obtain a full set of adsorption isotherms, the procedure is obtained from several runs at different initial gas quantities, $n_0$, to cover the whole pressure range of interest. Note that each run is performed at constant total quantity. During a run, all valves except *V2* and *V3* are closed and the cell is submerged in liquid nitrogen. The measurements starts at low temperature, for instance, at 77 K for neon or 130 K for nitrogen. The equilibrium pressure is recorded once it stabilizes at a given temperature plateau. Afterwards, the temperature is increased to the next plateau and this procedure is repeated until it reaches the maximum temperature.

After measurements, a mass balance is applied to the control volume displayed in dashed-red line from Figure 4.3 to determine the molar quantity in the cell, $n_c$, and two contributions must be calculated: the gas quantity remaining in the volumes of the manifold and in the calibrated volume. Summing up these contributions, the molar quantity in the cell, $n_c(T,P)$, at an equilibrium temperature, $T$, and pressure, $P$, is,

$$n_c(T,P) = n_0 - n_{CV}(T_{CV},P) - n_{GM}(T_{GM},P) \tag{4.5}$$

where $n_o$ is the total quantity in the system, $n_{\mathrm{CV}}(T_{\mathrm{CV}}, P)$ is the molar quantity in the calibrated volume and $n_{\mathrm{GM}}(T_{\mathrm{GM}}, P)$ is the molar quantity in the gas manifold at $T_{\mathrm{GM}}$. The molar quantity $n_{\mathrm{c}}(T, P)$ is then used to calculate the adsorbed molar quantity per gram of MOF material, $q(T, P)$, by using the following relation,

$$n_{\mathrm{c}}(T,P) = V_{\mathrm{c}}(\underbrace{\epsilon\rho_g(P,T)}_{\text{void space}} + \underbrace{(1-\epsilon)\rho_p q(P,T)}_{\text{adsorbed}}) \tag{4.6}$$

where $V_c$ is the volume of the adsorption cell, $\epsilon$ is the void fraction of the sample packed in the cell, $\rho_g$ is the density of the gas filling the void space between MOF particles and $\rho_p$ is the MOF particle density. The void fraction, $\epsilon$, corresponds to the volume fraction of the cell which is not occupied by the MOF sample, it corresponds to the void space between particles which are only occupied with gas. For an adsorbent with a known mass, $m_s$, $\epsilon$ is,

$$\epsilon = 1 - \frac{1}{V_c}\frac{m_s}{\rho_p} = 1 - \frac{\rho_a}{\rho_p} \tag{4.7}$$

where $\rho_a$ is the apparent density (weighed mass divided by the volume of the cell). In a ideal scenario, a perfect packing ($\epsilon = 0$) corresponds to $\rho_a = \rho_p$.

Finally, the adsorbed quantity per unit mass of MOF, $q(T, P)$, in terms of the system parameters (displayed in Table 4.2) is obtained by combining Equations (4.5) and (4.6),

$$\begin{aligned} q(T,P) &= \frac{1}{(1-\epsilon)\rho_p}\left(\frac{n_c(T,P)}{V_c} - \epsilon\rho_g(T,P)\right) \\ &= \frac{1}{(1-\epsilon)\rho_p}\left(\frac{n_0 - n_{\mathrm{CV}}(T_{\mathrm{CV}},P) - n_{\mathrm{GM}}(T_{\mathrm{GM}},P)}{V_c} - \epsilon\rho_g(T,P)\right) \end{aligned} \tag{4.8}$$

Table 4.2: Volumetric setup system parameters.

| Volume | Value (Figure 4.3) |
|---|---|
| 1st adsorption cell $V_{c1}$ | 7.63 $\mathrm{cm}^3$ |
| 2nd adsorption cell $V_{c2}$ | 5.71 $\mathrm{cm}^3$ |
| Calibrated volume $V_{\mathrm{CV}}$ | 150.26 $\mathrm{cm}^3$ |
| Gas manifold volume $V_{\mathrm{GM}}$ | 12.63 $\mathrm{cm}^3$ (between valves 0 and 3) |
| | + 6.35 $\mathrm{cm}^3$ (between valve 3 and cell) |

Let us note that to increase the adsorption capacity of the cell, it must be charged with the maximum MOF quantity as possible to reduce the void volume. But, if we consider the MOF particles as spheres with identical size, the densest ($\eta = 1-\epsilon$) packing that it can be obtained is only [45],

$$\eta_{\max} = \frac{\pi}{3\sqrt{2}} \approx 74.05\,\% \tag{4.9}$$

However, one way to improve the packing density ($\eta > \eta_{max}$) is to have a binary sphere packing, where the smaller particles can fill the space between the bigger ones, as displayed in Figure 4.5 [46]. Still, this would correspond to an ideal scenario, where the particles would have a perfectly ordered and periodic packing. A realistic filling is more likely to correspond to a random packing of spheres, which according to Torquato et al., gives a packing density of only $\eta \approx 64\,\%$( $\epsilon \approx 36\,\%$) [47]. Therefore, in any case, a simple way to improve the packing is to use a binary packing filling or a filling containing a particle size distribution.

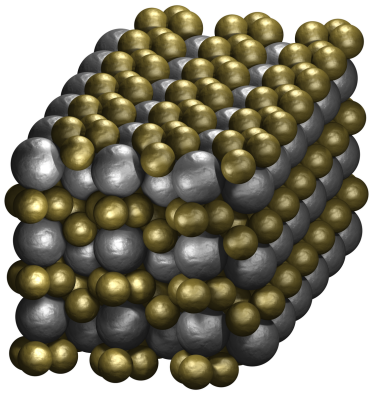

Figure 4.5: Binary sphere packing, this structure achieves a total packing density $\eta$ = 74.79 % ($\epsilon \approx 25\,\%$), reprinted from [48].

## 4.4 Experimental Results and Discussion

Since neon is a noble gas, it is less favorable to be adsorbed. Therefore, it was imperative to find a suitable adsorbing material for the development of the neon sorption compressor and three MOFs were selected and characterized for neon adsorption. In the case of the nitrogen, since adsorbing is less of a concern, it was only been studied with one MOF material: HKUST-1. Table 4.3 highlights the characterized pressure and temperature range of the selected MOFs.

Table 4.3: Summary of the tested MOFs: pressure and temperature range.

| Gas | MOF | Pressure Range | Temperature Range | Figure |
|---|---|---|---|---|
| Neon | HKUST-1 | 0 bar to 70 bar | 77 K to 400 K | Figure 4.6 |
| | UiO-66 | 0 bar to 100 bar | 77 K to 500 K | Figure 4.7 |
| | $Co_3(ndc)_3(dabco)$ | 0 bar to 100 bar | 77 K to 320 K | Figure 4.8 |
| Nitrogen | HKUST-1 | 0 bar to 100 bar | 130 K to 500 K | Figure 4.9 |

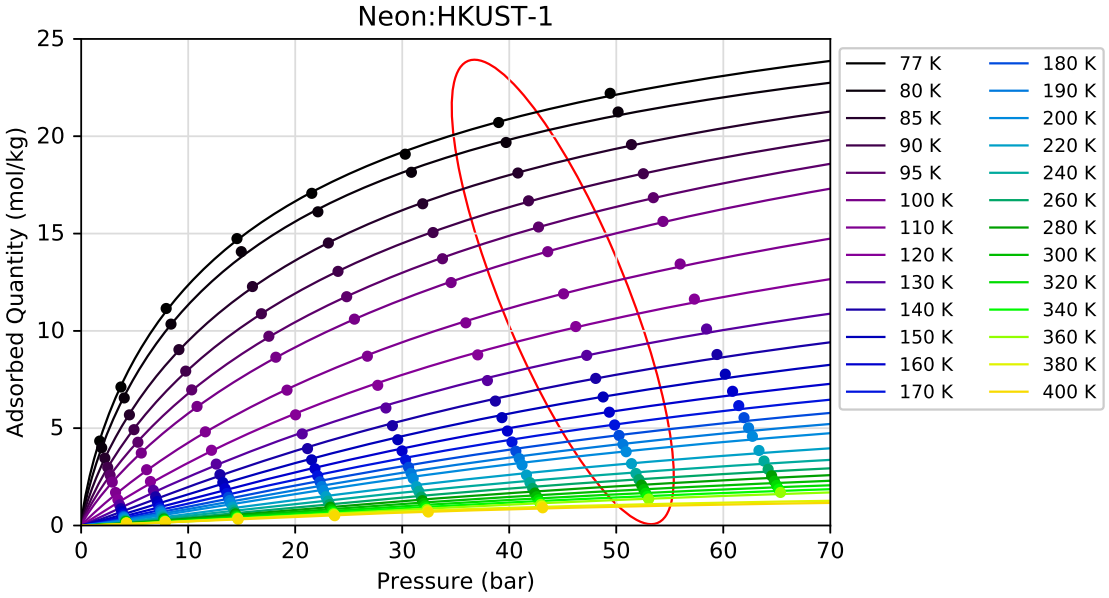


Figure 4.6: Neon adsorption equilibrium isotherms on HKUST-1. The solid lines correspond to the fitted Sips Equation (4.3) for each isotherm and its coefficients can be consulted in Appendix B. The red outline encloses the results obtained during one run at constant quantity. In this case, starting at (38 bar, 77 K) up to (53 bar, 360 K).

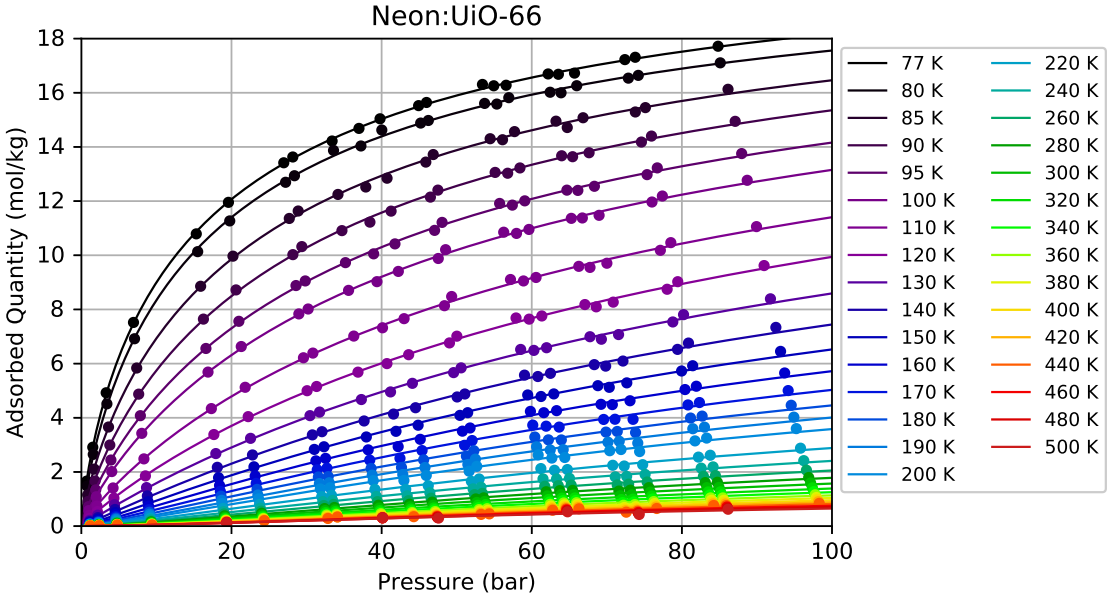


Figure 4.7: Neon adsorption equilibrium isotherms on UiO-66. The solid lines correspond to the fitted Sips Equation (4.3) for each isotherm and its coefficients can be consulted in Appendix B.

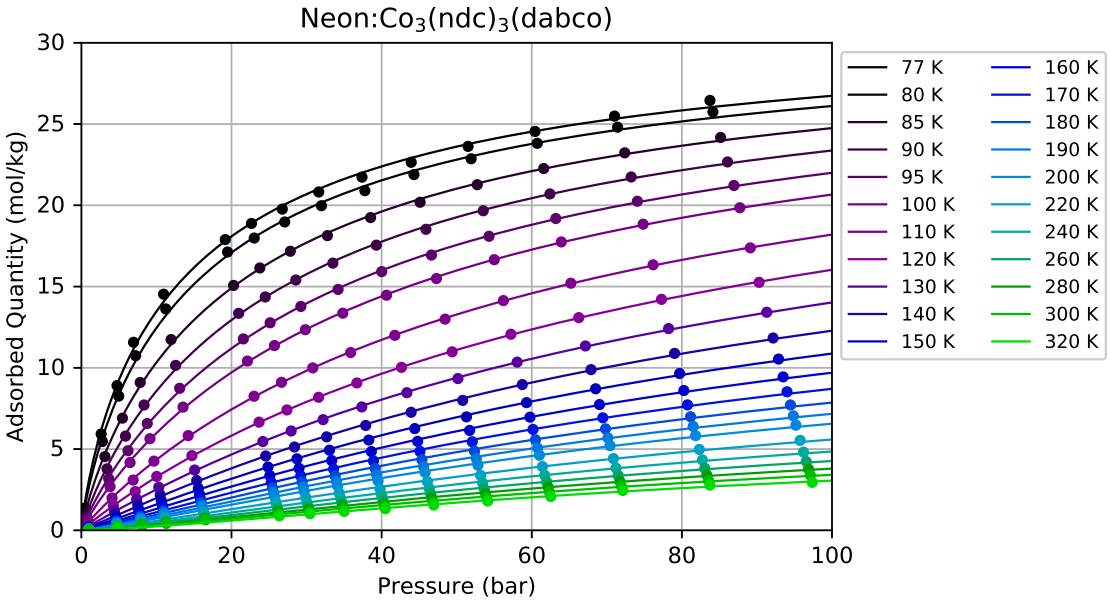


Figure 4.8: Neon adsorption equilibrium isotherms on $Co_3(ndc)_3(dabco)$ . The solid lines correspond to the fitted Sips Equation (4.3) for each isotherm and its coefficients can be consulted in Appendix B.

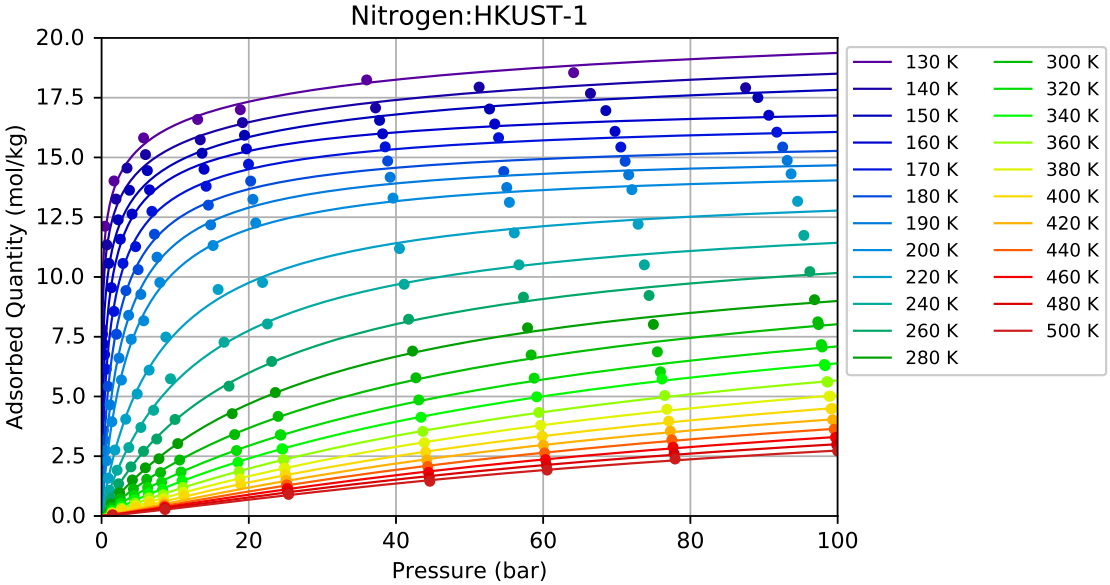


Figure 4.9: Nitrogen adsorption equilibrium isotherms on HKUST-1. The solid lines correspond to the fitted Sips Equation (4.3) for each isotherm and its coefficients can be consulted in Appendix B.

As visible in Figures 4.6 to 4.9, the Sips adsorption model seems adequate to correlate the experimental data for such wide range of pressure. The three variables of Sips equation were numerically obtained by fitting the experimental data with Equation (4.3). Since this procedure shall be performed for each adsorption isotherm and to simplify the parameters estimation, a Python script was developed that uses a non-linear least squares method to fit the experimental data[3]. The obtained Sips parameters of each MOF sample can be consulted in Appendix B.

Actually, for dimensioning the system, the quantity that should be evaluated is the total amount of gas per unit of volume cell, $q_V$. As a matter of fact, this value takes into account the adsorbed gas and the gas occupying the grain interspace (void space). Considering Equation (4.6), $q_V$ is obtained as,

$$q_V(T,P) = \frac{n_c(T,P)}{V_c} \tag{4.10}$$

As explained earlier and as visible in Figure 2.9, an important characteristic of the sorption compressor is how much quantity ($\Delta n$) can be delivered or adsorbed during a compression cycle between a low temperature, $T_L$, at low pressure, $P_L$, and a high temperature, $T_H$, at a high pressure, $P_H$. Then, $\Delta n$ can be calculated through Equation (4.10) as,

$$\Delta n = V_c[q_V(T_L,P_L) - q_V(T_H,P_H)] \qquad T_L < T_H, P_L < P_H \tag{4.11}$$

where $P_L$ corresponds to the vapour pressure of the working fluid, for neon $P_L^{Ne}$ =14 bar at 40 K and, nitrogen $P_L^{N_2}$ =1.38 bar at 80 K.

In Figure 4.10 is depicted on contour plots the released quantity per unit volume ($\Delta q_V = \Delta n / V_c$) for each of the tested pairs of adsorbent/adsorbate. Based on the filling tests, a void fraction, $\epsilon$, of 54% was considered in this analysis and a $P_H$ was set at 100 bar[4]. Unfortunately, as it is clearly visible, the neon-tested MOFs shows that the $\Delta q_V$ values are almost all negative for the characterized range of temperature and pressure. So, in other words, by cycling a neon sorption cell with any of those MOFs between two distinct states, $(P_H, T_H)$ and $(P_L, T_L)$, such cell will further adsorb neon rather than providing a gas flow to the JT stage. The main reason of this result is that $T_L$ is quite hot in respect to the very low adsorption properties of neon. Positive $\Delta q_V$ would substantially require lower $T_L$ as, for instance, the METIS case, where $T_L \leq$77 K.

[3] curve fit from *SciPy* library of Python

[4] This pressure value does not necessarily corresponds to the optimum pressure.

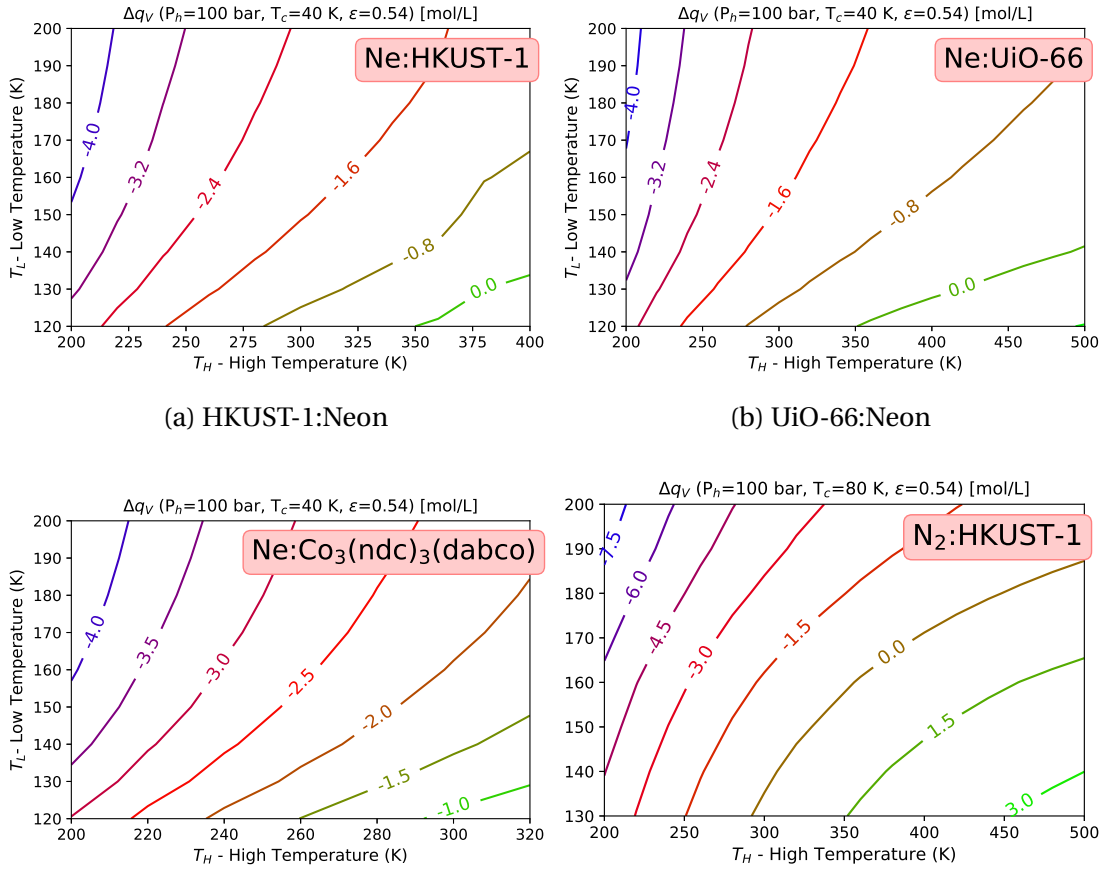


(a) HKUST-1:Neon

(b) UiO-66:Neon

(c) $Co_3(ndc)_3(dabco)$ :Neon

(d) HKUST-1:Nitrogen

Figure 4.10: Contour plots of the released quantity $\Delta q_V$ ($\mathrm{mol\,L^{-1}}$) as a function of the lowest ($T_L$) and the highest ($T_H$) working temperatures of the selected MOFs materials. In this analysis, $P_H = 100\,\mathrm{bar}$ and $\epsilon$ =54%.

The isosteric heat of adsorption, $L$, of both neon and nitrogen for each tested MOF sample can be obtained from the equilibrium isotherms measurements through Equation (4.4). $L$ is also another important input to be accounted during the design of a sorption compressor cell, it is obtained by linear regression of $\ln P$ versus $1/T$ at constant adsorbed quantity, for instance, as shown in Figure 4.11. Using such procedure, the heat of adsorption as a function of the adsorbed quantity, $q(T,P)$, was determined and displayed in Figure 4.12.

By inspection of Figure 4.12a, the results show that $L$ is of the same order of magnitude for all of the studied MOF samples and less than $20\,\mathrm{kJ\,mol^{-1}}$, which, typically, corresponds to a physical adsorption (van der Waals interaction forces). Also, the results show a similar trend: at low loadings, $L$ values are higher, which is an indication that the stronger binding sites (more favorable) are being occupied first; then, it stabilizes in a plateau (quasi-homogeneous adsorption); for higher fillings, it slightly decreases, indicating that the adsorption sites are decreasing. Comparatively, the UiO-66 sample

presents the highest heat of adsorption with the neon.

The heat of adsorption of nitrogen adsorption in HKUST-1 is displayed in Figure 4.12b. As expected, the binding energy of this pair is higher than that of neon/HKUST-1 (almost four times higher), showing that, since neon is a noble gas, its adsorption energy is much less than of the nitrogen.

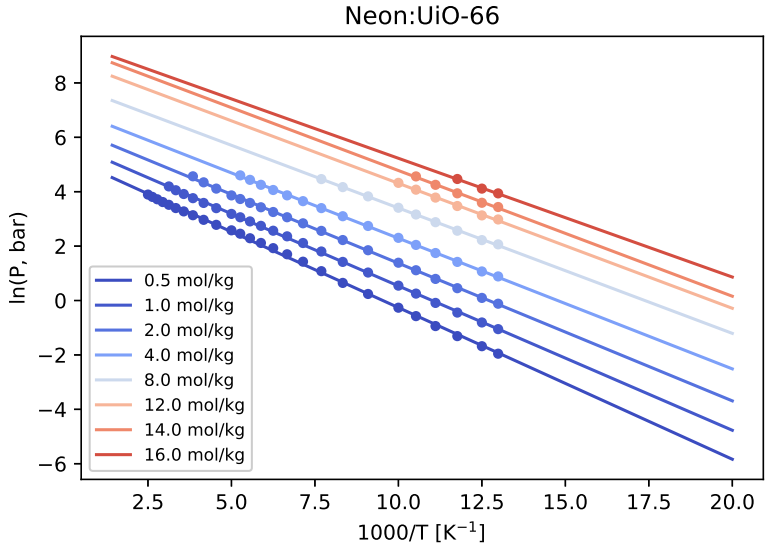


Figure 4.11: The linear regression of $\ln P$ versus $1000/T$, at constant adsorbed quantity, allows to obtain the isosteric heat of adsorption, $L$, through Equation (4.4). This figure shows the fitted isosteres of the neon adsorption on UiO-66.

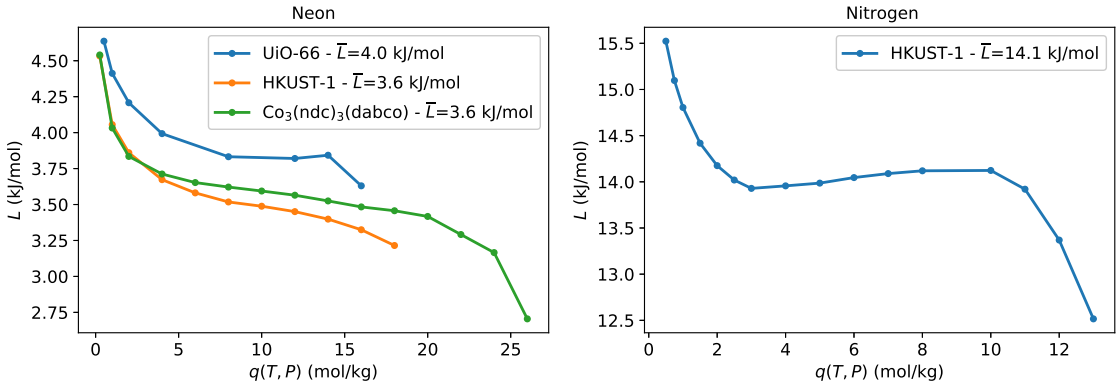


(a) Neon-tested samples

(b) Nitrogen-tested sample

Figure 4.12: Estimated isosteric heat of adsorption, $L$, for each of the characterized MOF samples showed as a function of the adsorbed quantity $q(T,P)$. In the legend, the average values of $L$ can be found.

Due to limited time and available resources, all the development of the VFC related to a configuration using neon as a working fluid has been put on hold until new adsorptive alternatives are found. Subsequent developments of the VFC will only consider,

for now, nitrogen as viable solution for an interface of 1.5 W at 80 K, because the pair nitrogen/HKUST-1 obtained positive $\Delta q_V$ values for $T_H$ higher than 300 K and $T_L$ less than 190 K, as visible in Figure 4.10d.

## 4.5 Optimization Numerical Model

Given the circumstances, it is envisaged a solution of a standalone 80 K JT stage using nitrogen as the working gas. Taking as a starting point the nitrogen stage shown in the initial configuration (Figure 3.8), it is still quite challenging to find a viable configuration within the requirements from ESA (Section 3.1). In such configuration, a large radiator surface is still needed to cycle the four adsorption cells between $T_L$ and $T_H$. For instance, by increasing $T_L$, the rejection capacity of the radiator increases, but as shown in Figure 3.5, the JT stage performance decreases since the high pressure flow exiting the sorption compressor is pre-cooled to the same heat-sink and, consequently, a higher mass flow rate is needed to sustain cooling with 1.5 W at 80 K. Actually, by keeping only one heat-sink, no solution was found without largely exceeding the maximum allowed surface radiator of 1.5 $m^2$ (Table 3.1).

Therefore, a new solution has to be found. An alternative configuration is shown in Figure 4.13: it uses two radiators, one dedicated to cool the nitrogen sorption compressor (main radiator); and another one just to further cool down the high pressure stream before entering the JT stage at a lower temperature than that of the main radiator. Such a configuration, globally improves the performance of the cooler, thereby reducing the required radiator surface.

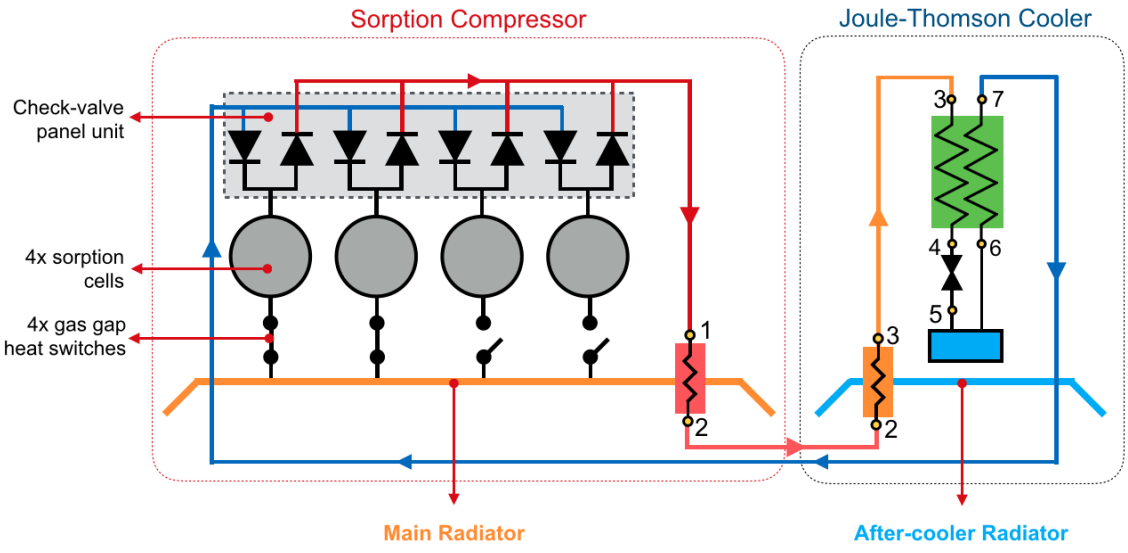


Figure 4.13: Dual radiator configuration of a standalone 80 K single-stage configuration.

The main radiator has the following heat sources:

- Heat input, $\dot{Q}_{\text{input}}$, to heat up the sorption cell, depicted in Figure 2.12;
- Parasitical heat load, $\dot{Q}_{\text{par}}$, coming from the cells at high temperature through the heat-switch OFF state;
- Precooling heat, $\dot{Q}_{\text{ac}}$, to cool down the stream of gas released from the sorption cells ($1 \rightarrow 2$, Figure 4.13);

Recalling the operation of four sorption cells operating in quadrature, shown in Figure 2.11, it is visible that, at any moment, the four distinct phases occurs simultaneously. So, by considering that all heat sources have to be rejected by the main radiator, the heat rejection capacity of the radiator, $\dot{Q}_{\text{R}}$, is determined as follows,

$$\dot{Q}_{\text{R}} = \dot{Q}_{\text{par}} + \dot{Q}_{\text{input}} + \dot{Q}_{\text{ac}} \tag{4.12}$$

Note that the after-cooler radiator (smaller one) only has to precool the gas coming from the main radiator ($2 \rightarrow 3$, Figure 4.13).

Considering Equations (3.1) and (4.12), the required radiator surface can be estimated from a set of input parameters, such as: high/low working pressure, high-/low Sorption Compressor (SC) working temperatures, heat-sink temperatures, cooling power and cold end temperature. Actually, the radiator surface estimation is an optimization problem, as the total radiator surface may be minimized by changing the input parameters.

In the following, the radiator optimization is performed considering the flowchart shown in Figure 4.14. Some parameters are fixed, such as, the cooling power and the cold end temperature of the JT stage, while others can be changed until a solution (minimization) of the problem is found. An Excel user-defined function was developed to automate the minimization problem, this function makes use of the Solver add-in[5] functions and the solution was found by using the following assumptions and constraints:

1. Minimum sorption compressor temperature, $T_{L,SC}$, was set at 150 K in order to avoid a low rejection capacity of the radiator.
2. Maximum sorption compressor temperature, $T_{H,SC}$, was set at 500 K to avoid MOF degradation and for safety reasons.
3. Minimum high pressure set at $1.2 \times \text{P}_{\text{crit}}$ to avoid operating close to the critical point and to prevent liquid-gas mixture in the heat-exchanger.
4. Maximum high pressure set at 100 bar for practical and safety reasons.
5. Cooling power set at 1.5 W plus 10% margin (ESA requirement).
6. Cold end JT temperature set at 80 K (ESA requirement).

[5] Microsoft Excel add-in program

7. CFHX assumed as perfect, negligible pressure-drop due to viscous losses.
8. Sorption cell temperature distribution considered homogeneous.
9. GGHS ON/OFF ratio = $0.8\,\mathrm{WK}^{-1}/12\,\mathrm{mWK}^{-1}$.
10. Sorption cell void fraction, $\epsilon$, set at 54%, similar to the obtained packing during the MOFs characterization.

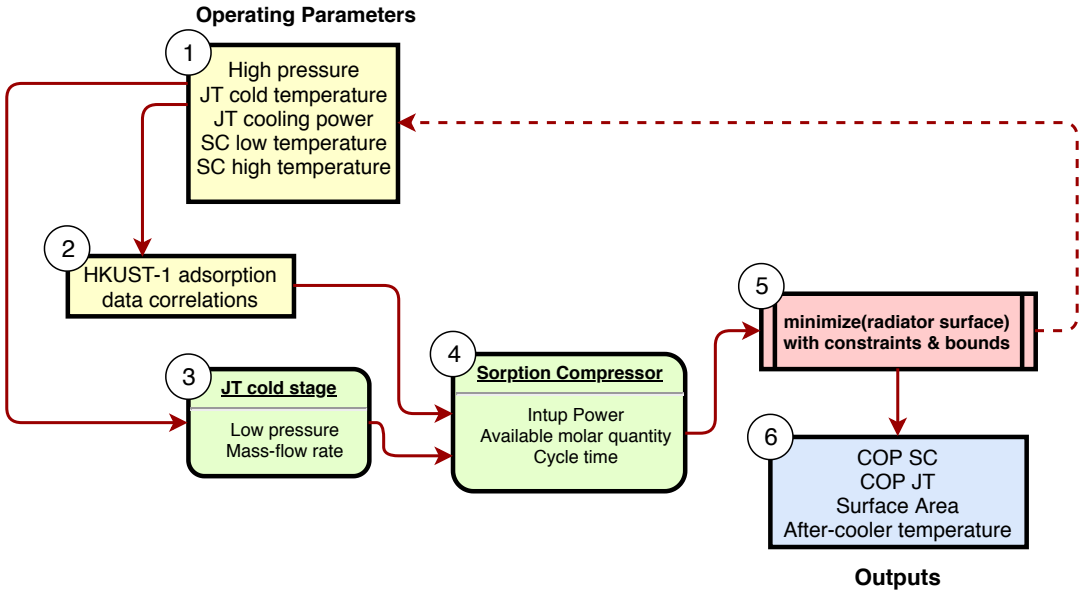


Figure 4.14: Optimization flowchart of the 80 K nitrogen cooler. SC stands for Sorption Compressor.

The found solution corresponds to the optimum operating parameters of the cooler and these parameters are crucial to design a functional sorption compressor, such results are shown in Table 4.4. It is worth mentioning that even in a single-stage configuration using nitrogen, the radiator surface ($1.80\,\mathrm{m}^2$=$1.47\,\mathrm{m}^2$+$0.33\,\mathrm{m}^2$) is still above the requirements, showing that finding a viable solution with these limitations is really quite challenging.

Table 4.4: Optimum nitrogen-stage working parameters.

| **Parameter** | **Value** | **Parameter** | **Value** |
|---|---|---|---|
| SC low temperature | 165 K | High pressure | 40 bar |
| SC high temperature | 360 K | $\Delta n$ | 1.67 mol |
| Mass flow rate | $11\,\mathrm{mg\,s}^{-1}$ | Quality $\chi$ | 22% |
| Main radiator temperature | 158.4 K | Main radiator surface | $1.47\,\mathrm{m}^2$ |
| After-cooler temperature | 116.7 K | After-cooler surface | $0.33\,\mathrm{m}^2$ |
| Sorbent Mass (HKUST-1) | 399 g ($\epsilon = 54\%$) | Total surface area | $1.80\,\mathrm{m}^2$ |
| Cycle Time | 262 min | Heat rejection capacity | 37.6 W |

Figure 4.15 shows the total radiator surface as a function of the high and low temperatures of the nitrogen sorption compressor. As expected, it is visible that the optimum solution corresponds to a minimum (within the studied pressure and temperature range): by increasing the releasing temperature, $T_{H,SC}$, higher heat loads are expected in the radiator (sensible heat and parasitical), thereby increasing its area; reducing the adsorbing temperature $T_{L,SC}$, requires a radiator rejecting at a lower temperature, thereby with reduced rejection capacity, therefore, a higher surface would be needed to sustain operation.

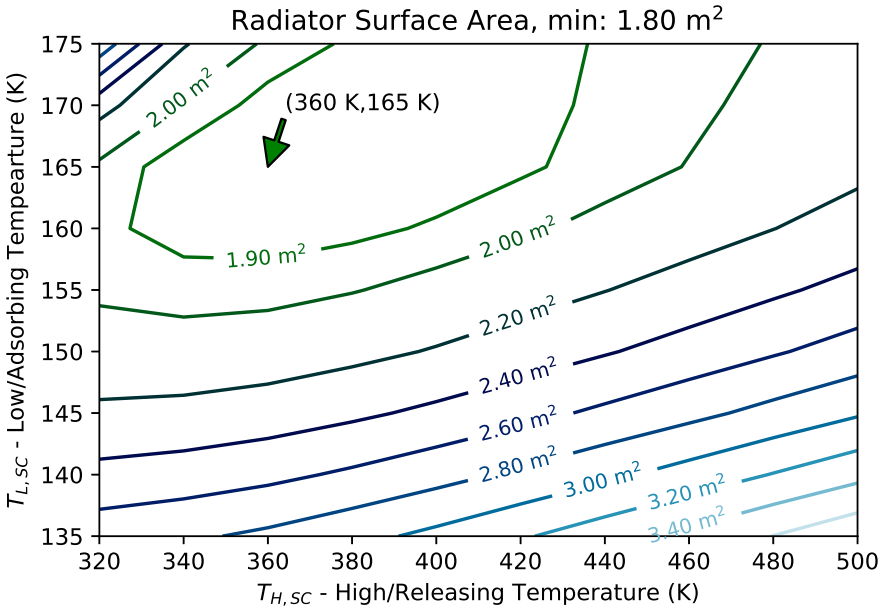


Figure 4.15: Total radiator surface area as function of sorption compressor working temperatures.

Furthermore, for any pair of temperatures, the optimization always led to a minimization of $P_H$ until reaching the third constraint ($1.2 \times P_{crit} \approx 40$ bar). This result is explained by the fact that as the high pressure decreases, the adsorbed gas reduces as well, thus, increasing the available gas quantity for circulation, since adsorption is promoted by pressure. To clarify this argument, in Figure 4.16 are displayed two compression cycles sharing the same temperatures ($T_{L,SC}, T_{H,SC}$), but operating at different high pressure. The net gas quantity gain is clearly visible by just reducing the high working pressure from 60 bar to 40 bar.

Considering the obtained adsorption isotherms of HKUST-1 and the found operating point, the temperature cycle of one sorption cell can be obtained by using a simple thermal model, further details later in Chapter 6, and the corresponding temperature profile is shown in Figure 4.17. As previously mentioned, in order to work

synchronously with the three other cells, each phase must have the same duration, independently of the temperature interval. During the heating phase, about 19.3 W are expected to heat up the cell from 165 K to 270 K over one quarter of the cycle period. While for the releasing phase, 22.3 W are needed, slightly higher during this phase to compensate the cooling effect due to desorption. Note that during the four cells operation, only one cell is at the releasing phase and another one at the heating phase, therefore, about 41.6 W of heat input is constantly needed to operate the nitrogen sorption compressor. Let us also mention that the optimum temperature of the main radiator is found to be approximately 159 K and the lowest temperature of the sorption cell is 165 K. This temperature difference exists since during the adsorption phase the heat generated by adsorption is rejected through the limited thermal conductance of the heat-switch ON state.

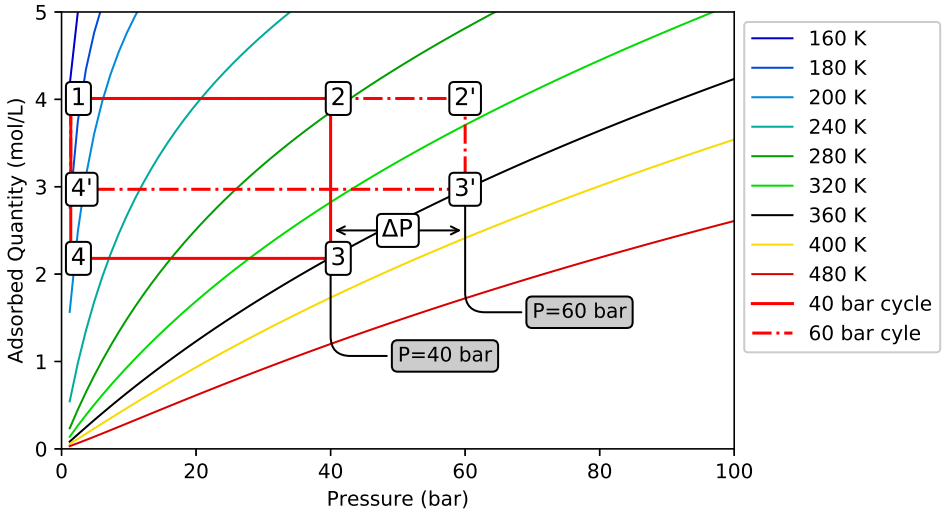


Figure 4.16: Released quantity, $\Delta q_V$, as a function of the high pressure. Observe the gain by just reducing the high working pressure, in the event that the working temperatures remain constant.

Regarding the after-cooler radiator, its temperature also corresponds to the inlet of the Joule-Thomson stage. According to the minimization solution, this temperature is 116 K which is below the critical temperature of nitrogen (≈127 K). Hence, the Joule-Thomson expansion occurs in the compressible liquid region, as visible in Figure 4.18. Notice that, in this region in particular, the isotherms are nearly vertical (state point 4). Therefore, after expanding into the two-phase dome, the vapour quality $\chi$ is more or less pressure independent and as well as the generated heat lift. Furthermore, this vapour fraction being quite low ($\chi < 25\%$) turns this region very attractive as less mass flow rate is needed to sustain cooling and, consequently, less heat load on the radiator which globally improves the performance of the VFC [49].

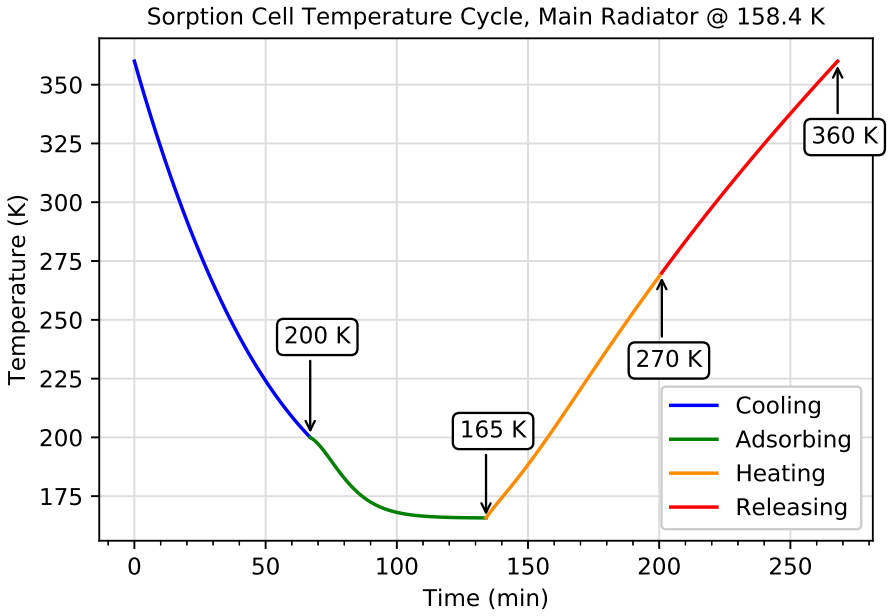


Figure 4.17: Expected sorption cell temperature cycle operating at the found optimum parameters.

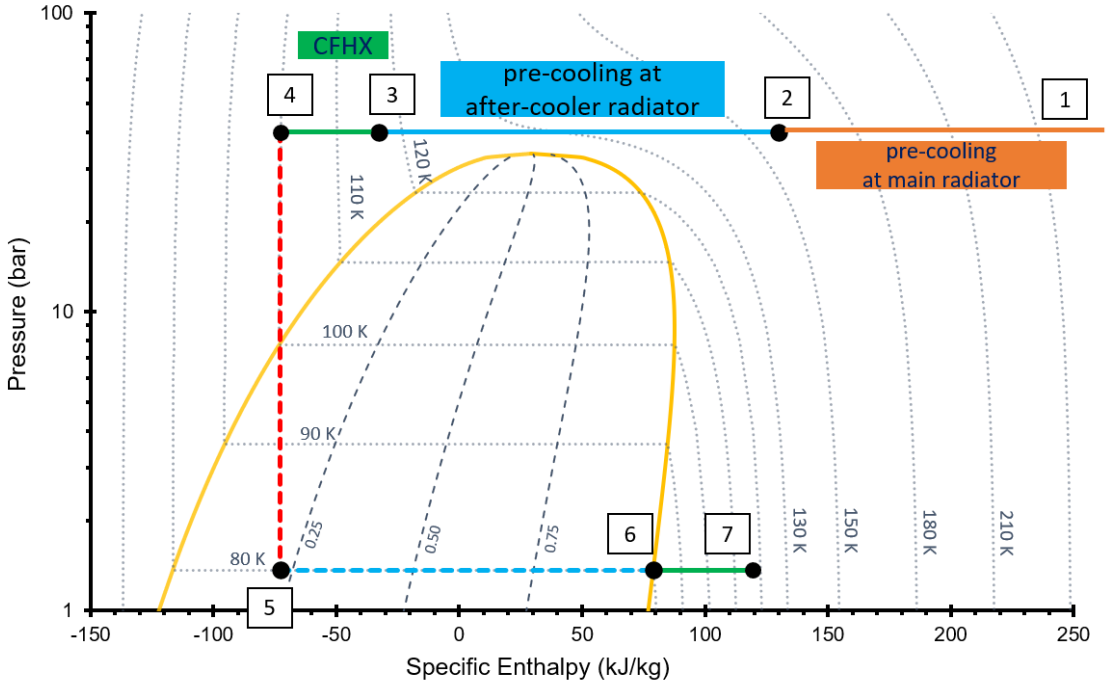


Figure 4.18: Nitrogen pressure-enthalpy diagram of the dual-radiator configuration at the found optimum parameters (Table 4.4). The state points, shown in squares, corresponds to the ones from Figure 4.13.

As previously mentioned, the highly ordered bimodal packing can reach a void-fraction low as $\epsilon \approx 25\%$. However, from our initial fillings it was not better than $\epsilon = 54\%$.

If such filling procedure is improved, there is substantial room to reduce the radiator surface, as visible in Figure 4.19 (while keeping the same operating parameters). For instance, by improving the void factor down to ≈ 42%, the surface area requirement of 1.5 $m^2$ would be met.

Even in a standalone cooler of nitrogen, finding a viable cooling solution showed to be quite challenging. Anyway, as just explained, by reducing the void fraction it provides some margin to further decrease the radiator surface. However, without a doubt, the weakness of this kind of compressors, at the time being, is its enormous dependence on the sorption material, a sorbent material with higher net capacity would allow it to operate within the requirements.

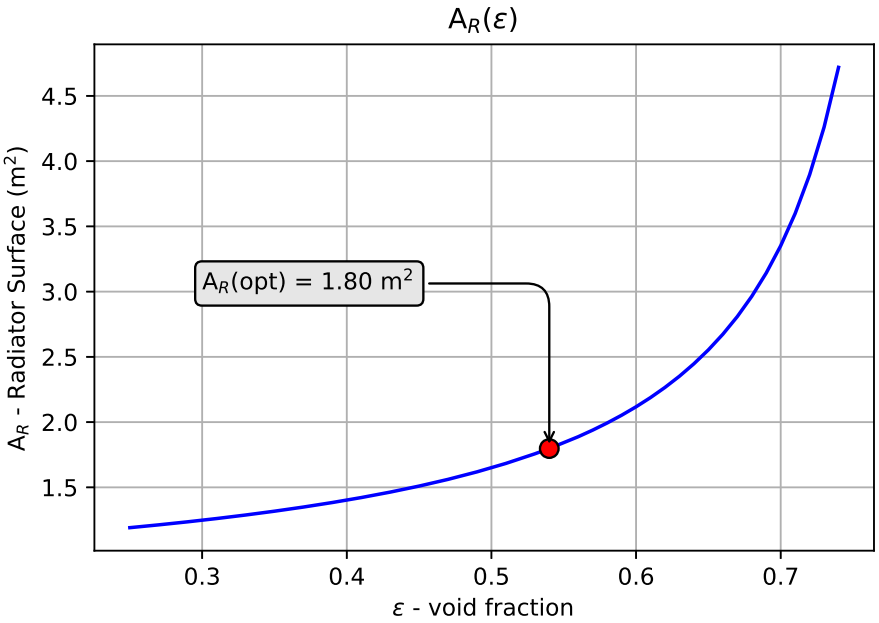


Figure 4.19: Radiator area, $A_R$, as a function of the void fraction, $\epsilon$, using the obtained optimum parameters (Table 4.4). The red-filled circle corresponds to a void-fraction of 54%.

CHAPTER 5

# Joule-Thomson Cold Stage Design and Demonstration

The different components of the 80 K Joule-Thomson stage are described in this chapter. The design, integration and functional characterization of each component is presented in detail.

## 5.1 Joule-Thomson Restriction Design and Demonstration

The JT restriction must provide an impedance to enable an isenthalpic expansion of nitrogen. In the literature, different solutions are found to create this impedance which depends on constraints associated with the construction and conditions of operation. Usually, such solutions are the orifice-plate, porous plug or long thin capillary.

The simplest and most common JT restriction is the orifice plate, it only consists in a small hole in a thin plate that can be placed in a pipe. It is widely used as a flowmeter (using calibrated orifices), as a pressure reducer or for flow restriction. For some applications, this hole can be so small that it ends up being very difficult to manufacture. Additionally, it is very sensitive to clogging by solidified gaseous impurities or solid particles [9]. It is important to note that this kind of restriction does not allow flow adjustment, it is limited to applications where the operating conditions are fixed (e.g. upstream pressure). The design of such restriction needs to take into account that most coolants are compressible when flowing through small apertures. So, when they expand, they may reach the local speed of sound (choked flow) which is a consequence of compressible flow phenomena. This behavior can further complicate the design of this kind of restriction.

Another solution is to use a long capillary with a reduced diameter to obtain a longitudinal pressure gradient over its length. Compared to the orifice plate, a larger diameter capillary is required to obtain the same mass-flow rate, by considering the same pressure-drop, $\Delta P$. The $\Delta P$ along the capillary can be calculated by the empirical Darcy-Weibasch equation [50],

$$\frac{\Delta P}{L} = f_{\mathrm{D}} \cdot \frac{\rho}{2} \cdot \frac{\mathbf{v}^2}{D_h}, \tag{5.1}$$

where $\Delta P/L$ is the pressure-drop per unit length, $\rho$ is the density of the fluid, $D_h$ is the hydraulic diameter, $\mathbf{v}$ is the mean flow velocity and $f_{\mathrm{D}}$ is the Darcy friction factor, a dimensionless quantity that accounts the friction losses in a pipe. For instance, this kind of restrictions were used for the 8 K helium JT stage of the METIS instrument to obtain a mass-flow rate of 106 mg s$^{-1}$ [17].

The porous plug uses sintered metals to produce a tortuous path where the gas is forced to flow through. Comparing to the orifice plate, it can provide larger cross-sectional areas, therefore, less susceptible to clogging. As previously mentioned, this kind of solution was the one adopted on the Planck's sorption cooler operating at 18 K [51]. Burger et al. also developed a porous plug restriction tuned to the desired flow at 4.5 K of a helium sorption cooler [52].

For our application, the pressure drop needed for the nitrogen stage is to high to allow the capillary solution ($\Delta P \approx 40$ bar), as it would be necessary a very long capillary to create such pressure drop with the desired mass-flow rate. Therefore, the orifice-plate was the selected solution: simple and commercially available in various calibrated hole diameters; it can be easily integrated in the system as a VCR® [1] gasket placed inline. To avoid clogging, inline filters have to be integrated in the system.

### 5.1.1 Orifice-Plate Restriction Design

To obtain an orifice plate with the desired discharge, its diameter must be estimated accordingly to some basic considerations and equations. Considering the flow of liquid or gas as incompressible, the mass-flow rate in a thin orifice plate, as schematically depicted in Figure 5.1, can be obtained from the Bernoulli equation,

$$\frac{v^2}{2} + gh + \frac{P}{\rho} = \text{constant} \tag{5.2}$$

where $v$ is the velocity of the flow, $g$ is the acceleration due to gravity, $h$ is the elevation, $P$ is the pressure and $\rho$ is the density of the fluid.

[1] Metal gasket face seal fittings from Swagelok®

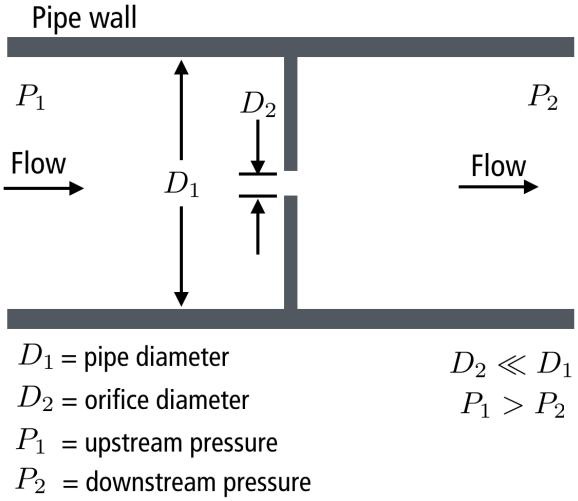


Figure 5.1: Schematic of a thin orifice plate in a pipe of diameter, $D_1$. The fluid will suffer a pressure drop, $\Delta P$, by traversing the small restriction with diameter, $D_2$.

By assuming steady-state, incompressible (constant density) flow in a horizontal pipe (no change in elevation) and negligible frictional losses, Equation (5.2) reduces to,

$$P_1 - P_2 = \frac{1}{2}\rho(v_2^2 - v_1^2) \tag{5.3}$$

where state point 1 refers to the upstream (left side of Figure 5.1) and state 2 to the downstream. Due to conservation of mass, the volumetric flow, $\dot{V}$, is constant, hence,

$$\dot{V} = A_1 v_1 = A_2 v_2 \tag{5.4}$$

where $A_1$ is the cross-sectional area of the pipe and $A_2$ is the cross-sectional area of the orifice. Considering that $A_1 \gg A_2$ and rearranging Equations (5.3) and (5.4) to obtain $\dot{V}$ as a function of the system parameters (pressure, diameter),

$$\begin{aligned} P_1 - P_2 &= \frac{1}{2}\rho\dot{V}^2\left(\frac{1}{A_2^2} - \frac{1}{A_1^2}\right) \\ \dot{V}^2 &= \frac{(P_1 - P_2)}{\frac{1}{A_2^2}\left(1 + \left(\frac{A_2}{A_1}\right)^2\right)} \\ \dot{V} &= A_2\sqrt{\frac{1}{1 - \left(\frac{A_2}{A_1}\right)^2}}\sqrt{\frac{2(P_1 - P_2)}{\rho}} \end{aligned} \tag{5.5}$$

if $(A_2/A_1)^2 = (D_2/D_1)^4 \approx 0$, then, the previous equation reduces to,

$$\dot{V} = A_2\sqrt{\frac{2(P_1 - P_2)}{\rho}} \tag{5.6}$$

Writing this relation in terms of mass flow rate ($\dot{m} = \rho \dot{V}$), one obtains,

$$\dot{m} = A_2 \sqrt{2\rho(P_1 - P_2)} \tag{5.7}$$

This equation shows that the mass-flow rate is only limited by the cross-sectional area of the orifice diameter, $A_2$. That is why the orifice plate is widely found as a mass-flow meter: once the diameter is known, the mass flow rate can be obtained by just measuring the pressure differential $\Delta P = P_1 - P_2$.

In general, Equation (5.7) is mostly applicable to liquids, where the compressibility effects can be neglected. For gases, since they can be easily compressed, particularly when flowing through an orifice plate, the decrease in pressure due to the passage of fluid through the orifice provokes a significant change in its density, so, Equation (5.2) is no longer valid.

In compressible flow regime for fluids flowing through small constrictions, upon certain conditions, the fluid's velocity increases until it reaches the local speed of sound (Mach number = 1) and becomes "choked". Choked flow is a limiting condition where the mass flow rate cannot be increased by decreasing the downstream pressure for fixed upstream conditions. Assuming ideal gas behavior, steady-state and isentropic flow, the flow becomes choked when the downstream pressure is below a critical value, $P^*$. This critical value is obtained from the dimensionless stagnation properties relations at supersonic flow conditions when the Mach number is unity [53],

$$\frac{P^*}{P_0} = \left(\frac{2}{\gamma + 1}\right)^{\frac{\gamma}{\gamma - 1}} \tag{5.8}$$

where $P_0$ corresponds to the stagnation pressure[2]. For instance, for nitrogen, which has a heat capacity ratio $\gamma = 1.4$ and assuming the upstream flow conditions stagnated, $P_0$, the pressure ratio is $P_1/P_2 = 1.89$. So, a factor of almost two is enough to reach choked flow conditions and to accelerate the fluid up to the local speed of sound at the orifice's throat. In such limiting condition, it can be shown that the mass flow rate is given by [54],

$$\dot{m} = A \sqrt{\gamma \rho_1 P_1 \left(\frac{2}{\gamma + 1}\right)^{\frac{\gamma+1}{\gamma-1}}} \tag{5.9}$$

This equation shows that the mass flow rate in an orifice is only dependent on the upstream conditions (state point 1) and of the orifice cross-sectional area, $A$.

Usually, in a JT cooler, the fluid starts from the compressible region (single-phase) and it directly expands into the two-phase region. Solving this problem under choked

[2]Stagnation pressure is the static pressure of a gas at null velocity (e.g gas stored at rest in a high pressure cylinder).

flow conditions and also including phase-change makes this problem complex. Actually, this was a case study of Maytal and Elias where they have presented correction factors applicable to Equation (5.9) [55]. However, such correction factors do not cover an expansion starting from the liquid compressible region, as imposed by the cycle proposed in the previous chapter Figure 4.18.

In conclusion, Equation (5.7) is applicable to incompressible flow regime: flows are treated as incompressible when the Mach number is less than 0.3, this roughly corresponds to a density change of 5% [56]; Equation (5.9) should be used for single-phase compressible choked flow; and, for two-phase choked flow, correction factors should be applied accordingly [55].

Considering the targeted operating point, the upstream conditions of the JT expansion are 100 K and 40 bar (Table 4.4), so, as already mentioned, starting from the liquid compressible region. The fluid then expands into the two-phase dome with an expected vapour quality, $\chi$, of 22%, while the orifice is expected to fix a discharge rate of 10.8 mg s$^{-1}$ to obtain 1.5 W at 80 K. In Figure 5.2, it is represented the mass flow rate as a function of the upstream pressure through Equation (5.7) and for an orifice diameter ranging from 11 µm to 15 µm.

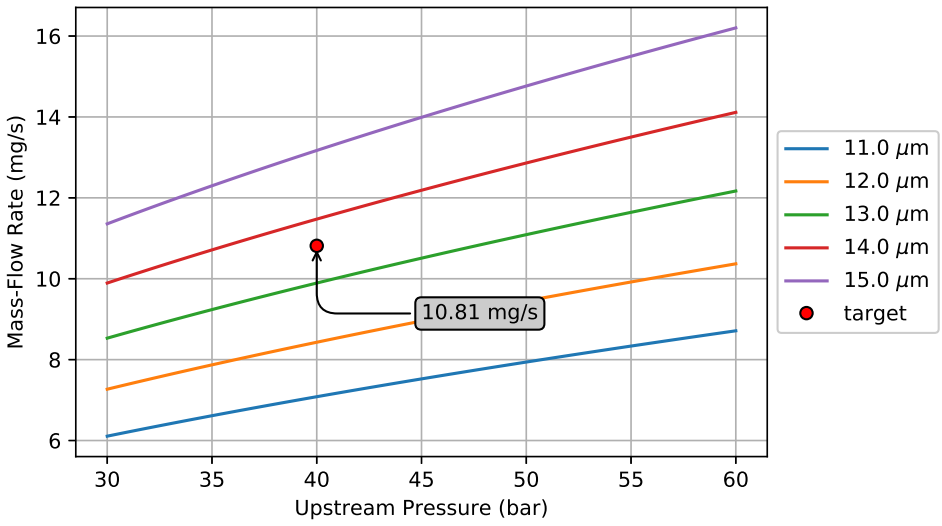


Figure 5.2: Mass-flow rate of orifice-plates ranging from 11 µm to 15 µm at the targeted upstream conditions: $P = 40$ bar, $T = 99.5$ K. The red circle in this plot corresponds to required discharge rate to obtain 1.5 W at 80 K.

Note that by using Equation (5.7) to estimate the required diameter, it implies that the flow regime is being treated as incompressible. Although, by considering the upstream conditions and using real gas density values from [44], the expanded fluid will experience a density change of 13% compared to its upstream state. So, this may actually correspond to a compressible flow regime. Anyway, it is not clear if this flow

achieves choked conditions and, as already mentioned, the studies found in the literature do not cover expansions starting from the liquid compressible region. So, to simplify the diameter estimation, Equation (5.7) was used and is actually not very far from reality, according to the experimental results shown in Section 5.1.3. In an attempt to mitigate this uncertainty, different orifice sizes, ranging 11 µm to 14 µm, were ordered and characterized.

### 5.1.2 Experimental Set-up

A screening from a batch of laser-drilled 1/8 inch gasket orifices was performed to find the one with the adequate discharge, i.e. closer to our goals. A simple set-up, displayed in Figure 5.3, was used to quickly obtain the discharge profile of each orifice.

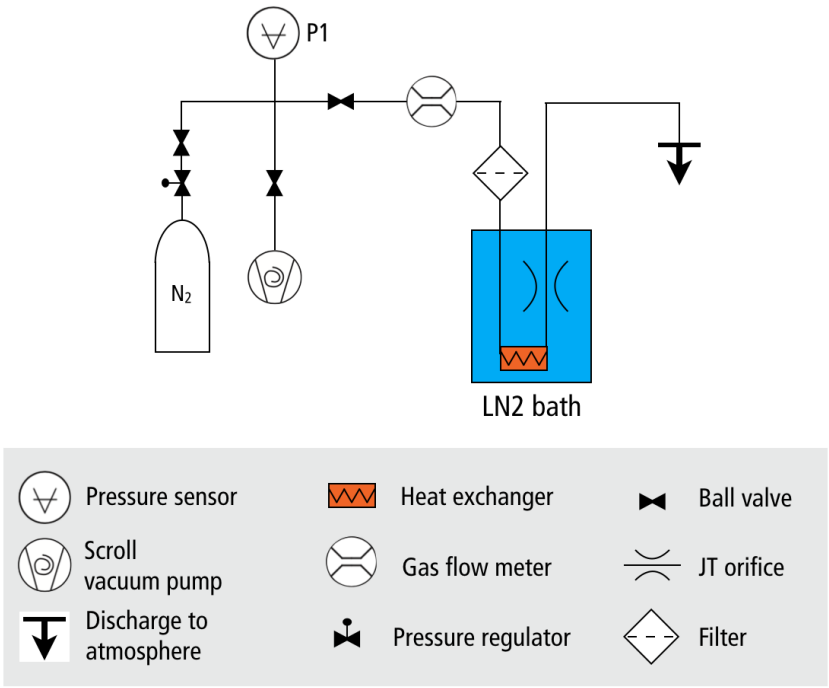


Figure 5.3: Orifice-plate mass flow rate experimental set-up.

In this set-up, initially at room temperature, the pressure is fixed between 10 bar to 100 bar and the mass flow rate through the orifice is recorded, then, the obtained values are compared with the the results coming from Equation (5.9), i.e. assuming compressible single-phase choked flow. After these measurements, the same orifice is submerged in a liquid nitrogen bath and its mass flow rate is recorded again and compared with Equation (5.7), assuming incompressible flow regime. The equipment used for this Joule-Thomson orifice measurement is presented in Table 5.1.

Table 5.1: Equipment for the JT orifice characterization.

| Equipment | Details |
|---|---|
| $N_2$ gas cylinder | Compressed nitrogen gas cylinder |
| Gas mass flow meter | Bronkhorst EL-FLOW digital thermal mass flow meter |
| Vacuum pump | Edwards: nXDS6i dry scroll pump (6.3 $m^3$/h) |
| Pressure transmitter | Keller-Druck Series 33X (0.01% FS, 100 bar max. pressure) |
| Particle filter | Swagelok 1/4 inch VCR High Purity Filter |
| Liquid Nitrogen Dewar | Air Liquide: TR11 Dewar |

### 5.1.3 Experimental Results and Discussion

A set of stainless-steel VCR® gasket orifices with diameters of 11, 12 and 14 µm was ordered from LENOX Lasers (USA). A close-up image of the 12 µm orifice, obtained with SEM, is displayed in Figure 5.4, where is visible the drilled orifice and as well as few drops of molten material from the laser-drilling procedure.

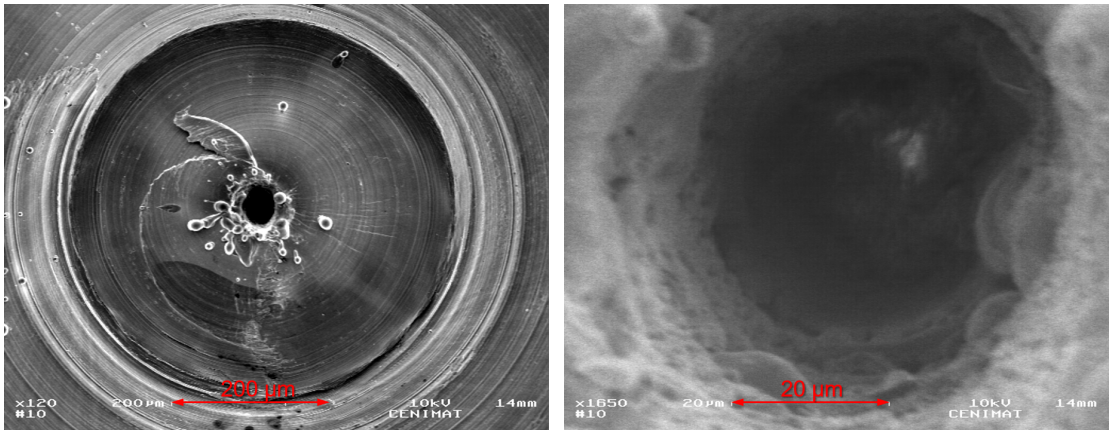


Figure 5.4: SEM image of a 12 µm laser-drilled VCR® gasket by LENOX Lasers, the image on the right side corresponds to the view along the hole.

As previously explained, a discharge characteristic was performed at room temperature, which allowed us to roughly estimate the orifice diameter and to detect possible clogging, the results are shown in Figure 5.5. According to the supplier, the orifices have a diameter uncertainty, in this sizing range, of ±10%. Apart from the 12 µm orifice, our experimental diameter determination fall within the range of the nominal uncertainty.

Figure 5.6 shows the obtained discharge rate for the same orifices submerged in a liquid nitrogen bath, so, with an upstream temperature of 77.3 K. Note that to evaluate the mass-flow rate at the targeted operating conditions (upstream $T$ = 99.5 K), the

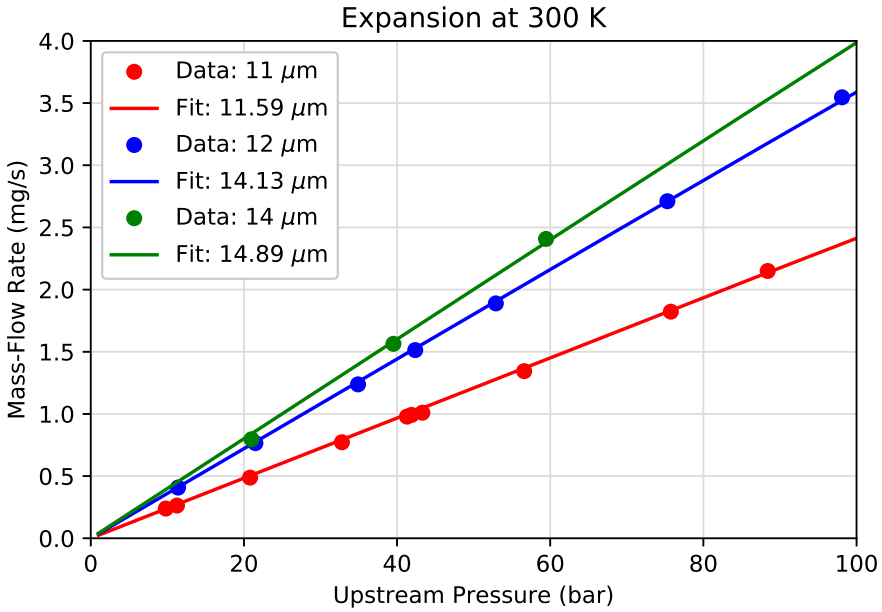


Figure 5.5: Characteristic orifice discharge of nitrogen at room temperature. The solid lines correspond to the values coming from Equation (5.9) by fitting with the experimental data (symbols).

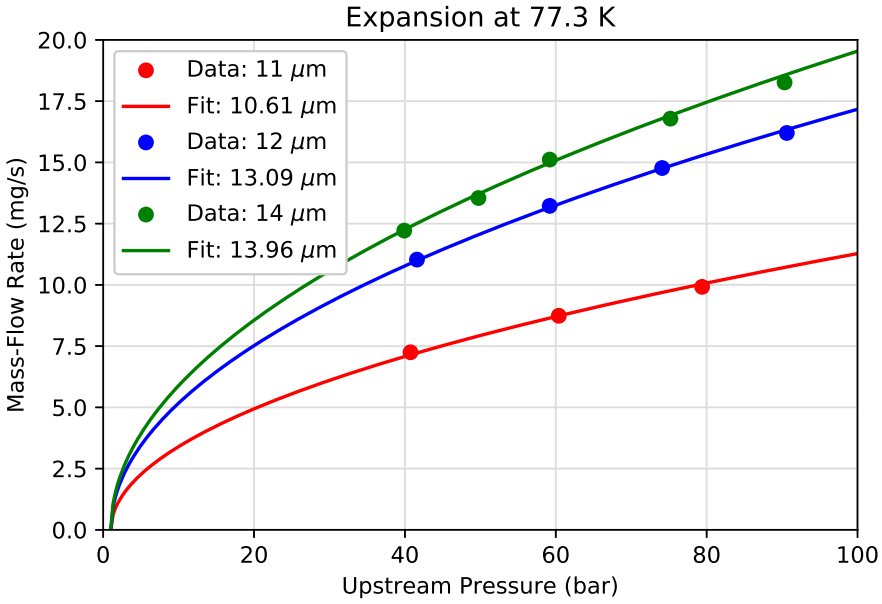


Figure 5.6: Characteristic orifice discharge of nitrogen at 77.3 K. The solid lines correspond to the values coming from Equation (5.7) by fitting with the experimental data (symbols).

results must be corrected accordingly as follows,

$$\dot{m}(P_H, T) = \dot{m}(P_H, T_{\mathrm{LN2}}) \underbrace{\sqrt{\frac{\rho(P_H, T)}{\rho(P_H, T_{\mathrm{LN2}})}}}_{\Gamma} \tag{5.10}$$

where $\Gamma$ is the correction factor, in this case $\Gamma = 0.93$. Through Equation (5.10), the expected mass-flow rate at the operating conditions is obtained and displayed in Table 5.2. The 14 µm orifice seems the most appropriate to be used as flow restriction for the 80 K JT stage and both 11 µm and 12 µm orifices were excluded for being far from the targeted value (10.81 $\mathrm{mg\,s^{-1}}$). Actually, later in section 5.4, it will be shown that the JT cold stage operated with this orifice very close of the optimum operating point.

Table 5.2: Expected mass-flow rate of the orifices after applying the correction factor of $\Gamma = 0.93$ and their relative deviation from the targeted mass flow rate of 10.81 $\mathrm{mg\,s^{-1}}$.

| Orifice | Mass-flow rate | Deviation |
|---|---|---|
| 11 µm | 6.57 $\mathrm{mg\,s^{-1}}$ | -39% |
| 12 µm | 10.01 $\mathrm{mg\,s^{-1}}$ | -8% |
| 14 µm | 11.39 $\mathrm{mg\,s^{-1}}$ | +5% |

## 5.2 Counter-Flow Heat Exchanger Design

Heat exchangers are categorized according to its flow arrangement and type of construction. The simplest and most common one consists in two concentric tubes ("tube-in-tube"), where the fluids move in the same or opposite direction and exchanges heat through the solid wall separating the tubes. Many other configurations exist: cross-flow heat exchanger, where the fluids move perpendicular to each other; compact heat exchanger, very dense arrays of finned tubes or plates to achieve very large heat transfer surface area per unit volume; shell-and-tube heat exchanger, consisting in its simplest form in a single tube and shell passes, suitable for high-pressure application and large flow processes (e.g oil refineries) [57].

For the VFC design, the "tube-in-tube" heat exchanger, with the fluids flowing in opposite directions, was the selected geometry, which is also the most used configuration in cryogenics due to its simplicity and compactness. As shown in Figure 5.7, the CFHX has two concentric tubes, creating two channels. Usually, for mechanically reasons, the inner tube (smaller diameter) contains the high-pressure flow and the outer, the low-pressure flow. The CFHXs can be shaped into helical coils to be compact and at both ends these tubes are joined with a splitter to separate the streams, as also visible in Figure 5.7.

Figure 5.7: Rendered view of the 2 m tube-in-tube configuration heat exchanger designed for the JT stage at 80 K.

### 5.2.1 CFHX Modelling

The overall heat transfer coefficient, $U$, is a measure of the overall ability of series of conductive and convective elements to transfer heat. It is commonly used to calculate the heat transfer in heat exchangers. In the case of a CFHX, $U$ can be used to determine the thermal conductance between both flow streams. Considering an energy balance in a differential segment of length d$x$ of a counter-flow heat exchanger, schematically represented in Figure 5.8, the rate of heat transfer d$\dot{Q}$ in this segment is,

$$\mathrm{d}\dot{Q} = U \Delta T \, \mathrm{d}A \tag{5.11}$$

where d$A$ is the exchange surface of the segment and $\Delta T$ is the temperature difference between both fluid streams. The coefficient $U$ is inversely proportional to the total thermal resistance $R_{\mathrm{tot}}$ between fluids, it accounts for the solid (wall) and convective conduction.

$$U = \frac{1}{R_{\mathrm{tot}}} = \frac{1}{R_{\mathrm{conv,h}} + R_{\mathrm{p}} + R_{\mathrm{conv,c}}} \tag{5.12}$$

where $R_{\mathrm{conv,h}}$ is the thermal resistance due to convective heat transfer from the hot fluid to the wall, $R_p$ is the thermal resistance of the conduction through the wall and $R_{\mathrm{conv,c}}$ is the thermal resistance due to convective heat transfer from the wall to the cold fluid stream.

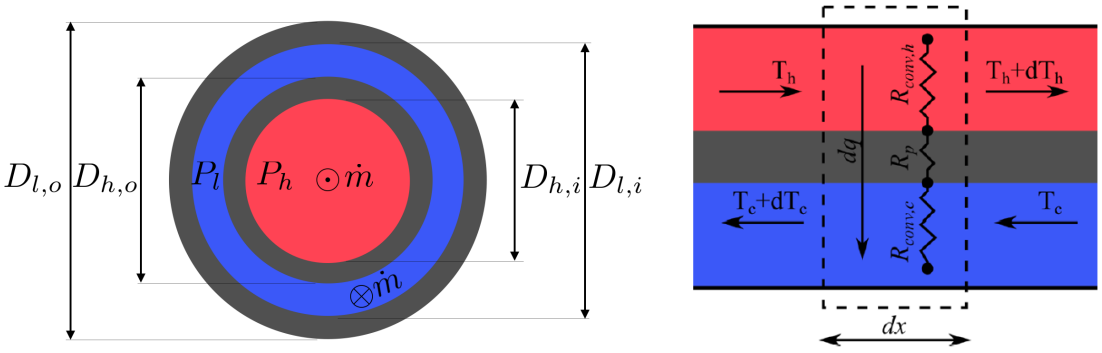


(a) Cross-sectional view of a CFHX.

(b) Energy balance in a differential element of a CFHX

Figure 5.8: Red, blue and grey colours represent the hot fluid (at high pressure), cold fluid (at low pressure) and the solid material between fluids, respectively. The dashed rectangle shows a differential segment.

Considering a cylindrical configuration, as schematically shown in Figure 5.8a, Equation (5.12) becomes,

$$\frac{1}{U} = \frac{1}{h_h} + \frac{D_{h,i}}{2k_p}\log\left(\frac{D_{h,o}}{D_{h,i}}\right) + \frac{D_{h,i}}{D_{h,o}}\frac{1}{h_l} \tag{5.13}$$

where the subscripts $h$ corresponds to the high-pressure side (hot), $l$ to the low-pressure side (cold), $o$ to outlet and $i$ to inlet, in respect to the flow direction, and $k_p$ is the thermal conductivity of the solid wall. The thermal resistance related to the convective heat transfer is inversely proportional to the convective heat transfer coefficient, $h = 1/R_{\text{conv}}$, and this coefficient, $h$, depends on the fluid properties, flow geometry and flow rate. It is convenient to describe this dependence using common dimensionless relationships from fluid dynamics, as the Reynolds number,

$$\text{Re} = \frac{\rho \mathbf{v} D_H}{\mu} = \frac{\mathbf{v} D_H}{\nu} \tag{5.14}$$

the Prandltl number,

$$\text{Pr} = \frac{c_p \mu}{k} \tag{5.15}$$

and lastly, the Nusselt number,

$$\text{Nu} = \frac{h D_H}{k_f} \tag{5.16}$$

where $D_H$ is the hydraulic diameter of the pipe, $\mathbf{v}$ is the mean velocity of the fluid, $\rho$ is the density of the fluid, $\mu$ is the dynamic viscosity of the fluid, $\nu$ is the kinematic viscosity ($\nu = \mu/\rho$), $c_p$ is the specific heat and $k$ is the thermal conductivity.

Those dimensionless relationships depend on the system geometry and whether if the flow regime is laminar or turbulent, and are typically obtained through empirical

equations. For instance, in a turbulent flow inside a smooth pipe with circular cross-section of diameter $D$, the empirical Dittus-Boelter equation should be used [57],

$$\mathrm{Nu} = 0.023\,\mathrm{Re}^{4/5}\,\mathrm{Pr}^{n} \tag{5.17}$$

where $n = 0.4$ for a fluid being heated up and $n = 0.3$ for cooling. For fully developed internal laminar flow, the Nusselt number is constant-valued. In the case of uniform surface heat flux for pipes, Nu is [57],

$$\mathrm{Nu} = \frac{48}{11} \simeq 4.36 \tag{5.18}$$

and in the case of constant surface temperature, Nu is [57],

$$\mathrm{Nu} = 3.66 \tag{5.19}$$

To predict the performance of a CFHX, the Logarithmic Mean Temperature Difference (LMTD) method determines the heat transfer between both ends if the inlet and outlet temperatures are known and considering the following assumptions [57]:

1. HX is insulated from its surroundings.
2. Axial conduction along the tube is negligible.
3. Fluid properties are constant (specific heat, density).
4. Overall heat transfer coefficient $U$ is constant.

Another method is also available: effectiveness-NTU method, for cases where only the inlet temperatures are known. However, none of methods referred above are completely adequate for this CFHX dimensioning, since the fluid properties (specific heat, thermal conductivity, viscosity) are expected to vary in the heat-exchanger due to temperature variations along it.

So, one solution is to solve the problem iteratively: an 1-dimensional static model was developed in MATLAB to estimate the fluid dynamics and the heat transfer in the CFHX. In such model, axial conduction and heat losses (like radiative heat transfer to surroundings) were not considered. Moreover, pressure drop in both sides were considered using Darcy-Weibasch Equation (5.1), since to obtain very effective CFHXs it usually requires long length tubes, hence, the pressure drop should be evaluated. To numerically solve the CFHX, it is convenient to define the effectiveness $\epsilon_{hx}$ of the CFHX, as the ratio of the actual heat transfer $\dot{Q}_{\mathrm{hx}}$ to the maximum possible heat transfer rate $\dot{Q}_{\mathrm{max}}$ in a heat exchanger,

$$\epsilon_{hx} = \frac{\dot{Q}_{\mathrm{hx}}}{\dot{Q}_{\mathrm{max}}} \tag{5.20}$$

By definition, $\epsilon_{hx}$ is dimensionless and must be in the range $0 \leq \epsilon_{hx} \leq 1$. The maximum possible heat transfer rate $\dot{Q}_{\mathrm{max}}$ in a CFHX is determined by an energy balance of an ideal heat exchanger (429.04 mW), Equation (2.8).

To obtain the required length $L_{\text{hx}}$ of the CFHX, the following boundary conditions defined by the inlet temperatures and pressures of both sides (Table 4.4) were considered in the developed MATLAB script,

$$T_{h,i}(x=0) = 116.30\,\text{K} \qquad T_{l,i}(x=L) = 80\,\text{K} \tag{5.21}$$

$$P_{h,i}(x=0) = 40\,\text{bar} \qquad P_{l,i}(x=L) = 1.37\,\text{bar} \tag{5.22}$$

and $L_{\text{hx}}$ was numerically obtained while aiming for a heat-exchanger very close to an ideal one, thus, by setting the following criteria $\epsilon_{hx} \geq 99.99\%$.

Using the tubing dimensions of Table 5.3, the numerical results showed that the nitrogen CFHX would need a minimum length of $L_{\text{hx}} = 1.15\,\text{m}$ and the variation of $T$ along the CFHX length is shown in Figure 5.9. In such configuration, the pressure drop in both sides is rather reduced, about $2.8 \times 10^{-2}$ mbar for the high-pressure side and $5.8 \times 10^{-1}$ mbar for the low-pressure side.

The implemented CFHX on the nitrogen stage uses the dimensions shown in Table 5.3 and a length $L_{\text{hx}} = 2\,\text{m}$. According to the numerical solution, this length is almost twice from what is needed. However, it was chosen to save a heat-exchanger already built for the neon stage. In addition, as the estimated pressure drop values are reduced, no major performance degradation is expected by using this long CFHX.

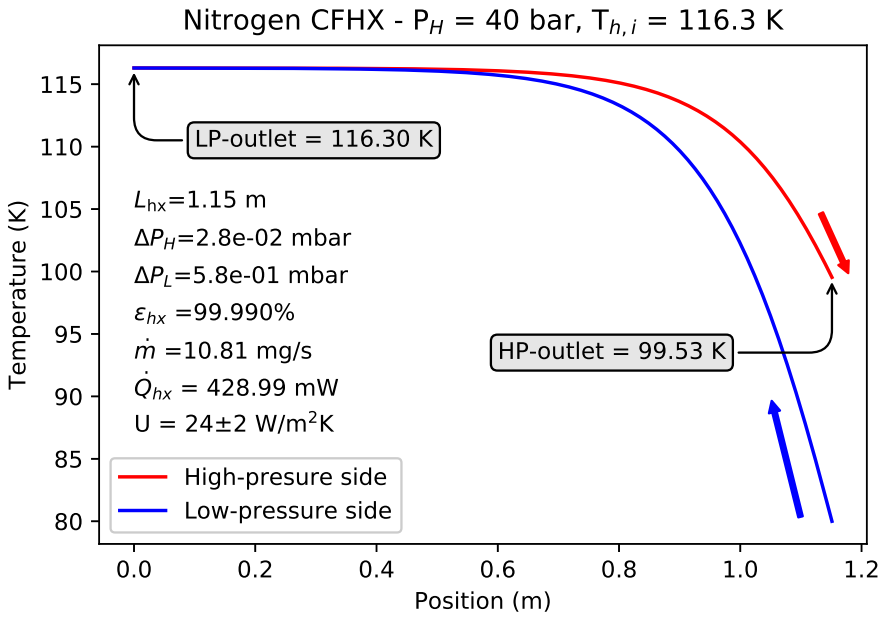


Figure 5.9: Numerical results of the nitrogen CFHX at the expected operating conditions. The arrows indicate the flow direction.

Table 5.3: CFHX dimensions and geometrical parameters.

| Parameter | Value | Description |
|---|---|---|
| $D_{h,i}$ | 2.0 mm | high-pressure internal diameter |
| $D_{h,o}$ | 2.5 mm | high-pressure external diameter |
| $D_{l,i}$ | 5.4 mm | low-pressure internal diameter |
| $D_{l,o}$ | 6.0 mm | low-pressure external diameter |
| $L_{\text{hx}}$ | 2 m | minimum heat-exchanger length: 1.15 m |
| Material | CuNi | copper-nickel alloy |

## 5.3 Evaporator Design

The evaporator (or liquid reservoir) is the cold finger of our 80 K nitrogen cryocooler, so, it is the interface for the load (e.g. IR sensor) that needs cooling. It also acts as a thermal energy storage unit, since it retains a certain quantity of liquid and, therefore, is able to provide cooling over a short period.

The VFC is expected to operate under microgravity environment, so, the liquid nitrogen must be correctly confined within the evaporator, otherwise, some liquid might exit and decrease the evaporator's energy storage. In our evaporator, the liquid confinement is achieved by filling the evaporator with a porous medium to retain the liquid by capillary forces enhanced by the small pores of the medium. By using Jurin's law [58] and modelling the porous medium, in a first approximation, as a series of capillary tubes, it is possible to calculate the required pore diameter, $\phi$, to retain the liquid in the evaporator's height, $h$, against the earth's gravity,

$$h = \frac{4\sigma\cos\theta}{\phi(\rho_L - \rho_V)g} \tag{5.23}$$

where $\rho_L$ represents the liquid density and $\rho_V$ the vapour density, $\sigma$ is the surface tension and $\theta$ is the contact angle between the liquid and the tube walls. $\theta$, quantifies the wettability of the solid/liquid interface. Fortunately, cryogenic fluids present good wettability, which means that a contact angle close to $\theta \approx 0$ is a good approximation and it may be used to estimate the capillary height [59]. Figure 5.10 shows the capillary height, $h$, of the liquid nitrogen as a function of temperature, estimated with surface tension values from [60–63].

From these calculations, to obtain a compact evaporator ($L \approx 20$ mm, Figure 5.11) able to confine the liquid, whatever the orientation, the porous material should have a porous mean size lower than $\phi \leq 250\,\mu$m to retain the liquid in its whole volume. Remind that these calculations give the needed pore size in an anti-gravity configuration, which is the worst case scenario. In micro-g conditions, the forces acting against capillary action will be considerably smaller [64].

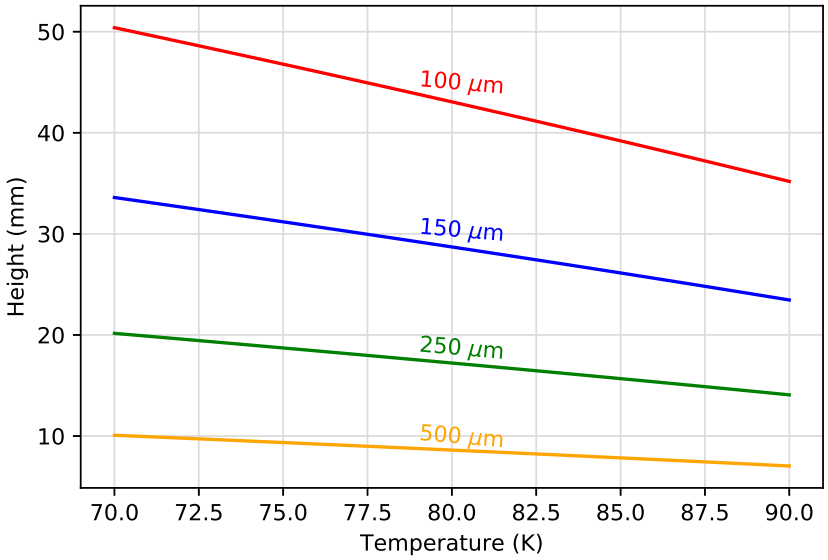


Figure 5.10: Wicking or capillary height, $h$, of nitrogen for different medium pore sizes, $\phi$, as a function of temperature.

The designed configuration consists in a cylindrical evaporator with a inner diameter of 10 mm and a height of 22 mm, which gives an internal volume of 1.73 $cm^3$. In Figure 5.11, is displayed such evaporator placed downstream of the JT orifice and filled with a copper foam from Versarien (UK) with a pore diameter below 500 µm. Also, by using a porous medium made of copper, we can take the advantage of its good thermal conduction and, thus, ensure a good thermal homogeneity within the evaporator. The evaporator was filled with four 5 mm thick sintered copper foam disks, in which a 2 mm hole was drilled along their thickness to allow the gas to easily flow when it is evaporated, this hole prevents the liquid from being pushed out of the evaporator. In the evaporator's body, a cap and two VCR® fitting connections were silver-brazed in a environment-controlled oven, as displayed in the right side of Figure 5.11. The selected copper foam has a measured porosity of $47 \pm 1\%$, which corresponds to a porous volume of 0.75 $cm^3$ that enables to store around 116 J (593 mg of LN2), by considering this volume completely full of liquid nitrogen at 80 K.

As also visible in Figure 5.11, a commercially available 1/8 inch VCR® sintered porous filter from Entegris (USA) was placed in-line and upstream of the orifice to prevent clogging. This filter has a retention capacity of at least 90% for particles larger than 1 µm, which is expected to be sufficient to prevent clogging by solid particles.

To check the correct liquid confinement in ground, where gravity exists, the evaporator was tested in any orientation with respect to earth's gravity without significant performance degradation, similarly to [20, 65–68]. The results of this test are shown in Section 5.4.2.2.

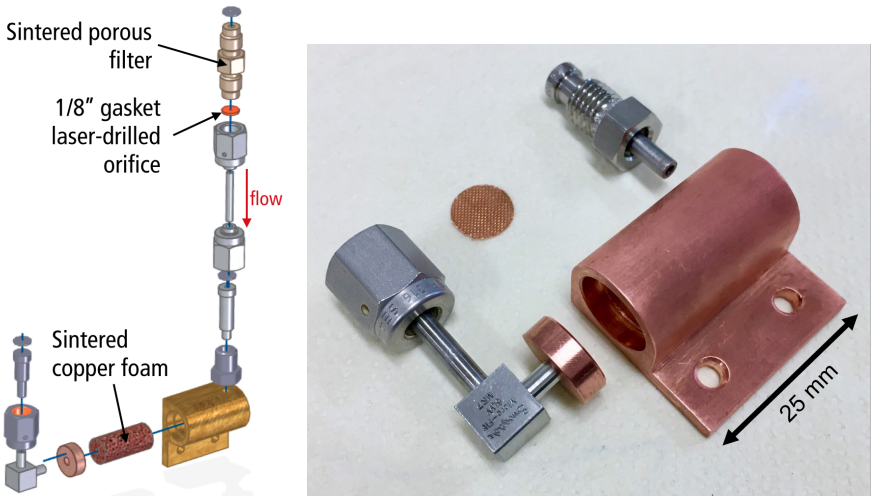


Figure 5.11: Left side: Nitrogen evaporator rendered model; Right side: Evaporator as built (prior to its brazing).

## 5.4 Joule-Thomson Cold Stage Demonstration

Now that every JT stage component is built, the complete stage can be tested at conditions close to the optimum operating point. During operation, the CFHX performance is evaluated by measuring its outlet temperatures and compared with the numerical results from Figure 5.9. Regarding the orifice restriction, if its characteristic discharge is close to expected (10.8 mg s$^{-1}$) and if the CFHX is effective, the cooling power of the JT cycle will be close to the target value of 1.5 W + 10% and, thus one may conclude that everything is working as desired. Lastly, the evaporator will require a dedicated testing after acceptance of both CFHX and JT restriction, since the evaporator performance shall be evaluated for any orientation with respect to earth's gravity to check the correct confinement of the liquid nitrogen through capillary forces.

### 5.4.1 Experimental Set-up

The test set-up is schematically represented in Figure 5.12. The parts under testing are assembled on a Gifford-MacMahon (GM) cryocooler (2 W at 20 K). Note that the demonstration of the JT cold stage is performed in open loop, i.e., the low-pressure gas is being exhausted into atmosphere. This forces the low pressure line at atmospheric pressure, which is slightly lower than the design pressure (1.37 bar for 80 K), but it does not alter the conclusions that can be drawn from this characterization, since this change has negligible consequences.

The second-stage (cold finger) of the GM cryocooler is used to precool the high pressure stream supplying the JT stage at a temperature around 116.7 K (Table 4.4). The pre-cooler (*preHX-1*) is a 10 cm long SS capillary (2 mm internal diameter) wounded

and brazed to a copper rod (15 mm diameter) which is thermalized on the cold finger of the GM, as visible in Figure 5.13.

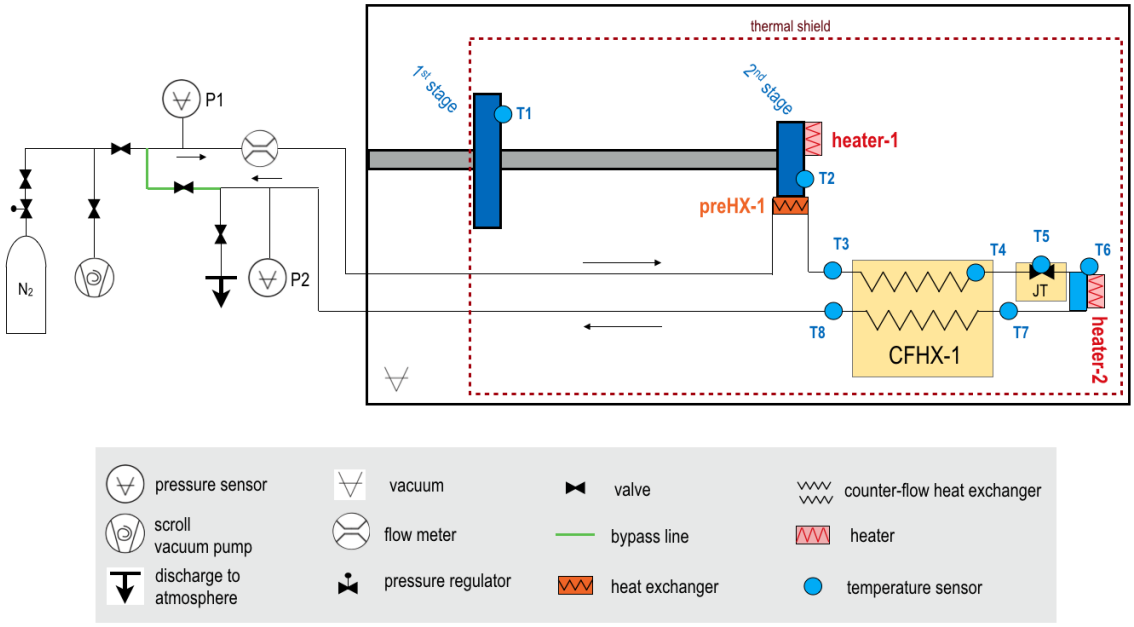


Figure 5.12: Test set-up of the many components of the JT 80 K circuit.

In this set-up, the temperature sensors are placed at different positions to obtain a good thermal characterization of the whole system, as visible in Figure 5.13: *T2* is a calibrated Cernox® temperature sensor mounted on the cold finger of the GM cryocooler; the remaining sensors are platinum resistors (Pt100) and each temperature reading is measured by a commercial cryogenic temperature controller.

The gas manifold has a high and a low pressure zone, each one equipped with an adequate pressure transducer. The high-pressure zone receives the high pressure flow provided from a high purity nitrogen gas cylinder and, afterwards, the gas flows through a thermal gas flowmeter to measure the mass-flow rate of the circuit. Then, this high pressure stream goes through the vacuum jacket of the GM cooler. In the vacuum chamber, the high pressure stream, after precooling in *preHX-1*, goes through the CFHX until it finally expands through the orifice and produces some liquid nitrogen at the evaporator. The heat lift produced by this JT expansion is meticulously measured by adjusting the heat load dissipated on a resistor (1.2 kΩ) attached to the evaporator in such way that the flow entering the low-pressure side of CFHX is, as far as possible, 100% saturated vapour. The supplied heat load would directly correspond to the effective cooling power of the JT stage, albeit it also includes some parasitical heat leaks. After vaporizing the liquid nitrogen, the gas flows back through the CFHX and cools the HP stream. At the LP exit, the fluid goes to the LP zone of the manifold and is discharged into the atmosphere.

In order to test the evaporator in any orientation with respect to earth's gravity, the GM cryocooler is placed in a rotating platform that allows to rotate the complete system from 0° to 360° [68]. The various equipments needed for this demonstration are shown in Table 5.4.

Table 5.4: Equipment used for the JT cold stage characterization.

| Equipment | Details |
|---|---|
| $N_2$ gas cylinder | Compressed nitrogen gas cylinder |
| Gas mass flow meter | Bronkhorst EL-FLOW digital thermal mass flow meter |
| Manifold vacuum pump | Edwards: nXDS6i dry scroll pump (6.3 $m^3$/h) |
| High pressure transmitter | Keller-Druck Series 33X (0.01% FS, 100 bar max. pressure) |
| Low pressure transmitter | Keller-Druck Series 33X (0.01% FS, 10 bar max. pressure) |
| Particle filter | Swagelok 1/4 inch VCR High Purity Filter |
| GM vacuum pump | Edwards: nXDS6i dry scroll pump (6.3 $m^3$/h) |
| GM cryocooler | CTI model 22, 2 W@20 K |
| Temperature Controller | Cryocon: model 34 |
| Power Supply | Agilent triple power supply |
| Acquisition system | Computer running LabVIEW with RS232, GPIB and USB interfaces |

During an experiment, some devices are in continuous communication with a home-made LabVIEW interface that receives, processes, stores and visualizes the data in real-time. This LabVIEW interface also allows to control some system parameters, such as the GM cold finger temperature or the evaporator applied load.

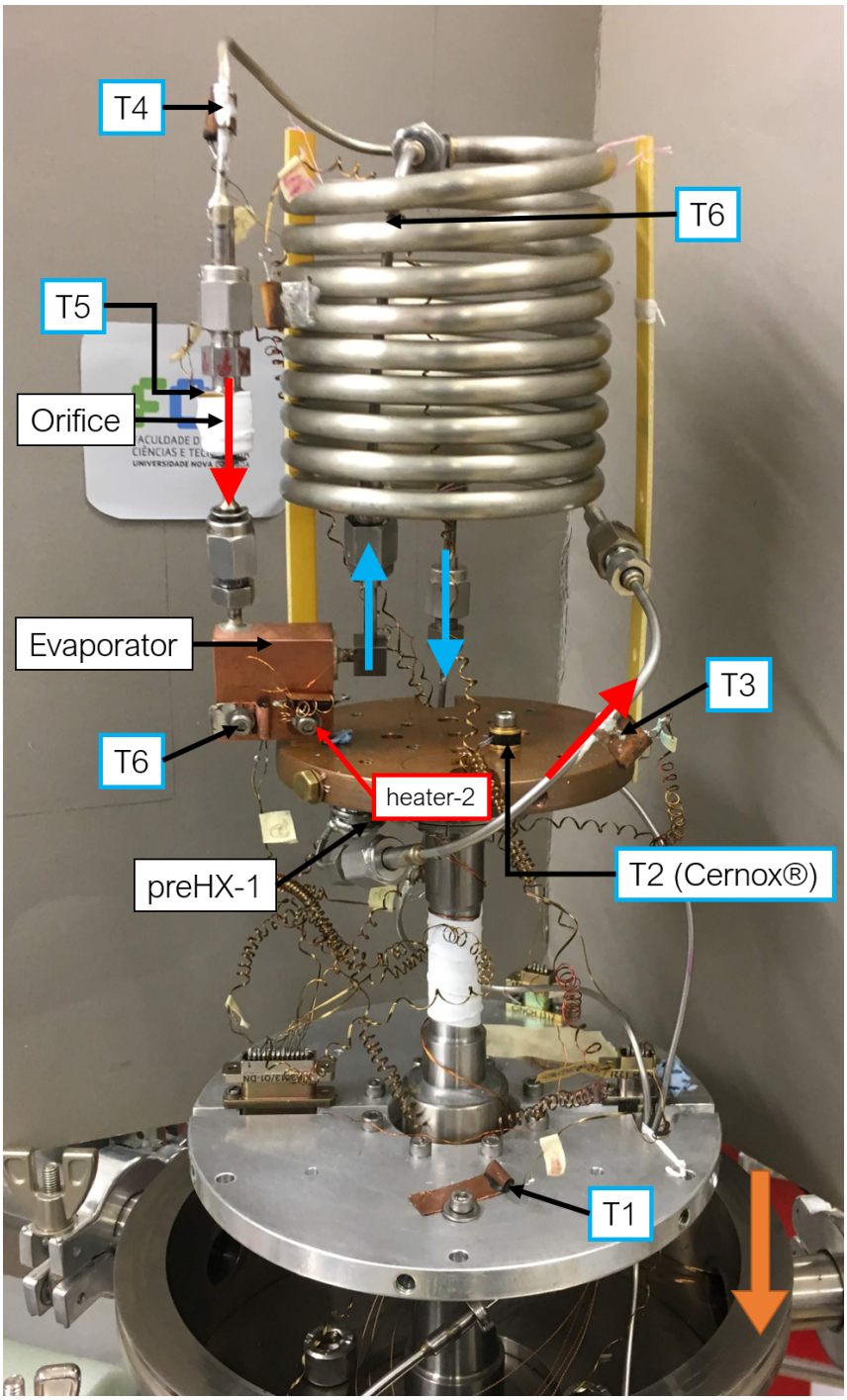


Figure 5.13: Assembly of the JT cold stage in the cryocooler. The red and blue arrows indicate the high and low pressure stream direction, respectively. The orange vertical arrow indicates the gravity direction: in this configuration the liquid formed in the JT orifice naturally falls by gravity to the evaporator. To test the performance of the copper foam, the whole cryocooler is turned by 180°, so, the evaporator becomes in a higher position in respect to the orifice.

#### 5.4.1.1 Test Procedure

- Test #1: *CFHX + JT restriction characterization*

  1. The system is initially assembled without the evaporator, this one being replaced by a capillary tube between the JT orifice and the low-pressure inlet of the CFHX. In this configuration, a small electrical resistor is glued to this capillary to provide the heat load needed for the cooling power determination.
  2. The system is pumped ($<1 \times 10^{-4}$ mbar) and cooled-down by setting the cold finger temperature at 116.7 K to precool the high pressure stream. At the same time, from our experience, a reduced pressure flow of nitrogen goes through the JT circuit to speed-up the cooling and to minimize clogging probability.
  3. When the inlet temperature (*T3*, Figure 5.12) of the CFHX is close to the cold finger set-point ($\approx$117 K), the high-pressure is set at its operating value ($P_h$ = 40 bar). From this point on, all the temperatures of the CFHX+JT decrease. This phase can last up to 2 h.
  4. When the high-pressure inlet of the CFHX is stable in its desired temperature, the cold end temperature (*T6*, Figure 5.12) should reach its minimum temperature (in this case, $T_c$ = 77.3 K). The end of this phase is characterized by a rapid cooling of the thermometer *T6* corresponding to liquid formation.
  5. Immediately after reaching $T_c$, an electrical current is set on the small resistor attached to the capillary to measure the cooling power. This current is adjusted in order to provide a stable temperature at the JT orifice output over few hours. Doing so, it is expected that the LN2 quantity is constant during this period and the heat load corresponds to the cooling power. More details regarding this step will be given in Section 5.4.2.

- Test #2: *Evaporator characterization for both normal and anti-gravity orientation*

  1. The evaporator is now included to the JT stage and the same procedure is performed as steps 2. and 3. from Phase 1. As in the precedent characterization, the liquid naturally falls to the evaporator (Figure 5.13).
  2. To test the evaporator performance, it is measured its emptying time after letting the evaporator to be completely full with liquid nitrogen. The complete filling is characterized by a sudden decrease of *T7*, indicating that the liquid is flowing out from the evaporator to the low-pressure inlet of the CFHX, further details in Section 5.4.2.2.

3. It is applied a small heat load to the evaporator (<35% of the cooling power) and recorded the needed time to completely empty the evaporator. A sudden increase of the evaporator's temperature is an indication that the evaporator is empty.

4. The previous step shall be repeated for other heat loads (between 0 mW to 525 mW).

5. The cryocooler's platform is rotated by 180° to repeat steps 3 and 4 and test the evaporator in the anti-gravity orientation.

### 5.4.2 Experimental Results and Discussion

#### 5.4.2.1 Test# 1: CFHX + JT orifice

The inlet conditions of the HP inlet of the CFHX were set at 119.91 K and 40.1 bar. After precooling the high pressure stream, an electrical current was set through the heater resistor attached to the thin capillary (replacing the evaporator) in a attempt to find an equilibrium state: the electrical current, dissipated by Joule effect, corresponds to the rate that is being produced liquid nitrogen. Actually, such task appeared to be a little tricky, since the JT cycle includes a recuperative path (CFHX). So, for any temperature change on one side of the CFHX, it instantaneously affects the opposite stream, thereby, changing the inlet conditions of the JT orifice: upstream temperature, mass flow rate.

Figure 5.14 shows a test run over 22 h of the pair CFHX+JT. By inspection of the upper chart of this figure is visible that the evaporator temperature (yellow) is stable over the whole experience, so, it was always receiving liquid nitrogen from the JT expansion and is not drying out, albeit according to this test results, the evaporator has a tendency to be full of liquid and, unfortunately, some liquid flows out of the evaporator to the low-pressure inlet of the CFHX (blue) which instantaneously provokes some instabilities in the CFHX, as clearly visible in the figure. And, as also visible in the bottom chart of Figure 5.14, this undesirable behavior turns out quite difficult to tune the heat load leading to an equilibrium. Note that as the HP outlet (green) fluctuates, the inlet conditions of the JT expansion changes and, so, the liquid rate formation.

If the CFHX is working as expected, the low-pressure outlet temperature should be very close to the high-pressure inlet temperature, since the low-pressure side heat capacity is inferior to that of the high-pressure side. The obtained average values, displayed in Table 5.5, from this experiment leads to a heat-exchanger effectiveness of $\epsilon_{HX} = 95.8\%$, however, this result is not very representative, since there is a lot of dispersion over the acquired data. Furthermore, note that the hot-side temperatures of

the CFHX are very similar, only 0.3% relative difference between them, this result is an indication that the CFHX is probably very effective.

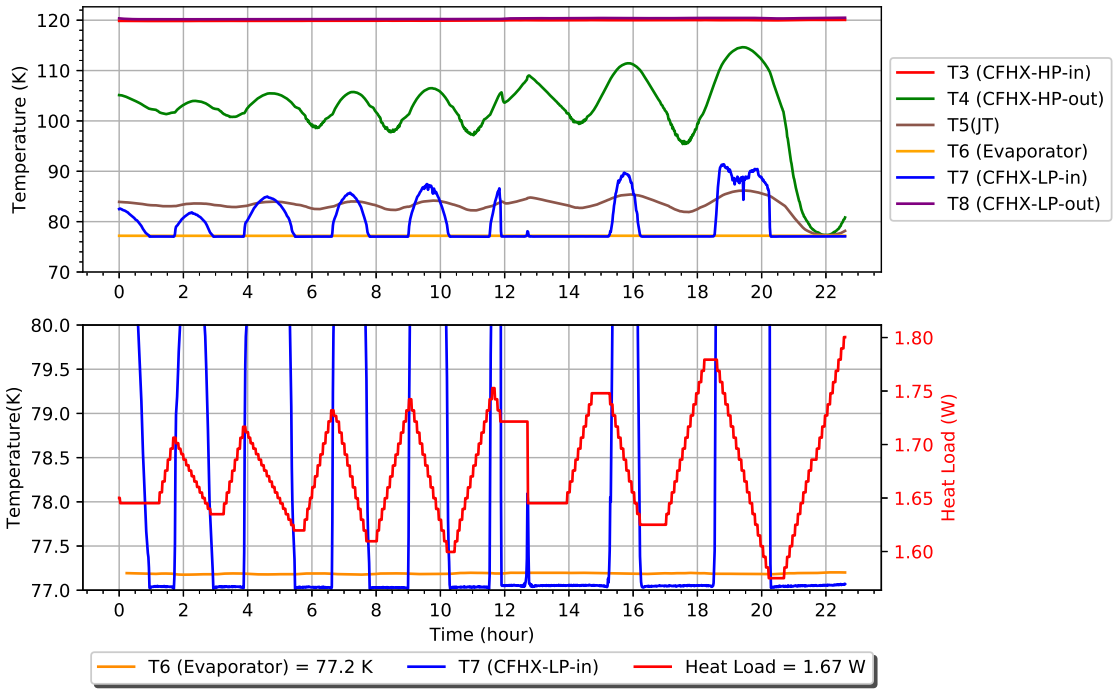


Figure 5.14: Example of a test run of the JT stage over 22 h. Upper figure: temperature variation on several parts of the JT stage. Lower figure: applied heat load (right axis scale) to measure the cooling power of the JT stage.

Despite some temperature instabilities, it was successfully obtained over 22 h a sustained liquefaction with an average cooling power of $1.67 \pm 0.05$ W, within the targeted value (cooling power requirement: 1.5 W+ 10% margin). However, by considering the applied inlet conditions of the JT stage and assuming an ideal CFHX, it was actually expected a higher cooling power of 1.74 W, but as already mentioned, the applied heat load may not correspond to the effective cooling power of this JT cycle, as part of it may be lost by heat leakage (e.g wiring, radiative heat transfer).

Another run was performed by setting the inlet conditions closer to the optimum operating values (Table 4.4): HP inlet temperature reduced from 120 K to 116 K. The JT circuit ran over 7 h in these new conditions and generated an average cooling power of $1.78 \pm 0.01$ W, as displayed in Figure 5.15. In these conditions, the hot-side temperatures of the CFHX were again very similar, only 0.4% relative difference between the high-pressure inlet and the low-pressure outlet. Furthermore, the average high-pressure outlet temperature, $T_4$, that sets the inlet conditions of the JT expansion, is $97 \pm 2$K. Considering the inlet conditions of the CFHX, the upstream temperature of the orifice was expected to be $97.8 \pm 0.1$K, therefore, our measurements are within the expected and, again, this JT cold stage seems to be working very close to the expected.

Table 5.5: Obtained average values from the JT stage characterization shown in Figure 5.14. Let us note that according to the supplier the Pt100 resistors have a tolerance of ±0.55 K at 73 K [69].

| **Parameters** | | **Mean Values** | **Expected** |
|---|---|---|---|
| High-pressure inlet | $T_3$ | $119.94 \pm 0.07$ K | - |
| High-pressure outlet | $T_4$ | $102 \pm 8$ K | $101.4 \pm 0.2$K |
| Evaporator | $T_6$ | $77.188 \pm 0.007$ K | - |
| Low-pressure inlet | $T_7$ | $80 \pm 5$ K | - |
| Low-pressure outlet | $T_8$ | $120.3 \pm 0.2$ K | $119.94 \pm 0.07$ K |
| Mass-flow rate | $\dot{m}$ | $12.00 \pm 0.08$ mg s$^{-1}$ | - |
| Cooling Power | $\dot{Q}$ | $1.67 \pm 0.05$ W | $1.74 \pm 0.02$ W |
| High-pressure | $P_H$ | $40.2 \pm 0.2$ bar | - |
| Low-pressure | $P_L$ | $1087 \pm 1$ mbar | - |

In order to measure the sensitivity of the cooling power, $\dot{Q}_c$, to the inlet conditions ($T_3$ and $P_H$), they were slightly changed around their optimum inlet values. The main results are:

$$\left.\frac{\partial \dot{Q}_c}{\partial T_3}\right|_{P_H} = -31\,\mathrm{mW\,K^{-1}} \qquad \left.\frac{\partial \dot{Q}_c}{\partial P_H}\right|_{T_3} = 23\,\mathrm{mW\,bar^{-1}} \tag{5.24}$$

Let us note that these results account for changes in the mass flow rate due to fluctuations in both pressure and temperature. The negative sign of $\partial \dot{Q}_c/\partial T_3$ is expected, because for each increase in the inlet temperature, the cooling power should decrease, since the vapour quality $\chi$ of the mixture after expansion increases, as can be inferred from the $P-h$ plane displayed in Figure 4.18. Furthermore, let us remind that the JT expansion occurs in a region where the isenthalps lines are nearly vertical in a P-h plane, therefore, the JT expansion is practically insensitive to changes on pressure. So, the positive value of $\partial \dot{Q}_c/\partial P_H$ is more likely to be caused by the variation of the mass-flow rate, which is fixed by the upstream conditions of the orifice. Dividing each term by the nominal cooling power (1.5 W), one can obtain its relative deviation: per unit temperature, a decrease of -2.1%; per unit pressure, an increase of 1.5%. These quantities are rather small compared to the 10% margin of the cooling power (Table 3.2). From this point of view, the JT cold stage operating in this uncommon region is expected to be very stable and weakly sensitive to fluctuations of the inlet conditions.

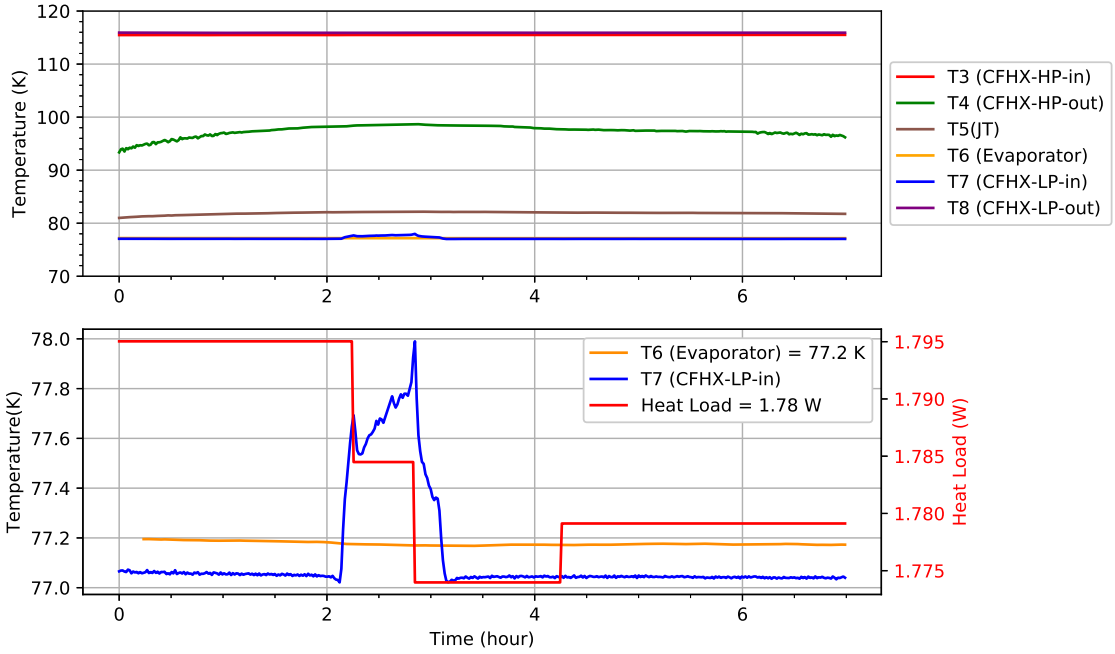


Figure 5.15: Example of a test run of the JT stage over 7 h close to the optimum operating values from Table 4.4. Upper figure: temperature variation on several parts of the JT stage. Lower figure: applied heat load (right axis scale) used to measure the cooling power of the JT stage.

#### 5.4.2.2 Test #2: Evaporator characterization

The second testing phase of the JT cold stage is dedicated to the characterization and acceptance of the evaporator under microgravity environment. Initially the evaporator is tested in the so-called normal orientation, as in Figure 5.13. In this orientation, the exhaust and the inlet are located at the top of cell, preventing the liquid to escape, and the liquid formed during the expansion falls naturally to the evaporator by effect of gravity. When rotating by 180° the whole cryocooler, the liquid must be properly confined by the copper foam or it will be spilled.

Figure 5.16 shows a run of the evaporator emptying time measurement. The evaporator was previously filled with liquid (procedure described in Section 5.4.1.1) and at $t = 5$ min, a constant heat load of 100 mW was applied and recorded the needed time to empty the evaporator. At $t = 20$ min, the evaporator increased its temperature, which is an indication that the evaporator is empty. Therefore, the emptying time corresponds to the difference between these two instants. Such measurements were performed for various heat loads to enable the estimation of the energy storage capacity, $E$, of the evaporator and as well as the confined volume/mass of liquid nitrogen.

Assuming that the liquid mass quantity, $m$, is maximum and the same for each run, the energy, $E$, needed to evaporate the liquid, with a known latent heat, $L$, is given by

$E = mL = \dot{Q}\Delta t$, then, in Figure 5.17 is plotted the heat load, $\dot{Q}$, as a function of the inverse of the emptying time, $1000/\Delta t$. The coefficient of proportionality corresponds to the stored energy, $E$, of the evaporator.

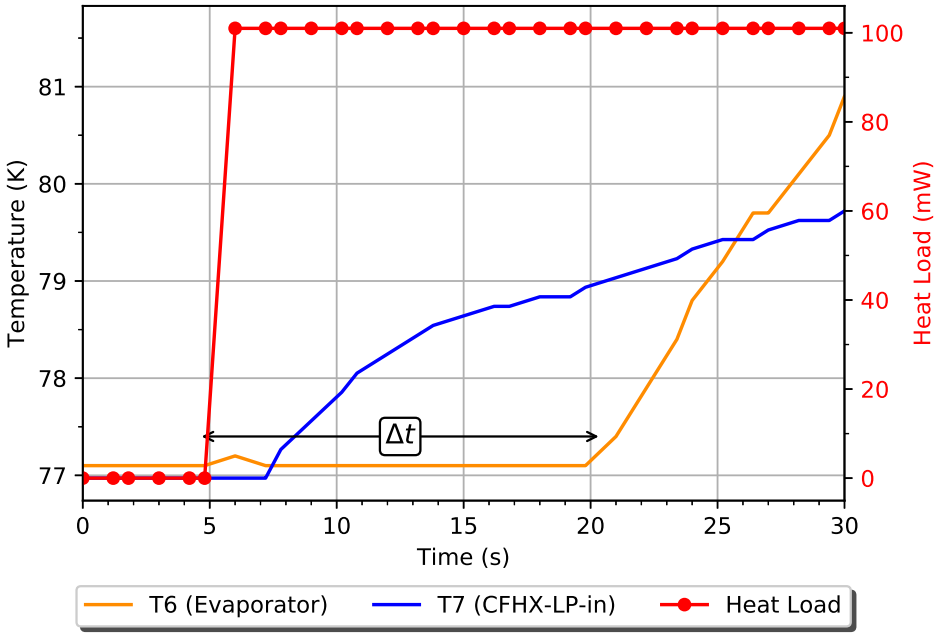


Figure 5.16: Emptying time, $\Delta t$, measurement example of the evaporator. Applying a heat load of 100 mW takes around 15 min to empty the evaporator.

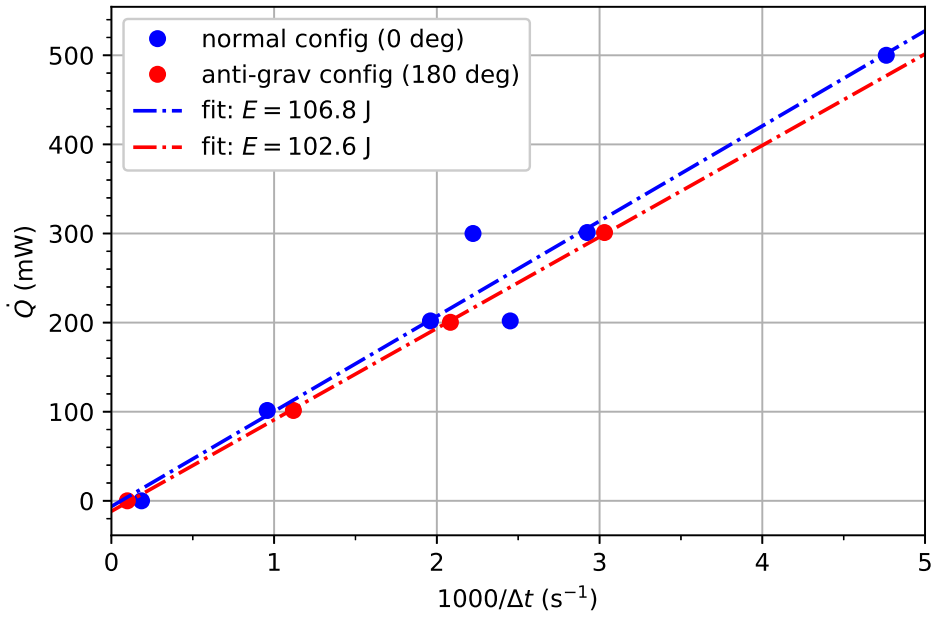


Figure 5.17: Evaporator thermal energy storage, $E$, capacity for both orientations.

Table 5.6 summarizes the obtained results for both orientations and they show similar stored energies. Notice that the normal configuration (0°) corresponds to the best-case scenario and the anti-gravity (180°) to the worst. Although the measured capacity in the normal orientation is below the expected capacity, no significant differences were observed between the two configurations and, therefore, the porous copper is able to confine the liquid by capillary forces.

Table 5.6: Obtained energy storage capacities from the evaporator characterization. We highlight the small difference obtained between the two configurations (about 4% less in the anti-gravity orientation).

| Orientation | Energy (J) | Mass (mg) | Volume ($cm^3$) |
|---|---|---|---|
| Normal (0°) | 106.8 | 536 | 0.66 |
| Anti-gravity (180°) | 102.6 | 515 | 0.64 |
| Expected | 120.0 | 602 | 0.75 |

CHAPTER 6

# Detailed Sorption Compressor Cell Design and Integration

This chapter presents in detail the design and integration of a sorption compressor cell. Some auxiliary components of the sorption compressor are presented: check-valves and gas-gap heat switch. The development and assembly of a new 200 L cryostat needed for the functional characterization of the sorption compressor is also presented.

## 6.1 Sorption Cell Design, Integration and Acceptance

The design of a sorption cell must take into account that they are pressure vessels[1], since it will store gas at a maximum pressure of 40 bar. In order to minimize very thick walls and/or high stresses on some regions of the vessel, two common shapes are used to store fluids at high pressures: spherical and cylindrical; the latter being widely used for storage in various applications due to its lower production cost. However, cylinders are not as strong as spheres because they have weak points at each end. The spherical geometry is theoretically the best way to contain pressure, since the generated stresses are evenly distributed. Furthermore, our sorption cells will undergo a high amplitude thermal cycle (up to 400 K), so, this motivates the spherical design due to its robustness.

The design shown in Figure 6.1, mainly developed at AST, consists of a thin spherical shell made of titanium (Ti4Al6V) designed to withstand an operation up to 500 K at 100 bar. Internally it contains a Copper Heat Exchanger (CuHX) to obtain a good thermal homogeneity of the MOF. At the bottom of the this cell there is an interface for a heat switch to obtain a controllable thermal link between the cell and the heat sink. To

[1] Pressure vessel: vessel containing a pressurized fluid with an energy level greater than or equal to 19.31 kJ or with a pressure greater than or equal to 0.69 MPa, or which can create a hazard if released.

avoid complicated mechanical issues existing in the solution described in Section 3.2.2 (GGHS distributed along the wall of the cell), a solution with a GGHS at the end of the CuHX and placed outside of the sorption cell was preferred. Essentially, the following aspects motivated this design:

- By using the spherical geometry, it is possible to obtain a thinner wall thickness compared to the cylindrical one and, therefore, less (thermal) mass.
- By using a cell made of titanium, an excellent combination of high strength-/weight is obtained when compared with other space-grade metals, such as, stainless steel or aluminum. In addition, the problematic aluminum welding is avoided.
- By placing the GGHS outside of the cell, it leads to a simpler configuration and a lower development risk since the heat switch may be independently developed and tested from the sorption cell. It is also possible to use hydrogen (best conducting gas for T>150 K) as the exchange medium of the GGHS and, thus, avoiding the well-known concern of embrittlement of titanium-based alloys in exposure to hydrogen [70].

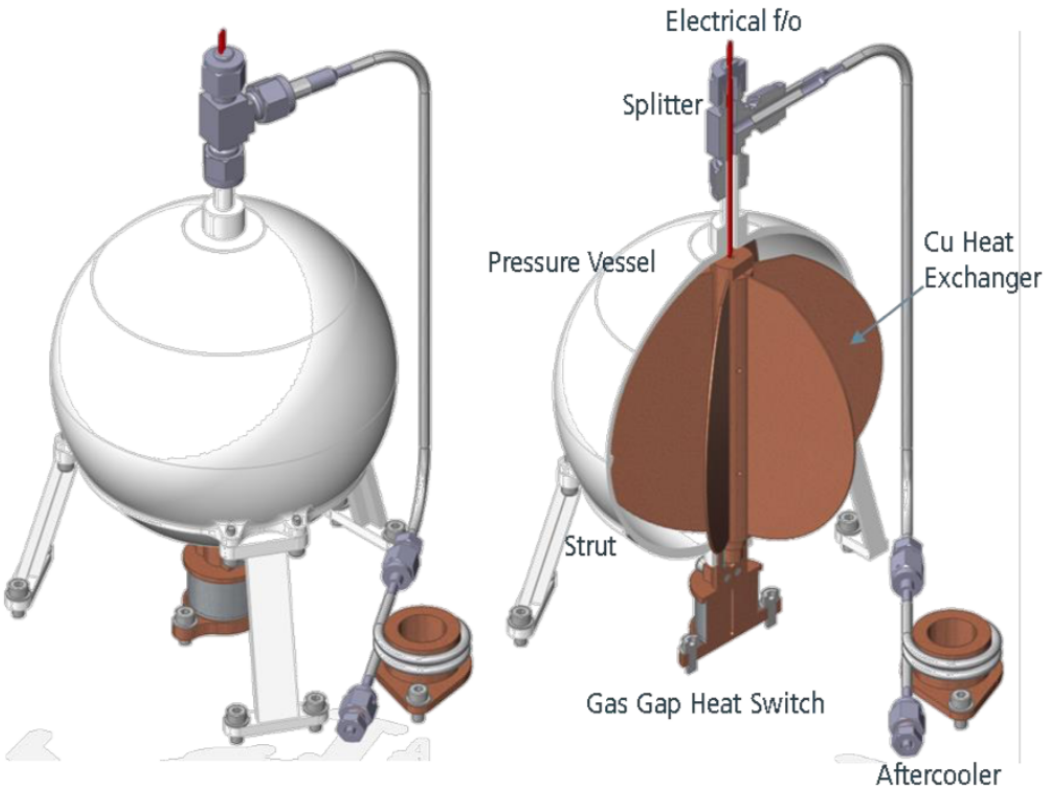


Figure 6.1: Sorption cell CAD design [71]. We highlight the location of the GGHS (outside of the sphere) and its interface to the interior of the sorption cell through the CuHX.

The spherical vessel shown in Figure 6.1 consists of two 120 mm diameter titanium hemispheres which are joint together with Electron-Beam Welding (EBW). The CuHX is placed inside and consists of six thin fins (0.5 mm thick) brazed to a 20 mm copper rod. The useful volume of the sorption cell is 0.913 L, this value was found through a trade-off between the cycle period and the quantity available for circulation, $\Delta n$. Let us note that by using cells of smaller volume have the advantage of reduced thermal mass but contain less adsorbent material, therefore, it requires a larger number of cells which makes it more complex to operate.

To measure and manage the sorption cell temperature, two type K thermocouples and two 50 W heater cartridges (one for redundancy) are brazed to the copper heat exchanger. Mineral insulated metal (SS-304) sheathed wires were used for the wiring of both thermocouples and heaters. The external stainless-steel surface of the sheathed wire was brazed to the splitter located at the top hemisphere (Figure 6.1). The GGHS is connected to the bottom part of the copper heat exchanger via a bimetallic adapter which is welded underneath the sorption cell. As visible in Figure 6.2, this bimetallic adapter is needed to obtain a leak tight transition from the inner part to the external part of the cell and allowing an efficient thermal path.

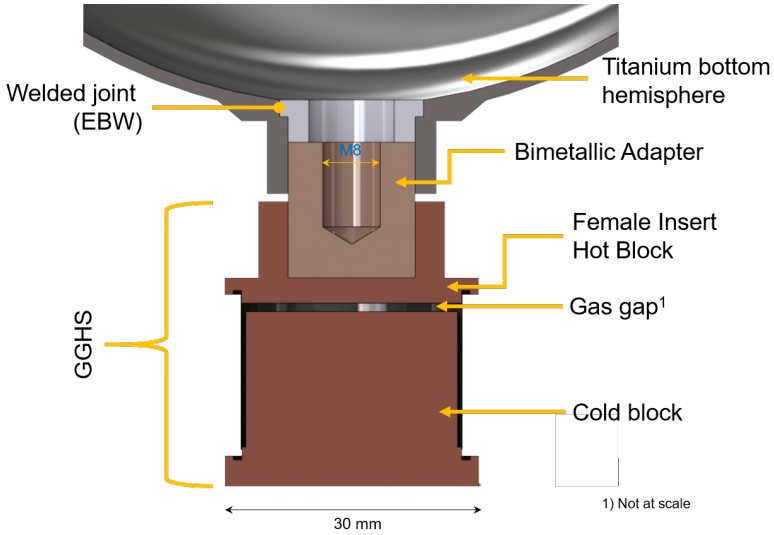


Figure 6.2: Cross section view of the gas-gap heat switch coupling to the bottom hemisphere using the bimetallic interface. Note that the titanium part of the bimetallic adapter allows to obtain a leak tight transition.

This adapter was machined out of two 30 mm rods of copper and titanium and joint together by friction welding, as visible in Figure 6.3a. The titanium side (internal part of the cell) is welded through EBW to the bottom hemisphere, while the CuHX is threaded to this adapter that contains a M8 threaded hole. Whereas the copper part (outside the cell) of the bimetallic adapter connects to the GGHS via a shrink-fitting coupling.

In order to verify the robustness of this bimetallic adapter, a tensile pull test was performed at Instituto Soldadura e Qualidade (Portugal), Figure 6.3b shows two tensile specimens. The test was performed at a temperature of 500 K, remind that the maximum working temperature according to the numerical optimization is only 365 K (Table 4.4). The sample rupture occurred close to the welding zone and its area reduction caused by the tensile pull was determined on the copper side, since on the titanium part was not observed any deformation. The measured yield strength was found to be 185 MPa and the rupture of 204 MPa, which is similar to the values of oxygen-free copper (210 MPa) [72]. Therefore, the rupture, in fact, occurred due to the lower stiffness of copper compared to that of titanium.


Figure 6.3: Cu/Ti bimetallic adapter: a) Machined bimetallic adapter; b) Tensile specimens machined for the tensile pull testing.

After successful manufacture and acceptance of the pieces, particularly both bimetallic adapter and CuHX, the integration of the sorption cell proceeded. Such procedure is depicted in Figure 6.4.

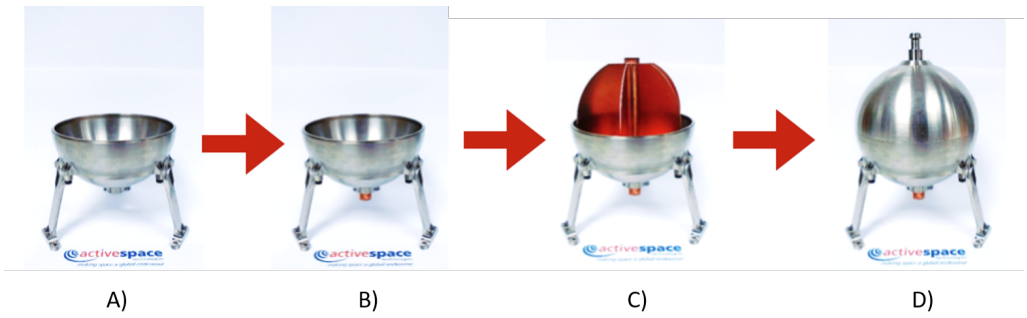


Figure 6.4: Sorption cell integration procedure: $A \rightarrow B$, bottom hemisphere and bimetallic adapter were joint together by equatorial EBW; $B \rightarrow C$, six thin copper fins brazed to the 20 mm rod of copper and fastened to the bimetallic adapter. The electrical connections (heaters and thermocouples) were fixed during this step. $C \rightarrow D$, top and bottom hemispheres were joint together by equatorial EBW.

### 6.1.1 Leak and Proof Pressure Test

According to [73], the sorption cell is classified as a pressure vessel because of its volume and high pressure combined and as well as being subjected to intense solicitations due to thermal cycling. Thus, before proceeding to its functional characterization, each sorption cell requires a qualification campaign to ensure functional and safety requirements: leak test (vacuum mode detection), pressurized leak test (sniffer leak detection) and proof pressure test at 150% working pressure.

The maximum admissible leak rate, $Q_{\text{leak}}$, in the cell's volume of $V_c = 0.913\,\text{L}$ is estimated considering a degradation of 1% of the cooler performance over 10 years. Considering Equations (2.10) and (2.18), one may conclude that the cooling power is proportional to the gas quantity released per each sorption cell, $\Delta n$. So, a reduction of 1% in the released gas quantity corresponds to a degradation of the same magnitude in the cooling power. In case of leakage, it is assumed that the gas amount at the adsorbed phase remains constant, but the gas occupying the void volumes may leak. By considering a void fraction, $\epsilon$, of 54%, the void volume of one cell, $V_\epsilon$, is 0.493 L and the gas amount lost by leakage is 1% of $\Delta n = 1.67$ (Table 4.4), the maximum admissible equivalent helium leak rate, $Q_{\text{leak}}$, is,

$$Q_{\text{leak}} = \frac{\mathrm{d}P}{\mathrm{d}t} V_\epsilon = 1.3 \times 10^{-6}\,\text{mbar}\,\text{L}\,\text{s}^{-1} \tag{6.1}$$

After a first vacuum leak detection test, no leak was detected ($<2 \times 10^{-10}\,\text{mbar}\,\text{L}\,\text{s}^{-1}$). Then, the vessel was pressurized with 60 bar (150% working pressure) of helium and placed inside of a plastic bag for accumulation detection using the sniffer mode and no signal was detected after 2 h of accumulation. The vessel leak-rate was measured again in vacuum mode and was found to be less than $7 \times 10^{-9}\,\text{mbar}\,\text{L}\,\text{s}^{-1}$. Thus, it can be concluded that the sorption cell successfully passed its qualification campaign.

### 6.1.2 Sorption Cell Filling

The sorption cell filling is a very critical procedure, since the amount of MOF that can be confined within the cell deeply impacts the required radiator surface, as displayed in Figure 4.19. As a matter of fact and as explained earlier in Section 4.3, a sorption cell filled with a poor packing factor will therefore contain a large void volume and, consequently, a larger temperature amplitude between cycles would be needed to supply the required gas quantity, $\Delta n$, to the Joule-Thomson stage. Furthermore, as also previously mentioned in Section 4.3, the MOF packing may be improved by filling with two different particle sizes (binary packing) or, in a ideal scenario, with a discrete particle

distribution. So, before filling the sorption cell with HKUST-1, various filling combinations were studied.

MOF Technologies (UK) was able to supply HKUST-1 in large quantities and also in different sizes and different geometries: pellets (0.5 mm diameter and length ranging from 2 mm to 5 mm), simple powder form (diameter ranging from 1 µm to 100 µm) and a batch of uncontrolled particle size powder (up to 150 µm). Then, different filling combinations were produced in a 100 mL graduated cylinder and their apparent density, $\rho_a$, measured, such results are displayed in Figure 6.5.

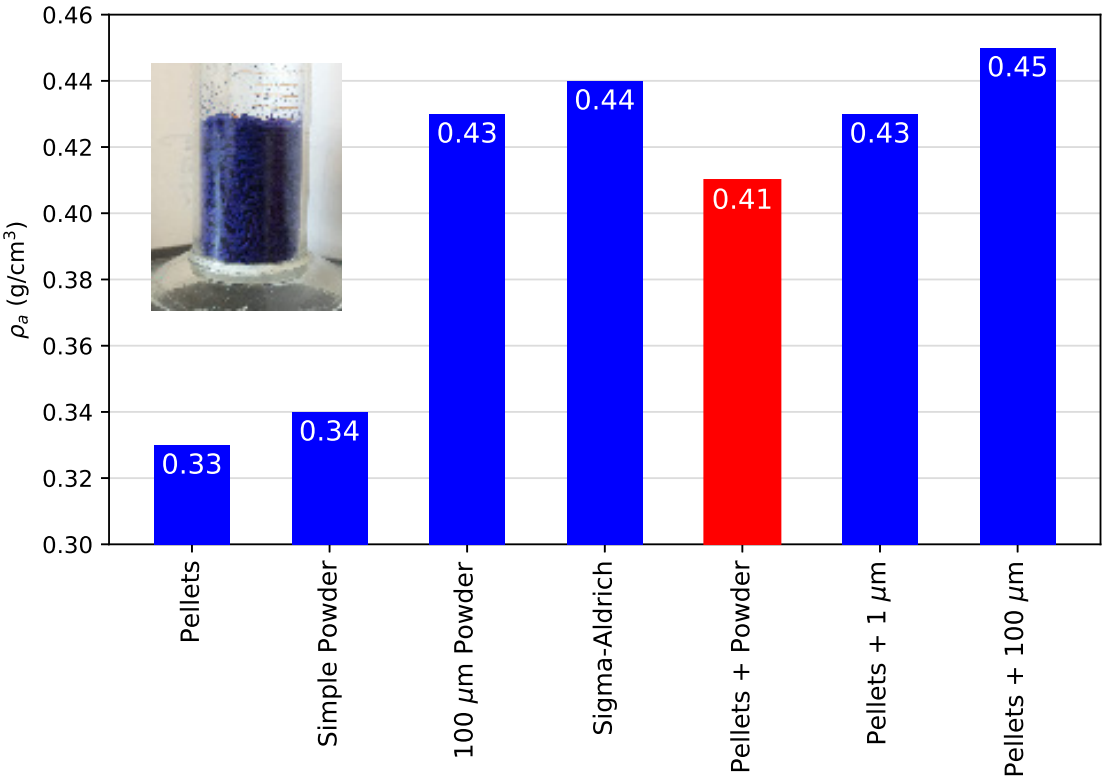


Figure 6.5: Apparent densities of the different filling combinations of HKUST-1 (particle density $\rho_p$ =0.95 g/cm$^3$). The red bar corresponds to the actual apparent density obtained in the sorption cell.

Some characteristics of the tested mixtures are noteworthy:

1. The single filling of pellets led to the worst packing. During filling, it was clearly visible a lot of empty space between particles, indicating that this filling was far from optimum.
2. The simple powder (uncontrolled particle size) also led to a low packing factor. During filling, some electrostatic forces were detected between the particles and also the presence of large agglomerates (up to 3 mm), probably due to the absorption of moisture by exposure to air.
3. The single filling using the Sigma-Aldrich sample or the 100 µm powder, obtained

a much higher density when compared to those of pellets or simple powder. Actually, the Sigma-Aldrich powder does not appears to interact with its neighbors and has little or no tendency to form agglomerates, while the 100 µm sample has a tendency to form clusters.

4. Mixing pellets with any powder (binary filling) greatly increases the packing, when compared to the single filling of pellets. The mix with the 100 µm powder led to the highest obtained density, corresponding to $\epsilon = 53\%$.

However, it is not convenient to fill the sorption cell through the 1/4 inch VCR® fitting located at the top hemisphere (Figure 6.4) with any mixture containing the 100 µm powder or the 1 µm, since they tend to flow very poorly due to electrostatic attraction and also with a tendency to form large clusters, which can result in a complete blockage of the narrow filling port, as visible in Figure 6.6, and further complicating the procedure.

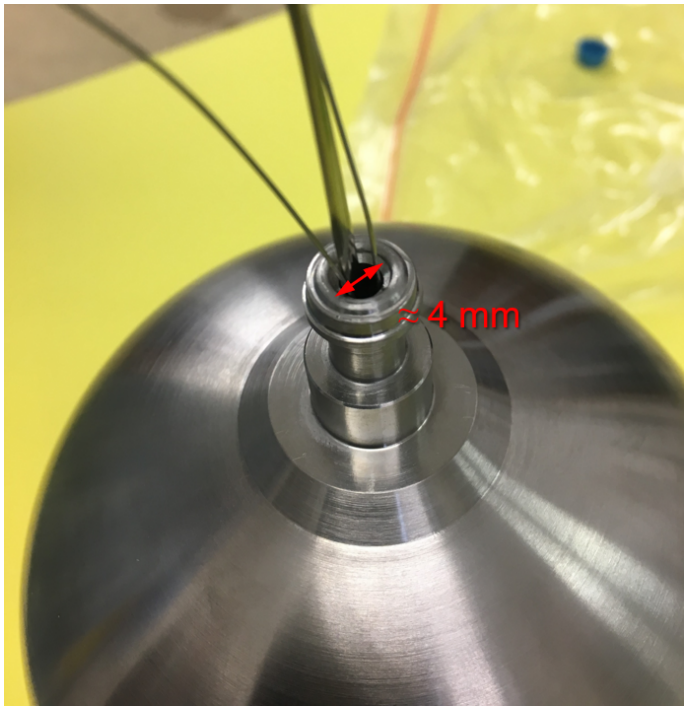


Figure 6.6: Close-up view of the filling port located at the top hemisphere of the sorption cell. Note that the instrumentation wiring of the cell shares the same feedthrough.

The most suitable filling combination through small apertures, at the time being, is the one using pellets mixed with simple powder (red bar). Such filling would correspond to a void fraction, $\epsilon$, of 57%. Let us note that this filling pair is still above from the obtained values during the HKUST-1 characterization (54%). Therefore, the filling of the sorption cell proceeded with an expected mixture of 50% pellets and 50% simple powder. However, the filling procedure through the 1/4 inch aperture was a hard and long task:

- Similar to the powder of controlled size, after exposure to the atmosphere, the simple powder also begins to form large clusters and consequently blocking the filling port.
- At the end, the filling was mostly performed with pellets, since they flowed much better than the powder form. Around 75% pellets were inserted into the cell.
- A homemade vibrating system was used to ease the flow through the filling port and to help the mixture between the particles, i.e, to fill the space between particles with smaller particles. Even so, it took around 10 working days to fill the sorption cell.
- 376.1 g of HKUST-1 were inserted into the cell which corresponds to an apparent density of $\rho_a$ =0.41 g/cm$^3$ (red bar of Figure 6.5) and a void fraction $\epsilon$ of 57%. Let us note that, according to the compressor optimization (Table 4.4), each sorption cell is expected to contain around 400 g ($\epsilon$ = 54%) of sorbent material.
- This filling would correspond to an increase of the radiator surface by 8%.

### 6.1.3 Gas-Gap Heat Switch

As already mentioned in Section 2.3.2, a controllable thermal link is needed between the radiator and each sorption cell to avoid unacceptable heat loads on the radiator during the heating phases of the sorption cells. This thermal link may be a GGHS which due to its simplicity and without the need of moving parts is a good solution for this application as it allows to vary its thermal conductance by several orders of magnitude, only through the presence or absence of gas in its narrow gap [15], as schematically shown in Figure 6.7.

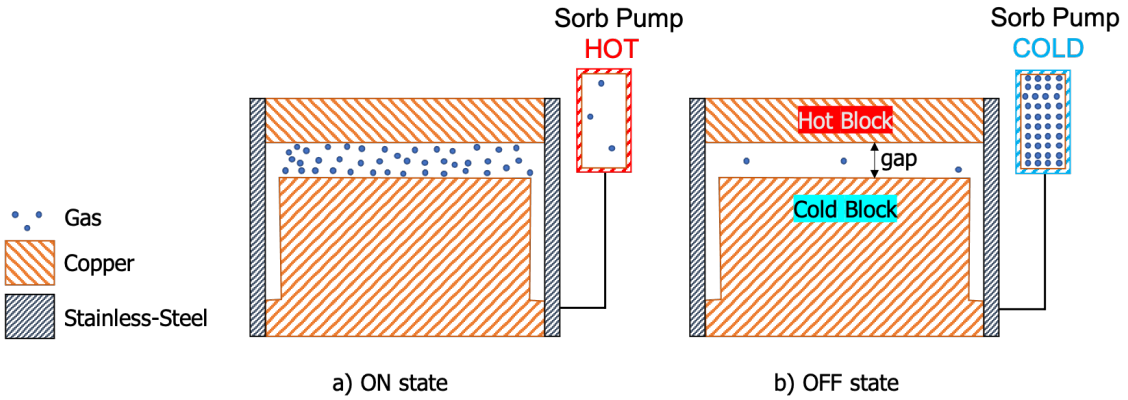


Figure 6.7: Schema of a GGHS integrated with a sorb pump to manage the thermal conductance of the GGHS through the presence or absence of gas in its gap: by heating this sorb pump, the highly conducting state is achieved since the gas is desorbed and fills the narrow gap; by cooling, the low conducting state is obtained since the gas is adsorbed and therefore removed from the gap.

During the preliminary designing phase of the VFC, three different prototypes of gas-gap heat switches using the differential dilation technique [74] were built and characterized with nitrogen, helium and hydrogen as exchange gas. The design, construction and tests resulted in a rather extensive work. Its detailed description was considered too large to be included in this dissertation; so, we present here a summary of the results, while the whole work can be consulted in Appendix A, as a first version of an article to be submitted to *Cryogenics* (journal).

Figure 6.8 shows one of the built and tested gas-gap heat switches. Let us note that two of three heat-switches obtained a gap length around 15 µm at 150 K, while 33 µm was obtained in the second prototype.

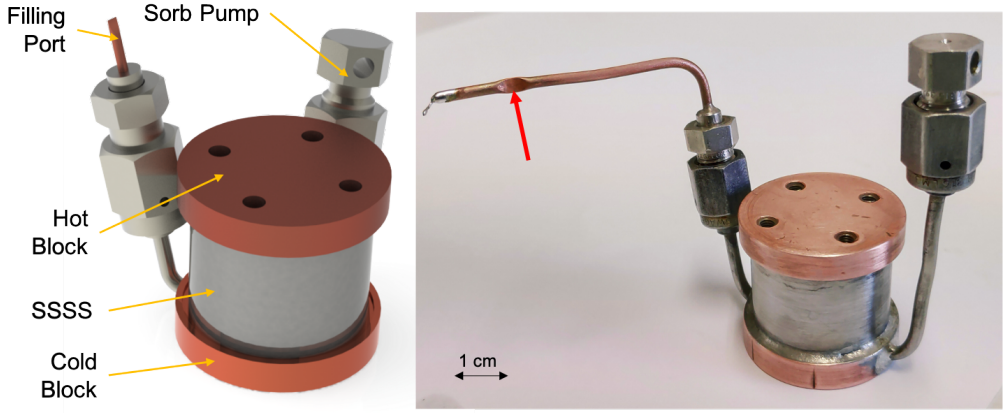


Figure 6.8: Rendered image of the second prototype of a dilation GGHS (left side) and as built (right side). The red arrow points to the location of the "pinch-off" sealing.

Considering the temperature range (150 K < $T$ < 400 K) of the sorption cell and to obtain the highest thermal conductance of the GGHS, it should be used hydrogen as the exchange gas since it is the best conducting gas for temperatures higher than 150 K [44]. In such a device, the gas management needed to obtain the switching action between a good (ON state) and a poor (OFF state) thermal conductance state is obtained by using a small sorb pump, filled with activated carbon, to pump (OFF) or to fill (ON) the narrow gap with gas. However, due to its adsorption properties, an operational sorb pump of hydrogen is usually limited to temperatures below 40 K which is far from our 150 K heat sink temperature.

Another way to adsorb hydrogen, is to use the ability of the intermetallic materials to reversely absorb and desorb hydrogen at temperatures compatible with our objectives. For instance, the metal hydride $ZrMn_2H_x$ seemed to be suitable for our application [75]. For that reason, around 5 g of this material was synthesized and 260 mg filled into the small sorb pump of the second prototype, shown in Figure 6.8. After some initial testing, we showed possible to manage the internal pressure of the GGHS (from 10 mbar

to 300 mbar) and, thus switch between both conductance states just by controlling the sorb pump temperature containing this metal hydride material. At $T \approx 150$ K, the OFF state was obtained with a measured thermal conductance of $K_{OFF} = 7.6\,mWK^{-1}$, while for temperatures higher than 250 K, the ON state was achieved with a measured conductance of $K_{ON} = 1.1\,WK^{-1}$. These characteristics show that a GGHS using hydrogen and $ZrMn_2H_x$ can vary its thermal conductance by more than two orders of magnitude through a hydrogen sorb pump varying its temperature between 150 K to 250 K and, then, being adequate for the thermal management of the sorption compressor cells.

However, of the three built heat-switches, only the third prototype was built with the adequate interface for bimetallic adapter of the sorption cell and, unfortunately, for various technical reasons, it was not possible to operate this switch using the metal hydride $ZrMn_2H_x$. Due to limited time and resources, this heat switch had to be sealed with nitrogen, therefore, with an ON conductance 7× lower compared to that can be obtained with hydrogen. The nitrogen GGHS thermal conductance dependence with a sorb pump filled with activated carbon was measured and is displayed in Figure 6.9. The results show that just by varying the sorb pump temperature roughly from 150 K to 250 K, the GGHS thermal conductance varies from $9.5\,mWK^{-1}$ to $269\,mWK^{-1}$, so, going from an OFF to an ON state. Furthermore, let us note that by using nitrogen gas instead of hydrogen as the exchange gas of the GGHS, as expected, it significantly impacts the cooling dynamics of the sorption cell and, therefore, does not allow the cooler to operate with the optimum parameters showed in Figure 4.17. However, is still possible to demonstrate the operation of the cooler by adjusting some parameters (heat-sink temperature), as shown later in Chapter 7.

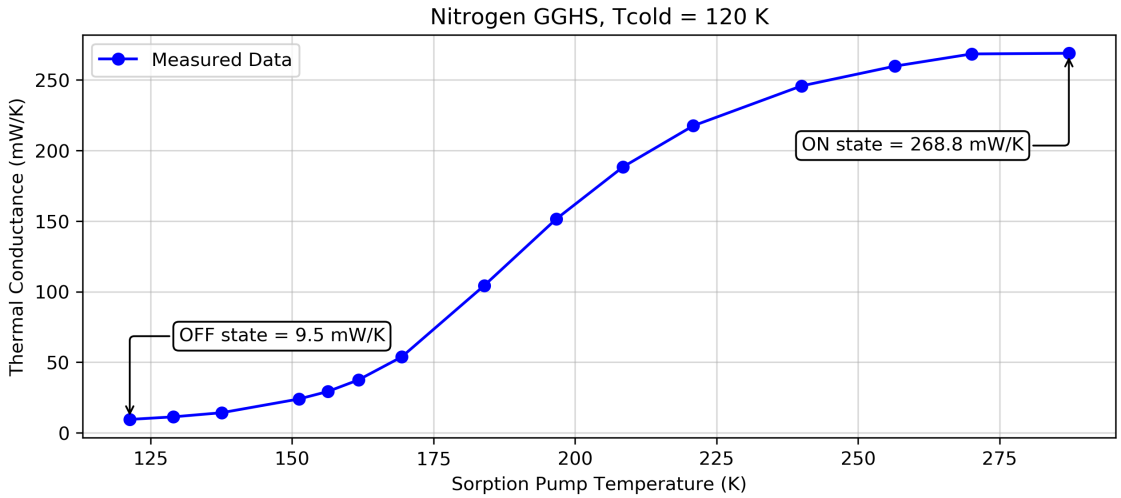


Figure 6.9: Nitrogen GGHS thermal conductance as a function of its sorb pump temperature.

### 6.1.4 GGHS Shrink-Fitting Coupling

The GGHS is coupled to the bimetallic adapter using the shrink-fitting technique. This is achieved by heating and/or cooling the components before joining them together and allowing it to return to room temperature to create a strong joint, thanks to the phenomenon of thermal expansion of materials. Due to the very strong forces existing between the two components after joining the parts, this technique allows reduced thermal contact resistance. However, this technique does not leave much room for failure, once the pieces are joined, they can no longer be separated.

As shown in Figure 6.10, the bimetallic adapter consists in a 15 mm diameter cylindrical male insertion made of copper and the GGHS contains a 9 mm depth female insertion using the same diameter as the male one. According to [71], this coupling is expected to have a thermal conductance as high as 10 $WK^{-1}$.

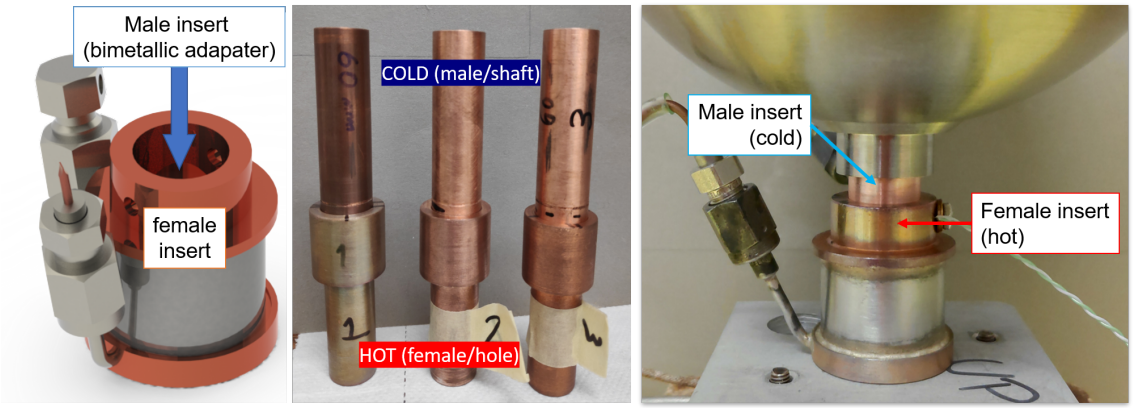


Figure 6.10: a) Rendered image of the GGHS, we highlight the female/hole insert located at the top; b) Shrink-fitting dummies fully-penetrated through the shrink-fitting technique; c) Sorption cell partially penetrated to the GGHS after using the shrink-fitting technique.

To train the reproducibility of this irreversible coupling technique, three dummies were built using the same dimensions as the bimetallic adapter and the GGHS, displayed in Figure 6.10b). To join the GGHS to the sorption cell, the bimetallic adapter (male insert) is cooled down in a liquid nitrogen bath in order to contract enough to obtain a clearance between the two pieces, while the GGHS (female insert) is heated up to a maximum temperature of 200 °C in order to expand.

The shrink-fitting pieces were designed as an interference fit[2], so, the male part slightly exceeds the female: considering the tolerances of the pieces (h5/S6, ISO 286), a maximum interference of 36 µm and a minimum interference of 18 µm is expected

[2]The dimensions of the male and female inserts are such that without interference from external force or shrink-fitting the assembly of the pieces is not possible.

at room temperature. By cooling down the male piece to 77 K and keeping the female piece at room temperature, a clearance of 17.5 µm is expected between the two parts. This clearance can be increased to 41.5 µm if the female piece is heated up to 200 °C.

The coupling will be considered successful if penetration is full, i.e., over a length of 9 mm. Three dummies were joint together, as visible in Figure 6.10b): two of them obtained full penetration, while another one (piece #3) only obtained around 90% penetration. Let us note that this procedure is performed manually, which turns out this procedure even more complex and, thus, subject to failure.

Afterwards, the GGHS and sorption cell were joint together, as displayed in Figure 6.10c). Unfortunately, only a partial penetration of 4 mm was obtained (total length = 9 mm). This imperfect penetration can be due to not respected tolerances or/and misalignment of the two pieces at the beginning of the procedure. As explained before, this process is highly irreversible and we had to continue with this imperfect coupling (44% of the expected thermal conductance). Actually, further results showed that this thermal conductance was far to be the limiting factor of the thermal path between the sorption cell and the heat-sink.

## 6.2 Cryostat Development

The functional characterization of the cooler includes four sorption cells, a JT stage and a check-valve panel (eight valves). Therefore, a completely new experimental set-up was designed to test the 80 K vibration-free cooler and is displayed in Figure 6.11. The whole volume of the cryostat is defined by a vacuum chamber (diameter of 500 mm; height of 700 mm) of ≈200 L including a circular aluminum plate cooled by a continuous flow of liquid nitrogen, similar to a system developed at ESO to test the optics detectors at low temperatures [76].

The cooling is obtained by pressurizing a LN2 transport dewar and, hence, forcing a flow of liquid nitrogen through the vacuum chamber. In the vacuum chamber, the liquid nitrogen flow is divided into three different paths (each path ≈1 m) to homogeneously cool the 450 mm aluminum cooling plate (10 mm thick), as visible in Figure 6.12 (technical drawing shown in Appendix C). The nitrogen coolant leaving the cryostat is warmed up and passes through a gas totalizer before being exhausted.

Considering the expected heat rejection capacity of the radiator (about 40 W), the cooling plate was designed with an expected cooling power of 100 W at 120 K. To allow temperature control of the aluminum plate, a temperature controller (model REX-P300) actuates over four cartridge heaters (100 W each) evenly distributed in this plate and the temperature reading is obtained with a RTD (platinum resistor), placed at the center of the cooling plate. Moreover, the pressure of the LN2 dewar was controlled through a

home-made pressure regulator in order to regulate the flow of LN2 entering the vacuum chamber.

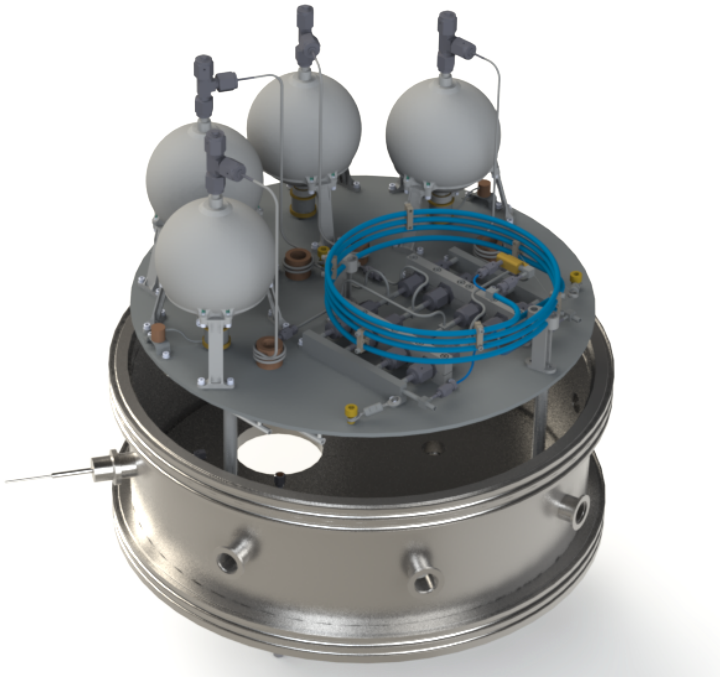

Figure 6.11: Design model of the cryostat chamber including the 80 K vibration-free cooler.

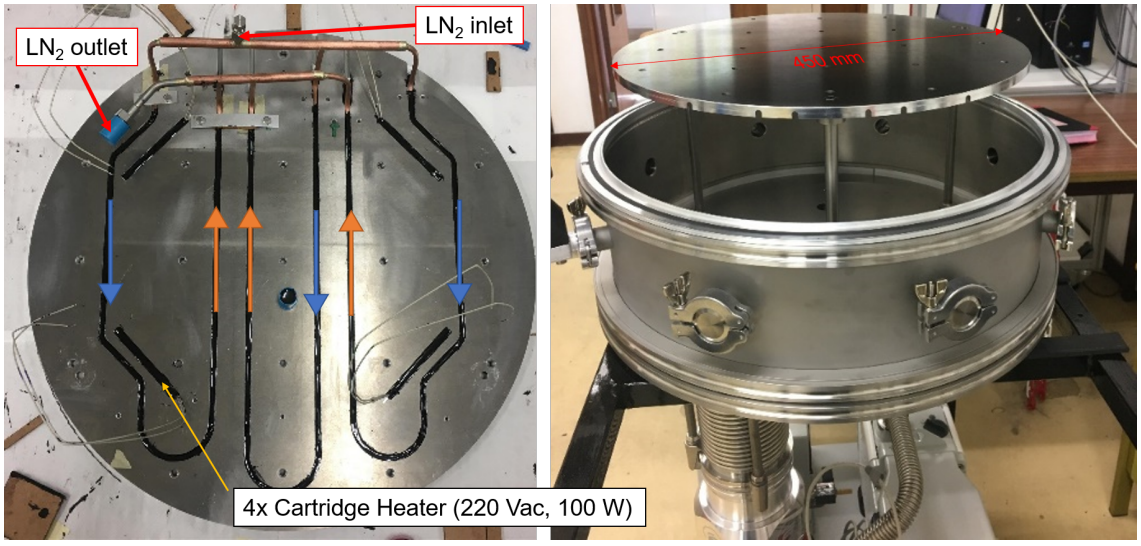


Figure 6.12: Liquid nitrogen cooling plate and vacuum chamber as built.

During operation, the cryostat is kept at a maximum pressure of $1 \times 10^{-6}$ mbar, which is successfully maintained by a high vacuum pump system including a 2.4 $m^3/h$ rotatory vacuum pump and a 200 $Ls^{-1}$ turbo-molecular vacuum pump.

Below the large 200 L vacuum chamber was installed an instrumentation vacuum skirt with 8 KF25 vacuum connections for several purposes (left side of Figure 6.12): electrical feedthrough (heaters, thermocouples, Pt100 resistors), liquid nitrogen transfer line couplings, vacuum pressure transducers and inlet/outlet JT stage lines. About 14 thermometers are needed just for the characterization of one single sorption cell and of the JT cold stage (9 RTD + 5 TC). Usually in cryogenics, the thermometry acquisition makes use of commercially available cryogenic temperature controllers. In our case, since the working temperatures are rather high (above 120 K), cheaper and more compact solutions may be used in this case. For this experimental set-up, we chose to use the CompactRIO controller from National Instruments (NI), which combines a processor running NI Linux Real-Time OS (able to run LabVIEW applications), a programmable FPGA and slots to connect modules, each module can read up to 16 sensors. Some specifications of this controller and its modules are shown in Table 6.1.

Table 6.1: CompactRIO controller and modules specifications.

| **Equipment** | **Model** | **Details** |
|---:|---|---|
| CompactRIO Controller | cRIO-9063 | 667 MHz Dual-Core CPU, 256 MB DRAM, 512 MB Storage, 4x modules slot |
| Digital I/O Module | NI-9375 | 32-Channel I/O, 6 V to 30 V |
| Thermocouple Temperature Input Module | NI-9213 | 16-Channel, 24-bit ADC |
| RTD Temperature Input Module | NI-9216 | 8-Channel 0 Ω to 400 Ω, 24-bit ADC |

To control the temperature, it was implemented in LabVIEW four PID controllers to run on the CompactRIO which makes use of the Pulse-Width Modulation (PWM) method to control the average voltage fed to the heating resistors, by turning the switch ON and OFF between a supply and a load as displayed in Figure 6.13. The PWM signal actuates over a power MOSFET that is used as a switch. Such component has very fast switching speeds and a high gate impedance which makes it ideal to operate with standard logic gates as, for instance, the digital I/O module of the CompactRIO.

After construction and validation of the cryostat, one sorption cell was assembled on the liquid nitrogen cooling plate, as visible in Figure 6.14. Actually, the sorption cell is screwed to an aluminum interface thermally coupled to the cooling plate. Also, another thin (0.5 mm thick) flexible copper interface makes the thermal connection between the GGHS and the aluminum interface to prevent excessive forces on the GGHS that could induce unacceptable deformation of the thin stainless-steel supporting shell of the GGHS.

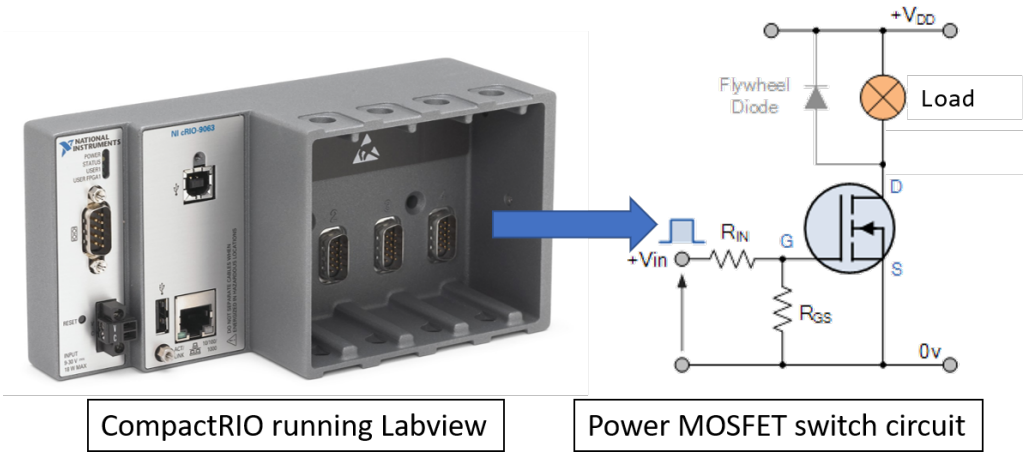


Figure 6.13: MOSFET switch circuit controlled with a PWM signal. The PWM signal comes from the digital I/O Module, which is controlled by a LabVIEW PID algorithm running on the CompactRIO controller.

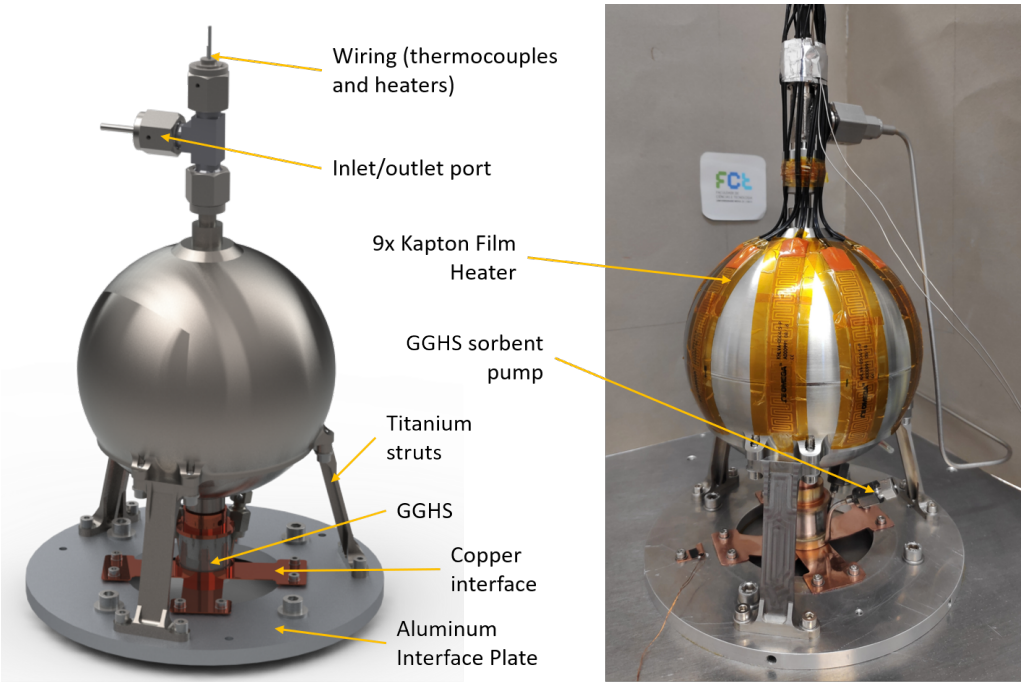


Figure 6.14: Left side: Sorption cell rendering including the gas-gap heat switch and its interfaces; Right side: Sorption cell as built including the nine film polymide (Kapton®) heaters.

By using this copper interface between the cooling plate and the GGHS, it is expected a decrease of the global thermal conductance between the sorption cell and the heat-sink, schematically represented in Figure 6.15. Such impact was considered and a solution was found based on a trade-off between both good thermal conductance and flexibility of this copper link. Using a finite element method (SolidWorks Simulation), such copper interface was found to have a thermal conductance of 441 $mWK^{-1}$

at 120 K. Considering the thermal path between the sorption cell and the heat-sink, a global conductance of 143 mW$K^{-1}$ is obtained, assuming a GGHS ON conductance of 269 mW$K^{-1}$ (with nitrogen) and a shrink-fit thermal contact resistance of 1 K$W^{-1}$.

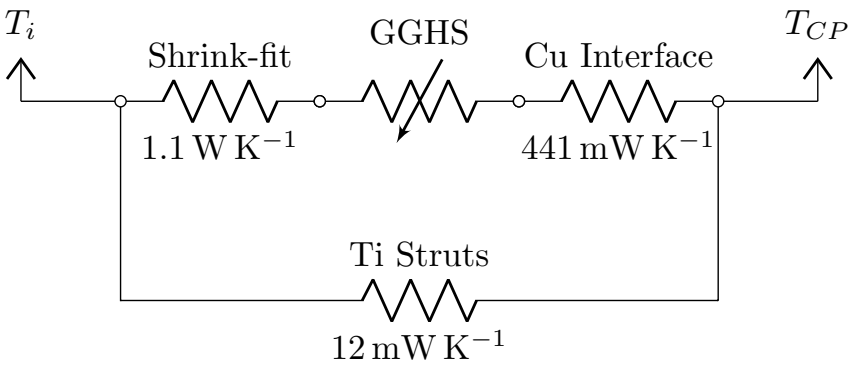


Figure 6.15: Heat conduction elements between the sorption cell and the cooling plate (CP).

To heat up the cell, two cartridge heaters are placed inside the cell (one for redundancy), brazed to the copper heat exchanger. However, due to a partial short-circuit of one of these heaters, nine 5 W Kapton® film heaters were glued on the external titanium surface of the sorption cell, as visible in Figure 6.14. Additionally, these Kapton® heaters may provide a better thermal homogeneity during heating, as the cell can be heated both internally and externally. In these conditions, around 45 W can be applied on the titanium surface and about 50 W on the inside.

## 6.3 Check-Valve Characterization

Check-valves are a crucial component to correctly operate the sorption compressor, as they convert a pressure swing into a constant pressure flow. In electronics, this behavior is called rectification: conversion of an alternating current (pressure swing) to a direct electric current (constant pressure). So, a check-valve can be viewed as an electric diode: it allows a fluid to flow through in one direction (forward direction), while blocking in the opposite direction (reverse direction).

Still like the diodes, check-valves only begin to "conduct" if a certain pressure differential (in diodes, threshold voltage) is present in the forward direction. Technically, it is called the cracking pressure and it corresponds to the minimum pressure differential to obtain the first indication of flow (steady stream of bubbles) [77]. Obviously, each check-valve must keep its influence to a minimum and operate effectively: reduced leak in the reverse direction, low cracking pressure, low pressure drop in forward direction,

reduced void volume, reliability at low temperatures. However, most of the commercially available check-valves do not have these requirements, particularly, reliability at low temperatures. For that reason, University of Twente has previously developed a space qualified check-valve for an application of a 4.5 K Joule-Thomson cryocooler [78]. However, developing such check-valve was out of the scope of this project and therefore it was planned to use the commercial off-the-shelf valves from Swagelok®:

- Check-valve #1: model SS-4C-VCR-4C-1/3; cracking pressure of 30 mbar; o-ring sealing in fluorocarbon (Viton®).
- Check-valve #2: model 6L-CW4VR4-BU; cracking pressure of 140 mbar; o-ring sealing in Buna-N (nitrile rubber).

Note that the existence of cracking pressure negatively impacts the performance of the sorption compressor. For instance, if the low-pressure line is kept at 1.37 bar and the check-valve has a cracking pressure of 370 mbar, the sorption compressor would have to operate at 1 bar to adsorb the gas coming from the JT stage. And, by operating the SC with a reduced low-pressure, less gas will be adsorbed and, consequently, less gas quantity is available to circulate through the JT stage. Therefore, this performance decrease should be estimated as a function of the cracking pressure, for dimensioning purposes, while keeping the radiator surface constant, as displayed in Figure 6.16a. Inversely, as shown in Figure 6.16b, if the cooling power is kept constant, the radiator surface would have to increase to release less amount of gas over a shorter period of time (to maintain the mass flow rate). Obviously, for designing purposes, the result shown in Figure 6.16b should be considered, since the cracking pressure influence is accounted for a targeted cooling power. Figure 6.16a is more likely to correspond to an increase of the check-valve cracking pressure, for instance, in-flight, where the radiator surface would be constant. In the latter case, a cracking pressure of 175 mbar is enough to obtain a degradation of 10%.

Regarding the results shown in Figure 6.16b, a degradation of the cooling power less than 1%, implies a cracking pressure lower than 30 mbar. Therefore, taking into account the available products from Swagelok®, check-valve #1 would be the most suitable for our application. Nonetheless, both models were ordered and tested in an experimental set-up for cracking pressure measurement and leak tightness in the reverse direction, such a set-up is displayed in Figure 6.17.

To measure the cracking pressure in such set-up, valves V3 and V4 must be closed, i.e., fluid flows in the green pipeline. Then, the pressure should be slowly increased until check valve opening, detectable by placing a mass flowmeter or by bubble detection at exhaust D1. The reverse direction, to verify its leak-tightness, valves V1 and V2 must be

closed, i.e. the fluid flows in the red pipeline, this test should be preferably performed at high pressure differential, up to 40 bar. An eventual leak may be detected by mass flowmeter or with bubble detection at D2.

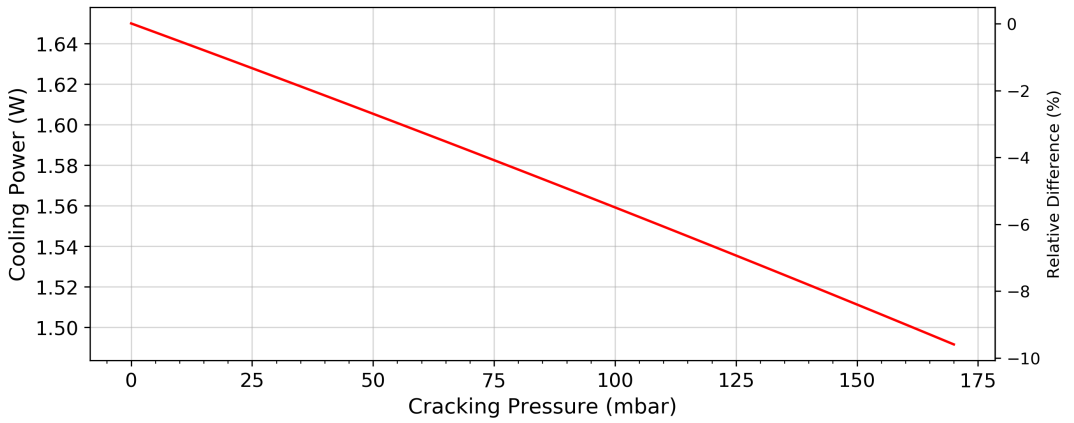


(a) Cooling power degradation as a function of the check-valve cracking pressure at constant radiator surface of 1.80 $m^2$.

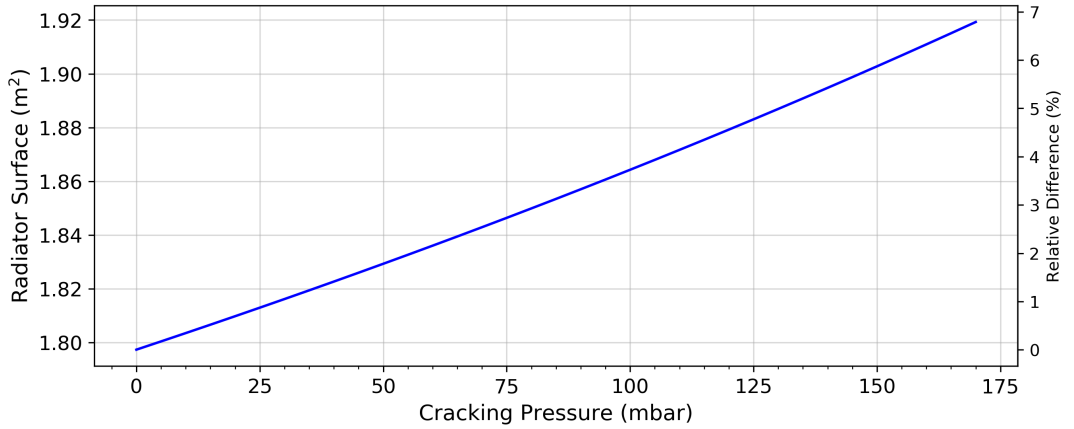


(b) Radiator surface increase as a function of the check-valve cracking pressure while keeping a constant cooling power of 1.65 W.

Figure 6.16: Cracking pressure impact analysis.

The cracking pressure measurements on check-valve #1 indicated a promising cracking pressure below 40 mbar and also allowed a large flow rate (at least 2 $L\,min^{-1}$) in the forward direction. Unfortunately, in the reverse direction, the results were not reproducible, as the valve is closing at much higher pressures, between 1 bar to 2 bar, making it not suitable for the target application. The other candidate, even though the manufacturer claims a cracking pressure 140 mbar, our measurements showed a cracking pressure between 50 mbar to 100 mbar. In the reverse direction, neither did the mass-flow meter measured anything nor the water showed bubble formation, corresponding to a leak rate in reverse direction less than 1 $mL\,min^{-1}$, equivalent to $1.7 \times 10^{-2}\,mbar\,L\,s^{-1}$.

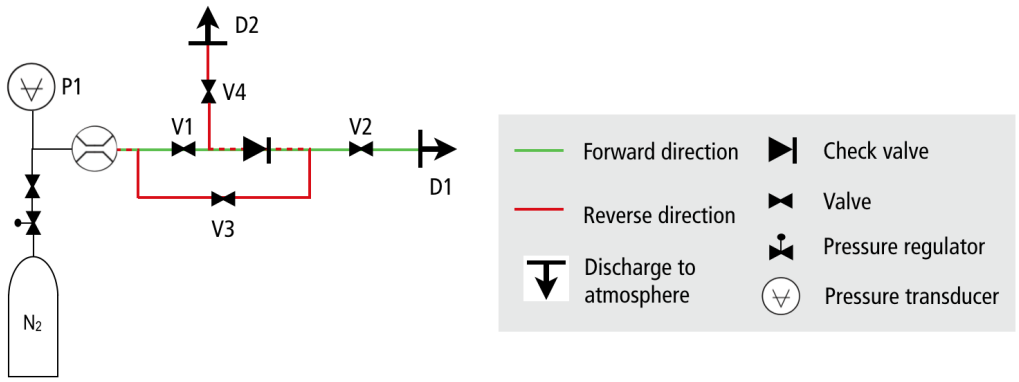


Figure 6.17: Check-valve test set-up for cracking pressure measurement and leak tightness verification.

Let us mention that at low flow rate discharge, audible vibrations were detected. This is a known issue occurring when a small flow cannot push the poppet of the check-valve to a fully open position. The solution found for this problem and experimentally verified is to bend the central poppet disk about 0.58 mm [17]. However, at the moment, the valves remains unchanged. Another concern with the check-valves is their leak tightness at low temperatures. Check-valve #2 has an o-ring sealing of Buna-N with a with a lower temperature limit of −40 °C (233 K). Therefore, it was tested at low temperatures in the reverse direction with a high pressure differential. Figure 6.18 shows the obtained volumetric flow rate as a function of the check-valve temperature.

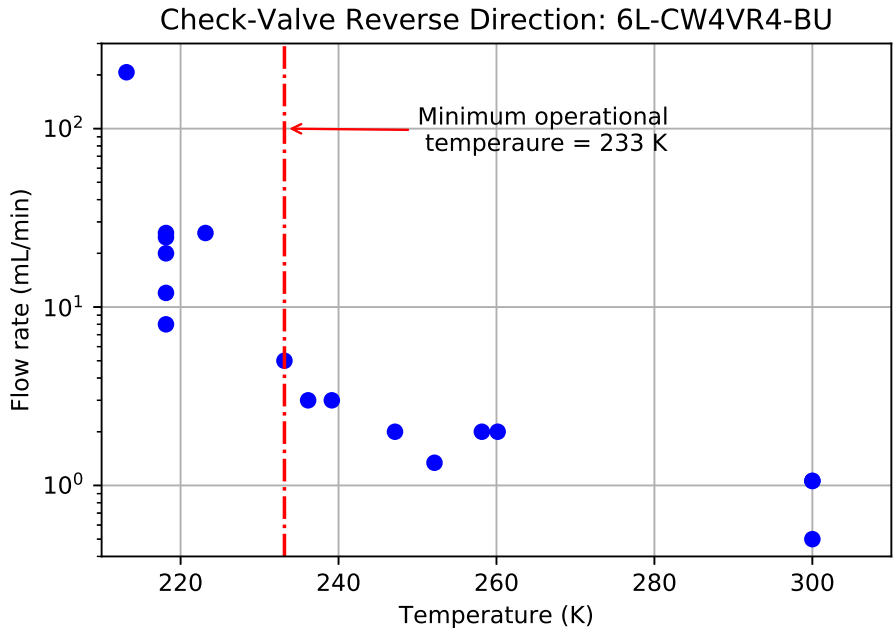


Figure 6.18: Reverse direction check-valve leakage at low temperatures.

Inspecting Figure 6.18, for temperatures approximately lower than 250 K, the flow rate is higher than 2 mL min$^{-1}$. The targeted mass-flow rate being around 519 mL min$^{-1}$ (10.81 mg s$^{-1}$), 2 mL min$^{-1}$ would correspond to a quite small degradation (0.4%) and then was considered as acceptable. However, it is also visible that for a temperature lower to the limit given by the manufacturer, the leakage increases very quickly.

Therefore, to avoid malfunctions with these check-valves, it was decided to operate them at a temperature higher than 260 K. A dedicated aluminum interface loosely coupled to the cooling plate and with temperature control was used to maintain the check-valves above this temperature limit, as shown on the following chapter (Figure 7.12).

Besides this thermal test, check-valve #2 underwent a series of vibrational testings to verify its mechanical reliability and capability to survive a launch. The check-valve was mounted in a shaker, at AST facilities, in two different positions, as displayed in Figure 6.19. The tests consisted of a sine qualification with an acceleration of 25 g in the frequency range of 25 Hz to 100 Hz followed by a random qualification test (20 Hz to 2000 Hz).

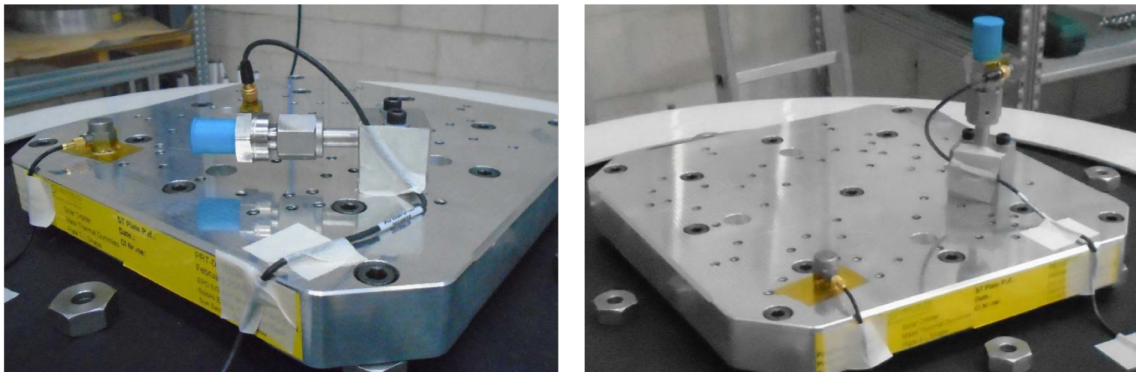

Figure 6.19: Check-valve ready for the vibrational test in different orientations.

After the vibrational tests, leak test and cracking pressure measurements were carried out again. The valve continued to operate correctly and within the previously obtained values. Leak-rate in reverse direction remained below 1 mL min$^{-1}$ at room temperature, less than 0.2% of the targeted mass-flow rate.

CHAPTER 7

# Single-Cell Functional Characterization

This chapter presents the functional characterization of the filled sorption cell. It includes an adsorption capacity measurement within the expected working pressure/temperature range. The most important outcome of this test is to measure the gas quantity available for circulation during an actual compression cycle. Afterwards, the temperature dynamics of the sorption cell is tested, thus, how long it takes to cool down to the lowest temperature and also how much heat input is needed to warm up the cell. The outcome of this test defines the cycle period of the compressor and, consequently, the mass-flow rate that can be delivered to the JT cold stage. After collecting this data, this fully characterized sorption cell was coupled to the nitrogen JT stage and a complete adsorption-compression cycle was performed and showing, despite the limitations, the functionality of the whole system.

For reasons mentioned earlier in Section 6.1.3, it was not possible to obtain an operational GGHS using hydrogen with the required interface for the sorption cell, so, this heat switch was instead sealed with nitrogen and integrated with a sorb pump of activated charcoal. As expected, this deeply impacts the dynamics of the sorption cell, since the thermal conductance of the GGHS was reduced by a factor of seven (considering the thermal conductivities of both hydrogen and nitrogen).

The optimum parameters shown in Table 4.4 were determined considering a thermal conductance between the sorption cells and the heat-sink of the same order of magnitude as the developed hydrogen GGHS (>0.8 $W K^{-1}$), which according to our calculations, turns it possible to cycle the SC between 165 K to 360 K with a heat-sink (main radiator) temperature of 158 K and a cycle period of 262 min. However, such parameters combination is not possible using a nitrogen GGHS, as it would greatly increase the cycle period of the compressor and, thus, not providing the required mass flow rate to obtain 1.5 W at 80 K. So, in order to demonstrate the operation of the single

sorption compressor cell using the nitrogen GGHS while keeping the same working temperature range of the sorption compressor (165 K to 360 K) and without increasing too much the cycle period, the cold plate temperature may be reduced down to ≈ 117 K to increase the temperature difference between the sorption cell and the heat-sink and, then, compensating the lower thermal conductance of the nitrogen GGHS. As visible in Figure 7.1, by reducing the heat-sink temperature and using the nitrogen GGHS we can still manage to obtain a similar temperature profile as the one using hydrogen (Figure 4.17).

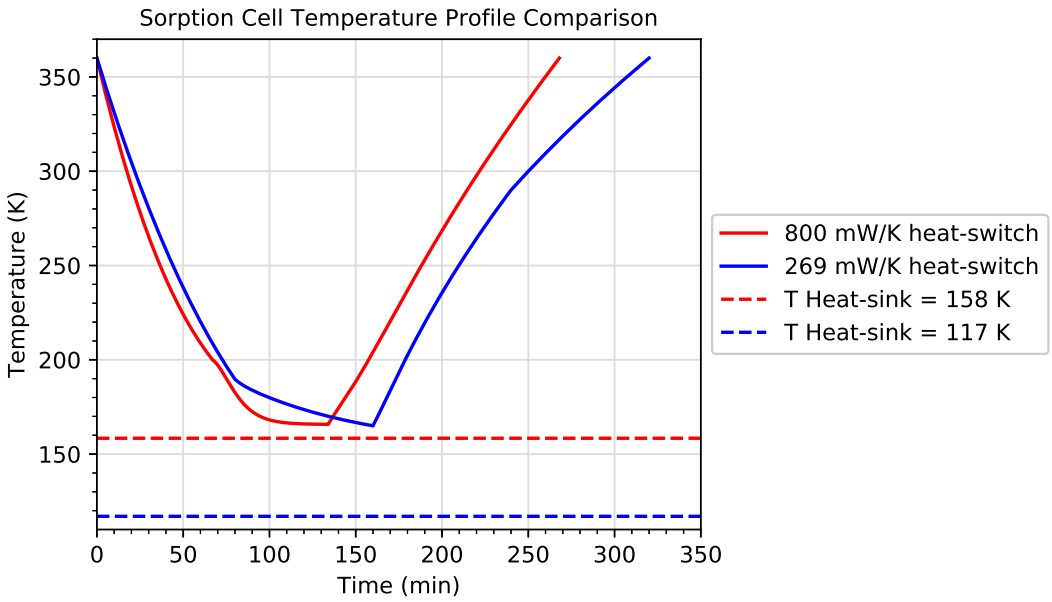


Figure 7.1: Sorption cell temperature profile comparison: the red curve represents the obtained temperature profile using a 800 mW K$^{-1}$ GGHS and with a heat-sink temperature of 158 K, cycle period of 262 min; the blue curve represents the profile using a 269 mW K$^{-1}$ GGHS (equivalent to the measured ON state shown in Figure 6.9) and with a heat-sink temperature of 117 K, cycle period of 320 min (22% increase).

## 7.1 Adsorption Capacity Measurement

The adsorption measurements of the filled sorption cell makes use of the same experimental set-up and methods previously described in Section 4.3. The adsorption copper cell was removed and substituted by the spherical sorption cell including its instrumentation (heater and thermocouples). Similar as before, the sorption cell was insulated with styrofoam and glass wool, before submerging into the liquid nitrogen bath. Then, the nitrogen adsorption equilibrium was measured in the temperature range of 130 K to 380 K and pressure range of 1 bar to 45 bar, as displayed in the left side of Figure 7.2.

The right side of Figure 7.2, shows a comparison between the obtained results from the spherical sorption cell and the ones previously obtained in Figure 4.9 (small copper cell). Let us note that this comparison only accounts the adsorbed gas (void volumes are not considered). As visible in this figure, there is a strong correlation between both data sets: Pearson correlation coefficient[1], $r_{xy}$, is 0.995, which indicates a very strong correlation between the two data sets. Therefore, the MOF properties are in line with the previous characterization, showing the same adsorption capability, despite the rather long time that the MOF stayed in contact with air and moisture without pumping during the filling procedure. So, this result shows a relatively good stability and reversibility of this MOF compound.

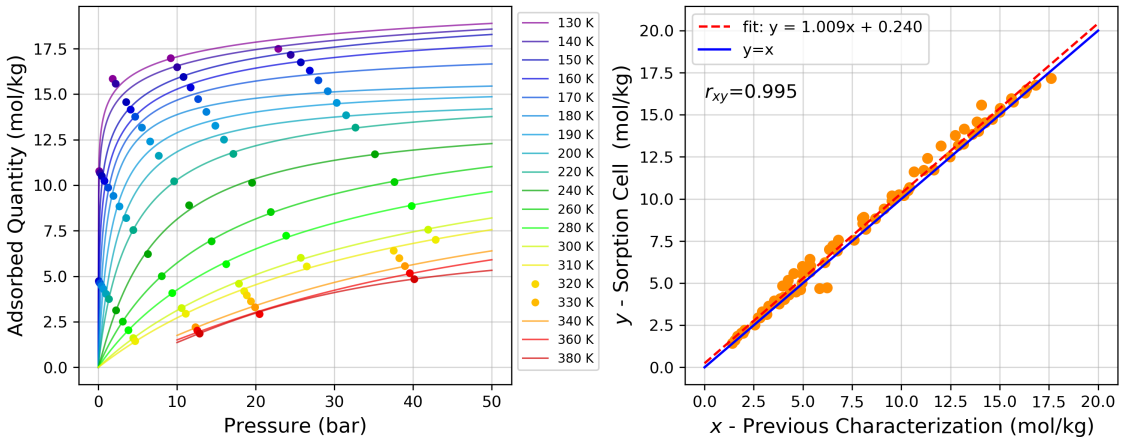


Figure 7.2: Left side: sorption cell adsorption isotherms of nitrogen on HKUST-1 which only accounts for the gas at the adsorbed phase; Right side: adsorbed quantity comparison/correlation with previous results from Figure 4.9.

Actually, considering the working principle of a sorption compressor, it is more convenient to plot the obtained isotherms data of Figure 7.2 in terms of total gas quantity. As a matter of fact, the void volume of the installed cell is not negligible ($\epsilon = 57\%$) and it deeply affects the gas quantity available for circulation. So, the total gas quantity is plotted versus the pressure, displayed in Figure 7.3.

According to the optimum working parameters from Table 4.4, it was expected a quantity of $\Delta n = 1.67$ mol to be released or adsorbed during a compression cycle. However, as the void fraction of this sorption cell was greater than expected, due to the difficulties during filling, $\Delta n$ reduces to 1.4 mol, if $T_{MAX} = 360$ K.

[1] Pearson's correlation coefficient is a statistical measure of the strength of a linear relationship between paired data. A perfect correlation corresponds to $r_{xy} = \pm 1$

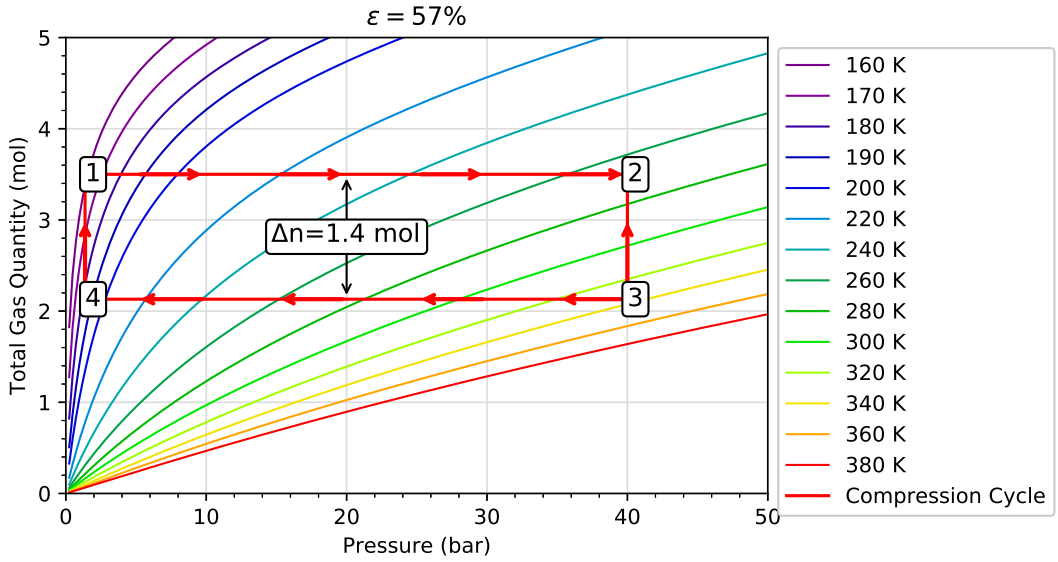


Figure 7.3: Total adsorbed gas quantity as a function of pressure considering a void fraction of $\epsilon = 57\%$, the red rectangle corresponds to a compression cycle operating in the temperature range of 165 K to 360 K.

## 7.2 Sorption Cell Dynamics

The sorption cell dynamics has the objective to measure the cooling and heating temporal profile of the filled sorption cell under temperature and pressure conditions close to the optimum values. Thanks to such a study, it will be possible to determine the cycle period of the cell and, hence, estimate the mass-flow rate that can be delivered/adsorbed by this sorption cell to operate the JT cold stage.

Figure 7.4 shows the experimental set-up for this characterization and the various thermometers placed on the sorption cell. The sorption cell is assembled on the cooling plate of the cryostat and it is connected to a gas manifold, placed outside at room temperature, for pressure measurement and gas management (purge, filling). The calibrated volume, $V_{cal}$, of roughly 1.1 L was needed to charge up the system with a known gas quantity before starting the measurements.

To verify both adsorption behavior and dynamics of the cell, the following test procedure is performed:

1. Warm up the sorption cell to a temperature slightly above room temperature (up to 400 K);
2. Pump down the cell through the gas manifold to remove unwanted moisture at the system (<1 h) while keeping it at high temperature;
3. Let the cell cool-down again to room temperature;
4. With valve $V_e$ closed, pump and purge the gas manifold and fill the calibrated volume with a known quantity of nitrogen through the gas cylinder;

5. After temperature and pressure stabilization of $V_{cal}$, the charged gas quantity into $V_{cal}$ is calculated.
6. Open valve $V_e$ and wait for both temperature and pressure stabilization of the system (sorption cell and calibrated volume);
7. Initiate the liquid nitrogen flow of the cooling plate by setting a low temperature set-point ($T$ = 120 K) and let the sorption cell cool-down begin (keeping GGHS ON), while recording its temperature and pressure;
8. The test ends either by reaching the targeted temperature (≈160 K) or a low-pressure of 1.37 bar;

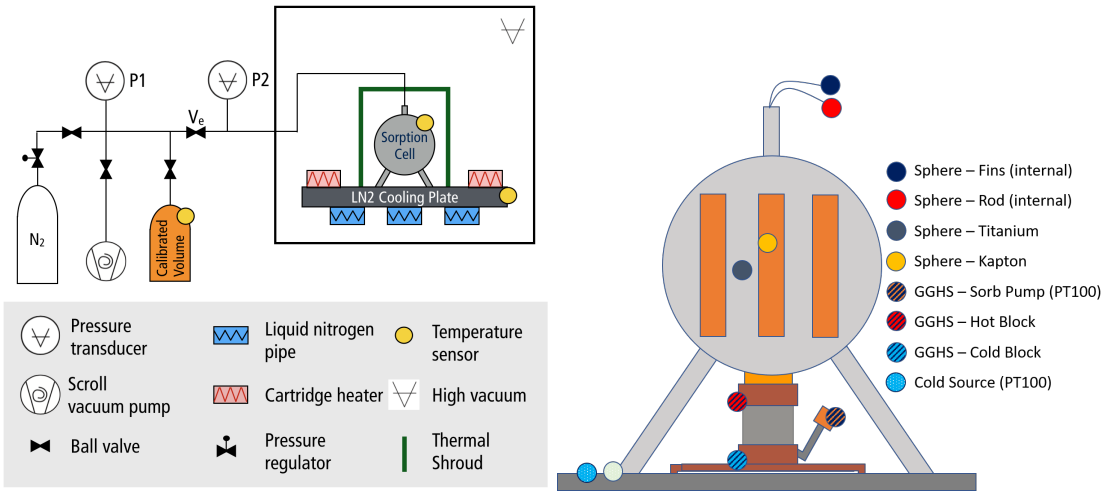


(a) (b)

Figure 7.4: a) Experimental set-up for the sorption dynamics test; b) Thermometers location.

The first cool-down of the cell was targeted to achieve a low-pressure of 1.37 bar at a temperature close to 160 K. So, for that to happen, the calibrated volume was loaded with an amount of 3.7 mol to achieve such equilibrium at low temperature. Figure 7.5 shows the obtained results of the first cool-down: Plot a) shows the obtained temperature profile and the first thing that jumps out is its rather large cooling time needed to reach the lowest temperature of 148 K, around 6 h were needed just to cool-down the cell; Plot b) shows the pressure profile ($P2$) during the cool-down showed in plot a). During this period, the calibrated volume had a pressure decrease of 34.4 bar which corresponds to the gas quantity, $\Delta n$, that has left the volume towards the sorption cell and remained there in both adsorbed phase and gaseous form. $\Delta n$ is estimated by applying a mass balance to the calibrated volume ($V_{cal}$ = 1.1 L) as follows,

$$\Delta n = V_{cal}(\rho_A - \rho_B) \tag{7.1}$$

where the subscripts $A$ and $B$ correspond to the beginning and end of the cooling procedure, respectively. Using Equation (7.1), we found this quantity $\Delta n$ to be 1.7 mol.

Still referring to Figure 7.5, plots b) and c) shows some red-filled circles which correspond to the measured temperatures during the same period, that allows to obtain the total quantity in the cell during the cool-down, between instants $A$ and $B$, as displayed in plot c). If we consider instant $A$ as stable and at equilibrium, the total adsorbed quantity at the sorption cell is $n_{c,A} = 2.8\,\text{mol}$. Whereas, the final state $B$, after cooling, is found by accounting the gas quantity that has left the calibrated volume through $n_{c,B} = n_{c,A} + \Delta n = 4.5\,\text{mol}$ and is visible that by using the measured quantity $\Delta n$ from Equation (7.1), the state B precisely falls in the isotherm of 150 K which roughly corresponds to the measured temperature (148 K) at that instant. The same is valid for the the state corresponding to the 160 K isotherm.

On the other hand, as visible in plot c), the other pressure-temperature states (red circles) are slightly away from its corresponding isotherms. This can be ascribed to a thermal inhomogeneity of the cell, which was found to be $\approx 10\,\text{K}$ by inspecting the deviation between the measured pressure/temperature and its correspondent isotherm. If we assume that adsorption has not achieved equilibrium for each of the considered pairs of pressure/temperature during cool-down and by comparing with the isotherms showed in plot c), each considered state (red circle) would actually corresponds to an higher temperature than measured, thus, less adsorbed quantity, albeit the measured temperatures were lower. Therefore, it is quite likely that some regions of the cell are at higher temperatures than others and, so, a higher pressure was measured, since less gas is adsorbed. This behavior would also be expected if the cooling rate was faster than the adsorption dynamics, but, according to this experiment, this does not seem the case, since the cooling time was very long.

Another dynamics test was performed: it consists in a complete cycle between 160 K and 330 K which allowed us to obtain the amount of gas delivered by the sorption cell during the releasing phase and also the adsorbed gas during the adsorption phase. In such a test, it was obtained the heating profile of the sorption cell, while keeping the GGHS OFF, and was also simulated the release of gas from the cell towards the calibrated volume, while a constant high pressure of 40 bar was maintained during this procedure. As soon as all possible nitrogen gas was released from the cell, it was cooled down again to low temperatures and, similarly, it was simulated an adsorption phase as soon as a low pressure of 1.37 bar was reached during cool-down. Figure 7.6 shows such this procedure and note that according to the experimental setup displayed Figure 7.4a the check-valves were not used in this procedure. So, valve $V_e$ was manually opened and closed in order to start the adsorption and releasing phases.

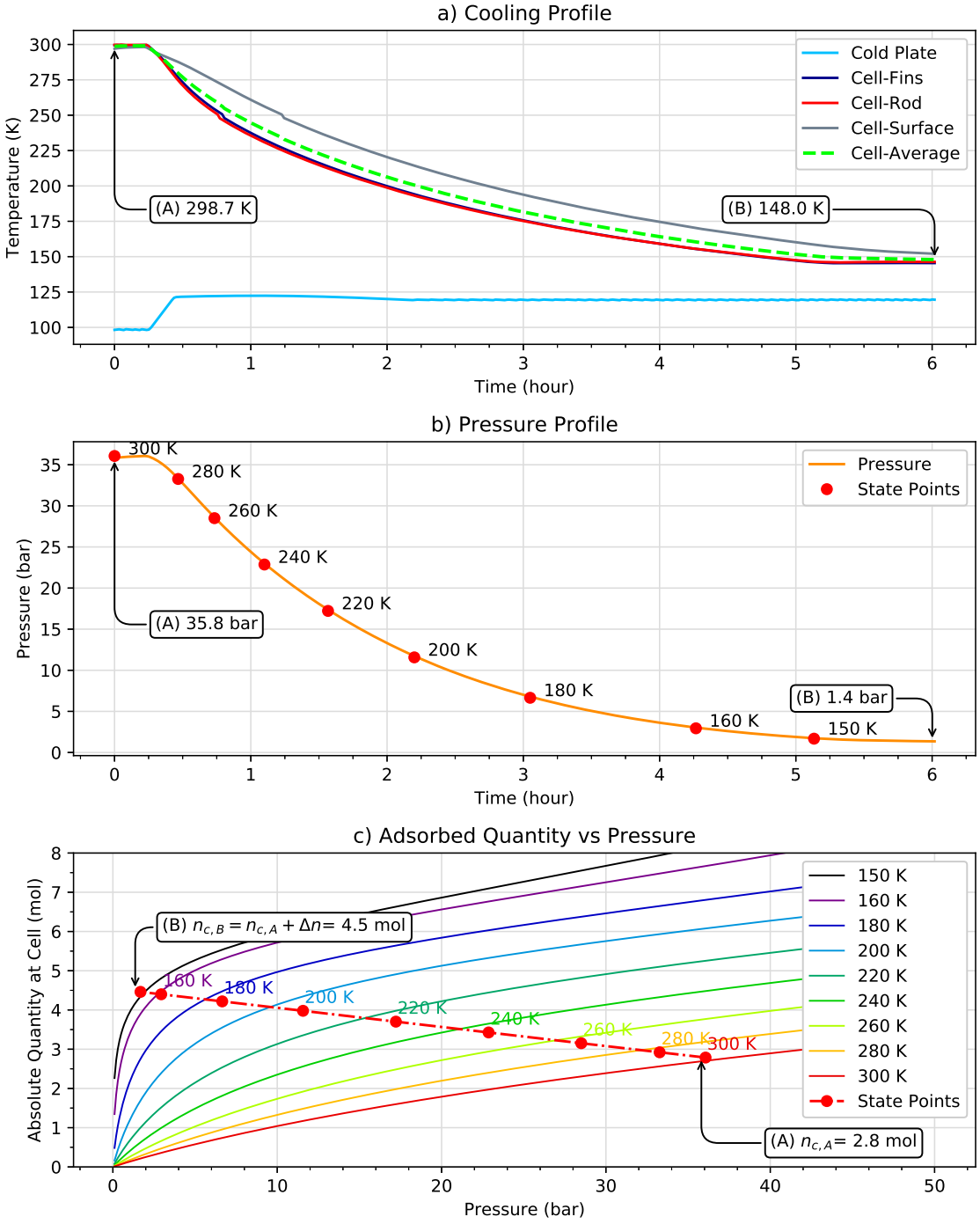


Figure 7.5: First sorption cell cool-down from room temperature down to 150 K. During this cool-down, the calibrated volume pressure decreases from 35.8 bar to 1.4 bar, which corresponds to a quantity of 1.7 mol leaving the calibrated volume. The cell-average temperature (dashed-line) corresponds to the average temperature from the sensors placed in the CuHX rod, fins and the titanium surface of the cell.

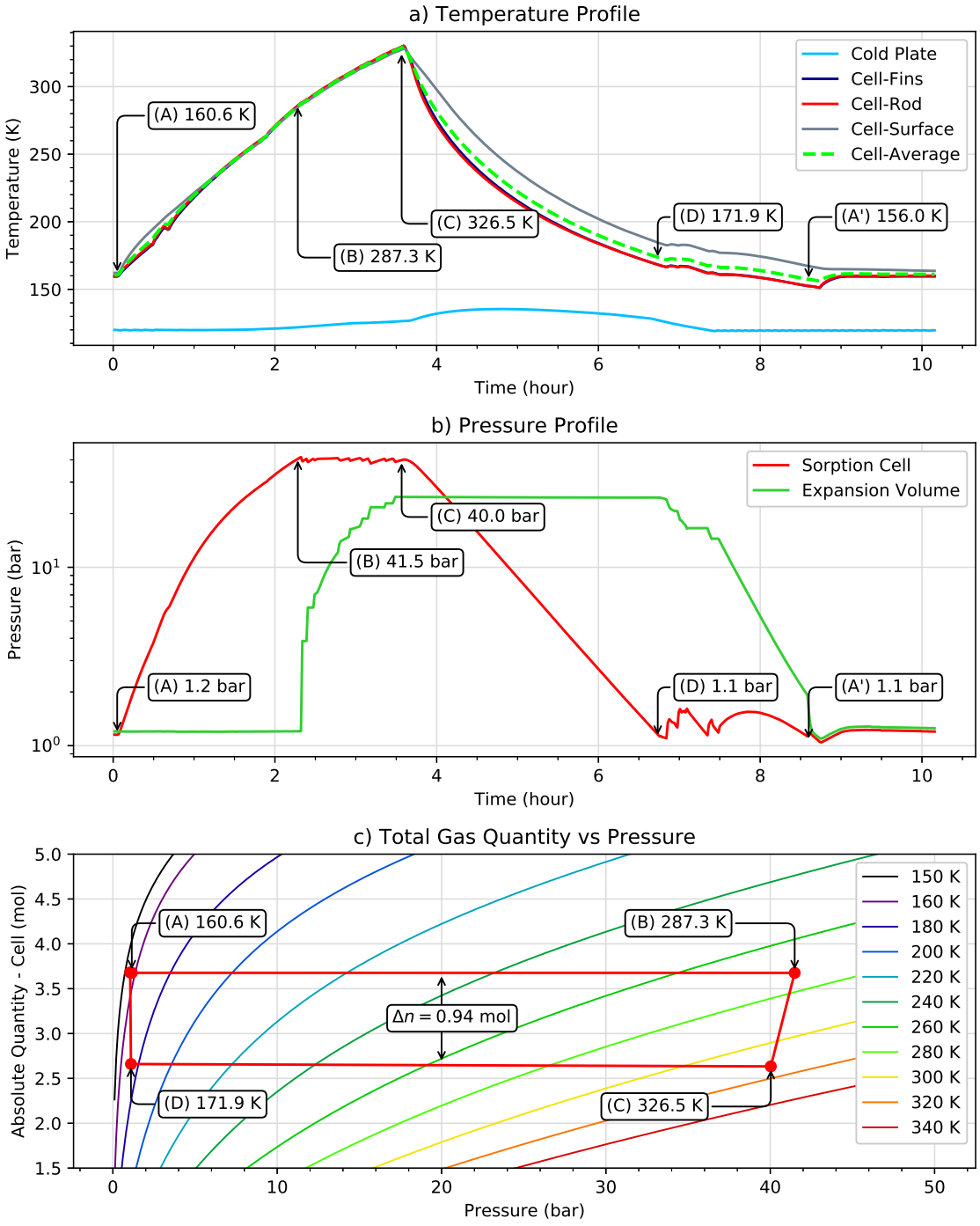


Figure 7.6: Complete sorption cell temperature cycle between 160 K and 330 K.

From instants $A$ to $B$, a heating power of 19 W was applied on the previously charged cell at 160 K. This warming corresponds to the so called heating phase. In this period, the valve $V_e$ was kept closed and the pressure increased inside the cell, since the adsorbed gas is being released from the sorbent bed and remained in the closed volume of the cell. As displayed in Figure 7.3, from $1 \rightarrow 2$, this heating phase occurs at constant quantity.

The instant $B$ corresponds to the moment when the internal pressure of the cell reaches 40 bar. Then, in this instant, valve $V_e$ was carefully opened to let the nitrogen gas escape from the sorption cell and charge the calibrated volume, while the cell's pressure was maintained, as far as possible, close to 40 bar. This releasing phase continues up to 327 K and, as a matter of fact, due to the fragility of the heaters, we chose this maximum temperature to prevent some burning or short-circuit.

During the releasing phase, the calibrated volume pressure has roughly increased by 24 bar (1 mol), as visible in Figure 7.6 (green line, plot b), and about 27 W were needed to heat the sorption cell. This heating power is higher compared to the 19 W needed during the heating phase (from $A$ to $B$). Actually, during this phase, it is necessary to deliver, beyond the sensible heat to increase the temperature of the system, the latent heat of adsorption to desorb the gas from the MOF surface.

At instant $C$, it was no longer possible to maintain a stable pressure of 40 bar and, so, the regeneration process must start: $V_e$ was manually closed and the cell was cooled at constant gas quantity. The temperature dropped from 327 K to 172 K and reached instant $D$ when the pressure of the cell was roughly 1 bar. Similarly to the releasing phase, at instant $D$, valve $V_e$ was carefully opened while maintaining the pressure below $\approx 1.5$ bar and letting the nitrogen gas flow from the calibrated volume to be adsorbed by the cooled sorption cell. The cycle was completed when it was no longer able to maintain a stable low-pressure in the pipeline. If everything went as expected, during this phase, the calibrated volume should have released the same amount that was previously released by the sorption cell, and that was precisely what happened since the pressure in the calibrated volume has decreased 24 bar (Figure 7.6, plot b). The thermal characteristics of this point $A'$ are very close of these corresponding to the point $A$ (starting point of the cycle).

Summarizing, a complete cycle was successfully performed, despite some thermal inhomogeneity and a rather long cycle length. The measurements from the calibrated volume confirmed that the same quantity of gas released by the cell was afterwards absorbed just by controlling the temperature of the sorption cell. This test also showed that the sorption cell is working coherently, considering its adsorptive capacity, showed in Figures 7.3 and 7.6. Furthermore, by considering the temperatures at instants $A$ and $C$ as stable, the expected gas quantity to be released or adsorbed by this sorption cell is

0.94 mol, which is close to both measured released and adsorbed quantities calculated through the pressure variation of the calibrated volume. Table 7.3 summarizes the obtained results from this complete compression cycle.

Table 7.1: Summary of the first complete sorption cell cycle temperature and power requirements.

| Phase | Temperature Range | Duration (min) | $\Delta n$ (mol) | Power (W) |
|---|---|---|---|---|
| Heating ($A$ to $B$) | 160.6 K to 287.3 K | 2 h:16 min | const | 19 |
| Releasing ($B$ to $C$) | 287.3 K to 326.5 K | 1 h:18 min | −1.04 mol | 27 |
| Cooling ($C$ to $D$) | 326.5 K to 171.9 K | 3 h:13 min | const | 0 |
| Adsorbing ($D$ to $A$) | 171.9 K to 156.0 K | 1 h:54 min | +1.02 mol | 0 |
| Total | 160.6 K to 326.5 K | 8 h:41 min | – | 46 W |

In a first attempt to understand the unexpected long period of both cooling and heating, the thermal conductance of the existent elements between the sorption cell and the cooling plate were measured, approximately, at 120 K, by applying a constant heating power (up to 6 W) and measuring the temperature difference across each element. The values obtained from this test are shown in Table 7.2, these results will be discussed later after a more detailed thermal analysis. Let us note, however, that the thermal conductances are close to expected, except for the OFF state of the GGHS which is almost three times higher than expected. Regarding the shrink-fitting coupling, due to its imperfect penetration, only 44% of the nominal thermal conductance was expected. However, the measured value was found to be even lower, only 11% of the nominal value.

Table 7.2: Measured thermal conductance/resistance values of the different elements between the sorption cell and the heat-sink.

| Element | Measured | Expected |
|---|---|---|
| Shrink-fit | 1.1 $WK^{-1}$ | 10 $WK^{-1}$ |
| GGHS-ON | 329 $mWK^{-1}$ | 269 $mWK^{-1}$ |
| GGHS-OFF | 29 $mWK^{-1}$ | 9.5 $mWK^{-1}$ |
| Cu interface | 433 $mWK^{-1}$ | 441 $mWK^{-1}$ |

Figure 7.7a) shows the temperature variation in the different points along the thermal path between the sorption cell and the cooling plate during the measurements shown in Figure 7.6. Despite being obtained in a non-equilibrium state, this temperature profile allows a more detailed thermal analysis. For instance, by assuming the copper interface conductance as constant during the whole experiment and equal to

433 mWK$^{-1}$ (Table 7.2), this interface can be used to determine the heat flux along this thermal path, supposing that this heat flux remains constant along this path. Then, by using the temperature difference of each component, their thermal conductances can be calculated. These results are displayed in Figure 7.7b).

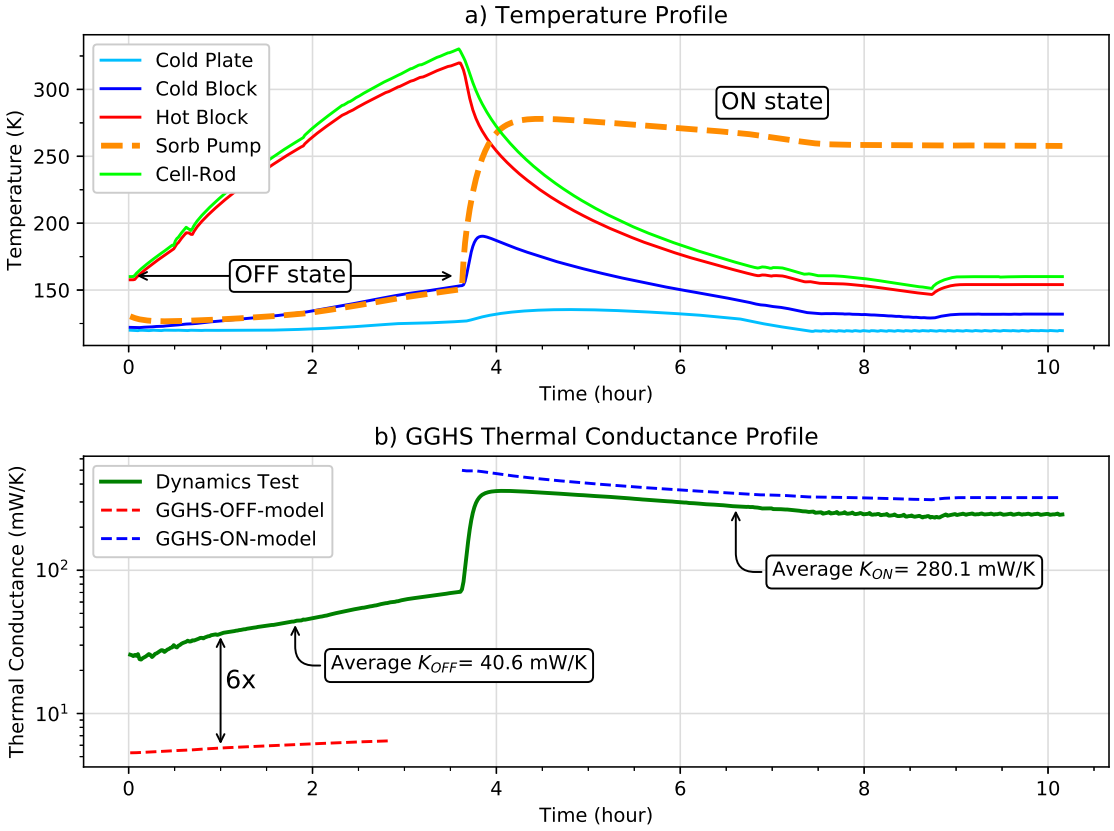


Figure 7.7: Gas-gap heat switch temperature profile and estimated thermal conductance over a complete temperature cycle. The copper interface was used as a heat flux meter to determine the GGHS thermal conductance.

As previously measured in static mode (Table 7.2) and shown in Figure 7.7, the OFF state of the GGHS is indeed very degraded. During the first 4 h, the GGHS was kept in the OFF state and the calculated conductance from this analysis was, in average, 41 mWK$^{-1}$, which is almost six times worse than expected (9.5 mWK$^{-1}$, Figure 6.9). Before switching to the ON state at ≈ 3.5 h, the OFF conductance reached an OFF-value of 68 mWK$^{-1}$, this value is quite high, particularly, when the cell was at the highest temperature of the cycle.

Let us also note that during the first 4 h, the sorb pump temperature rose from 120 K to 150 K, probably due to some parasitical heat coming from the hot sorption cell, but looking to the results of Figure 6.9 this does not seem sufficient to explain the obtained OFF values of the GGHS. The GGHS operating in such condition, will require more heating power to heat up the sorption cell. It is also visible that after switching the

GGHS to the ON state, the cold plate temperature increased. This is an indication that the heat load reaching the cooling plate is greater than its cooling power. In conclusion, a malfunction of the GGHS can partially explain the long period of the cycle.

So, to a better understanding of the obtained dynamics, a simple transient model was developed: it considers the sorption cell temperature as homogeneous, albeit a 10 K temperature gradient within the cell was roughly estimated from Figure 7.5, a total mass of 1.1 kg, and it assumes that the cell it is connected to the heat-sink via a thermal path that consists of the shrink-fit, the GGHS and the copper interface (Figure 6.15). The time variation of the sorption cell, $T_i(t)$, can be iteratively obtained through the following heat balance equation applied to such system,

$$-K_T(T_i - T_{CP}) + P + L\frac{\mathrm{d}n}{\mathrm{d}t} - \dot{Q}_{\mathrm{rad}} \pm \dot{Q}_{\mathrm{par}} = \frac{T_{i+1} - T_i}{\Delta t}\sum_{j=1}^{n=3}\left(m_j c_{p_j}(T_i)\right) \tag{7.2}$$

where $K_T$ is the global conductance, schematically represented in Figure 6.15 as a set of thermal resistances arranged in series and parallel; $P$ is the applied electrical input power to warm up the cell; $T_i$ is the sorption cell temperature at instant $i$; $T_{CP}$ is the cold plate temperature; $L$ is the heat of adsorption; $\dot{Q}_{\mathrm{rad}}$ is the radiative heat transfer between the surface of the cell and the environment; $\dot{Q}_{\mathrm{par}}$ is the parasitical heat; $\mathrm{d}n/\mathrm{d}t$ is the molar flow rate ($\mathrm{d}n < 0$ for desorption and $\mathrm{d}n > 0$ for adsorption); $m_j$ is the mass of each element $j$ of the cell (copper, titanium, HKUST-1) and $c_{p_j}$ is the specific heat of each element $j$ using the values for titanium and copper from [79] and HKUST-1 from [80].

Figure 7.8 shows some studied scenarios to explain the very slow dynamics obtained in the four phases of the compression cycle (solid lines) by changing some variables of Equation (7.2). In these figures, for sake of clarity, each phase starts at $t = 0$ and the chosen parameters for each scenario (dashed lines) are indicated in Table 7.3.

According to the optimal values, each phase of the compression cycle is expected to have a duration close to 67 min, as shown in Figure 4.17. However, by inspecting the scenario zero, calculated using the nominal values (dashed lines), one may conclude that it is not comparable with the experimental results (solid lines).

The first scenario corresponds to a heat-switch thermal conductance degradation according to the obtained results shown in Figure 7.7. It is visible that by making this adjustment, both heating and releasing phases are slightly closer to the measurements, although it is not enough to match with the obtained results. Note that the cooling and adsorbing phases remain virtually unchanged after the reduction of the global ON conductance from 164 $\mathrm{mWK}^{-1}$ to 147 $\mathrm{mWK}^{-1}$.

In a attempt to explain, in particular, the cooling and adsorbing phases, the second scenario corresponds to a further degradation of the heat-switch ON state conductance,

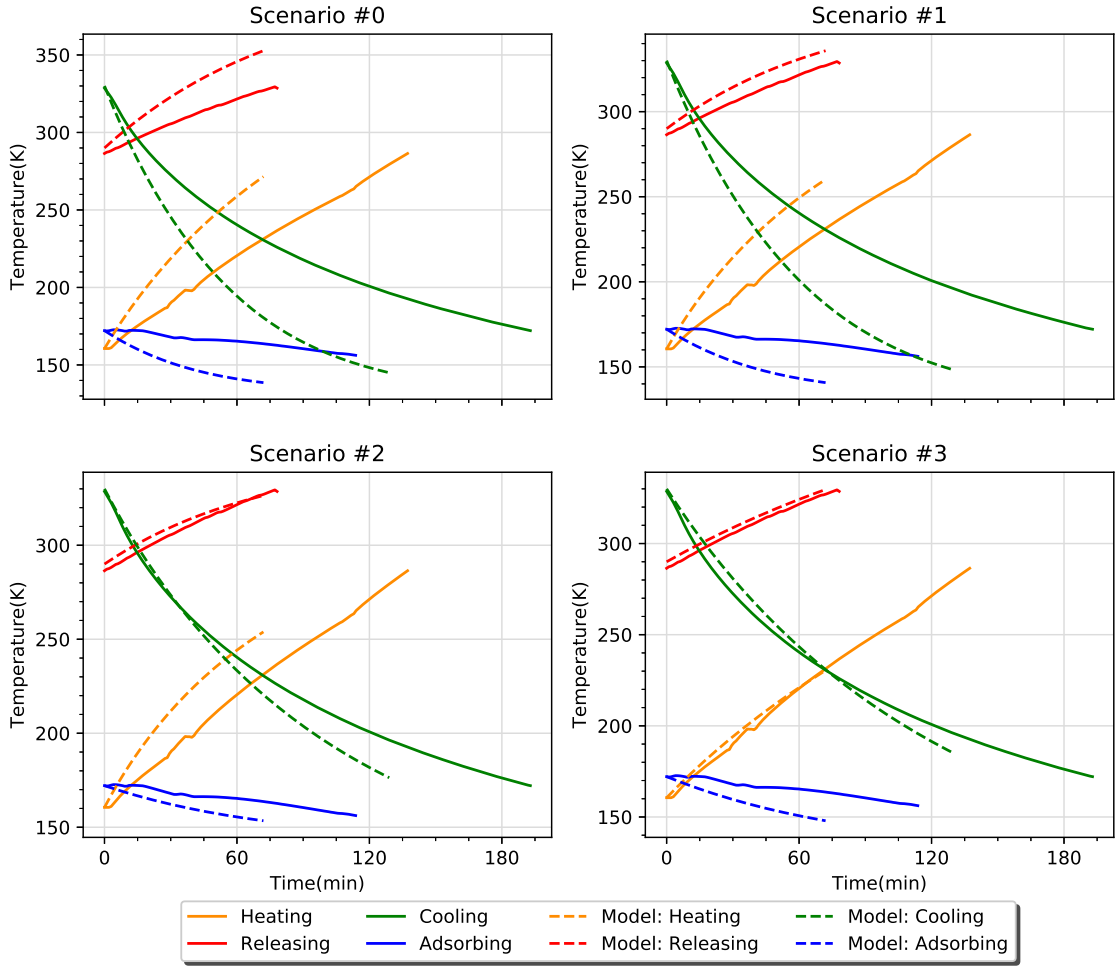


Figure 7.8: Thermal model correlation with the obtained dynamics results coming from Figure 7.6.

Table 7.3: Sorption cell thermal model parameters. All scenarios include the same radiative heat transfer between the cell and the copper thermal shroud surrounding the cell. Emissivities of 0.5 and 0.2 were considered for the titanium surface of cell and the copper surface of the shroud, respectively.

| **Parameter** | **Scenario #0** | **Scenario #1** | **Scenario #2** | **Scenario #3** |
|---|---|---|---|---|
| $K_T$(ON) | 164 mWK$^{-1}$ | 147 mWK$^{-1}$ | 90 mWK$^{-1}$ | 164 mWK$^{-1}$ |
| $K_T$(OFF) | 33 mWK$^{-1}$ | 65 mWK$^{-1}$ | 65 mWK$^{-1}$ | 33 mWK$^{-1}$ |
| Copper's mass | | 380 g | | 1.9 × 380 g |
| Ti4Al6V's mass | | 370 g | | 1.9 × 370 g |
| HKUST-1's mass | | 376 g | | 1.9 × 376 g |

down to 90 $mWK^{-1}$, albeit we do not have measured such value. After making this adjustment, the cooling and adsorbing phases are closer to the measured values, however, still not enough to match the results. Anyway, it seems to be certain that such slow dynamics is most likely related with the GGHS poor performance. A gas contamination (non-adsorbable gases) in the GGHS or a poor performance of the sorb pump (unable to reach low-pressure) would explain such behavior.

Unknown parasitical heat sources (e.g. wiring, tubes) were considered in this study (not shown). However, we have concluded that they cannot simultaneously explain both slow heating and slow cooling since they would have the same signal (i.e. heat into or out of the cell) over the compression cycle. For instance, the various wires connecting the cell and the acquisition equipment at room temperature during a full compression cycle will correspond to a heat leak into the cell (i.e. additional heat to be removed), so, slowing down the cooling dynamics, but assisting in the heating phases, therefore, never explaining simultaneously both slow heating and slow cooling. Regarding the temperature inhomogeneity of the cell, this would lead to a faster temperature dynamics since some regions of the cell would be loosely coupled and we would have detected a delay between the temperature and the equilibrium pressure.

Actually, the best fit corresponds to the third scenario which was obtained by multiplying the heat capacity by a factor of $\approx 2$ on each component of the cell (copper, titanium and HKUST-1). However, this value is not at all compatible with the literature data, but it can indicate what type of parasitical heat source should be investigated to fully understand the obtained results.

## 7.3 Compression Cycle Test

After the adsorption characterization and the thermal dynamics study, the sorption cell was coupled to the JT stage to perform a full compression cycle test. This test has the objective to demonstrate the operation of the built JT cooler powered by this sorption cell, unfortunately, with some experimental limitations. The most important is that only one cell is installed, preventing a continuous operation; the second one being that, due to the slow thermal dynamic, the gas flow is substantially reduced, leading to a cooling power reduction in the same proportion. In this section, we will describe in detail the found solution to overcome these limitations and to show that the cooler is still able to operate under these conditions.

The previous dynamics study showed that is not possible to perform the temperature cycle with the expected rate (67 min for each phase), therefore, by joining this sorption cell to the JT cooler, it will not be possible to obtain the targeted cooling power

at 80 K. However, by taking into account the obtained dynamics of this sorption cell and the available gas quantity for circulation, it can be estimated the mass-flow rate that can be provided to the JT stage and make the required adjustments to demonstrate the JT cooler operation powered by this sorption cell.

As previously mentioned in Section 7.2, the cooling and adsorption phases were significantly slower than both heating and releasing phases, in average, a heating rate of 0.50 $\mathrm{K\,min^{-1}}$ and a cooling rate of $-0.14\,\mathrm{K\,min^{-1}}$ were obtained. Considering these rates, the mass flow rate that can be provided or adsorbed by this sorption cell is estimated and shown in Figure 7.9a. Note that by joining this sorption cell to the JT stage, it is important that the mass flow rate provided or adsorbed by the cell matches the discharge rate of the orifice. If such condition is not met, this cell will not be able to maintain the high and low pressures lines within the expected levels and the cooling power will be reduced.

By inspection of Figure 7.9a and considering the obtained heating and cooling rate of the dynamics study, this cell is only able to provide a discharge rate, during the releasing phase, of 6 $\mathrm{mg\,s^{-1}}$ and, during the adsorbing phase, lower than 2 $\mathrm{mg\,s^{-1}}$. Both rates are lower than that obtained with the 14 µm orifice (10 $\mathrm{mg\,s^{-1}}$). So, to overcome this limitation, one solution would require to replace this orifice, while keeping the targeted upstream conditions of the JT expansion.

Figure 7.9b shows the mass flow of rate using the nominal upstream conditions ($P_H = 40$ bar, $T = 99.8$ K) as a function of the orifice diameter. It is visible that an orifice of roughly 10 µm is needed to match the heating rate, whereas 6 µm is needed for the cooling rate. As the two rates are different, therefore, they require different orifices, which turns out this problem even more complex. In addition, ordering a new orifice has a considerable lead time and would require a new qualification campaign before being integrated into the system.

Another solution is to maintain the 14 µm orifice and reduce the high pressure in such way that the discharge rate condition is met. From Figure 7.9a, the heating rate of the installed sorption cell allows to operate the JT cooler at ≈ 20 bar with a mass flow rate of ≈ 6.3 $\mathrm{mg\,min^{-1}}$, this corresponds to a cooling power degradation of 89%. However, under these conditions, the high pressure is below the critical pressure of nitrogen and, consequently, the JT expansion is ineffective in this region (cf. Figure 4.18), since the expanded two-phase fluid will contain a high vapour fraction, $\chi = 88\%$ (at 40 bar, $\chi = 22\%$). Taking this into account, the JT cooler is expected to supply around 166 mW of cooling power. Although this value is low compared to the requirements (1.5 W), it still allows to demonstrate the operation of this sorption compressor cell integrated with the JT stage. Moreover, by operating at 20 bar, it allows to obtain an higher molar quantity, $\Delta n$, of 2.1 mol available for circulation, as depicted in Figure 7.10.

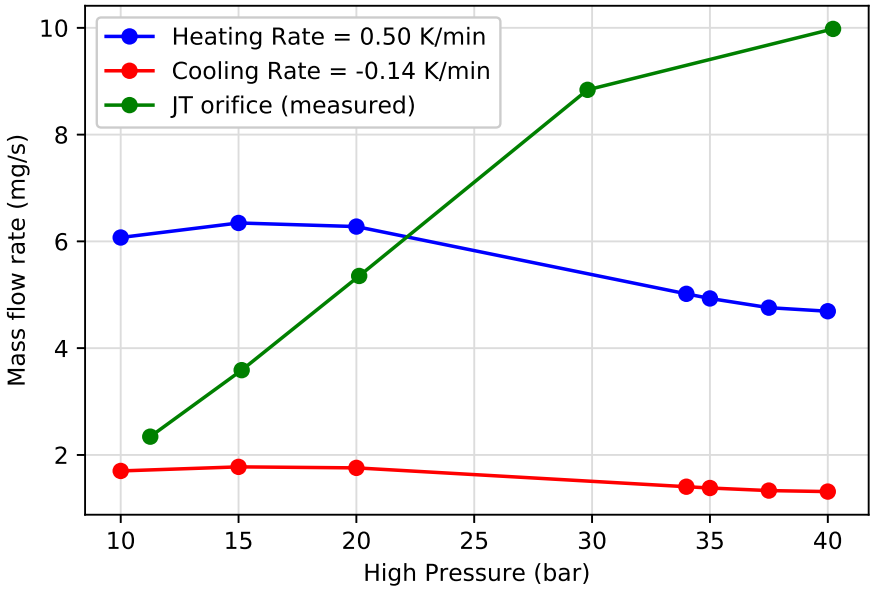


(a)

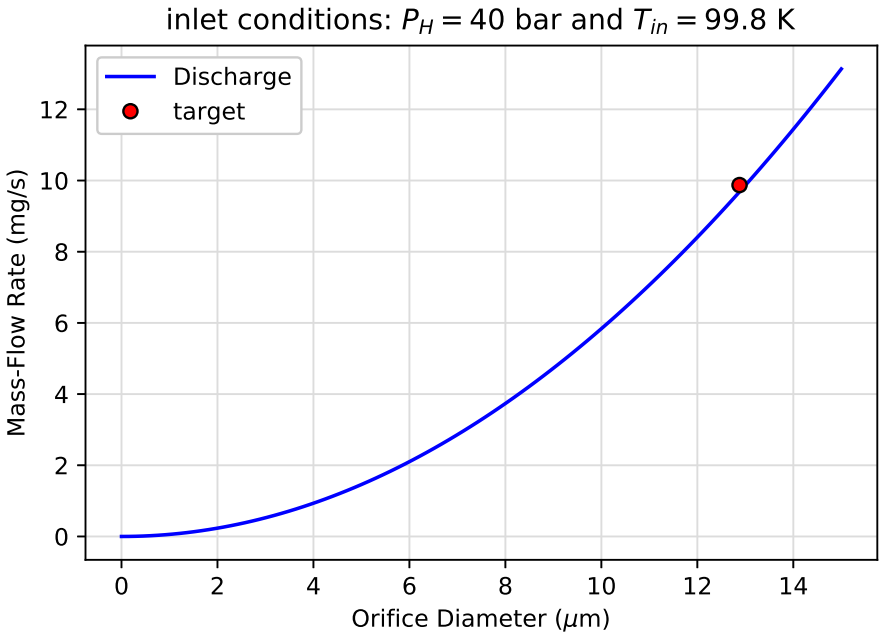


(b)

Figure 7.9: a) Expected mass-flow rate provided by the sorption cell in comparison with the implemented 14 µm orifice discharge rate as a function of the high pressure; b) Mass flow rate at constant upstream pressure of 40 bar and upstream temperature of 100 K as a function of the orifice diameter.

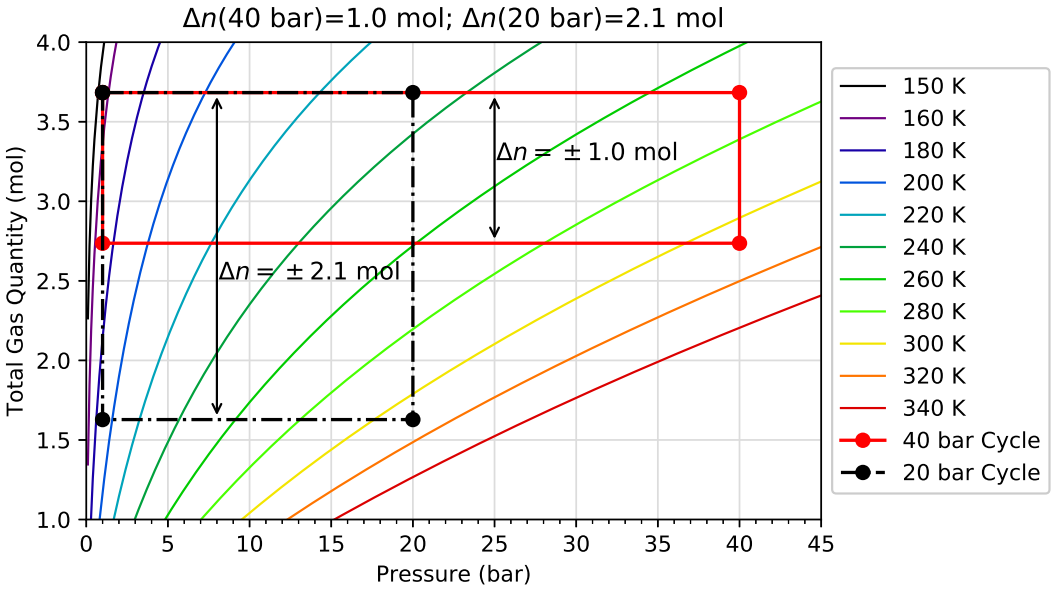


Figure 7.10: Comparison of two compression cycles operating at $P_H$ =20 bar and at $P_H$ =40 bar. Operating at 20 bar allows to double the circulating gas quantity.

Ultimately, by considering the mass-flow rate fixed by the orifice at 20 bar and the gas quantity, $\Delta n$, supplied by the sorption cell, we expect a releasing or adsorbing phase duration close to the one previously obtained and, therefore, enabling to feed the JT stage with this sorption cell.

### 7.3.1 Experimental Set-up

In Figure 7.11 is depicted the experimental set-up and the gas flow path during the four phases of the compression cycle. Let us note that to obtain a continuous supply of nitrogen to the JT stage using a single sorption cell, a gas cylinder was coupled to the circuit to supply a gas flow whenever it not possible.

- **Heating Phase** During this phase, the sorption cell is not ready to supply a stream of nitrogen gas to the JT stage, since it is increasing its temperature to build up pressure from 1 bar to 20 bar. So, the JT stage has to receive nitrogen from the gas cylinder. The internal pressure of the cell, $P3$, is higher than $P1$ and lower than $P2$, therefore, the check-valves $C1$ and $C2$ are passively closed and, then, the cell is being heated at constant quantity. The two mass flow meters ($M1$, $M2$) should indicate the same reading.

- **Releasing Phase** Due to continuous heating, the pressure of the cell exceeds 20 bar and the check-valve $C1$ opens: the valve $V1$ is manually closed and the cell releases a steady flow of gas towards the JT stage (by controlling the heating rate).

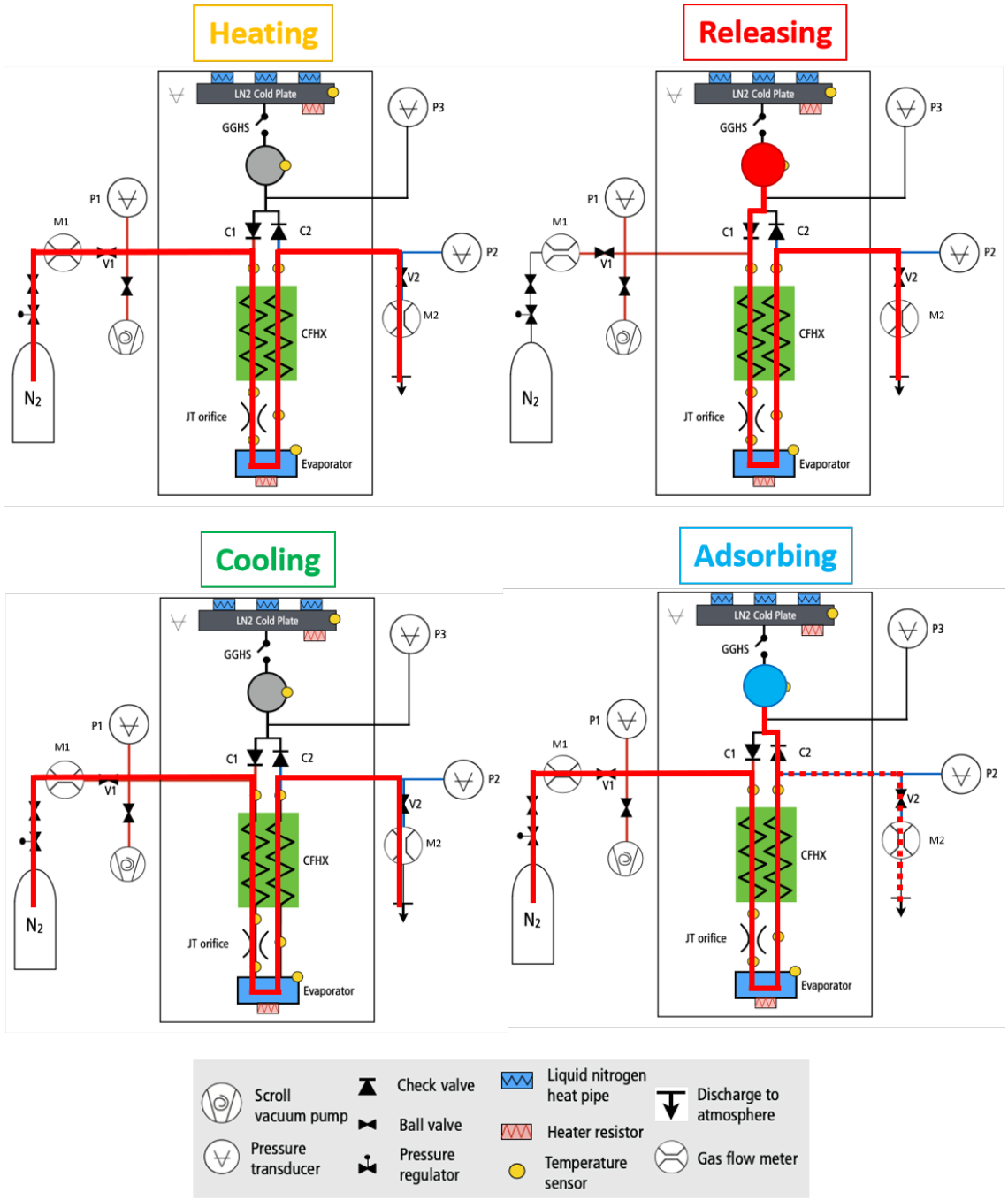


Figure 7.11: Compression cycle test experimental procedure, the red thick line corresponds to the flow path during each phase. Note that this test now includes a pair of check-valves to ensure the correct flow direction.

The flowmeter $M2$ should indicate the same reading as before, whereas $M1$ falls to zero.

- **Cooling Phase** When is no longer possible to provide a stable stream of gas at 20 bar, the cooling phase must start and the valve $V1$ must be reopened to feed the JT stage via the gas cylinder. Then, as soon as the temperature of the sorption cell decreases, the pressure $P3$ decreases below 20 bar and the check-valve $C1$ passively closes. The cell is again operating at constant quantity and decreasing its pressure down to 1 bar. The two mass flow meters ($M1$, $M2$) should indicate again the same reading.

- **Adsorbing Phase** When the cell's pressure, $P3$, is low enough to open the check-valve $C2$ ($P3 < P2$), the cell is ready to adsorb the gas flowing out the JT stage. Being the adsorbing phase the slowest of all, the sorption cell is not able to adsorb with the same rate as it flowing out from the JT stage, since it would need to operate at 10 bar, instead of 20 bar, to match both sorption cell intake and orifice discharge rate, as visible in Figure 7.9a. However, by keeping the exhaust valve $V2$ opened and $P_H = 20$ bar, it is possible to release the excess gas to the atmosphere which was not adsorbed by the cell. The flowmeter $M1$ should still indicate the expected flow rate at 20 bar and $M2$, a reading, ideally, close to zero. When is no longer possible to adsorb, i.e. when $M1$ and $M2$ indicate the same reading, the adsorbing phase is completed. Note that by keeping this valve open it will force the low pressure line to the atmospheric pressure during the whole process.

Figure 7.12 shows the components (sorption cell, check-valves and JT stage) required for this compression cycle test mounted on the cooling plate. This set-up allows to test and drive the JT stage using only one sorption cell by following the different steps indicated in Figure 7.11 and described in the previous paragraphs.

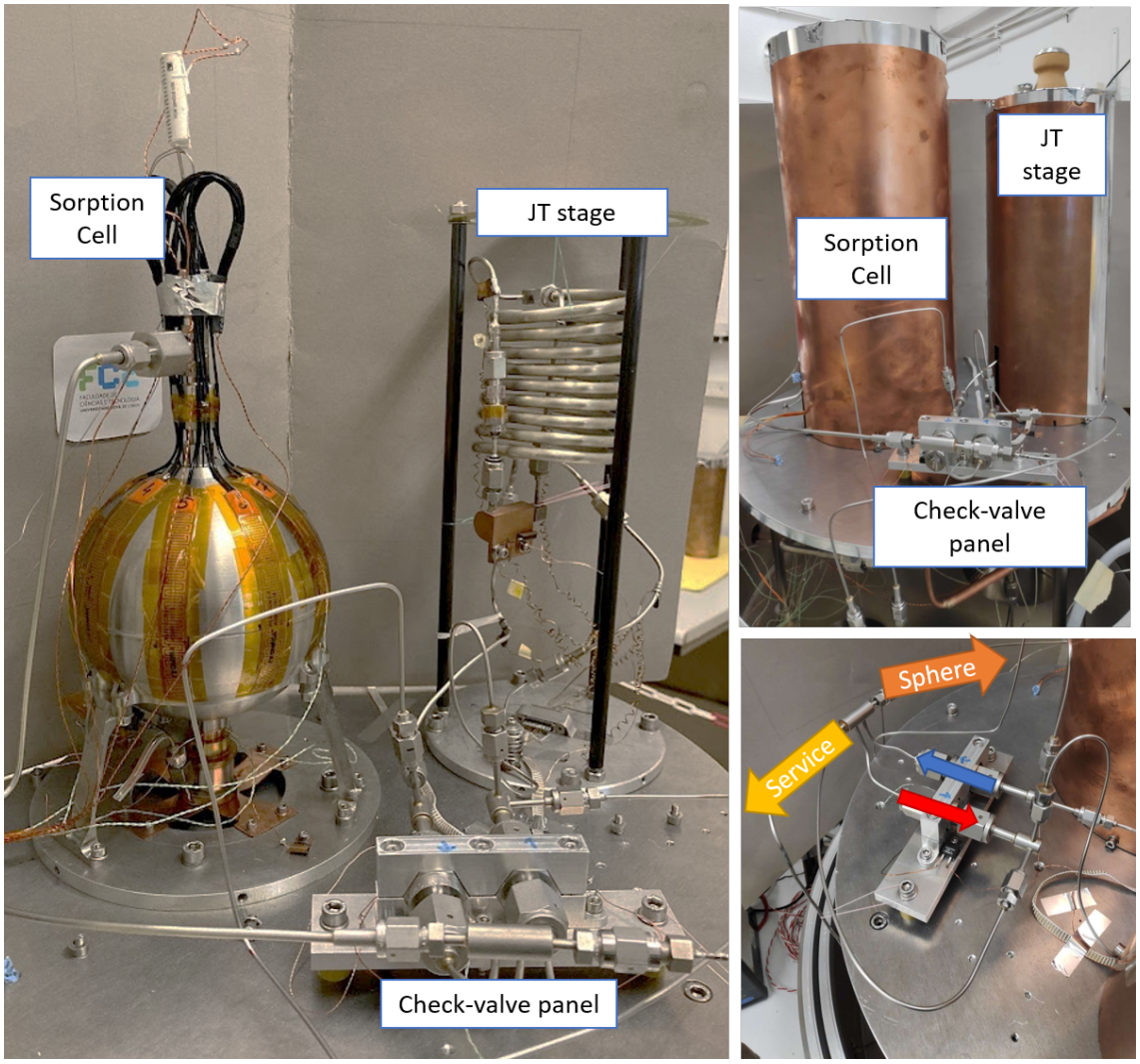


Figure 7.12: Pictures of the system built to perform the compression cycle test. The top right picture shows the thermal shroud used to protect the sorption cell and the JT stage from the RT thermal radiation, they are thermalized at the cooling plate and the shroud's temperature was measured to be ≈ 125 K during operation. The check-valves are thermally insulated from the cooling plate and assembled in a small aluminum interface containing two small resistors and a thermocouple to control at a temperature higher than 260 K that prevents leakage, particularly, in the reverse direction.

### 7.3.2 Results and Discussion

Figure 7.13 shows the temperature (plot a) and pressure (plot b) behavior during two and half compression cycles. Each compression cycle had an average runtime of 8 h and 24 min which is similar to the slow dynamics obtained earlier (Table 7.3) and the average range of temperature of the sorption cell was between 162 K and 318 K.

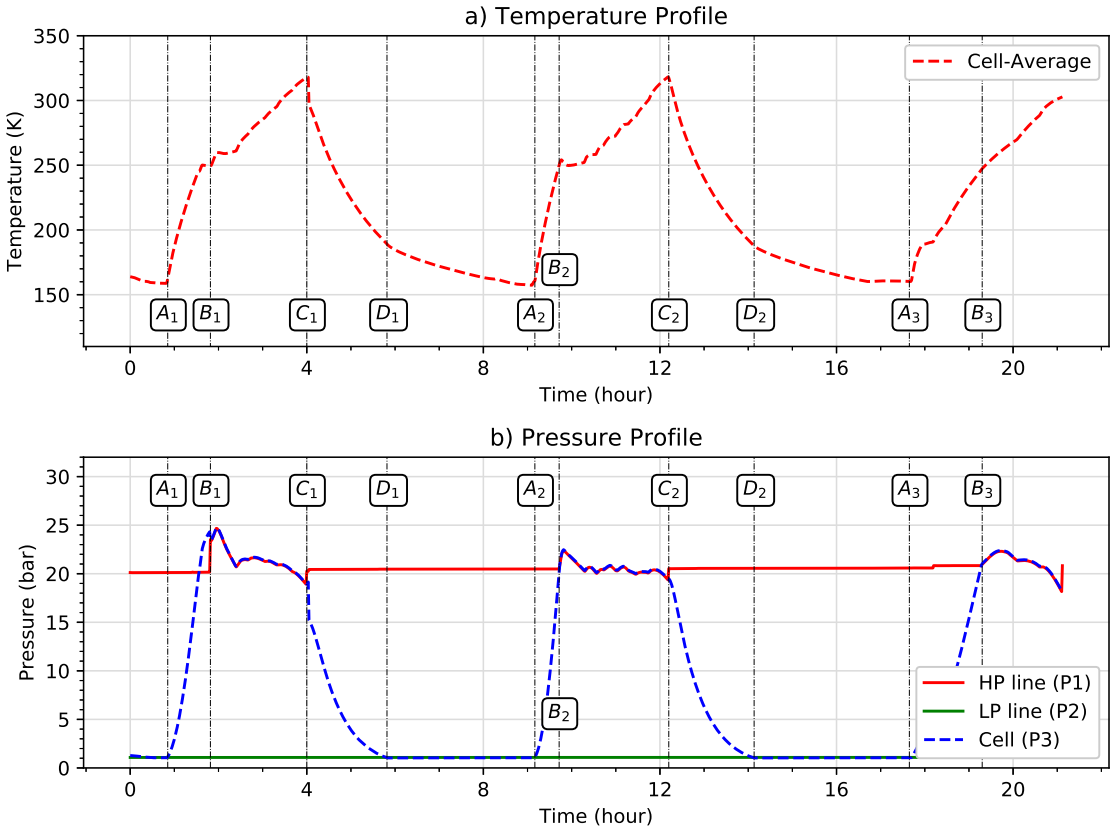


Figure 7.13: Compression cycle test results: a) shows the temperature profile over the two and half compression cycles, the sorption cell cycled between 160 K and 320 K; b) shows the pressure profile of the low and high pressure lines and as well as the internal pressure of cell (dashed blue line). The squared labels refers to the beginning/ending of each phase: $A \rightarrow B$, heating; $B \rightarrow C$, releasing; $C \rightarrow D$, cooling; and $D \rightarrow A$, adsorbing.

At instant $A$, the sorption cell is closed and its temperature increased by applying, in average, 45 W, until, at instant $B$, the pressure of the cell ($P3$) is greater than that of the high pressure line ($P1$). Therefore, the check-valve in the forward direction ($C1$) to the JT stage opens and starts to release a flow of nitrogen towards the JT stage (releasing phase). Figure 7.14 shows the $B_2 \rightarrow C_2$ releasing phase in detail, the upper plot shows the pressure profile of the cell and of the HP line, while the bottom plot shows the mass flow meter readings during the same period.

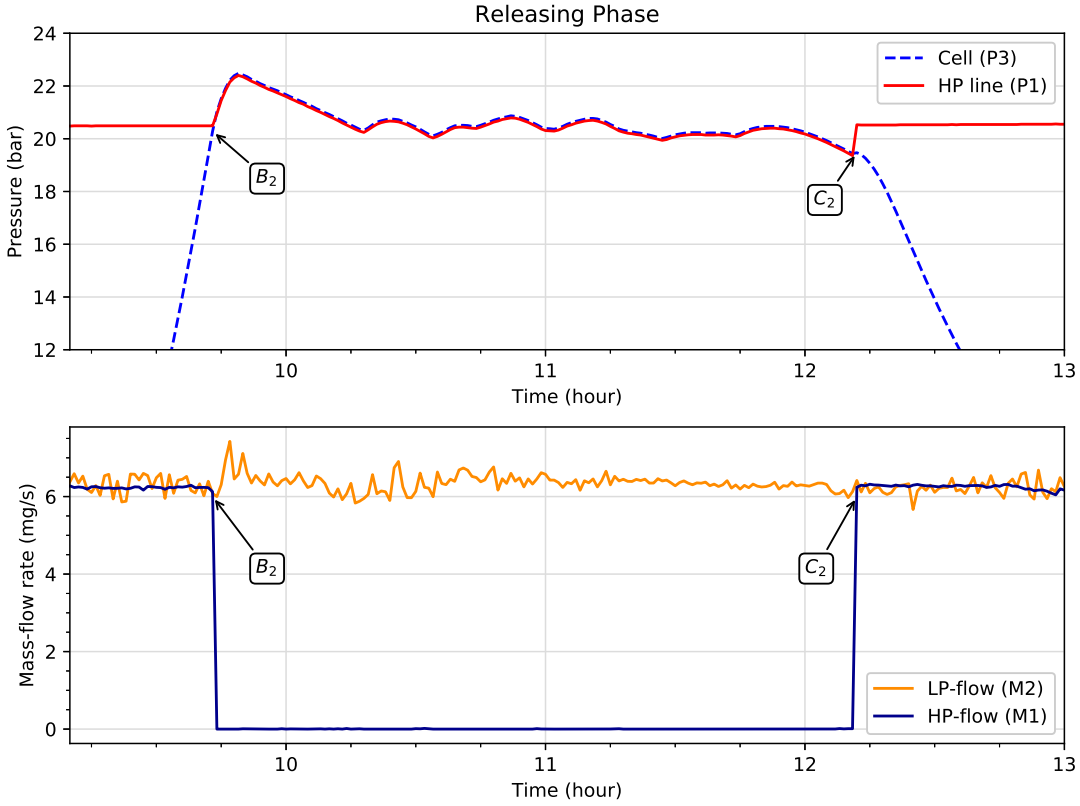


Figure 7.14: Releasing phase in detail between instants $B_2$ and $C_2$, coming from the results shown in Figure 7.13. The upper plot shows the pressure profile of the cell ($P3$-dashed blue) and the high-pressure line ($P1$-red); the bottom plot shows the mass flow meter readings $M1$ (coming from the high pressure cylinder) and $M2$ (output of the system) during the the same period.

Let us insist on some specific points during this releasing phase ($B_2 \rightarrow C_2$):

- Before instant $B_2$ and as visible in the bottom plot of Figure 7.14 (flowmeter $M1$, dark blue line), the nitrogen flow is being supplied by the gas cylinder.
- Before instant $B_2$, it is visible in the upper plot that the pressure of the cell (dashed-blue) is increasing due to heating.
- At instant $B_2$, $P3$ becomes greater than $P1$, so, the high-pressure check valve opens and the gas cylinder valve ($V1$) is manually closed, therefore and as visible, the $M1$ flow reading falls down to zero.
- Meanwhile, between $B_2$ and $C_2$, the LP flow meter ($M2$) continues to measure the same flow as it had previously ($\approx 6.2\,\mathrm{mg\,s^{-1}}$), indicating that the flow of nitrogen is actually being delivered into the JT stage through the sorption cell. We will see later that to this releasing phase is effectively associated a cooling power.
- By integration of the $M2$ flow meter reading data, around 38.9 L of nitrogen were released by the sorption cell during this phase. This quantity is equivalent to 2.17 mol, which matches the expected value calculated in Figure 7.10.

- Between $B_1$ and $C_1$ (another releasing phase), the sorption cell releases 2.20 mol and, thus, showing a good coherence between cycles. Let us note that at instant $B_1$ (first passive check-valve opening) a pressure higher than 24 bar was needed to force the valve opening. This anomaly was interpreted as some sticking of this valve and does not occurred on the following $B$ points. For instance, as shown in Figure 7.14, for the $B_2$ point, $P_3$ never becomes higher than $P_1$.

At instant $C$, it is no longer possible to maintain a stable pressure in the HP line, so, the gas cylinder valve is manually reopened, the heating of the sorption cell is turned off and the GGHS is switched from OFF to ON to start the cooling phase of the sorption cell. During the cooling phase ($C \rightarrow D$), the pressure in the cell roughly decreases from 20 bar down to 1 bar. At instant $D$, as soon as the pressure of the cell is sufficiently below the LP line, the LP check-valve ($C2$) passively opens and the sorption cell starts to adsorb. Figure 7.15 shows an adsorbing phase in detail, the upper plot shows the pressure profile of the cell and of the LP line, while the bottom plot shows the mass flow meter readings during the same period.

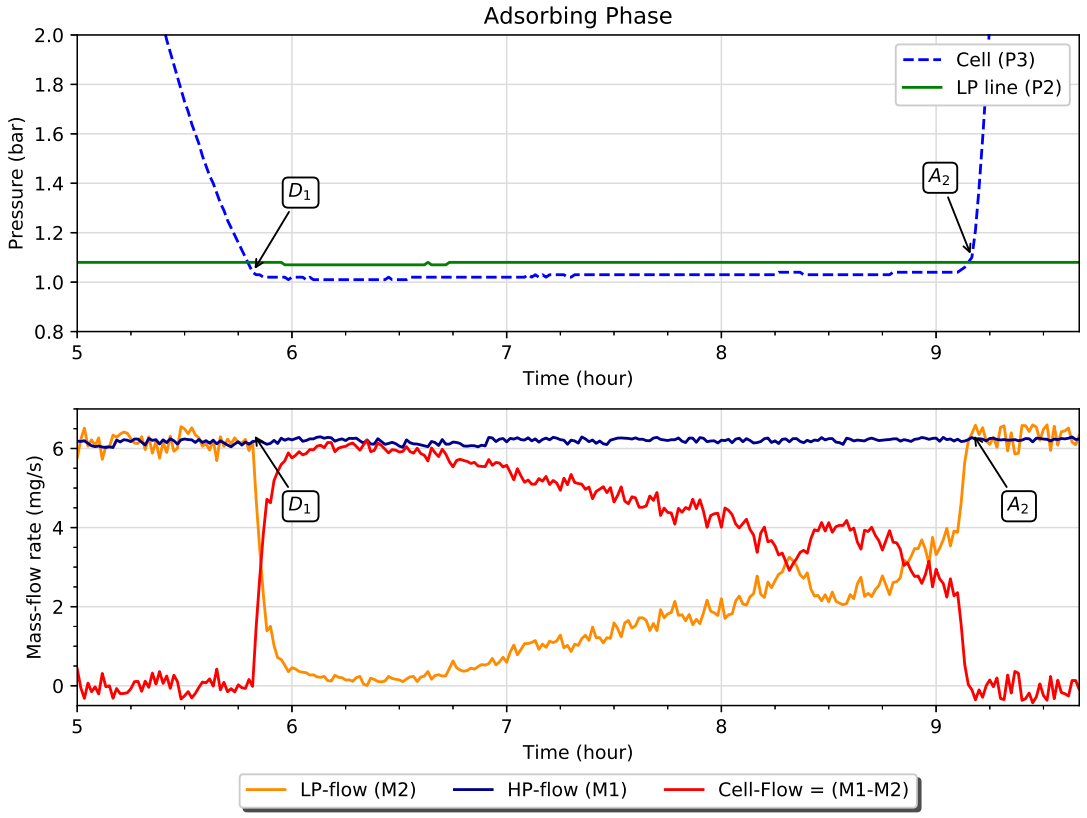


Figure 7.15: Adsorption phase in detail between instant $D_1$ and $A_2$ coming from the results shown in Figure 7.13. The upper plot shows the pressure profile of the cell ($P3$-dashed blue) and the low-pressure line ($P2$-green); the bottom plot shows the mass flow meter readings ($M1$ and $M2$) and the mass flow rate towards the sorption cell in red.

Let us insist on some specific points during this adsorbing phase ($D_1 \rightarrow A_2$):

- During this phase ($D_1 \rightarrow A_2$), the JT stage is always supplied by the gas cylinder ($M1$ flowmeter).
- At instant $D_1$, immediately after the LP check-valve opening, the LP flowmeter (orange line), located on the exhaust pipeline, falls rapidly to zero, while the HP pressure flow (blue line) remains constant. This is an indication that the nitrogen gas leaving the JT stage is being fully adsorbed by the sorption cell, note that the JT stage is still being supplied from the gas cylinder.
- Between 6 h to 7 h, since the LP flow reading is close to zero, we can conclude that the sorption cell is able to adsorb with the same rate as it is flowing out of the JT stage.
- After 6 h and 45 min, some gas flow is detected at $M2$: from that moment on, the sorption cell would need a higher cooling rate to match the adsorption rate corresponding to the nitrogen flow crossing the JT valve.
- The gas flow into the sorption cell can be calculated as the difference between the flowmeter readings: $M1 - M2$ (thick red line, bottom plot of Figure 7.15).
- By integration of $(M1 - M2)$, the gas quantity adsorbed by the sorption cell is obtained. Such a procedure leads to an adsorbed quantity of 2.16 mol, a value very close to the quantity released by the sorption cell.
- Let us note that, after instant $A_2$, the cell contains up to 2.16 mol. Then, with its volume closed, its temperature increased between $A_2$ and $B_2$, and, afterwards, between $B_2$ and $C_2$, the sorption cell precisely released the same quantity as it adsorbed before, this shows the good coherence between cycles.
- Between $D2$ and $A_3$ (another adsorbing phase) the sorption cell adsorbed 2.03 mol. Again, the absorbed amount matches with the other active phases of sorption cell.

During the two and half compression cycles ($A_1 \rightarrow B_3$), the JT stage was alternatively fed by a gas cylinder or through the sorption cell, with a more or less constant flow. Let us focus on the JT stage performance, which independently from the source of nitrogen, successfully sustained liquefaction through throttling. Figures 7.16 and 7.17 shows the JT stage temperatures and the heat load applied on the evaporator during the same test run shown in Figure 7.13. These data were used to determine the cooling power of the system.

Although some instabilities occur during this long 20 h run, we can see in Figure 7.17 that the evaporator is receiving liquid nitrogen during the whole experiment, apart from two anomalies where it dried out: one at 4 h, caused by loss of control; and another one at 16 h, for unknown reasons. Let us note that that the system seemed to be more unstable by operating the JT stage at 20 bar compared to the operation at 40 bar. Therefore, it was more difficult to adjust the heating power of the evaporator to determine the

cooling power of the cycle. In any case, a sustained liquefaction was obtained over 20 h with an average cooling power of 96.5 mW, although lower than expected (166 mW).

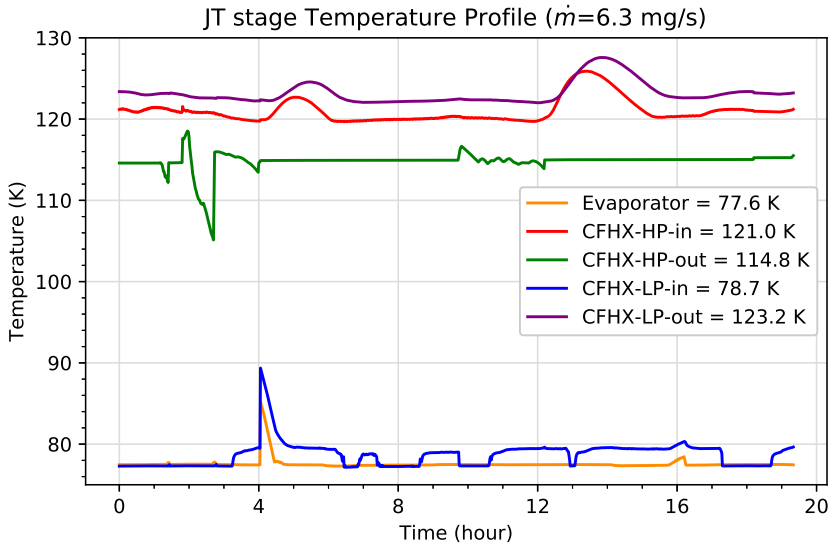


Figure 7.16: Temperatures in the JT stage during the compression cycles shown in Figure 7.13. The values indicated in the legend correspond to the average value.

Let us also remind that during the releasing phases of the sorption cell, the JT stage was being completely fed by the sorption cell. In Figure 7.17 it can be seen that the JT stage worked as desired during these periods, in particular by successfully maintaining a constant temperature in the evaporator. We have also showed with this characterization that this system has a very coherent behavior, providing the expected amount of gas under this operating conditions at 20 bar.

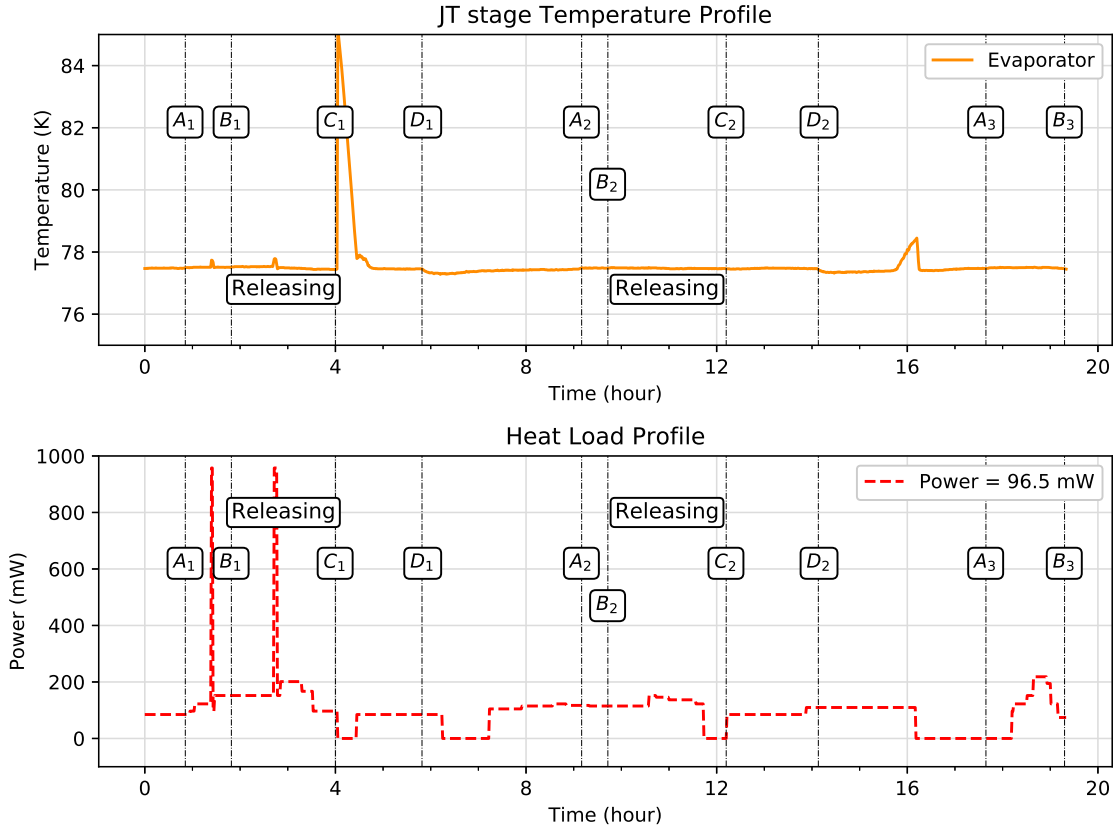


Figure 7.17: Evaporator temperature and heat load profile of the JT evaporator during the compression cycles shown in Figure 7.13.

## 7.4 Conclusions

Let us summarize the main results obtained during these tests using one single adsorption cell:

- We succeeded to put a system consisting of a single sorption cell coupled to JT stage running for two and half compression cycles. During three phases of the compression cycle (cooling, adsorbing and heating), the JT stage was being powered by an external source and during the releasing phase, the JT stage was directly receiving a nitrogen gas flow from this sorption cell.

- Due to the poor thermal dynamics of the cell, the initial 10 mg s$^{-1}$, corresponding to the 1.5 W, was not possible to obtain. Then, to overcome this limitation and test the installed compressor cell integrated with the JT stage, we had to reduce the working high pressure from 40 bar to 20 bar to match the slow dynamics of the cell. Although it did not compromise this test, this adjustment led to a decrease of the cooling power from 1.5 W to 0.1 W.

- By integrating the flow meters data, we showed that during the two and half cycles the gas flow balance was coherent between cycles: what was adsorbed, was released later. In addition, this released/adsorbed quantity ($\Delta n = 2.1\,\mathrm{mol}$) was close to what was expected from the adsorption data shown in Figure 7.10.
- During this compression cycle test, we verified that both check-valves operated as expected. Let us note however, as expected, they needed a special interface in order to maintain their temperatures above 260 K, as visible in Figure 7.12.
- Although volume buffers, required to damp pressure fluctuations in both high and low pressure lines of the system, were not needed for this test, these buffers would be most likely needed if we had more sorption cells operating in parallel, since significant pressure fluctuations could occur between the various phase transitions.

CHAPTER 8

# Conclusions

## 8.1 Final Remarks

To answer the needs of vibration-free cooling solutions for Earth observations missions in the temperature range of 40 K to 80 K, we proposed a solution consisting in two parallel Joule-Thomson stages, each one powered by a single-stage sorption compressor. After a trade-off analysis, nitrogen and neon were selected as the adequate fluids.

**Adsorbent Materials Characterization** Considering the stringent requirements and, particularly, the weak interaction of neon with porous materials, we started to look for and investigate alternative adsorptive materials showing good capture of neon. After an initial screening of the materials that showed good adsorption capacities and that were commercially available, three MOF compounds were identified as viable solutions (UiO-66, $Co_3(ndc)_3(dabco)$ and HKUST-1). The adsorption capacity of these three materials was measured with neon over a wide range of temperature and pressure (77 K to 500 K and 0 bar to 100 bar). Unfortunately, these materials showed limited adsorption capacities of neon and do not allowed us to proceed with an operating solution at 40 K meeting the requirements of the project. In the case of nitrogen, the HKUST-1 material was found adequate to proceed with the development of a configuration at 80 K.

The results coming from this adsorption characterization allowed us to numerically obtain the optimum operating parameters of the nitrogen cooler through an optimization tool developed for the whole system (from the radiator to the JT's cold finger). After some trade-off analysis, a solution using two radiators was envisaged and required the sorption compressor to cycle between 165 K to 360 K (1 bar to 40 bar) to provide a stable mass flow rate of 10.8 $mg\,s^{-1}$ to sustain the JT stage operation at 80 K (Chapter 4).

**Joule-Thomson Cold Stage Design and Demonstration** The JT stage was then designed and it consisted in a 2 m long counter-flow heat exchanger, a 14 µm orifice restriction and a copper evaporator able to confine the liquid under micro-gravity environment through capillary forces. Each component was carefully characterized and worked as expected. The whole JT stage was initially assembled without the evaporator and tested. It ran over 30 h while providing a sustained liquefaction with an average cooling power of 1.67 W, working as intended. Then, the evaporator was integrated into the JT stage and tested by rotating the test cryostat. We demonstrated that this JT stage is working against gravity, the liquid being confined by superficial tension effect in the evaporator. This test validated a correct operation in micro-gravity environment (Chapter 5).

**Detailed Sorption Compressor Cell Design and Integration** The sorption compressor cell was designed by AST and integrated in the laboratory of cryogenics. It was necessary to design and build a new cryostat, which included a 450 mm diameter aluminum cooling plate that provides cooling by a continuous supply of liquid nitrogen to the parts under testing. The signal conditioning, acquisition and control used a programmable FPGA from NI.

The selected check-valve, after an initial screening, was tested as a function of temperature in the required pressure range. Such testing confirmed that they require temperatures higher than 240 K to operate correctly. Therefore, a special interface in aluminum was built, loosely coupled from the cooling plate and equipped with a temperature control to keep the check-valves operating at the required temperature level.

In parallel, a gas gap heat switch prototype was designed using hydrogen as the conducting gas and integrated with a sorption pump filled with the metal hydride $ZrMn_2H_x$ to manage the heat-switch thermal conductance for temperatures higher than 150 K. By using this metal hydride, we were able to vary the GGHS's thermal conductance from 7.6 $mWK^{-1}$ to 1100 $mWK^{-1}$, just by controlling the temperature of the sorb pump. However, the final version of the GGHS (the one with the interface for the sorption cell) was not successful, as the metal hydride did not absorbed hydrogen. Therefore, to avoid delays in the project development, this GGHS's exchange gas was replaced with nitrogen and its sorb pump charged with activated charcoal. Obviously, such an alternative solution corresponds to a longer cooling time of the sorption cell due to the lower thermal conductivity of nitrogen compared to the hydrogen gas.

Due to some misconception in the design and electrostatic aggregation of the MOF powder, the filling procedure of the sorption cell with HKUST-1 was a difficult task and led to void factor of 57% (expected 54%). The coupling procedure between the GGHS and the cell, using the shrink-fitting technique, also presented some difficulties (partial

coupling). Actually, the many complications and setbacks throughout the integration of the first compressor cell, prevented the construction of the remaining cells due to limited time and available resources. But, it did not hinder the progress of the project, as the functional characterization of one sorption cell was still possible (Chapter 6).

**Single-Cell Functional Characterization** After successful integration of the first sorption cell it was possible to start its functional characterization, although by changing some operating parameters, for instance, reducing the cold plate temperature down to 117 K, to compensate the worse performance of the nitrogen GGHS when compared to the one using hydrogen.

The adsorption behavior of the filled sorption cell was measured in the 130 K to 380 K temperature range and 1 bar to 50 bar pressure range. The adsorption capacity of this sorption cell charged with HKUST-1 was in line with the previous characterization. This MOF compound also showed good stability, since it remained in contact with air and moisture for a long period without pumping during the filling procedure. To test its functionality, this cell was cycled between 160 K to 330 K. A slower dynamics than expected was obtained (+63% cycle period), which can be partially attributed to the poor performance of the GGHS, for reasons currently unknown.

So, to demonstrate the operation of the JT stage powered by this sorption cell, after some trade-off, the working high pressure had to be reduced down to 20 bar to match with the discharge rate of the implemented orifice on the JT stage and, thus enabling it to demonstrate both sub-systems operating together.

During the compression cycle test, we successfully sustained liquefaction with a cooling power of 96.5 mW at 77 K up to 19 h, the JT part being alternatively fed by the sorption cell or by an external gas source. We also observed that the amount of gas entering and leaving the sorption cell between consecutive cycles was very coherent and its value very similar to the expected (Chapter 7).

Let us remind that the cooling power obtained in this characterization was far from its initial objective (1.5 W at 80 K) due to the limitations of the installed sorption cell. For instance, the reduction of the working high pressure down to 20 bar and consequent expansion in the two-phase region, as expected, it greatly impacts the efficiency of the cooler. However, if the thermal path between this cell and the cold source was greatly improved (for instance, by implementing the hydrogen GGHS with the adequate interface), it would enable to perform a compression cycle with a higher cooling and heating rate and, thus, providing an operation with the desired cooling power.

## 8.2 Lessons Learned and Future Work

The development of even more sophisticated sensors for Earth observation missions will surely continue to rely on cryogenics, therefore, the demand for cooling solutions without vibrations will very probably increase. We hope that the work presented in this dissertation has generously contributed to the development of new cooling solutions and has started to pave the way towards the search and characterization of new adsorption class materials that can answer to the diverse needs existing in the scientific community and also serve as a source of inspiration for new technological advances. However, some lessons learned during this work and future perspectives are noteworthy before finishing this dissertation:

- The development of a cooling solution meeting the requirements of the project, even only with a single nitrogen stage, proved to be quite challenging. However, we believe that it is important to continue looking and studying new sorbent materials within the very large portfolio of MOFs in order to proceed with the development of the neon stage. Let us remind that the HKUST-1 was the available solution at the time and it was not necessarily the best solution (within the MOFs portfolio for nitrogen adsorption). A material with a greater sorption capacity will greatly improve the overall performance of the VFC.

- As already mentioned throughout this work, many complications ocurred during the integration of the first sorption cell. The internal heaters of the cell were not robust enough, since one of them had a short-circuit a couple of times and prevented us to let the cell reach higher temperatures. For safety reasons and to have the required power to heat up the cell, nine Kapton heaters were placed on the external surface of the sorption cell and worked quite well, in fact, their integration guaranteed a good thermal homogeneity of the cell during heating. Therefore, the external heating solution should be evaluated in the integration of the remaining sorption cells, since it brought some advantages.

- Regarding the shrink-fit coupling, it is undoubtedly a delicate procedure that can compromise the functioning of the sorption cell. However, it is mandatory that the tolerances of the parts are properly respected to avoid further complications. It would also be of value that the thermal conductance (contact resistances) of these pieces were studied in a dedicated experimental set-up.

- The filling procedure of the spherical sorption cell was longer than desired and rather complex. In the end, it ended up being not so close of the expected mass

value (large void volume) and, hence reducing the amount of gas available for circulation by 22%. So, it is mandatory to reduce these empty volumes, as it deeply affects the overall performance. A solution would start by rethinking the filling procedure to turn it more efficient and reliable. Let us note that the sorption cell design was initially intended for an operation at 100 bar. Since this working pressure was reduced to 40 bar after the numerical optimization, from a mechanical point of view, the possibility of having a filling port larger than the current one should be evaluated.

- The next developments of the thermal heat switches should include the metal hydride $ZrMn_2H_x$ to enable the use of hydrogen, so that the thermal dynamics of the cells may be greatly improved. As demonstrated in a GGHS prototype, it achieved good results, working in the desired temperature range and with a thermal conductance ratio compatible with our needs. It should be noted that this material is highly reactive with air, therefore, the filling procedure of the sorb pump will still need some improvements in order to guarantee its correct and desired functioning. Let us note that a heat switch working in this temperature range can also find applications in other systems.

- It is still possible to study the current system (sorption cell + JT stage) under the expected operational parameters, by changing the orifice restriction accordingly. This would allow for further characterization of this sorption cell, however with lower cooling power than required.

- The remaining cells must be built taking into account the suggestions mentioned in the paragraphs above. Each one of them would have to go through a qualification and integration campaign similar to the first cell. Finally, the cryostat should be prepared to receive the four sorption cells and then test the compressor's quadrature operation while feeding the JT cooler.

# References


[1] R. Ross. "Aerospace Coolers: A 50-Year Quest for Long-Life Cryogenic Cooling in Space." In: *Cryogenic Engineering*. Ed. by K. D. Timmerhaus and R. P. Reed. New York, NY: Springer New York, 2007, pp. 225–284. ISBN: 978-0-387-46896-9. DOI: 10.1007/0-387-46896-X_11. URL: https://doi.org/10.1007/0-387-46896-X_11.

[2] L. Duband. "Space Cryocooler Developments." In: *Physics Procedia* 67 (2015). Proceedings of the 25th International Cryogenic Engineering Conference and International Cryogenic Materials Conference 2014, pp. 1 –10. ISSN: 1875-3892. DOI: https://doi.org/10.1016/j.phpro.2015.06.003. URL: http://www.sciencedirect.com/science/article/pii/S1875389215003843.

[3] ESA. *Statement of Work - Development of a 40-80K vibration-free cooler*. Reference: TEC-MTT/2014/3859/ln/ThT, Issue Data: 04/08/2014.

[4] J. Burger, H. ter Brake, H. Rogalla, and M. Linder. "Vibration-free 5 K sorption cooler for ESA's Darwin mission." In: *Cryogenics* 42.2 (2002), pp. 97 –108. ISSN: 0011-2275. DOI: https://doi.org/10.1016/S0011-2275(02)00008-5. URL: http://www.sciencedirect.com/science/article/pii/S0011227502000085.

[5] T Tirolien, M Linder, and M Branco. "Spacecraft Cryogenic Developments and Perspectives at the European Space Agency." In: *Cryocoolers 20* (2018), pp. 377–386. ISSN: 1549-1757. URL: https://cryocooler.org/resources/Documents/C20/377.pdf.

[6] J. Tauber. "The Planck mission." In: *Advances in Space Research* 34.3 (2004). Astronomy at IR/Submm and the Microwave Background, pp. 491 –496. ISSN: 0273-1177. DOI: https://doi.org/10.1016/j.asr.2003.05.025. URL: http://www.sciencedirect.com/science/article/pii/S0273117703011773.

[7] G Morgante, D Pearson, F Melot, P Stassi, L Terenzi, P Wilson, B Hernandez, L Wade, A Gregorio, M Bersanelli, C Butler, and N Mandolesi. "Cryogenic characterization of the Planck sorption cooler system flight model." In: *Journal of Instrumentation* 4.12 (2009), T12016–T12016. DOI: 10.1088/1748-0221/4/

12/t12016. URL: https://doi.org/10.1088%2F1748-0221%2F4%2F12%2Ft12016.

[8] R. Carlisle and S. American. *Scientific American Inventions and Discoveries: All the Milestones in Ingenuity–From the Discovery of Fire to the Invention of the Microwave Oven*. Wiley, 2005. ISBN: 9780471660248. URL: https://books.google.pt/books?id=pDbQVE3IdTcC.

[9] B. Z. Maytal and J. M. Pfotenhauer. *Miniature Joule-Thomson cryocooling: Principles and practice*. 2013. ISBN: 9781441982858. DOI: 10.1007/978-1-4419-8285-8.

[10] J. Monroe. "Recent Progress from the MiniCLEAN Dark Matter Experiment." In: *Journal of Physics: Conference Series* 375.1 (2012), p. 012012. DOI: 10.1088/1742-6596/375/1/012012. URL: https://doi.org/10.1088%2F1742-6596%2F375%2F1%2F012012.

[11] L. e. a. Wade, P Bhandari, R. Bowman, C Paine, G Morgante, C. Lindensmith, D Crumb, M Prina, R Sugimura, and D Rapp. "Hydrogen sorption cryocoolers for the Planck mission." In: *Advances in cryogenic engineering* 45.A (2000), pp. 499–506.

[12] Y. Wu, D. Zalewski, C. Vermeer, H. Holland, B. Benthem, and H. ter Brake. "Baseline design of a sorption-based Joule-Thomson cooler chain for the METIS instrument in the E-ELT." In: *Cryogenics* 84 (2017), pp. 37 –52. ISSN: 0011-2275. DOI: https://doi.org/10.1016/j.cryogenics.2017.04.003. URL: http://www.sciencedirect.com/science/article/pii/S0011227517300449.

[13] Y. Wu, C. Vermeer, H. Holland, B. Benthem, and H. ter Brake. "Development of a switchless sorption compressor for the cryogenic refrigeration within the METIS instrument: Part II. Experimental demonstration." In: *International Journal of Refrigeration* 82 (2017), pp. 529 –540. ISSN: 0140-7007. DOI: https://doi.org/10.1016/j.ijrefrig.2017.06.023. URL: http://www.sciencedirect.com/science/article/pii/S0140700717302578.

[14] G. Wiegerinck, J. Burger, H. Holland, E. Hondebrink, H. ter Brake, and H. Rogalla. "A sorption compressor with a single sorber bed for use with a Linde–Hampson cold stage." In: *Cryogenics* 46.1 (2006), pp. 9 –20. ISSN: 0011-2275. DOI: https://doi.org/10.1016/j.cryogenics.2005.08.006. URL: http://www.sciencedirect.com/science/article/pii/S001122750500158X.

[15] I. Catarino, G. Bonfait, and L. Duband. "Neon gas-gap heat switch." In: *Cryogenics* 48.1 (2008), pp. 17 –25. ISSN: 0011-2275. DOI: https://doi.org/10.1016/j.cryogenics.2007.09.002. URL: http://www.sciencedirect.com/science/article/pii/S0011227507001233.

[16] J. Burger. "Cryogenic Microcooling, A micromachined cold stage operating with a sorption compressor in a vapor compression cycle." Undefined. Doctoral dissertation. Netherlands, Jan. 2001. ISBN: 90-365-1536-X.

[17] R. Wu. "Development of a Sorption-based Joule-Thomson Cooler for the METIS Instrument on E-ELT." English. Doctoral dissertation. University of Twente, Nov. 2015. ISBN: 978-90-365-3993-7. DOI: 10.3990/1.9789036539937.

[18] Y. Wu, D. Zalewski, C. Vermeer, and H. ter Brake. "Optimization of the working fluid for a sorption-based Joule–Thomson cooler." In: *Cryogenics* 58 (2013), pp. 5 –13. ISSN: 0011-2275. DOI: https://doi.org/10.1016/j.cryogenics.2013.07.007. URL: http://www.sciencedirect.com/science/article/pii/S0011227513000659.

[19] G. Wiegerinck, H. ter Brake, J. Burger, H. Holland, and H. Rogalla. "Thermodynamic optimization of sorption-based Joule–Thomson coolers." In: *Cryogenics* 47.3 (2007), pp. 143 –152. ISSN: 0011-2275. DOI: https://doi.org/10.1016/j.cryogenics.2006.11.006. URL: http://www.sciencedirect.com/science/article/pii/S0011227506001810.

[20] D. Martins, P. B. de Sousa, I. Catarino, and G. Bonfait. "40 K Liquid Neon Energy Storage Unit." In: *Physics Procedia* 67 (2015). Proceedings of the 25th International Cryogenic Engineering Conference and International Cryogenic Materials Conference 2014, pp. 1193 –1198. ISSN: 1875-3892. DOI: https://doi.org/10.1016/j.phpro.2015.06.188. URL: http://www.sciencedirect.com/science/article/pii/S1875389215005696.

[21] J.-C. NASA and ESA. *PIA16874: The Universe Comes into Sharper Focus*. https://photojournal.jpl.nasa.gov/catalog/PIA16874, Accessed: 08-10-2019.

[22] G. Morgante, D. Pearson, F. Melot, P. Stassi, L. Terenzi, P. Wilson, B. Hernandez, L. Wade, A. Gregorio, M. Bersanelli, C. Butler, and N. Mandolesi. "Cryogenic characterization of the Planck sorption cooler system flight model." In: *Journal of Instrumentation* 4.12 (2009), T12016–T12016. ISSN: 1748-0221. DOI: 10.1088/1748-0221/4/12/T12016. URL: http://stacks.iop.org/1748-0221/4/i=12/a=T12016?key=crossref.17741ae66bf92af3799313535171d427.

[23] G. Morgante, D. Barber, P. Bhandari, R. C. Bowman, P. Cowgill, D. Crumb, T. Loc, A. Nash, D. Pearson, M. Prina, A. Sirbi, M. Schemlzel, R. Sugimura, and L. A. Wade. "Two hydrogen sorption cryocoolers for the Planck mission." In: *AIP Conference Proceedings* 616.1 (2002), pp. 298–302. DOI: 10.1063/1.1475648. eprint: https://aip.scitation.org/doi/pdf/10.1063/1.1475648. URL: https://aip.scitation.org/doi/abs/10.1063/1.1475648.

[24] R. F. Boyle and R. G. Ross. "Overview of NASA space cryocooler programs." In: *AIP Conference Proceedings* 613.1 (2002), pp. 1037–1044. DOI: 10.1063/1.1472126. eprint: https://aip.scitation.org/doi/pdf/10.1063/1.1472126. URL: https://aip.scitation.org/doi/abs/10.1063/1.1472126.

[25] B. R. Brandl, O. Absil, T. Agócs, N. Baccichet, T. Bertram, F. Bettonvil, R. van Boekel, L. Burtscher, E. van Dishoeck, M. Feldt, P. J. V. Garcia, A. Glasse, A. Glauser, M. Güdel, C. Haupt, M. A. Kenworthy, L. Labadie, W. Laun, D. Lesman, E. Pantin, S. P. Quanz, I. Snellen, R. Siebenmorgen, and H. van Winckel. "Status of the mid-IR ELT imager and spectrograph (METIS)." In: *Ground-based and Airborne Instrumentation for Astronomy VII*. Ed. by C. J. Evans, L. Simard, and H. Takami. Vol. 10702. International Society for Optics and Photonics. SPIE, 2018, pp. 582 –596. DOI: 10.1117/12.2311492. URL: https://doi.org/10.1117/12.2311492.

[26] Y. Wu, C. Vermeer, H. Holland, B. Benthem, and H. ter Brake. "Development of a switchless sorption compressor for the cryogenic refrigeration within the METIS instrument: Part I. Theoretical design." In: *International Journal of Refrigeration* 82 (2017), pp. 520 –528. ISSN: 0140-7007. DOI: https://doi.org/10.1016/j.ijrefrig.2017.06.029. URL: http://www.sciencedirect.com/science/article/pii/S0140700717302633.

[27] C. Chan, E. Tward, and K. Boudaie. "Adsorption isotherms and heats of adsorption of hydrogen, neon and nitrogen on activated charcoal." In: *Cryogenics* 24.9 (1984), pp. 451 –459. ISSN: 0011-2275. DOI: https://doi.org/10.1016/0011-2275(84)90001-8. URL: http://www.sciencedirect.com/science/article/pii/0011227584900018.

[28] J. P. Mota. *Private communication*. 2016.

[29] R. Yamk, U. Yamk, C. Heiden, and J. G. Daunt. "Adsorption isotherms and heats of adsorption of neon and hydrogen on zeolite and charcoal between 20 and 90 K." In: *Journal of Low Temperature Physics* 45.5 (1981), pp. 443–455. ISSN: 1573-7357. DOI: 10.1007/BF00654492. URL: https://doi.org/10.1007/BF00654492.

[30] J. Barreto, M. D. G. Xavier, R. P. P. L. Ribeiro, D. Martins, I. A. A. C. Esteves, M. Branco, T. Tirolien, J. P. B. Mota, and G. Bonfait. "Neon Adsorption on HKUST-1 and UiO-66 Metal–Organic Frameworks over Wide Pressure and Temperature Ranges." In: *Journal of Chemical & Engineering Data* (2019). DOI: 10.1021/acs.jced.9b00606. eprint: https://doi.org/10.1021/acs.jced.9b00606. URL: https://doi.org/10.1021/acs.jced.9b00606.

[31] R. P. Ribeiro, J. Barreto, M. D. G. Xavier, D. Martins, I. A. Esteves, M. Branco, T. Tirolien, J. P. Mota, and G. Bonfait. "Cryogenic Neon Adsorption on Co3(ndc)3(dabco) Metal-Organic Framework." In: *Microporous and Mesoporous Materials* (2020), p. 110055. ISSN: 1387-1811. DOI: https://doi.org/10.1016/j.micromeso.2020.110055. URL: http://www.sciencedirect.com/science/article/pii/S1387181120300585.

[32] K. Foo and B. Hameed. "Insights into the modeling of adsorption isotherm systems." In: *Chemical Engineering Journal* 156.1 (2010), pp. 2 –10. ISSN: 1385-8947. DOI: https://doi.org/10.1016/j.cej.2009.09.013. URL: http://www.sciencedirect.com/science/article/pii/S1385894709006147.

[33] H. Freundlich. "Kapillarchemie, Eine Darstellung der Chemie der Kolloide und verwandter Gebiete." In: *Nature* 85.2156 (1911), pp. 534–535. ISSN: 1476-4687. DOI: 10.1038/085534a0. URL: https://doi.org/10.1038/085534a0.

[34] N. Tzabar and H. J. M. ter Brake. "Adsorption isotherms and Sips models of nitrogen, methane, ethane, and propane on commercial activated carbons and polyvinylidene chloride." In: *Adsorption* 22.7 (2016), pp. 901–914. ISSN: 1572-8757. DOI: 10.1007/s10450-016-9794-9. URL: https://doi.org/10.1007/s10450-016-9794-9.

[35] F. Rouquerol, J. Rouquerol, and K. Sing. "CHAPTER 2 - Thermodynamics of Adsorption at the Gas–Solid Interface." In: *Adsorption by Powders and Porous Solids*. Ed. by F. Rouquerol, J. Rouquerol, and K. Sing. London: Academic Press, 1999, pp. 27 –50. ISBN: 978-0-12-598920-6. DOI: https://doi.org/10.1016/B978-012598920-6/50003-8. URL: http://www.sciencedirect.com/science/article/pii/B9780125989206500038.

[36] R. A. Patil, C. A. Weatherly, and D. W. Armstrong. "Chapter 11 - Chiral Gas Chromatography." In: *Chiral Analysis (Second Edition)*. Ed. by P. L. Polavarapu. Second Edition. Elsevier, 2018, pp. 468 –505. ISBN: 978-0-444-64027-7. DOI: https://doi.org/10.1016/B978-0-444-64027-7.00012-4. URL: http://www.sciencedirect.com/science/article/pii/B9780444640277000124.

[37] R. Singh and Geetanjali. “25 - Metal organic frameworks for drug delivery.” In: *Applications of Nanocomposite Materials in Drug Delivery*. Ed. by Inamuddin, A. M. Asiri, and A. Mohammad. Woodhead Publishing Series in Biomaterials. Woodhead Publishing, 2018, pp. 605 –617. ISBN: 978-0-12-813741-3. DOI: https://doi.org/10.1016/B978-0-12-813741-3.00026-1. URL: http://www.sciencedirect.com/science/article/pii/B9780128137413000261.

[38] H. Furukawa, K. E. Cordova, M. O’Keeffe, and O. M. Yaghi. “The Chemistry and Applications of Metal-Organic Frameworks.” In: *Science* 341.6149 (2013). ISSN: 0036-8075. DOI: 10.1126/science.1230444. eprint: https://science.sciencemag.org/content/341/6149/1230444.full.pdf. URL: https://science.sciencemag.org/content/341/6149/1230444.

[39] S. T. Meek, J. A. Greathouse, and M. D. Allendorf. “Metal-Organic Frameworks: A Rapidly Growing Class of Versatile Nanoporous Materials.” In: *Advanced Materials* 23.2 (2011), pp. 249–267. DOI: 10.1002/adma.201002854. eprint: https://onlinelibrary.wiley.com/doi/pdf/10.1002/adma.201002854. URL: https://onlinelibrary.wiley.com/doi/abs/10.1002/adma.201002854.

[40] J. P. B. Mota, D. Martins, D. Lopes, I. Catarino, and G. Bonfait. “Structural Transitions in the MIL-53(Al) Metal–Organic Framework upon Cryogenic Hydrogen Adsorption.” In: *The Journal of Physical Chemistry C* 121.43 (2017), pp. 24252–24263. DOI: 10.1021/acs.jpcc.7b06861. eprint: https://doi.org/10.1021/acs.jpcc.7b06861. URL: https://doi.org/10.1021/acs.jpcc.7b06861.

[41] J. P. Mota. *Report LATPE-VFC-2*. 2016. LABQV-REQUIMTE.

[42] Z. Hulvey, K. V. Lawler, Z. Qiao, J. Zhou, D. Fairen-Jimenez, R. Q. Snurr, S. V. Ushakov, A. Navrotsky, C. M. Brown, and P. M. Forster. “Noble Gas Adsorption in Copper Trimesate, HKUST-1: An Experimental and Computational Study.” In: *The Journal of Physical Chemistry C* 117.39 (2013), pp. 20116–20126. DOI: 10.1021/jp408034u. eprint: https://doi.org/10.1021/jp408034u. URL: https://doi.org/10.1021/jp408034u.

[43] M. D. G. Xavier. *Development of a system for adsorption measurements in the 77-500 K and 1-100 bar range*. 2016.

[44] E. W. Lemmon, M. L. Huber, and M. O. McLinden. *NIST Standard Reference Database 23: Reference Fluid Thermodynamic and Transport Properties - REFPROP*. 9.0. National Institute of Standards and Technology, Standard Reference Data Program. Gaithersburg, 2007.

[45] E. W. Weisstein. *Kepler Conjecture*. From MathWorld–A Wolfram Web Resource. https://mathworld.wolfram.com/KeplerConjecture.html, Accessed: 29-07-2020.

[46] P. I. O'Toole and T. S. Hudson. "New High-Density Packings of Similarly Sized Binary Spheres." In: *The Journal of Physical Chemistry C* 115.39 (2011), pp. 19037–19040. DOI: 10.1021/jp206115p. eprint: https://doi.org/10.1021/jp206115p. URL: https://doi.org/10.1021/jp206115p.

[47] S. Torquato, T. M. Truskett, and P. G. Debenedetti. "Is Random Close Packing of Spheres Well Defined?" In: *Phys. Rev. Lett.* 84 (10 2000), pp. 2064–2067. DOI: 10.1103/PhysRevLett.84.2064. URL: https://link.aps.org/doi/10.1103/PhysRevLett.84.2064.

[48] T. Hudson. *Binary sphere packing LS3*. https://commons.wikimedia.org/wiki/File:Binary_sphere_packing_LS3.png, CC BY-SA 3.0, Accessed: 22-05-2020.

[49] J. Barreto, D. Martins, M. Branco, R. Ribeiro, I. Esteves, J. Mota, J. Branco, A. Gonçalves, T. Tirolien, and G. Bonfait. "80 K vibration-free cooler for potential future Earth observation missions." In: *IOP Conference Series: Materials Science and Engineering* 755 (2020), p. 012016. DOI: 10.1088/1757-899x/755/1/012016. URL: https://doi.org/10.1088%2F1757-899x%2F755%2F1%2F012016.

[50] E. ToolBox. *Darcy-Weisbach Pressure and Major Head Loss Equation*. https://www.engineeringtoolbox.com/darcy-weisbach-equation-d_646.html, Accessed: 25-05-2020.

[51] C. Paine. "Characterization of porous sinter materials as Joule–Thomson restrictors for the Planck sorption cooler." In: *Cryogenics* 44.6 (2004). 2003 Space Cryogenics Workshop, pp. 425 –429. ISSN: 0011-2275. DOI: https://doi.org/10.1016/j.cryogenics.2004.02.015. URL: http://www.sciencedirect.com/science/article/pii/S0011227504000554.

[52] J. F. Burger, H. J. Holland, R. J. Meijer, A. Sirbi, and H. J. M. ter Brake. "VIBRATION FREE 4.5 K SORPTION COOLER." In: *AIP Conference Proceedings* 985.1 (2008), pp. 1613–1620. DOI: 10.1063/1.2908529. eprint: https://aip.scitation.org/doi/pdf/10.1063/1.2908529. URL: https://aip.scitation.org/doi/abs/10.1063/1.2908529.

[53] M. C. Potter. *Mechanics of Fluids*. CL Engineering, 2001. ISBN: 0534379966. URL: https://www.xarg.org/ref/a/0534379966/.

[54] D. W. Green and R. H. Perry. *Perry's Chemical Engineers' Handbook, Eighth Edition*. eng. 8th. New York: McGraw-Hill Education, 2008. ISBN: 9780071422949. URL: https://www.accessengineeringlibrary.com/content/book/9780071422949.

[55] B.-Z. Maytal and E. Elias. "Two-phase choking conditions of real gases flow at their critical stagnation temperatures and closely above." In: *Cryogenics* 49.9 (2009), pp. 469 –481. ISSN: 0011-2275. DOI: https://doi.org/10.1016/j.cryogenics.2009.06.009. URL: http://www.sciencedirect.com/science/article/pii/S0011227509001039.

[56] J. D. A. Jr. *Fundamentals of Aerodynamics*. McGraw-Hill Education, 2010. ISBN: 0073398101. URL: https://www.xarg.org/ref/a/0073398101/.

[57] F. P. Incropera. *Fundamentals of Heat and Mass Transfer*. John Wiley and Sons, 2006. ISBN: 0471457280. URL: https://www.xarg.org/ref/a/0471457280/.

[58] A. W. Adamson. *Physical Chemistry of Surfaces*. Wiley-Interscience, 1997. ISBN: 0471148733. URL: https://www.xarg.org/ref/a/0471148733/.

[59] D. Fester, R. Eberhardt, and J. Tegart. *Behavior of fluids in a weightless environment*. 1977. URL: https://ntrs.nasa.gov/search.jsp?R=19770010736.

[60] E. C. C. Baly and F. G. Donnan. "XCIII.—The variation with temperature of the surface energies and densities of liquid oxygen, nitrogen, argon, and carbon monoxide." In: *J. Chem. Soc., Trans.* 81 (0 1902), pp. 907–923. DOI: 10.1039/CT9028100907. URL: http://dx.doi.org/10.1039/CT9028100907.

[61] F. B. Sprow and J. M. Prausnitz. "Surface tensions of simple liquids." In: *Trans. Faraday Soc.* 62 (0 1966), pp. 1097–1104. DOI: 10.1039/TF9666201097. URL: http://dx.doi.org/10.1039/TF9666201097.

[62] D Stansfield. "The Surface Tensions of Liquid Argon and Nitrogen." In: *Proceedings of the Physical Society* 72.5 (1958), pp. 854–866. DOI: 10.1088/0370-1328/72/5/321. URL: https://doi.org/10.1088%2F0370-1328%2F72%2F5%2F321.

[63] M. G OSTROMOUKHOV V. B; OSTRONOV. "Surface tension of liquid O2-N2 solutions at 54-77 K." Russian. In: *Russian journal of physical chemistry* (1994). ISSN: 0036-0244.

[64] P. B. d. Sousa. "Liquid hydrogen thermal energy storage unit for future ESA science missions." Doctoral dissertation. Portugal: Universidade Nova de Lisboa, 2016. URL: https://run.unl.pt/handle/10362/18353.

[65] P. B. de Sousa, D. Martins, M. Linder, J. Noite, and G. Bonfait. "Liquid-gas hydrogen energy storage unit for the 15–17K temperature range using an expansion volume at room temperature." In: *Applied Thermal Engineering* 125 (2017), pp. 1239 –1252. ISSN: 1359-4311. DOI: https://doi.org/10.1016/j.applthermaleng.2017.06.134. URL: http://www.sciencedirect.com/science/article/pii/S1359431117324146.

[66] J. Afonso, D. Martins, I. Catarino, R. Patrício, A. Rocaboy, T. Tirolien, and G. Bonfait. "Liquid–gas cryogenic energy storage units operating at constant temperature." In: *Applied Thermal Engineering* 95 (2016), pp. 178 –185. ISSN: 1359-4311. DOI: https://doi.org/10.1016/j.applthermaleng.2015.11.059. URL: http://www.sciencedirect.com/science/article/pii/S1359431115013058.

[67] J. Afonso, I. Catarino, R. Patrício, A. Rocaboy, M. Linder, and G. Bonfait. "Liquid nitrogen energy storage unit." In: *Cryogenics* 51.11 (2011), pp. 621 –629. ISSN: 0011-2275. DOI: https://doi.org/10.1016/j.cryogenics.2011.09.008. URL: http://www.sciencedirect.com/science/article/pii/S001122751100169X.

[68] D. F. Martins. "40 K Neon liquid energy storage unit." Doctoral dissertation. Portugal: Universidade Nova de Lisboa, 2014. URL: https://run.unl.pt/handle/10362/14565.

[69] R. Components. *Platinum Resistance Thermometer (PRT) Selection Guide*. https://docs.rs-online.com/8631/0900766b815e770e.pdf, Accessed: 20-04-2020.

[70] E. Tal-Gutelmacher and D. Eliezer. "The hydrogen embrittlement of titanium-based alloys." In: *JOM* 57.9 (2005), pp. 46–49. ISSN: 1047-4838. DOI: 10.1007/s11837-005-0115-0. URL: https://doi.org/10.1007/s11837-005-0115-0http://link.springer.com/10.1007/s11837-005-0115-0.

[71] A. S. Technologies. *Design Description and Justification File*. 2017.

[72] MatWeb. *MatWeb material property data - Copper, Cu; Annealed*. https://tinyurl.com/y2v79phl, Accessed: 26-06-2020.

[73] *Space Engineering: Structural general requirements, ECSS-E-ST-32C Rev. 1*. 2008.

[74] J. Franco, B. Galinhas, P. B. de Sousa, D. Martins, I. Catarino, and G. Bonfait. "Building a Thinner Gap in a Gas-Gap Heat Switch." In: *Physics Procedia* 67 (2015). Proceedings of the 25th International Cryogenic Engineering Conference and International Cryogenic Materials Conference 2014, pp. 1117 –1122. ISSN: 1875-3892. DOI: https://doi.org/10.1016/j.phpro.2015.06.173. URL: http://www.sciencedirect.com/science/article/pii/S1875389215005544.

[75] S. Vanapalli, B. Colijn, C. Vermeer, H. Holland, T. Tirolien, and H. [ter Brake]. "A Passive, Adaptive and Autonomous Gas Gap heat Switch." In: *Physics Procedia* 67 (2015). Proceedings of the 25th International Cryogenic Engineering Conference and International Cryogenic Materials Conference 2014, pp. 1206 –1211. ISSN: 1875-3892. DOI: https://doi.org/10.1016/j.phpro.2015.06.191. URL: http://www.sciencedirect.com/science/article/pii/S1875389215005726.

[76] J. L. Lizon and M. Accardo. "LN2 continuous flow cryostats: a compact vibration free cooling system for single to multiple detector systems." In: *Modern Technologies in Space- and Ground-based Telescopes and Instrumentation*. Ed. by E. Atad-Ettedgui and D. Lemke. Vol. 7739. International Society for Optics and Photonics. SPIE, 2010, pp. 1226 –1232. DOI: 10.1117/12.856013. URL: https://doi.org/10.1117/12.856013.

[77] NEOPERL. *Glossary for check valves*. https://www.neoperl.net/en/oem/products/checkvalves/glossary.html, Accessed: 24-04-2020.

[78] T. Veenstra, G. Venhorst, J. Burger, H. Holland, H. ter Brake, A. Sirbi, and H. Rogalla. "Development of a stainless steel check valve for cryogenic applications." In: *Cryogenics* 47.2 (2007), pp. 121 –126. ISSN: 0011-2275. DOI: https://doi.org/10.1016/j.cryogenics.2006.10.004. URL: http://www.sciencedirect.com/science/article/pii/S0011227506001767.

[79] N. I. of Standards and T. (U.S.) *NIST Monograph*. NIST Monograph n.º 177. U.S. Department of Commerce, National Institute of Standards and Technology, 1992. URL: https://books.google.pt/books?id=TxRWAAAAYAAJ.

[80] F. Kloutse, R. Zacharia, D. Cossement, and R. Chahine. "Specific heat capacities of MOF-5, Cu-BTC, Fe-BTC, MOF-177 and MIL-53 (Al) over wide temperature ranges: Measurements and application of empirical group contribution method." In: *Microporous and Mesoporous Materials* 217 (2015), pp. 1 –5. ISSN: 1387-1811. DOI: https://doi.org/10.1016/j.micromeso.2015.05.047. URL: http://www.sciencedirect.com/science/article/pii/S1387181115003248.

APPENDIX A

# GGHS article

The design, construction and tests of three GGHSs prototypes resulted in a rather extensive work. Its detailed description was considered too large to be included in this dissertation; so, the whole work can be consulted here as a first version of an article to be submitted to *Cryogenics* (journal).

# New hydrogen dilatation GGHS operating in the 150 K to 400 K temperature range

*Jorge Barreto[a], Daniel Martins[b], Moritz Branco[b,c], Joaquim Branco[d], António Pereira Gonçalves[d], Grégoire Bonfait[a]*

a) LIBPhys, Departamento de Física, Faculdade de Ciências e Tecnologia, Universidade NOVA de Lisboa, 2829-516 Caparica, Portugal

b) Active Space Technologies S.A., Parque Industrial de Taveiro, Lote 12, 3045-508 Coimbra, Portugal

c) European Space Agency, ESTEC, E0053A, 2200 AG Noordwijk, The Netherlands

d) C2TN, Departamento de Engenharia e Ciências Nucleares, Instituto Superior Técnico, Universidade de Lisboa, 2695-066 Bobadela, Portugal

**Corresponding Author**

Grégoire Bonfait (e-mail: gb@fct.unl.pt)

**Author Contributions**

The manuscript was written through contributions of all authors. All authors have given approval to the final version of the manuscript.

**Abstract**

A prototype of a compact hydrogen gas gap heat switch (GGHS), built using the difference in the linear thermal expansion coefficients of copper and stainless steel, was designed to work in the temperature range of 150 K to 400 K. Using hydrogen, nitrogen and helium as working gas, a gap of 18 micrometers was measured. With hydrogen, an ON/OFF switching ratio higher than 100 was obtained at 150 K. A sorption pump was integrated to the GGHS and filled with the metal hydride ZrMn2 to overcome the very low adsorption of hydrogen with activated carbon, material frequently used to manage the pressure in the gap. This solution allowed to reach both ON and OFF states by varying its temperature between 150 K and 300 K. The results obtained suggest that the proposed design allows for the development of tunable hydrogen heat switches while keeping the assembly very simple and sturdy.

**Keywords**

Gas Gap Heat Switch; Adsorption; Hydrogen, Metal Hydride

## 1. Introduction

The cryogenic heat switches are devices able to vary their thermal conductance by several orders of magnitude [1]–[3] and are fundamental pieces of some dynamic cryogenic systems. For instance, they have been used for a long time in adiabatic demagnetization refrigerators [4], they would be useful to (de)couple redundant cryocoolers of the system to be cooled [5], they were also used in the Herschel satellite for thermal management of the $^3$He cryocooler [6] and also attached to high enthalpy reservoirs for cryogenic thermal energy storage units [7], [8]. In these two last applications, Gas Gap Heat Switches (GGHS) were developed: they consist in two highly conducting blocks, usually copper, separated by a narrow gap. Introducing gas into this gap at a pressure corresponding to the viscous regime (mean free path $\lambda$ << gap length $\Delta$) leads to a highly conducting state (ON state), whereas pumping it down to the molecular regime ($\lambda$ >> $\Delta$) allows to drastically reduce the conduction between the two blocks. Actually, in a GGHS, this very low conducting state (OFF state) is usually limited by the thermal conductance of the mechanical support of the blocks, in parallel to the block-gap-block thermal path, that maintains the two blocks separated and aligned [9]. The main benefits of a GGHS are that no mobile parts are needed, avoiding problems due to complicated mechanisms or material fatigue. Thanks to these advantages, they are very suitable for cryogenic systems in which long lifetimes are expected without any maintenance as in satellites, for instance.

In a GGHS, the shorter the gap, the greater the ON thermal conductance. In "usual" GGHS, gap lengths as small as 100 μm were obtained thanks to precise machining and somewhat delicate alignment procedures. Recently, a technique based on the difference in the linear thermal expansion coefficients (CTE) between the copper blocks and the stainless-steel (SS) mechanical support was used to obtain smaller gap lengths (down to 17 μm) without the need of such complicated procedures [10], [11]. GGHSs built using such technique were tested and showed good features in the 4 K to 300 K temperature range. However, one issue with this technique is that such small gaps were obtained through a soft soldering procedure (180 °C) to join the stainless-steel support to the copper blocks, and the poor mechanical properties of this joint turns out this device not reliable if submitted to high vibration levels, as it occurs during the launch of a satellite, for instance.

In this paper, we describe a dilatation GGHS to be integrated between a sorption compressor cell and a heat sink at a temperature of 150 K. As this sorption cell temperature has to vary in the 160 K to 400 K range, such a GGHS offers the ability to thermally (de)couple these two

parts and, thus, to optimize and control the dynamics of the heating and cooling phases of the sorption compressor [12].

After a brief description of how were calculated some basic features of such devices, we show the thermal characteristics of a dilatation GGHS entirely assembled with a new brazing process at 650 °C, turning it much more structurally robust than the earlier. Thermal conductance measurements were performed in the temperature range of 100 K to 300 K with hydrogen, nitrogen and helium gas to determine experimentally its gap length and its thermal conductance as a function of pressure to obtain the characteristic OFF to ON transition. For low temperature GGHS, the gas gap pressure management is usually obtained by using a small adsorption pump (referred as "cryopump" on the following) filled with activated carbon: the very low pressure (OFF state) is reached by cooling it; whereas on heating, gas is desorbed and the ON state can be achieved. Unfortunately, a cryopump for both helium and hydrogen (the highest conducting gases, so, the most suitable for GGHS) is limited to the low temperature range, typically below 20 K for helium and 40 K for hydrogen, very far from our 150 K heat sink temperature. As already experienced [7, 8] or proposed [15], another way to pump hydrogen gas down to suitable pressures to achieve the switching action of a GGHS (typically below $10^{-1}$ mbar) is $H_2$ adsorption using adequate intermetallic materials. In the second part of this article, the features of a GGHS integrating a cryopump filled with the intermetallic compound ZrMn2 are described and compared to what was expected in the 150 K to 300 K temperature range.

## 2. Dilatation GGHS and Experimental Set-up

### 2.1 Dilatation GGHS Principle

The ON↔OFF switching mechanism of a dilation GGHS is based on the same principle of an usual GGHS, the difference being that the gap is obtained thanks to the CTE difference between the material used for the supporting shell (stainless steel) and the two conducting blocks (copper) [11]. In the devices presented in this paper, these two copper blocks are cylindrical and are maintained face-to-face thanks to a Stainless Steel Supporting Shell (SSSS), consisting in a thin wall tube (Figure 1a). The SSSS length is such that it allows physical contact between the copper blocks after mounting: the gap between the copper blocks is then null before brazing and must be kept as short as possible, ideally null, during the brazing process. After brazing and during cooling, due to the higher CTE of copper in respect to stainless steel, the total length of the copper blocks becomes shorter in comparison with that of the SSSS and a gap is formed (Figure 1b). One advantage of such technique is that it requires a much simpler manufacturing

and assembly procedure, since the gap is “naturally” obtained and the delicate machining and alignment procedures to prevent contact between the copper pieces in usual GGHS are avoided.

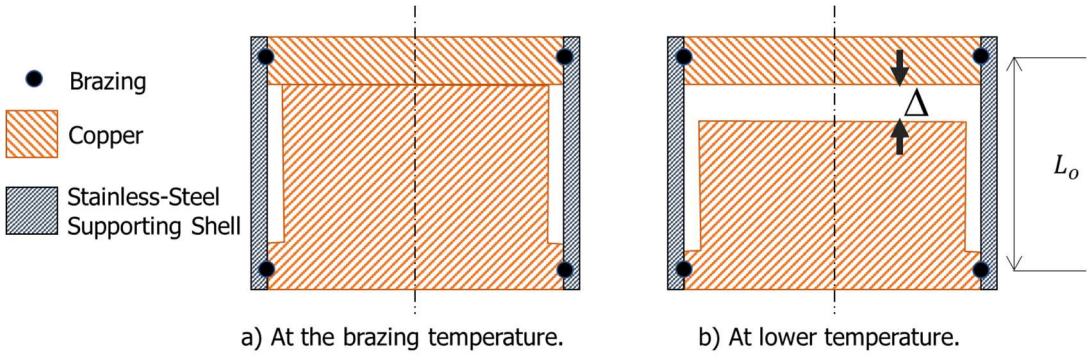


**Figure 1:** Cross-sectional schematic view of a dilation GGHS at the brazing temperature (left) with the copper blocks in contact, and after brazing and during cooling (right) where a gap, Δ, naturally appears due to the difference in the CTE of copper and stainless-steel.

Such dilatation GGHSs were built and tested between 20 K and room temperature with relative success [10], [11]: below 80 K, where CTE become negligible, a gap length of 17 µm was obtained, significantly longer than the 6 µm previously calculated [9]. Due to the gap formation technique, the soldering/brazing temperature, $T_0$, should be as low as possible to minimize the gap appearing due to the device cooling from $T_0$ down to room temperature. In [10], a common soft-soldering was used with a melting point of 180°C to reduce this effect. However, at that time, such soldering procedure was performed on a workbench and the external surface of the SSSS was exposed to air and naturally cooled by convection, so, remaining over a significant length at a temperature lower than that of the copper blocks: after soldering and during cooldown, the SSSS contracted less than expected, explaining why the gap length was found significantly longer than calculated (6 µm at 80K), assuming a homogeneous temperature during soldering. Despite this issue, such device was tested with helium and nitrogen gas and its thermal features found in good agreement with developed thermal models. However, for some applications, as its integration in a satellite thermal bus, such soft soldering cord is not mechanically strong enough to withstand the high levels of vibration. Consequently, a new dilatation GGHS was built using a silver brazing procedure ($T_0 = 650$°C) that turns out this mechanical joint sturdier. Moreover, to minimize de gap, special care was taken to avoid temperature inhomogeneity during brazing, as occurred previously.

## 2.2. Gap length calculation

Three slightly different dilatation gas gap heat switches were built (GGHS #1, #2 and #3). Their main parts (Figure 2) are cylindrical and their geometrical characteristics shown in Table 1. The cylindrical copper blocks were machined from "normal" copper (RRR between 50 and 100). The supporting shells were obtained from a commercial tube (GGHS #1) or machined by us (GGHS #2 and #3). To avoid long thermal response times during the characterization tests, one of the copper blocks (hot side) was designed as short as possible to reduce its mass and, therefore, the length to be considered for dilatation and thermal conductance calculus is mainly the cold block one. The GGHS #2, shown in Figure 2, includes a small cryopump connected by a ≈20 mm length stainless steel capillary (further details in Section 4).

Contrarily to the procedure used in the previous versions of the dilatation GGHS [10], to avoid a significant temperature difference between the copper blocks and the SSSS during brazing, the whole device was heated up to the brazing paste melting point temperature ($T_o$ = 650°C) in a temperature-controlled oven filled with nitrogen gas.

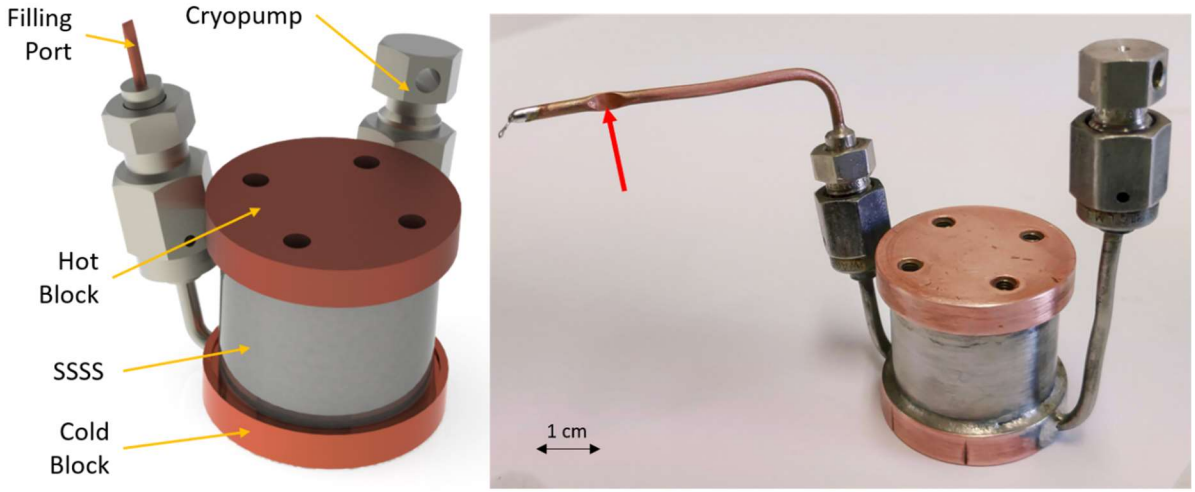


**Figure 2:** Dilation GGHS #2 rendered image (left side) and as built (right side). The red arrow points to the location of the "pinch-off" sealing. This sealed switch is the one used to obtain the results "Sealed Desorption/Absorption" displayed in Figure 8.

Considering the GGHS geometry, if the two copper blocks are in contact at $T_o$, while considering the entire length of the SSSS also at the same temperature during this procedure, the gap length Δ(T) at a temperature $T$ can be calculated as follows:

$$\Delta(\mathrm{T}) = L_o \int_{T_0}^{T} \left(\alpha_{Cu}(T) - \alpha_{SS}(T)\right) dT \qquad \textbf{Equation 1}$$

where $L_o$ is the length of the SSSS at $T_0$, $\alpha_{Cu}$ and $\alpha_{SS}$ are the CTE of copper and stainless steel, respectively.

**Table 1:** GGHS geometrical characteristics and expected thermal performance at 150 K with hydrogen as the exchange gas.

| GGHS number / Feature | #1 | #2 | #3 |
|---|---|---|---|
| GGHS total length | 24.8 mm | 29 mm | 34 mm |
| Inner copper block length ($L_{Cu}$=$Lo$) | 17.0 mm | 17.0 mm | 17.0 mm |
| Inner copper block diameter | 17.5 mm | 24.8 mm | 25.0 mm |
| Face to face area (A) | 2.41 $cm^2$ | 4.83 $cm^2$ | 4.91 $cm^2$ |
| Mass | 64.0 g | 167.4 g | 160.1 g |
| SSSS external diameter | 18.92 mm | 26.26 mm | 26.27 mm |
| SSSS thickness | 110 µm | 130 µm | 114 µm |
| SSSS length ($L_{SSSS}$) | 18.8 mm | 18.8 mm | 18.8 mm |
| $\alpha_{Cu}$ (300 K) [16] | $16.6x10^{-6}$ | | |
| $\alpha_{SS}$ (300 K) [16] | $15.4x10^{-6}$ | | |
| Gap Δ at 150 K | ≈ 15 µm | | |
| Gas-gap conductance (H2) | 1.60 W/K | 3.21 W/K | 3.27 W/K |
| Cu block conductance | 5.23 W/K | 10.5 W/K | 10.7 W/ K |
| K-ON | 1.23 W/K | 2.46 W/K | 2.50 W/K |
| K-OFF (SSSS) | 3.9 mW/K | 6.3 mW/K | 5.6 mW/K |
| ON/OFF ratio | $3.2\times 10^2$ | $3.9\times 10^2$ | $4.5\times 10^2$ |

The linear expansion coefficients obtained from various databases (NIST [16], Matweb [17], Touloukian [18]) present small differences and, the gap length depending on the difference of two very similar CTE coefficients (Table 1), these discrepancies can lead to quite different gap length: for instance, a relative uncertainty of 1% on each CTE leads to a gap uncertainty of 40%. So, in such conditions, a precise Δ(T) calculation becomes quite challenging. Then, to obtain a rough approximation of the gap values, we decided to calculate it by considering the NIST values for copper and SS316 in the temperature range of 4 K to 300 K and keeping constant the differential CTE from room temperature up to the 650°C. This calculation leads to the Δ(T) displayed in Figure 3 ($\Delta_o = 0$ line). The experimental gap determinations obtained with various gases, as explained in the following section, are presented on the same figure, and show that this crude extrapolation may not be so far from reality. In any case, below 90 K, the calculated gap length is almost constant, reflecting that, as for most metals, the CTE of copper and SS become residual in this temperature range. In the range 100 K to 300 K, the NIST data lead to a linear behaviour of the gap length variation with temperature (nearly constant α for

both metals in this range). Usually, for temperatures higher than 300 K, the CTE tends to increase. Then, extrapolating this linear behaviour for higher temperatures would mean, for instance, that this increase is equal for both materials. Using this rough extrapolation, the gap obtained at 150 K would be about 15.2 µm (considering $\Delta = 0$ at 650°C). If for any mechanical reason (e.g. high roughness, solid impurities between the two blocks, parallelism defect of the copper blocks) the gap at the brazing temperature $\Delta_o = \Delta(T_0)$ is not zero, the final gap will be obtained by adding $\Delta_o$ to the calculated values of Figure 3.

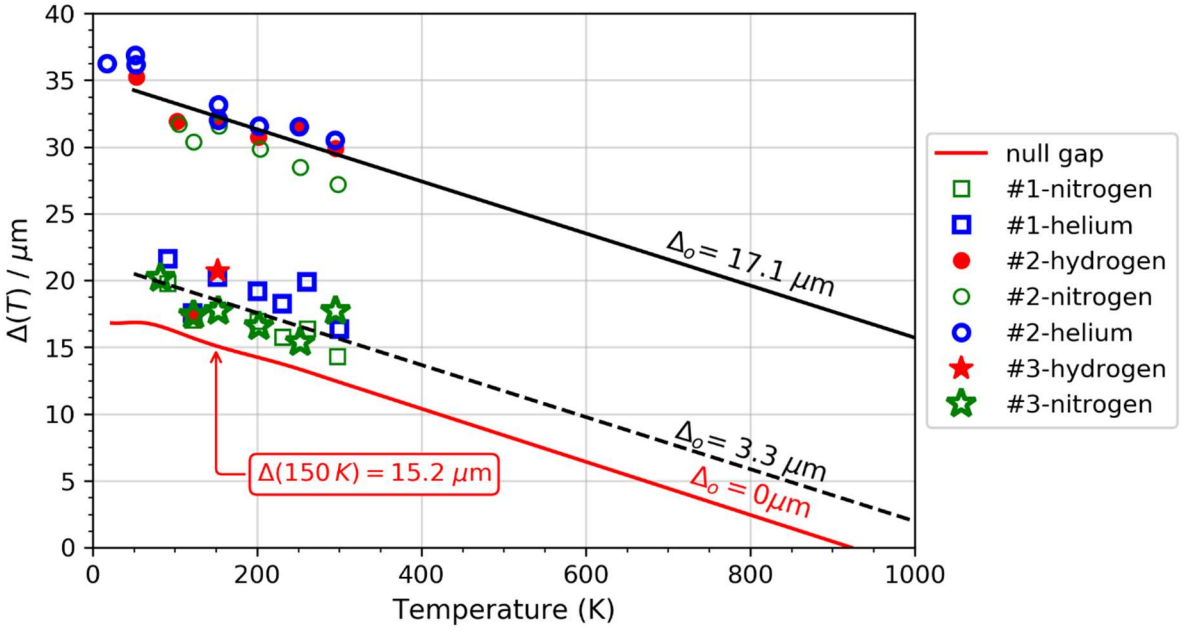


**Figure 3:** Gap length $\Delta(T)$ as a function of temperature considering $L_o$ =17 mm and various values for the gap length $\Delta_o$ at $T_0$. The symbols represent the experimental gap determination for GGHS#1-3 using various gases as explained in Section 2.3.

### 2.3 Experimental Setup and Thermal Conductance Determination

The experimental setup is very similar to those used in previous GGHS characterizations [9], [10]. The long copper block (cold block) is thermally coupled to the cold finger of a 4 K Gifford-McMahon cryocooler and three previously calibrated thermometers are thermalized to the copper block and to the cryopump (if any); one small heater (1.2 kΩ electronic resistor) is attached to the shorter copper block (hot block) to create a heat flux across the switch; for GGHS #2, another resistor was placed on the cryopump to control its temperature. A short stainless-steel capillary is brazed to the cold block and ends by a female connector. For GGHS#1 and #3, a 1-meter long SS capillary, ended by the male part, links the inner part of the switch to a room temperature gas manifold for gas management and pressure measurements. For GGHS #2, as depicted in Figure 2, a small portion of soft copper capillary is placed between

the long SS capillary and the male connector: Pinching this portion will allow to permanently seal the device (Cf. Section 4.2) and turn it easily autonomous. To precisely measure the thermal conductance, the cold block temperature, $T_{CB}$, was kept constant and various heat loads, $\dot{Q}$, were applied on the hot block ($T_{HB}$) while keeping, in most cases, $\Delta T = T_{HB} - T_{CB}$ below ≈10 K. At equilibrium, the corresponding temperature $T_{HB}$ was measured and the thermal conductance $K$ is then calculated as the slope of $d\dot{Q}/dT_{HB}$. Such method allows to minimize errors due to some parasitical heat loads or small calibration imperfections. However, this method imposes equilibrium states that can be very long to be reached if the thermal conductance decreases. Then, to speed up the conductance measurements as a function of the cryopump temperature, $T_{sorb}$, a dynamic method, similar to that used for specific heat determination [8], [9], was used and lead to the results of Figure 8. In such a method, the hot block temperature is maintained slowly drifting, keeping $\Delta T$ around 10 K, by applying some external heating for instance, and its temperature variation $T_{HB}(t)$ is recorded. By (numerical) time derivative, $dT_{HB}/dt, \dot{T}_{HB}$ is calculated and the thermal conductance can be obtained as:

$$K(\bar{T})(T_{HB} - T_{CB}) = \dot{Q} - C\dot{T}_{HB} \qquad \textbf{Equation 2}$$

where $K(\bar{T})$ is the mean conductance between $T_{HB}$ and $T_{CB}$, $\dot{Q}$ is the heat input applied to the hot block (considered much higher than parasitical heat load) and $C$ is the hot block heat capacity. Which is calculated using its mass (≈ 33 g) and the NIST data for copper [16]. Simultaneously, by varying (slowly) also the cryopump temperature $T_0$ between ≈150 K and ≈400 K (Section 4) and using Equation 2, the measurements of the GGHS conductance during the OFF↔ON transition is obtained in only one run (typically one day). Though this method is not as precise as that using static conditions, it allows a much faster characterization since the long stabilization times of the hot block temperature and of the cryopump are not required. From previous measurements [10], the contribution of the thermometer, the heater and other small pieces to the hot block heat capacity were estimated to be equivalent to ≈3 g of copper, value found coherent after comparing the dynamic results to the static ones.

## 3. Experimental Results (without cryopump)

### 3.1 ON Thermal Conductance and Gap Length Determination

The ON state conductance of the GGHS, $K_{ON}$, is obtained when the gas in the gap is in the viscous regime, characterized by a thermal conductivity independent of the pressure. To

confirm if such regime is achieved, it is then experimentally verified that two $K_{ON}$ determinations at different pressures give the same results. Figure 4 shows the ON thermal conductance of the GGHS #2 in this regime for three different gases. The pressure in the heat-switch used for these measurements was kept constant and measured at room temperature (450 mbar, 520 mbar, 620 mbar for $H_2$, He and $N_2$ respectively).

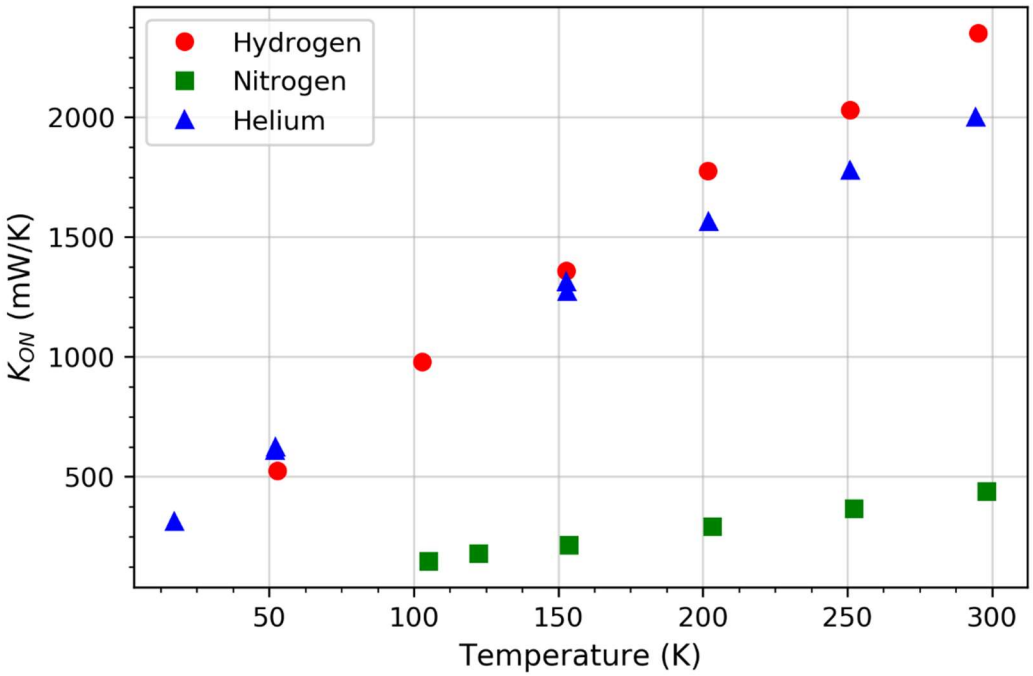


**Figure 4:** Experimental thermal conductance $K_{ON}$ of GGHS #2 using various exchange gases. Note the higher conductance values with hydrogen for T>150 K.

To obtain the gap length from these results, the ON conductance must be divided into two major contributions:

- $K_{\Delta}$, arising from the gas thermal conduction through the gap.
- $K_{Cu}$, coming from the conduction along the copper block, which can be calculated as $k_{Cu} \times L_{Cu}/A$ ($k_{Cu}$: copper thermal conductivity [16], $k_{Cu}$: face-to-face area of copper blocks).

Considering these two thermal path in series, $K_{\Delta}$ can be calculated as $K_{\Delta} = K_{Cu} \times K_{ON}/(K_{Cu} - K_{ON})$ and, in the viscous regime, the gap length is given by $\Delta = k_{gas} \times A/K_{\Delta}$ ($k_{gas}$ : gas thermal conductivity values [19]). $\Delta(T)$ was calculated from the $K_{ON}(T)$ experimental values of GGHS#1-3 and these results are displayed in Figure 3 to be compared with the expected results ($\Delta_0 = 0$ line). In the same chart, are also plotted two other lines ($\Delta_o = 3.3$ µm, $\Delta_o =$ 17.1µm) representing $\Delta(T)$ calculated from the differential CTE, as previously described, but only differing by a vertical shift $\Delta_o$ which corresponds to a non-zero gap value at the brazing

temperature $T_0$. These $\Delta_o$ values were adjusted to describe the experimental results for the gap length. Some remarks are noteworthy:

- Within the experimental errors, the experimental gas gap determination is independent of the exchange gas, which validates our data analysis.
- The results for two different GHHS (#1 (squared) and #3 (stars)) are identical and not far from the $\Delta_0 = 0$ prediction. This could indicate that $\Delta_0$ is effectively null for these two switches but that the extrapolation for the 300 K to 900 K temperature range of the CTE coefficients leading to a linear dependence of $\Delta(T)$ in this range is not valid. For instance, the obtained value of $\Delta_0$ could be explained by an increase of the differential CTE, $\left(\alpha_{Cu}(T) - \alpha_{SS}(T)\right)$, in the extrapolated temperature range. Let us mention that the relatively small values of $\Delta_0$ (≈3 μm) could also be compatible with some mechanical imperfections that may occur during the manufacture or assembly of the parts, which would prevent a full contact between the two copper surfaces when the brazing procedure begins. The fact that $\Delta_0$ is similar for the two devices would be a coincidence.
- On the other hand, the data obtained for the GGHS#2 (circles) corresponds to a large shift ($\Delta_0 \approx 17$ μm) which, most likely, can be attributed to some troubles that occurred during its manufacture and/or brazing, leading to a real large gap at the brazing temperature.

### 3.2 OFF Thermal Conductance

To obtain the lowest conductance state (OFF state), the pressure between the two blocks must be low enough to reach the ballistic (or molecular, or Knudsen) regime in which the conduction through the gas becomes linear with pressure. In this regime, the thermal conductance through the gas-gap can becomes much lower than that through the SSSS. Then, in this condition, the heat load $\dot{Q}(T_{HB}, T_{CB})$ through the GGHS is given by:

$$\dot{Q}(T_{HB}, T_{CB}) = \frac{A_{SSSS}}{L_{SSSS}} \int_{T_{CB}}^{T_{HB}} k_{ss}(T) dT \qquad \textbf{Equation 3}$$

where $A_{SSSS}$ represents the cross-sectional surface of the SSSS and $k_{SS}$ is the thermal conductivity of the stainless steel. The results of this equation for GGHS#2 are displayed in Figure 5 as a function of $\Delta T = T_{HB} - T_{CB}$ (solid line, "model SS") with $T_{CB} = 150$ K.

In the same figure are also displayed the corresponding experimental data of $\dot{Q}(\Delta T)$ for the GGHS#2 in the OFF state obtained by two ways. The first one (circle symbols) is obtained on the GGHS#2 before the cryopump functionalization (i.e. no absorption material inside): the inner volume of the device was connected directly to the vacuum (< $10^{-4}$ mbar) existing in the vacuum jacket of the cryocooler. This configuration leads to a very low pressure in the gap and thus ensures that the OFF state is reached. On the other hand, the squared symbols correspond to data obtained with the same GGHS after the installation of the operational cryopump (right side of Figure 2) filled with an intermetallic material and sealed by pinching off the soft copper capillary with a charge of gas $H_2$ that allows to reach the ON state if heated (further details in Section 4). For these measurements, the cryopump temperature is maintained at 150 K, temperature at which the intermetallic compound is expected to reduce drastically the $H_2$ pressure. These two sets of data show that either with the device sealed or not, the OFF-state performance is similar in both scenarios, showing that the cryopump is able to ensure the OFF state. For $\Delta T \leq 60$ K (dashed blue line), both results agree with the model, leading to an OFF conductance of approximately ≈ 8.4 mW/K. For higher $\Delta T$, the discrepancy between the data and the model can be explained considering the radiative heat transfer between the copper blocks. For instance, the simple Stefan-Boltzmann equation, $\dot{Q} = \varepsilon\sigma A(T_{HB}^4 - T_{CB}^4)$, using an emissivity, $\varepsilon$= 0.35 and an exchange surface $A$ equal to the cross-sectional area of the copper blocks, leads to the red dot-dashed line in very good agreement with experimental data. Similar agreements were found for GGHS #1 and #3.

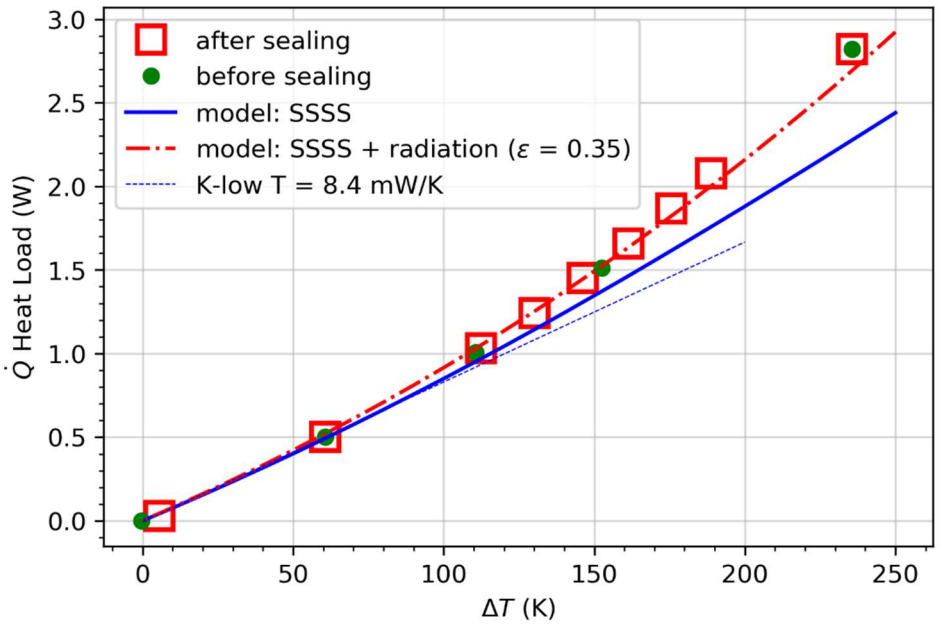


**Figure 5:** Heat load through GGHS#2 versus $\Delta T = T_{HB} - T_{CB}$ in the OFF state, $T_{CB} = 150$ K.

### 3.3 ON↔OFF Transition

In general, in such GGHS, the ON↔OFF transition is controlled by varying the pressure, $P$, in the gap thanks to heating/cooling a cryopump containing a material able to desorb/adsorb the working gas. The correct operation of this actuator is then dependent of the adequate adsorptive capacities of the pair gas/adsorbent in the targeted operating temperature range. That is why the variation of the GGHS #2 thermal conductance $K(P)$ in respect to the working gas pressure has been carefully measured without adsorbing material in cryopump. This conductance was measured for $T_{CB} = 150$ K in the pressure range $4 \times 10^{-3}$ mbar to 800 mbar for both $H_2$ and $N_2$, the results (symbols) are displayed in Figure 6. The experimental results are also fitted to a previously developed thermal model where the gas gap conductance in the intermediate regime is calculated by considering a contribution of both ballistic and viscous conduction regimes [20]. For the ballistic regime, the accommodation coefficients, which are dependent of the gas and of the surface material, were obtained by fitting the experimental results and were found to be 0.38 and 0.83 for hydrogen and nitrogen gas, respectively, in line with previous works [15]. The resulting fits of the thermal conductance are displayed as lines in Figure 6.

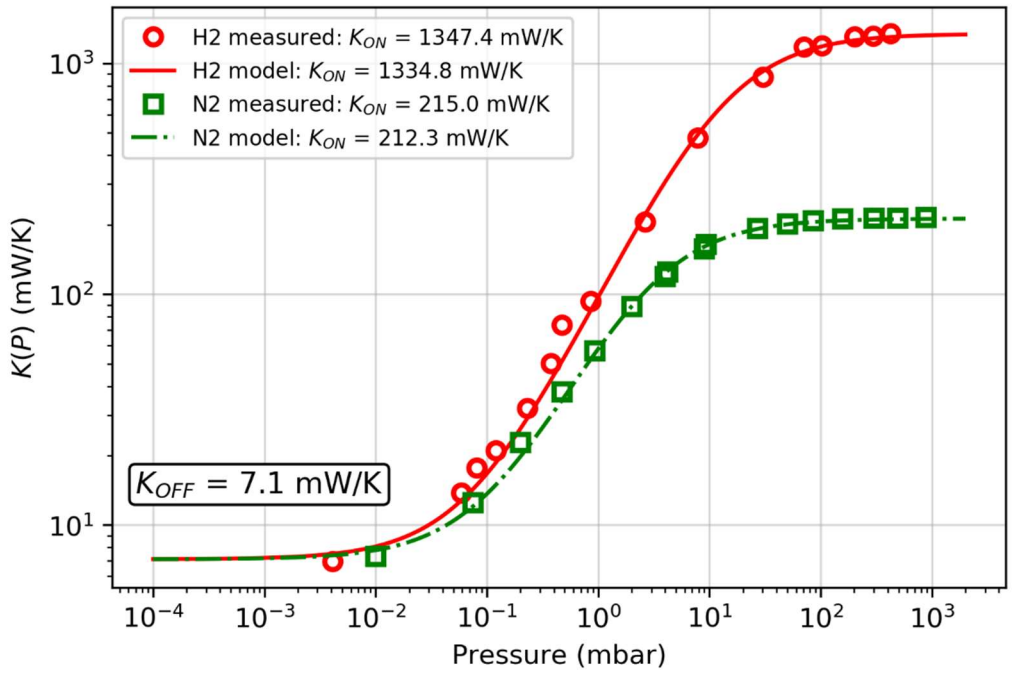


**Figure 6:** Measured thermal conductance $K(P)$ as a function of pressure for GGHS #2 using hydrogen (circle) and nitrogen (square) as exchange gas. The solid lines correspond to the fit of the conductance using an accommodation coefficient of 0.38 for hydrogen and 0.83 for nitrogen.

As expected, in the high pressure regime, the GGHS conductance ($\sim$1350 mW/K for $H_2$ and $\sim$215 mW/K for $N_2$) does not depend on pressure and is the same as previously obtained in the viscous regime measurement at 150 K (Figure 4). On the other hand, at low pressure, the gas gap conductance becomes very low and the SSSS ensures the main thermal path leading to both pressure and gas independent OFF constant value ($\approx$7.1 mW/K). Between these two extreme states, the smooth transition ON$\leftrightarrow$OFF is very well described by our model for both $H_2$ and $N_2$ gas. Considering these results, the cryopump adsorbent material required to obtain the ON$\leftrightarrow$OFF switching action must be able to vary the gap pressure by four orders of magnitude: from $\approx$100 mbar at high temperature to $\approx$ 0.01 mbar for $T_{sorb}$ =150 K.

## 4. GGHS driven by a metal hydride cryopump

### 4.1 ZrMn2 Preparation and Characterization

As previously explained, the ON thermal conductance is strongly dependent on the thermal conductivity of the working gas. From this point of view, helium and hydrogen are the best choices. However, both gases require low temperatures to be sufficiently adsorbed by a cryopump filled with activated charcoal, typically 20 K for helium [7] and 50 K for hydrogen [21], [22] temperatures not in accordance with the present requirements (base temperature at 150 K). Nevertheless, in the case of hydrogen another possibility is to use the ability to be reversely adsorbed and desorbed in metal hydrides, which can occur at temperatures a priori compatibles with our goal [15]. Let us note that intermetallic hydrides have already been used in the space scientific mission Planck, from ESA, to build a hydrogen sorption compressor [23] and for hydrogen storage in a thermal energy storage unit working at 15 K [14]. In the present application, to avoid a cryopump working at high temperatures, the hydrogen desorption leading to the ON state should occur up to 400 K, whereas adsorption, leading to the OFF state, needs an equilibrium pressure of 0.01 mbar (Figure 6) for $T \geq 150$ K. Despite the extensive investigation performed on materials for $H_2$ absorption, only few data are available in this temperature and pressure range; taking into account these criteria, the intermetallic $ZrMn_2H_2$ (hydrogenate form) seems to be the most appropriate choice (Figure 7 solid lines) [15], [24].

The $ZrMn_2$ intermetallic materials were prepared by arc melting a mixture of 99.9% pure metals under argon atmosphere. Due to the high vapor pressure of manganese, and to compensate their possible losses by evaporation during melting, a 10-20% excess of this metal was considered. After each melting procedure, the sample was turned out and re-melted again for three times to

obtain a homogeneous material. Powder X-ray diffraction patterns were collected at room temperature from fine powdering the samples and using Cu Kα radiation with a 2θ-step size of 0.02º from 10º to 70º. The analysis of the diffractograms indicate that the samples are mainly constituted by $ZrMn_2$ (~95% vol.) with minor amounts of Mn (~5% vol.). Following the process described in [25], [26], the activation of $ZrMn_2$ under $H_2$ was made at 50 bar under pure hydrogen on a stainless steel (316) plug & flow type reactor (continuous type reactor). A pressure controller to manage the reactor internal pressure and a mass flow controller to adjust the hydrogen flow (50 $cm^3$/min) were used. The following procedure was employed:

i) Reactor purge at atmospheric pressure with hydrogen (50 $cm^3$/min; 30 min);
ii) Raise of pressure until 50 bar;
iii) Raise of temperature until 600 ºC;
iv) At 600 ºC for 1h;
v) Decrease of temperature until room temperature, maintaining the pressure at 50 bar;
vi) Release of pressure until atmospheric pressure.

This treatment was repeated three times. A nitrogen-filled glove box ($O_2$ and $H_2O$ content < 3 ppm) was used to handle the activated samples.

A rudimentary experimental setup was built to check if the pressure-temperature equilibrium curve of this material was compatible with our requirements in the 150 K to 400 K range. The setup consisted in a 0.5 $cm^3$ SS cell filled with ≈ 2 g of ZrMn2 and connected to a ≈ 26 $cm^3$ volume at room temperature. A thermocouple type K and a heating resistor was thermally coupled to this cell to manage its temperature. This cell is slowly introduced in a partially filled liquid nitrogen Dewar or heated in this $N_2$ atmosphere to obtain a characterization over the temperature range of interest. The equilibrium pressure is measured by two different pressure transducers (0-13 mbar, capacitance sensor and 0-20 bar, piezoresistive sensor).

Figure 7 shows the obtained results for two different batches compared to literature data [15], [24]. Despite their rough character, these measurements showed that the equilibrium pressure $P(T)$ seems significantly higher compared to the literature, further studies should be carried out to verify these results. Let us note that these measurements were performed with a [H]/[Mn] (total number of hydrogen atoms / total number of manganese atoms) ratio of about 60% to avoid saturation of ZrMn2 by hydrogen. Some measurements performed in the 300 K to 400 K temperature range (not shown) indicate that, at constant temperature, the equilibrium pressure increases as the [H]/[Mn] ratio increases; once again, a more rigorous characterization is needed

to determine if such increase is intrinsic to this compound or if monophasic samples would lead to an independent equilibrium pressure with hydrogenation, as far saturation is not reached as it is the case, for instance, for a $LaNi_5$ ($LaNi_5H_5$) compound [27]. However, even with this equilibrium pressure being higher than expected, this material seems to fulfill our needs: 0.01 mbar is reached at a temperature of 140 K and 100 mbar around 290 K. So, it was decided to use this material for the hydrogen cryopump.

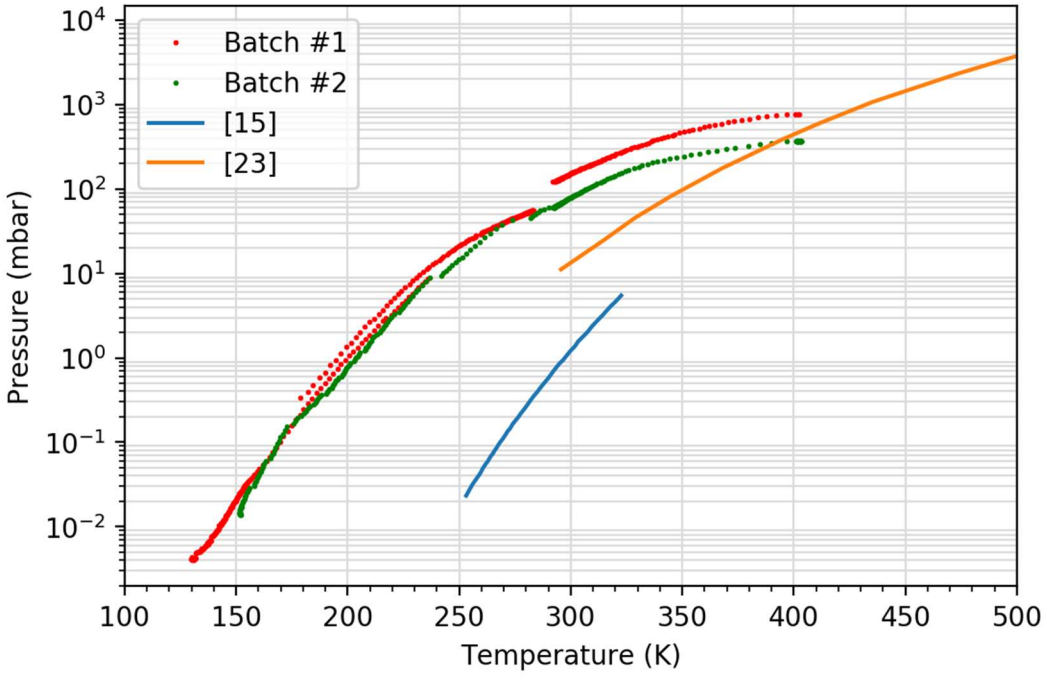


**Figure 7:** Equilibrium pressure-temperature curve of two synthetized batches of the metal hydride $ZrMn_2H_x$ and comparison with literature.

### 4.2 Results with ZrMn2 cryopump

As depicted in Figure 2, a small cryopump was coupled through a short SS capillary (≈ 30 mm) to the cold block of GGHS #2. This cryopump was thermalized to the same part by a copper thermal link to speed up its cooling. Its volume was around 0.08 $cm^3$ and charged with 260 mg of ZrMn2 (batch #2) in an argon-filled glove box. For the first characterizations, the small copper portion was not pinched and the GGHS was connected to the room temperature gas manifold to charge it with hydrogen gas. Three different hydrogen fillings were tested using low [H]/[Mn] ratio to turn more favorable the OFF state at 150 K.

The full GGHS functionality was tested by measuring the ON↔OFF transition curve by varying the cryopump temperature. The conductance results, obtained with the dynamic method (Section 2.3), are displayed in Figure 8 for these three hydrogen fillings. The “S-shaped”

curves, similar to those of Figure 6, indicates that, as expected, the $H_2$ pressure in the gap increases with the cryopump temperature. At $T \approx 150$ K, the GGHS conductance reaches the OFF-state value (≈8 mW/K) for the 1.1 % and 5.4 % filling whereas, for the 16% filling, it seems not fully reached. In the transition regime, at a given temperature, the heat switch conductance clearly increases with the $H_2$ quantity in the system, confirming that the $P-T$ equilibrium curve of this $ZrMn_2$ material is then dependent of the adsorbed H2 quantity. For instance, at $T = 250$ K and combining the data from Figure 7 and Figure 8, it can be deduced that the pressure in the switch is approximately 0.65 mbar, 1.1 mbar and 3.5 mbar for the 1.1%, 5.4% and 16% filling ratios respectively. As already mentioned for the GGHS using activated charcoal [9], [20], such a characteristic can be useful as it allows to tune the ON and OFF switching temperatures in a certain range just by varying the $H_2$ quantity in the system.

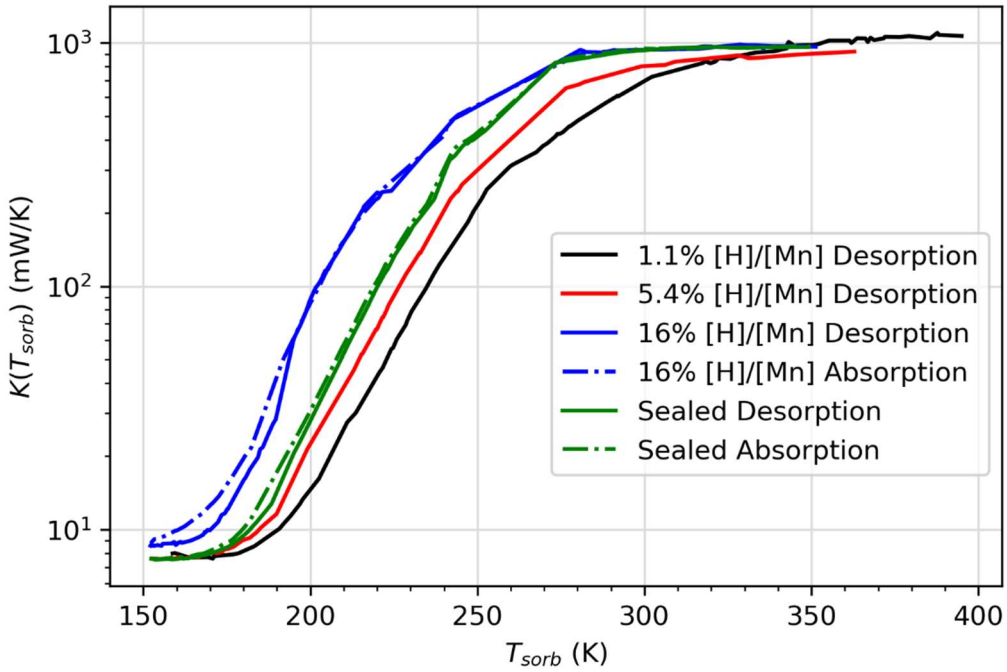


**Figure 8:** Measured thermal conductance of the GGHS #2 as a function of the hydrogen cryopump temperature for different filling [H]/[Mn] ratios.

Regarding the ON state (cryopump at high temperature), the thermal conductance reaches a constant value (≈ 1000 mW/K) for all $H_2$ fillings, as expected for the viscous conduction regime. However, note that this value is slightly less than the value obtained without cryopump (≈1350 mW/K, referring to Figure 6). This fact could be explained by supposing that the gas desorbed from the $ZrMn_2$ on heating it up to 330 K is not enough to reach the pressure needed to achieve a full viscous conduction. Comparing with the results displayed in Figure 6, this value of 1000 mW/K would correspond to a gas-gap pressure of 30 mbar whatever the $H_2$ filling

ratio. This pressure value is rather small compared to the obtained $P-T$ equilibrium curve (Figure 7), where this pressure is reached at ≈ 250 K. We looked without success for some experimental errors that could explain this discrepancy between these two ON state conductance values. Additional work is needed to understand if this issue is due to $ZrMn_2$ absorption characteristics or to another unknown reason.

A significant hysteresis during a desorption-absorption cycle would further complicate the use of such GGHS, then its thermal conductance was determined in both heating and cooling of the cryopump using, approximately, the same heating/cooling rate (±12 K/hour). Figure 8 displays these results for the 16% filling in dashed and thick lines for absorption (cooling) and desorption (heating) respectively. Within the experimental error, no significant hysteresis was detected, and a similar conclusion was obtained for the other two filling ratios.

In the framework of the future use of this device, we were more interested in avoiding high cryopump temperatures to reach the ON state rather than a very low OFF conductance, then we decided to seal the GGHS with a $H_2$ quantity corresponding to the 16% filling ratio. After this sealing, the new ON↔OFF curve was measured (green lines of Figure 8): its extreme conductance values of both ON and OFF conductance values remained similar to those measured before and no significant hysteresis is detected. The main difference between the 16% curve is that the S-shaped curve became significantly narrower (temperature axis): the intermediate region between +10% of the OFF value and -10% of the ON value was ≈105 K, 110 K and 125 K for the 16%, 5.4% and 1.1% filling ratio respectively, and it decreased down to 80 K after sealing the GGHS. This result can be understood by accounting that, after the sealing, the hydrogen gas remaining in the SS capillary connected to the gas manifold is no longer included in the system. Then, less gas is needed to be absorbed to reach the OFF state and the pressure decreases faster as the cryopump is cooled. As already mentioned, the OFF state obtained with this sealed switch was characterized on a larger heating power range (Figure 5) and the results are like those obtained by external gas pumping. The thermal characteristics of such sealed device shows that the main goal of this GGHS were fulfilled.

Let us note that this resulting GGHS is not only able to toggle between two distinct conducting states. As a matter of fact, this not so reduced temperature interval of 80 K between these two extreme states can be easily used to turn this device into a tuneable thermal link able to vary smoothly its thermal conductance by more than two orders of magnitude.

## 5. Conclusions

Three dilatation GGHSs were built and tested in the 150 K to 300 K temperature range. Contrarily to those presented in earlier works, the different parts were joint together by a high temperature silver brazing, which turns these devices more structurally reliable. Using an improved brazing procedure with temperature control to avoid inhomogeneities which may lead to greater gap lengths, gap length as short as 18 µm at 150 K were obtained in two devices due to the natural difference of the CTE between copper and SS. To obtain the highest possible ON state thermal conductance in this temperature range, the GGHS should use hydrogen gas and one of the devices was extensively characterized using such gas where a ON/OFF thermal conductance ratio of 145 was measured. To turn this device compact and autonomous, a hydrogen cryopump was integrated using the intermetallic $ZrMn_2H_x$ to allow the switching action of the GGHS just by controlling the cryopump temperature. Using such an alloy, we showed that both ON and OFF states can be obtained within the temperature range of interest (for $T \geq 150$ K). The sealed device, 260 mg of $ZrMn_2$ in the cryopump, offers a $T_{OFF}/T_{ON}$ temperature of 170 K / 250 K. An extended study of this intermetallic material could lead to substantial improvements of the device and would show how tunable are its characteristics. Moreover, beyond $ZrMn_2$, the extensive investigation performed on the materials suitable for $H_2$ storage should be revisited to build a GGHS working at higher temperatures than that studied in this article, while keeping $H_2$, the best conducting gas, as the transport medium.

## 6. References


[1] M. Dietrich, a. Euler, and G. Thummes, "A compact thermal heat switch for cryogenic space applications operating near 100K," *Cryogenics (Guildf).*, vol. 59, pp. 70–75, Jan. 2014, doi: 10.1016/j.cryogenics.2013.11.004.

[2] S. Vanapalli, R. Keijzer, P. Buitelaar, and H. J. M. ter Brake, "Cryogenic flat-panel gas-gap heat switch," *Cryogenics (Guildf).*, vol. 78, pp. 83–88, Sep. 2016, doi: 10.1016/j.cryogenics.2016.07.006.

[3] M. Donabedian, *Spacecraft Thermal Control Handbook, Volume II: Cryogenics*. 2004.

[4] M. J. Dipirro and P. J. Shirron, "Heat switches for ADRs," *Cryogenics (Guildf).*, vol. 62, pp. 172–176, 2014, doi: 10.1016/j.cryogenics.2014.03.017.

[5] B. Marland, D. Bugby, and C. Stouffer, "Development and testing of an advanced cryogenic thermal switch and cryogenic thermal switch test bed," *Cryogenics (Guildf).*,

vol. 44, no. 6–8, pp. 413–420, Jun. 2004, doi: 10.1016/j.cryogenics.2004.03.014.

[6] L. Duband, L. Clerc, E. Ercolani, L. Guillemet, and R. Vallcorba, “Herschel flight models sorption coolers,” *Cryogenics (Guildf).*, vol. 48, no. 3–4, pp. 95–105, Mar. 2008, doi: 10.1016/j.cryogenics.2008.03.016.

[7] G. Bonfait, I. Catarino, J. Afonso, D. Martins, M. Linder, and L. Duband, “20K Energy storage unit,” *Cryogenics (Guildf).*, vol. 49, no. 7, pp. 326–333, Jul. 2009, doi: 10.1016/j.cryogenics.2009.03.003.

[8] I. Catarino, J. Afonso, D. Martins, M. Linder, L. Duband, and G. Bonfait, “6K solid state Energy Storage Unit,” *Cryogenics (Guildf).*, vol. 50, no. 2, pp. 102–110, Feb. 2010, doi: 10.1016/j.cryogenics.2009.12.002.

[9] I. Catarino, G. Bonfait, and L. Duband, “Neon gas-gap heat switch,” *Cryogenics (Guildf).*, vol. 48, no. 1–2, pp. 17–25, Jan. 2008, doi: 10.1016/j.cryogenics.2007.09.002.

[10] J. Franco, D. Martins, I. Catarino, and G. Bonfait, “Narrow gas gap in cryogenic heat switch,” *Appl. Therm. Eng.*, vol. 70, no. 1, pp. 115–121, Sep. 2014, doi: 10.1016/j.applthermaleng.2014.04.062.

[11] J. Franco, B. Galinhas, P. B. de Sousa, D. Martins, I. Catarino, and G. Bonfait, “Building a Thinner Gap in a Gas-Gap Heat Switch,” *Phys. Procedia*, vol. 67, pp. 1117–1122, 2015, doi: 10.1016/j.phpro.2015.06.173.

[12] J. Barreto *et al.*, “80 K vibration-free cooler for potential future Earth observation missions,” *IOP Conf. Ser. Mater. Sci. Eng.*, vol. 755, p. 012016, Jun. 2020, doi: 10.1088/1757-899X/755/1/012016.

[13] D. Pearson, R. Bowman, M. Prina, and P. Wilson, “The Planck sorption cooler: Using metal hydrides to produce 20K,” *J. Alloys Compd.*, vol. 446–447, pp. 718–722, 2007, doi: 10.1016/j.jallcom.2006.11.202.

[14] P. Borges de Sousa, D. Martins, M. Linder, J. Noite, and G. Bonfait, “Liquid-gas hydrogen energy storage unit for the 15–17 K temperature range using an expansion volume at room temperature,” *Appl. Therm. Eng.*, 2017, doi: 10.1016/j.applthermaleng.2017.06.134.

[15] S. Vanapalli, B. Colijn, C. Vermeer, H. Holland, T. Tirolien, and H. J. M. ter Brake, “A Passive, Adaptive and Autonomous Gas Gap heat Switch,” *Phys. Procedia*, vol. 67, pp.

1206–1211, 2015, doi: 10.1016/j.phpro.2015.06.191.

[16] E. D. Marquardt, J. P. Le, and R. Radebaugh, “Cryogenic Material Properties Database,” in *Cryocoolers 11*, 2002.

[17] “Online Materials Information Resource - MatWeb.” p. 2909, 2002.

[18] Y. S. Touloukian, R. . Kirby, R. E. Taylor, and P. D. Desai, “Volume 12 : Thermal expansion - Metallic Elements and Alloys,” *Thermophys. Prop. Matter-the TPRC Data Ser.*, 1970.

[19] E. W. Lemmon, M. L. Huber, and M. O. Mclinden, “REFPROP 9.1,” *NIST Stand. Ref. database*, 2013.

[20] D. Martins *et al.*, “Sorption characterization and actuation of a gas-gap heat switch,” *Sensors Actuators A Phys.*, vol. 171, no. 2, pp. 324–331, Nov. 2011, doi: 10.1016/j.sna.2011.08.017.

[21] A. O. R. P. Der Nigohossian G., “Adsorption de L’Helium 4 par le Charbon Actif,” *Colloq. Int. du Vide du Froid, Grenoble, Fr.*, p. 22, 1969.

[22] D. Martins, I. Catarino, J. Franco, L. Ribeiro, and G. Bonfait, “Controlled actuation of a Gas-Gap Heat Switch,” in *ICEC 24*, 2012.

[23] G. Morgante *et al.*, “Cryogenic characterization of the Planck sorption cooler system flight model,” *J. Instrum.*, vol. 4, no. 12, pp. T12016–T12016, Dec. 2009, doi: 10.1088/1748-0221/4/12/T12016.

[24] J. F. Burger, “Cryogenic Microcooling, A micromachined cold stage operating with a sorption compressor in a vapor compression cycle,” Twente University Press (TUP), Netherlands, 2001.

[25] M. Yoshida and E. Akiba, “Hydrogen absorbing-desorbing properties and crystal structure of the ZrTiNiMnV AB2 Laves phase alloys,” *J. Alloys Compd.*, 1995, doi: 10.1016/0925-8388(95)01518-3.

[26] T. Kodama, “An attempt to estimate the extent of the single phase region of the ZrMn2 phase by means of the X-ray diffraction-profile halfwidths,” *J. Alloys Compd.*, vol. 256, no. 1–2, pp. 263–268, 1997, doi: 10.1016/S0925-8388(96)03015-0.

[27] P. Bhandari *et al.*, “Sorption Cryocooler Development for the Planck Surveyor Mission,” *Astrophys. Lett. Commun.*, vol. 37, p. 227, 2000.

APPENDIX B

# Sips Parameters

Table B.1: Sips parameters of nitrogen on HKUST-1 adsorption isotherms.

| $T$[K] | $C_0$ [mol kg$^{-1}$] | $n$ | $a$[$\times 10^{-3}$bar$^{-1}$] | Dev. [%] |
|---|---|---|---|---|
| 130 | 25.724 | 4.129 | 1.0E+0 | 2.4 |
| 140 | 23.548 | 3.542 | 1.0E+0 | 3.0 |
| 150 | 20.826 | 2.583 | 1.0E+0 | 2.7 |
| 160 | 17.822 | 1.674 | 1.0E+0 | 1.3 |
| 170 | 16.963 | 1.452 | 658.6E-3 | 1.6 |
| 180 | 15.994 | 1.258 | 466.0E-3 | 1.9 |
| 190 | 15.339 | 1.130 | 328.3E-3 | 2.3 |
| 200 | 14.753 | 1.064 | 239.0E-3 | 2.1 |
| 220 | 13.999 | 1.063 | 121.2E-3 | 2.3 |
| 240 | 13.120 | 1.044 | 73.5E-3 | 2.3 |
| 260 | 12.532 | 1.040 | 45.6E-3 | 1.8 |
| 280 | 11.856 | 1.025 | 32.3E-3 | 2.1 |
| 300 | 11.864 | 1.048 | 21.6E-3 | 2.6 |
| 320 | 11.473 | 1.039 | 16.5E-3 | 2.6 |
| 340 | 10.862 | 0.998 | 14.3E-3 | 2.4 |
| 360 | 10.201 | 0.979 | 12.5E-3 | 2.8 |
| 380 | 9.529 | 0.960 | 11.3E-3 | 3.4 |
| 400 | 8.900 | 0.942 | 10.3E-3 | 3.9 |
| 420 | 7.613 | 0.885 | 11.2E-3 | 2.3 |
| 440 | 7.002 | 0.870 | 10.8E-3 | 3.2 |
| 460 | 6.574 | 0.864 | 10.1E-3 | 5.8 |
| 480 | 5.973 | 0.845 | 10.1E-3 | 6.9 |
| 500 | 5.432 | 0.822 | 10.1E-3 | 14.1 |

Table B.2: Sips parameters of neon

| | UiO-66 | | | | HKUST-1 | | | | $Co_3(ndc)_3(dabco)$ | | | |
|---|---|---|---|---|---|---|---|---|---|---|---|---|
| $T$[K] | $C_0$ [mol kg$^{-1}$] | $n$ | $a$[$\times 10^{-3}$] | Dev. [%] | $C_0$ [mol kg$^{-1}$] | $n$ | $a$[$\times 10^{-3}$bar$^{-1}$] | Dev. [%] | $C_0$ [mol kg$^{-1}$] | $n$ | $a$[$\times 10^{-3}$bar$^{-1}$] | Dev. [%] |
| 77 | 22.624 | 1.262 | 59.23 | 0.5 | 32.262 | 1.278 | 54.38 | 0.7 | 32.171 | 1.198 | 67.50 | 3.5 |
| 80 | 21.842 | 1.217 | 55.67 | 0.7 | 30.315 | 1.204 | 53.81 | 0.8 | 31.840 | 1.175 | 59.46 | 3.3 |
| 85 | 21.648 | 1.207 | 40.31 | 1.0 | 30.536 | 1.195 | 38.57 | 0.3 | 31.303 | 1.130 | 44.90 | 2.4 |
| 90 | 21.331 | 1.186 | 30.63 | 1.1 | 30.229 | 1.168 | 30.31 | 0.3 | 30.868 | 1.100 | 34.94 | 2.0 |
| 95 | 20.473 | 1.152 | 25.37 | 1.1 | 31.038 | 1.162 | 22.74 | 0.4 | 30.602 | 1.081 | 27.59 | 1.6 |
| 100 | 19.983 | 1.128 | 20.94 | 1.1 | 31.245 | 1.142 | 18.30 | 0.3 | 30.296 | 1.063 | 22.51 | 1.3 |
| 110 | 19.398 | 1.094 | 14.76 | 1.2 | 26.873 | 1.044 | 17.50 | 1.3 | 29.826 | 1.039 | 15.92 | 0.8 |
| 120 | 19.240 | 1.072 | 10.74 | 1.1 | 23.264 | 0.970 | 16.97 | 2.8 | 29.597 | 1.023 | 11.87 | 0.5 |
| 130 | 16.785 | 0.999 | 10.49 | 2.1 | 20.192 | 0.920 | 16.50 | 3.8 | 26.838 | 0.977 | 10.92 | 1.6 |
| 140 | 14.675 | 0.942 | 10.28 | 3.9 | 17.572 | 0.882 | 16.22 | 4.6 | 23.669 | 0.933 | 10.74 | 3.2 |
| 150 | 12.903 | 0.898 | 10.20 | 5.3 | 15.551 | 0.851 | 15.89 | 5.7 | 21.077 | 0.898 | 10.59 | 4.6 |
| 160 | 11.309 | 0.865 | 10.20 | 6.4 | 13.792 | 0.829 | 15.68 | 6.4 | 18.884 | 0.872 | 10.49 | 5.7 |
| 170 | 10.009 | 0.842 | 10.09 | 7.6 | 12.320 | 0.812 | 15.49 | 7.1 | 17.050 | 0.851 | 10.37 | 6.6 |
| 180 | 8.924 | 0.820 | 9.99 | 8.8 | 11.083 | 0.798 | 15.33 | 7.9 | 15.427 | 0.836 | 10.32 | 7.2 |
| 190 | 8.047 | 0.794 | 9.95 | 9.9 | 10.040 | 0.788 | 15.21 | 8.4 | 14.091 | 0.821 | 10.29 | 8.1 |
| 200 | 7.201 | 0.783 | 9.92 | 10.0 | 9.164 | 0.777 | 15.09 | 8.9 | 12.937 | 0.809 | 10.23 | 8.6 |
| 220 | 5.755 | 0.773 | 10.03 | 9.8 | 7.709 | 0.763 | 14.95 | 9.6 | 11.067 | 0.791 | 10.16 | 9.4 |
| 240 | 4.835 | 0.761 | 9.94 | 10.5 | 6.626 | 0.765 | 14.69 | 9.5 | 9.626 | 0.778 | 10.12 | 10.2 |
| 260 | 4.130 | 0.745 | 9.92 | 11.3 | 5.774 | 0.744 | 14.69 | 11.0 | 8.463 | 0.767 | 10.13 | 10.7 |
| 280 | 3.590 | 0.735 | 9.90 | 12.0 | 5.108 | 0.738 | 14.58 | 11.4 | 7.540 | 0.758 | 10.12 | 11.4 |
| 300 | 3.183 | 0.729 | 9.82 | 12.5 | 4.556 | 0.733 | 14.50 | 11.9 | 6.778 | 0.745 | 10.12 | 11.6 |
| 320 | 2.826 | 0.723 | 9.76 | 13.2 | 4.116 | 0.727 | 14.40 | 12.5 | 5.900 | 0.713 | 10.54 | 6.6 |
| 340 | 2.543 | 0.714 | 9.79 | 13.5 | 3.723 | 0.725 | 14.35 | 12.7 | | | | |
| 360 | 2.312 | 0.705 | 9.76 | 14.2 | 3.397 | 0.720 | 14.30 | 13.0 | | | | |
| 380 | 2.112 | 0.698 | 9.78 | 14.5 | 1.986 | 0.748 | 22.03 | 10.2 | | | | |
| 400 | 1.949 | 0.693 | 9.73 | 15.8 | 1.820 | 0.751 | 21.96 | 10.4 | | | | |
| 420 | 1.802 | 0.687 | 9.74 | 16.5 | | | | | | | | |
| 440 | 1.679 | 0.688 | 9.67 | 17.0 | | | | | | | | |
| 460 | 1.412 | 0.651 | 10.90 | 9.8 | | | | | | | | |
| 480 | 1.326 | 0.667 | 10.81 | 10.2 | | | | | | | | |
| 500 | 1.247 | 0.702 | 10.61 | 11.2 | | | | | | | | |

APPENDIX C

# Technical Drawings

Let us note that many pieces and their drawings were developed in collaboration with Active Space Technologies and, therefore, cannot be published in this dissertation.

| ITEM NO. | PART Name | QTY. |
|---|---|---|
| 1 | Vessel | 1 |
| 2 | Vessel Cap | 1 |
| 3 | Gland 1/4" SWLK | 1 |
| 4 | Split Nut 1/4" SWLK | 1 |
| 5 | Blind 1/8" SWLK | 1 |
| 6 | Female Nut 1/8 SWLK | 1 |
| 7 | 1/4" Heater | 1 |

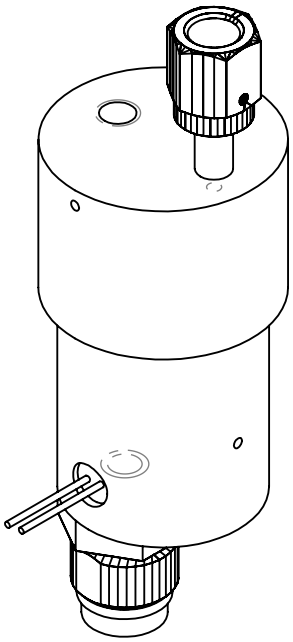

Isometric View

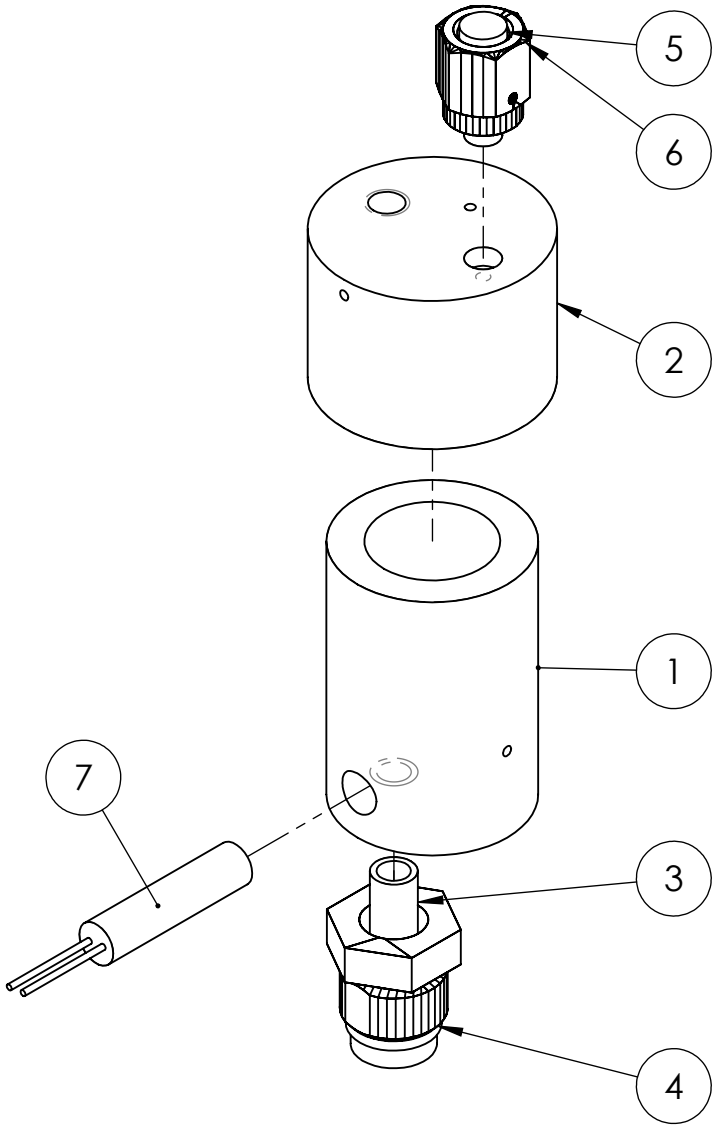


Exploded View

**Ajustamento deslizante justo para brazagem entre:**
- Vessel (1) e Gland 1/4" SWLK (3)
- Vessel Cap (2) e Blind 1/8" SWLK (4)

**Ajustamento deslizante justo entre:**
- 1/4" heater (7) - Vessel (2)

| | | | | | | |
|---|---|---|---|---|---|---|
| UNLESS OTHERWISE SPECIFIED:<br>DIMENSIONS ARE IN MILLIMETERS<br>SURFACE FINISH:<br>TOLERANCES:<br>LINEAR:<br>ANGULAR: | | FINISH: | | DEBUR AND BREAK SHARP EDGES | DO NOT SCALE DRAWING | REVISION |
| | NAME | SIGNATURE | DATE | | TITLE: | |
| DRAWN | Jorge Barreto | | 27-09-16 | | | |
| CHK'D | Gregoire Bonfait | | 27-09-16 | | | |
| APPV'D | | | | | | |
| MFG | | | | | | |
| Q.A | | | | MATERIAL: | DWG NO. Célula de Adsorção | A4 |
| | | | | | | |
| | | | | | | |
| | | | | WEIGHT: | SCALE:1:2 | SHEET 1 OF 1 |

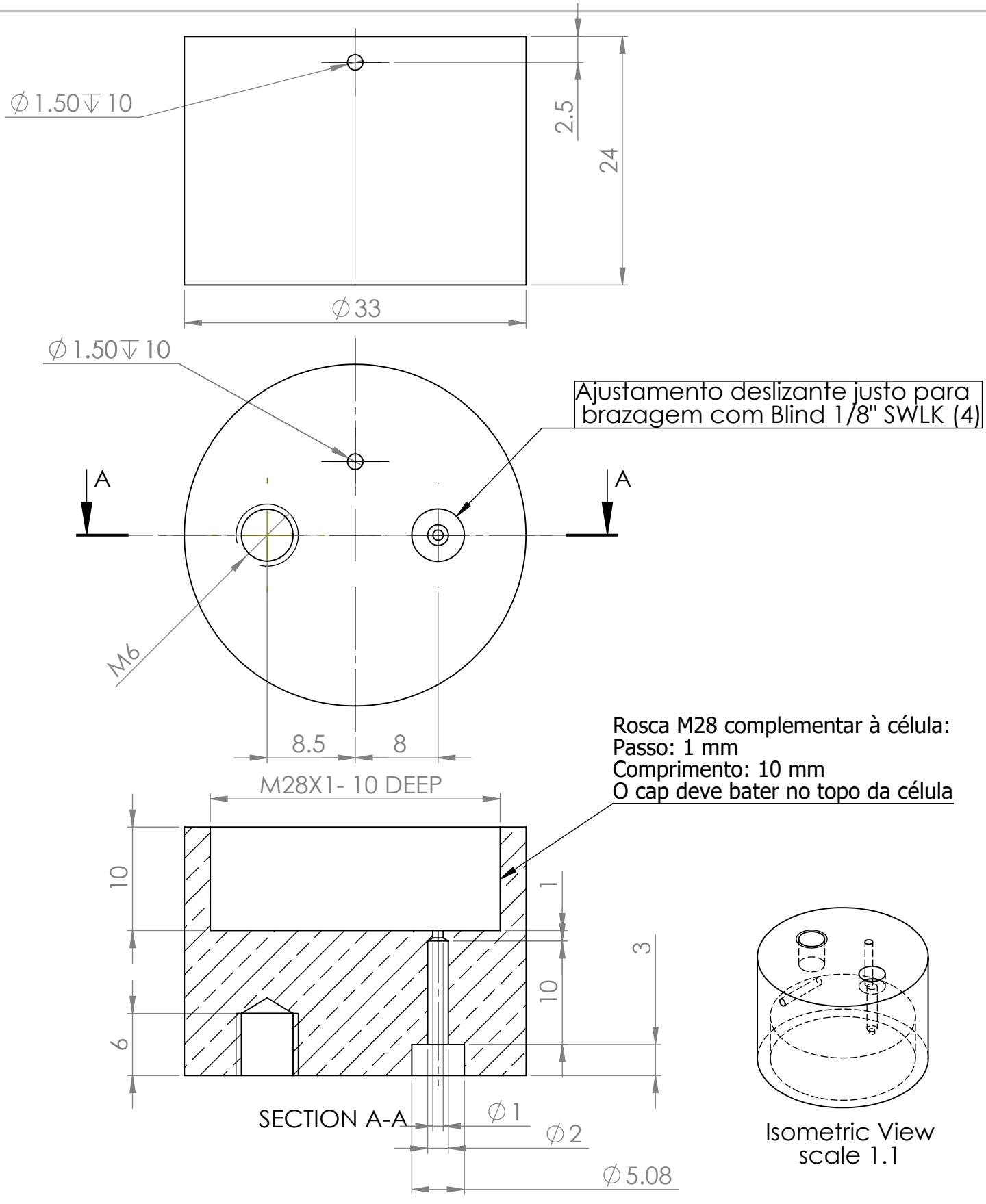




Isometric View
scale 1.1

| | | | | | | |
|---|---|---|---|---|---|---|
| UNLESS OTHERWISE SPECIFIED:<br>DIMENSIONS ARE IN MILLIMETERS<br>SURFACE FINISH:<br>TOLERANCES:<br>LINEAR: 0.1<br>ANGULAR: | | FINISH: | | DEBUR AND BREAK SHARP EDGES | DO NOT SCALE DRAWING | REVISION |
| | NAME | SIGNATURE | DATE | | TITLE: | |
| DRAWN | Jorge Barreto | | 27-09-16 | | Cap da célula de adsorção p/ altas pressões ver.2 | |
| CHK'D | Gregoire Bonfait | | 27-09-16 | | | |
| APPV'D | | | | | | |
| MFG | | | | | | |
| Q.A | | | | MATERIAL: | DWG NO. | A4 |
| | | | | Cobre | Cap2 | |
| | | | | WEIGHT: | SCALE:2:1 | SHEET 1 OF 1 |

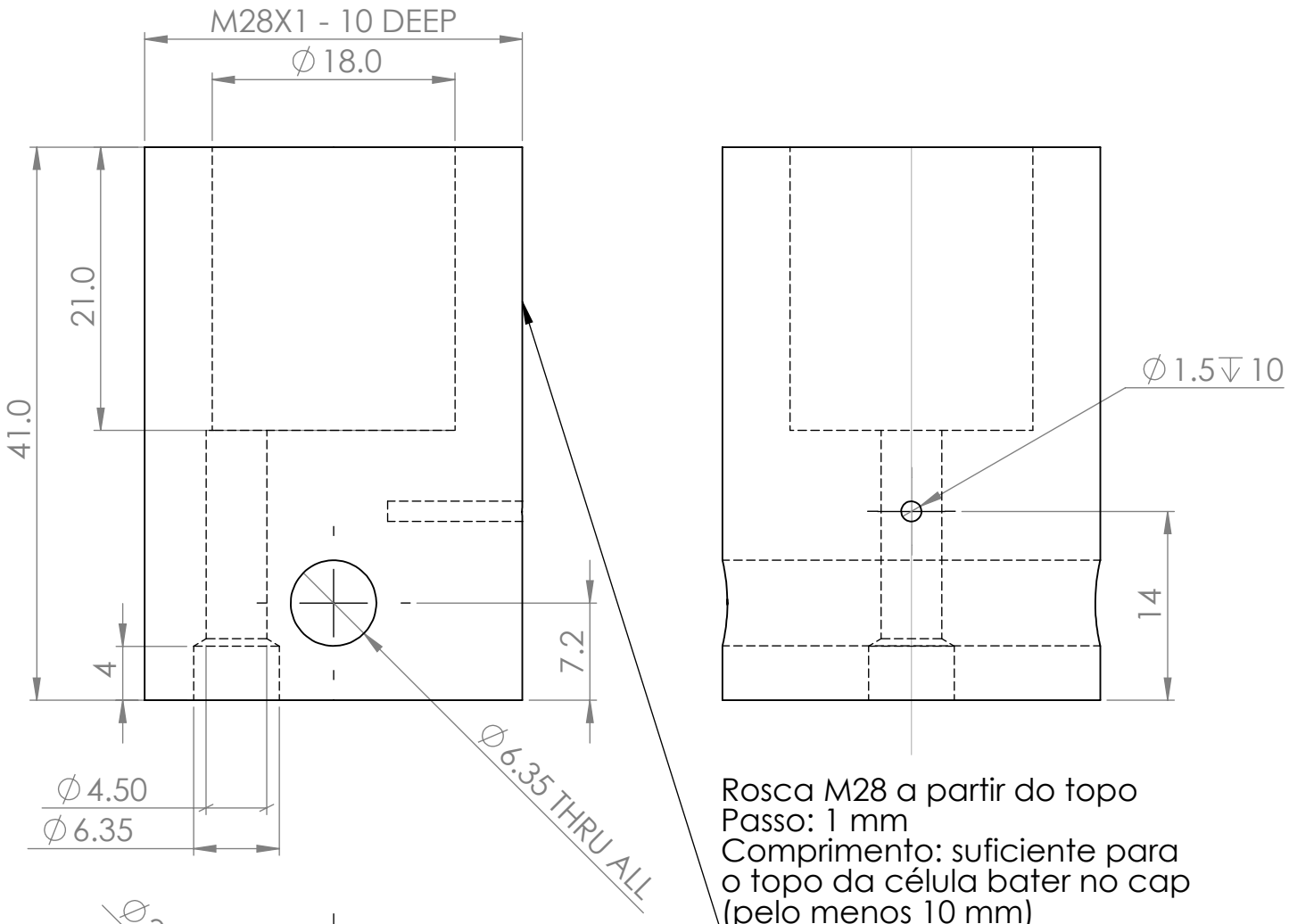


Rosca M28 a partir do topo
Passo: 1 mm
Comprimento: suficiente para o topo da célula bater no cap (pelo menos 10 mm)

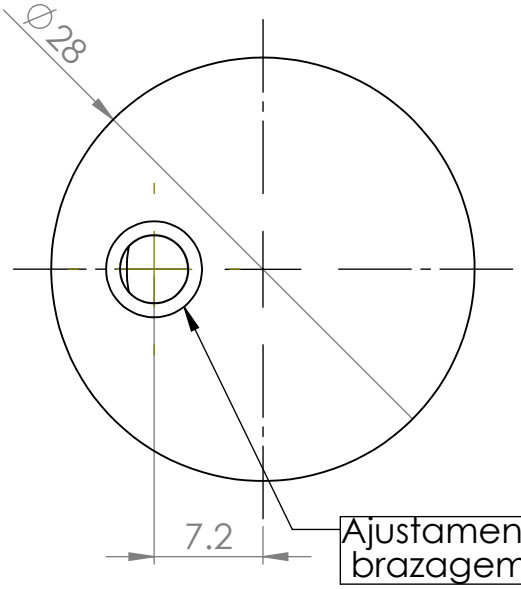


Ajustamento deslizante justo para brazagem com Gland 1/4" SWLK (3)

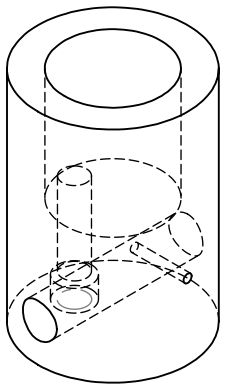

Isometric View
scale 1:1

| | | | | | | |
|---|---|---|---|---|---|---|
| UNLESS OTHERWISE SPECIFIED:<br>DIMENSIONS ARE IN MILLIMETERS<br>SURFACE FINISH:<br>TOLERANCES:<br>LINEAR: 0.1<br>ANGULAR: | | FINISH: | | DEBUR AND BREAK SHARP EDGES | DO NOT SCALE DRAWING | REVISION |
| | NAME | SIGNATURE | DATE | | TITLE: | |
| DRAWN | Jorge Barreto | | 27-09-16 | | Célula de adosorção p/ altas pressões ver.2 | |
| CHK'D | Gregoire Bonfait | | 27-09-16 | | | |
| APPV'D | | | | | | |
| MFG | | | | | | |
| Q.A | | | | MATERIAL: Copper | DWG NO. Vessel | A4 |
| | | | | WEIGHT: | SCALE:2:1 | SHEET 1 OF 1 |

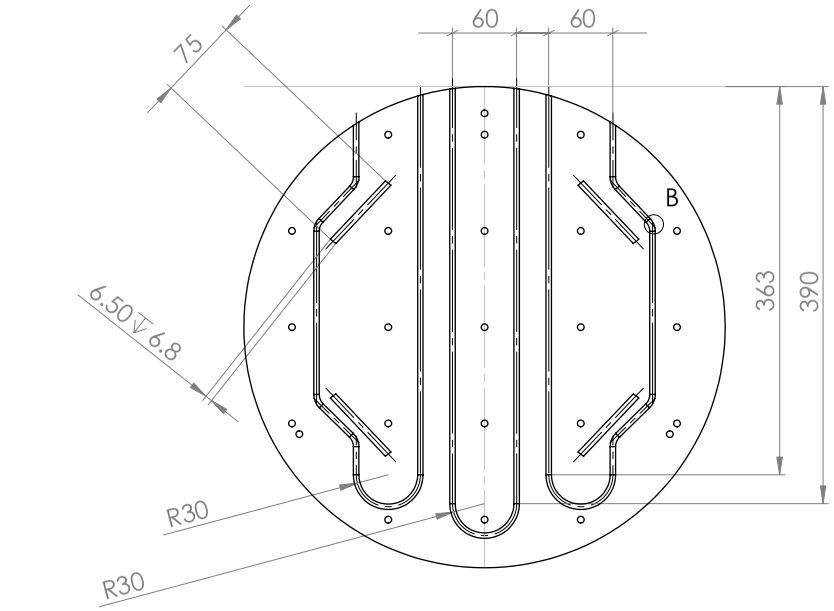


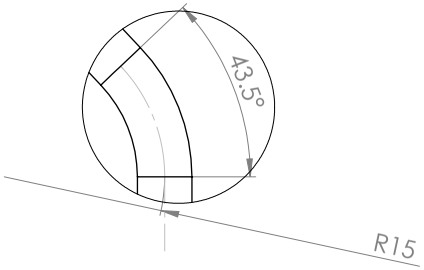


DETAIL B
SCALE 2 : 1

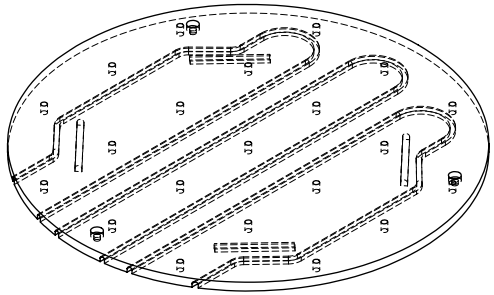

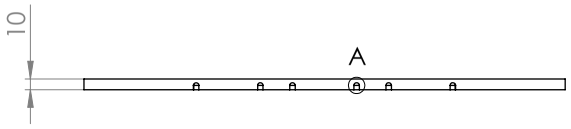


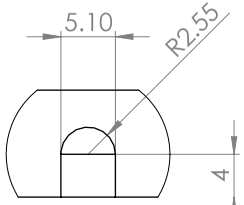


DETAIL A
SCALE 2 : 1

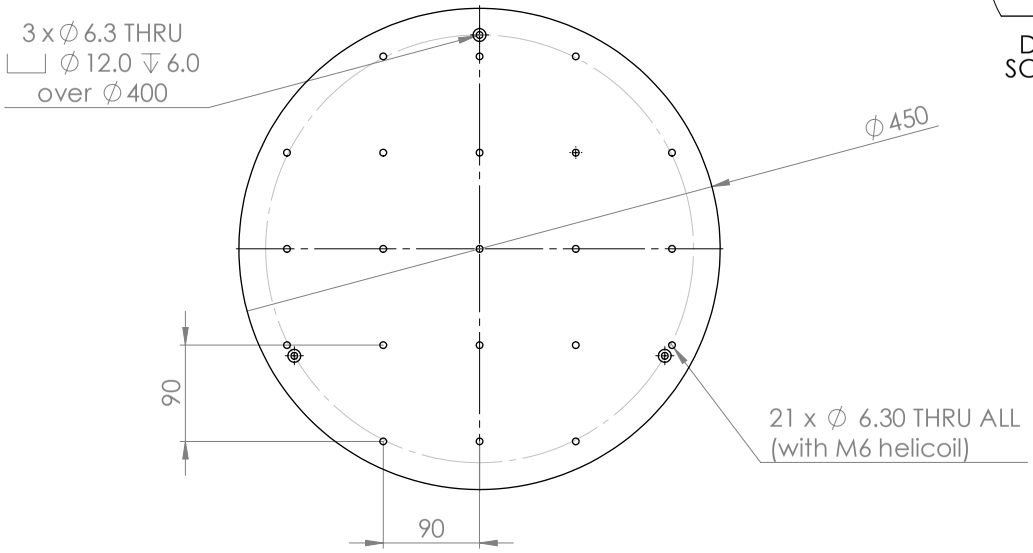


| | | | | | | | |
|---|---|---|---|---|---|---|---|
| UNLESS OTHERWISE SPECIFIED: DIMENSIONS ARE IN MILLIMETERS SURFACE FINISH: TOLERANCES: LINEAR: ANGULAR: | | FINISH: | | DEBURR AND BREAK SHARP EDGES | | DO NOT SCALE DRAWING | REVISION |
| | NAME | SIGNATURE | DATE | | | TITLE: Al. Cold Plate | |
| DRAWN | J. Barreto | | 27/03/17 | | | | |
| CHK'D | | | | | | | |
| APPV'D | | | | | | | |
| MFG | | | | | | | |
| Q.A | | | | MATERIAL: Aluminum 6082-T6 | | DWG NO. ColdPlate | A3 |
| | | | | WEIGHT: 4.1 kg | | SCALE:1:5 | SHEET 1 OF 1 |